Laser-Induced Breakdown Spectroscopy and Plasmas Containing Cyanide

A Dissertation Presented for the

Doctor of Philosophy

Degree

The University of Tennessee, Knoxville

Christopher Matthew Helstern

December 2020

© by Christopher Matthew Helstern, 2020
All Rights Reserved.

I would like to dedicate this dissertation to my wife, Lyndsey, for her undying love and support.

Acknowledgments

Throughout my academic career at the University of Tennessee, I have received encouragement, support, and contributions from several individuals in completing this work. First, I would like to thank my mentor and advisor, Dr. Christian Parigger for his guidance, motivation, inspiration, and commitment. I would also like to thank my committee members: Dr. Reza Abedi, Dr. Marianne Breinig, and Dr. Steve Johnston for their time and effort providing valuable insight and recommendations. Additionally, I would like to thank Alexander Terekhov with the Center for Laser Applications and classmate Ghaneshwar Gautum for their assistance in conducting experiments for this dissertation. Lastly, I would like to thank Kevin Fu for his consultation and advice on many topics within this dissertation and my daughter, Aubrey Johnson, for her assistance in the design of figures within this work.

The secret to doing anything is believing that you can do it. Anything that you believe you can do strong enough, you can do. Anything. As long as you believe.

Robert Ross

Abstract

This dissertation focuses on laser-induced plasma of diatomic molecular cyanide. Optical breakdown plasma generation is produced by high-peak-power 1064 nm Q-switched nanosecond pulsed radiation. Laser-induced breakdown is performed on a 1:1 molar gas mixture of carbon dioxide and nitrogen held at a fixed pressure of 101 kPa (760 Torr), a 1:1 molar gas mixture of carbon dioxide and nitrogen held at a fixed pressure of 276 kPa (2070 Torr), and a flowing 1:1 molar gas mixture of carbon dioxide and nitrogen flowing at a rate of 100 mL per minute. Plasma shockwave measurements in laboratory air are shown to determine the shock front geometry and confirm the shockwave dynamics in the carbon dioxide and nitrogen gaseous mixtures are similar to that of air. Of specific interest are the effects of the shockwave on the cyanide plasma distribution at early time delays. Analysis of line-of-sight measurements determine the excitation temperatures and electron densities. Specifically, atomic carbon spectra show increased electron densities near the shockwave, which are determined by inferred Stark widths and Stark shifts of an atomic carbon line overlapping with the cyanide violet band heads. Fitting of measured diatomic molecular cyanide spectra to theoretically produced cyanide spectra allow for the determination of excitation temperatures, which showed higher excitation temperatures near the shockwave. Lastly, inferences of the spatiotemporal plasma distribution are performed using integral inversion techniques.

Table of Contents

1 Introduction **1**

1.1 Motivation 1

1.2 Laser-Induced Breakdown Spectroscopy 3

1.3 Molecular Spectroscopy 5

2 Experimental Details **9**

2.1 Experimental Details of Shadowgraph Imaging 9

2.2 Laser-Induced Breakdown in a Fixed Volume of Gas 11

2.3 Laser-Induced Breakdown in a Flowing Gas 15

3 Theoretical Basis **17**

3.1 Laser-Induced Shockwave 17

3.2 Electron Density 21

3.2.1 Atomic Carbon Line Interference 21

3.2.2 Line Broadening and Deconvolution 24

3.2.3 Method for Calculating Electron Density 25

3.3 Nelder-Mead Temperature Fitting 25

3.4 Abel Inversion 29

4 Results and Discussion **33**

4.1 Shadowgraphs 33

4.2 Cyanide Spectra 40

4.2.1 CO_2 and N_2 Gaseous Mixture of Fixed Volume 40

4.2.2 Flowing CO_2 and N_2 Gaseous Mixture 50
4.3 Cyanide Temperature 50
4.3.1 CO_2 and N_2 Gaseous Mixture of Fixed Volume at Atmospheric Pressure 50
4.3.2 CO_2 and N_2 Gaseous Mixture of Fixed Volume at 276 kPa (2070 Torr) 57
4.3.3 CO_2 and N_2 Flowing Gaseous Mixture 62
4.4 Calculated Electron Densities 65
4.4.1 Stark Widths and Stark Shifts in the CO_2 and N_2 Gaseous Mixture of Fixed Volume at Atmospheric Pressure 65
4.4.2 Stark Shifts in the CO_2 and N_2 Gaseous Mixture of Fixed Volume at 276 kPa (2070 Torr) 76
4.4.3 Stark Widths and Stark Shifts in the CO_2 and N_2 Flowing Gaseous Mixture 81
4.5 Abel Inverted Cyanide Spectra 87
4.5.1 Abel Inverted CN Spectra in a Fixed Volume of the 1:1 Molar CO_2 and N_2 Gaseous Mixture Held at Atmospheric Pressure 87
4.5.2 Abel Inverted CN Spectra in a Fixed Volume of the 1:1 Molar CO_2 and N_2 Gaseous Mixture Held at 276 kPa (2070 Torr) 92
4.5.3 Abel Inverted CN Spectra in the 1:1 Molar CO_2 and N_2 Flowing Gaseous Mixture 106

5 Conclusions **115**

Bibliography **119**

Appendices **131**

A Matlab NMT Fitting Routine **132**

B Matlab Peak Fitting Routine **141**

C Matlab Abel Inversion **143**

D Chemical Equilibrium with Applications (CEA) **152**

E Publications and Presentations **154**

Vita **158**

List of Tables

3.1 Computed shockwave radii for SATP air and for molar CN mixture, 160 mJ 19

3.2 Computed shockwave radii for SATP air and for molar CN mixture, 200 mJ 19

3.3 Computed shockwave velocity for SATP air and for molar CN mixture, 160 mJ 19

3.4 Computed shockwave velocity for SATP air and for molar CN mixture, 200 mJ 20

3.5 Computed shockwave Mach numbers for SATP air and for molar CN mixture, 160 mJ 20

3.6 Computed shockwave Mach numbers for SATP air and for molar CN mixture, 200 mJ 20

4.1 Computed shockwave radii versus measured shockwave radii for SATP air, 170 mJ 39

4.2 Calculated shockwave velocities and Mach numbers for SATP air, 170 mJ . . 39

4.3 Measured plasma kernel radii for SATP air, 170 mJ 39

4.4 Computed shockwave radii versus plasma radius for 1:1 molar CO_2:N_2 gaseous mixture held at atmospheric pressure, 170 mJ 71

4.5 Computed shockwave radii versus plasma radius for the 1:1 molar CO_2:N_2 flowing gaseous mixture, 170 mJ 86

List of Figures

1.1 Electronic, vibrational, and rotational spectra as a result of molecular potentials between two electronic levels. 6
1.2 Potential curves of CN. 8

2.1 Schematic of the apparatus used for the shadowgraph experiments. 10
2.2 Schematic of the apparatus used for the laser-induced breakdown experiments. 13
2.3 Pictures of the gas chamber (top left), the mechanical vacuum pumps connected to the pressure system (top right), and the differential pressure gauge (bottom). 14
2.4 Picture of the gas chamber and flowmeter. 16

3.1 Recorded raw spectra 3.7 µs after optical breakdown in a 1:1 CO_2:N_2 atmospheric gas mixture [69]. 22
3.2 Recorded raw spectra 0.45 µs after optical breakdown in a 1:1 CO_2:N_2 atmospheric gas mixture. The * near 386.2 nm represents the atomic carbon line measured in second order [63, 69]. 23
3.3 Peakfit script applied to a measured line-of-sight CN spectra. 26
3.4 Fit to measured CN spectra at a slit height of 6.9 mm at a time delay of 1.2 µs, Temperature = 8748 K, fit FWHM = 0.39 nm 28
3.5 Line-of-sight geometry and Abel inversion method. 30

4.1 Single-shot shadowgraph of expanding laser-induced plasma initiated with a 170 mJ, 6 ns, 1064 nm focused beam, and imaged using a 5 ns, 532 nm backlight that was time-delayed by 0.20±0.05 µs. 34

4.2 Single-shot shadowgraph of expanding laser-induced plasma initiated with a 170 mJ, 6 ns, 1064 nm focused beam, and imaged using a 5 ns, 532 nm backlight that was time-delayed by 1.00±0.05 µs. 35
4.3 Single-shot shadowgraph of expanding laser-induced plasma initiated with a 170 mJ, 6 ns, 1064 nm focused beam, and imaged using a 5 ns, 532 nm backlight that was time-delayed by 1.20±0.05 µs. 36
4.4 Single-shot shadowgraph of expanding laser-induced plasma initiated with a 170 mJ, 6 ns, 1064 nm focused beam, and imaged using a 5 ns, 532 nm backlight that was time-delayed by 2.20±0.05 µs. 37
4.5 Single-shot shadowgraph of expanding laser-induced plasma initiated with a 170 mJ, 6 ns, 1064 nm focused beam, and imaged using a 5 ns, 532 nm backlight that was time-delayed by 4.20±0.05 µs. 38
4.6 Optical breakdown CN spectra in a 1:1 molar CO_2:N_2 gas mixture held at atmospheric pressure for time delays of (**a**) 200 ns, (**b**) 450 ns, (**c**) 700 ns, and (**d**) 950 ns. Spectrometer-detector gatewidth: 125 ns. ⋆, second-order atomic carbon line [70]. 41
4.7 Optical breakdown CN spectra in a 1:1 molar CO_2:N_2 gas mixture held at atmospheric pressure for time delays of (**a**) 1200 ns, (**b**) 1450 ns, (**c**) 1700 ns, and (**d**) 1950 ns. Spectrometer-detector gatewidth: 125 ns. ⋆, second-order atomic carbon line. 42
4.8 Optical breakdown CN spectra in a 1:1 molar CO_2:N_2 gas mixture held at atmorspheric pressure for time delays of (**a**) 2200 ns, (**b**) 2450 ns, (**c**) 2700 ns, and (**d**) 2950 ns. Spectrometer-detector gatewidth: 125 ns. ⋆, second-order atomic carbon line. 43
4.9 Optical breakdown CN spectra in a 1:1 molar CO_2:N_2 gas mixture held at atmospheric pressure for time delays of (**a**) 200 ns, (**b**) 450 ns, (**c**) 700 ns, and (**d**) 950 ns, recorded with 309 nm cut-on wavelength filter for suppression of 193.09 nm second order atomic carbon line [70]. 44

4.10 Optical breakdown CN spectra in a 1:1 molar CO_2:N_2 gas mixture held at atmospheric pressure for time delays of (**a**) 1200 ns, (**b**) 1450 ns, (**c**) 1700 ns, and (**d**) 1950 ns, recorded with 309 nm cut-on wavelength filter for suppression of 193.09 nm second order atomic carbon line. 45
4.11 Optical breakdown CN spectra in a 1:1 molar CO_2:N_2 gas mixture held at atmospheric pressure for time delays of (**a**) 2200 ns, (**b**) 2450 ns, (**c**) 2700 ns, and (**d**) 2950 ns, recorded with 309 nm cut-on wavelength filter for suppression of 193.09 nm second order atomic carbon line. 46
4.12 Optical breakdown CN spectra in a 1:1 molar CO_2:N_2 gas mixture held at 276 kPa (2070 Torr) for time delays of (**a**) 200 ns, (**b**) 450 ns, (**c**) 700 ns, and (**d**) 950 ns. Spectrometer-detector gatewidth: 125 ns. $\star$, second-order atomic carbon line. 47
4.13 Optical breakdown CN spectra in a 1:1 molar CO_2:N_2 gas mixture held at 276 kPa (2070 Torr) for time delays of (**a**) 1200 ns, (**b**) 1450 ns, (**c**) 1700 ns, and (**d**) 1950 ns. Spectrometer-detector gatewidth: 125 ns. $\star$, second-order atomic carbon line. 48
4.14 Optical breakdown CN spectra in a 1:1 molar CO_2:N_2 gas mixture held at 276 kPa (2070 Torr) for time delays of (**a**) 2200 ns, (**b**) 2450 ns, (**c**) 2700 ns, and (**d**) 2950 ns. Spectrometer-detector gatewidth: 125 ns. 49
4.15 Optical breakdown CN spectra in a 1:1 molar CO_2:N_2 flowing gas mixture for time delays of (**a**) 200 ns, (**b**) 450 ns, (**c**) 700 ns, and (**d**) 950 ns. Spectrometer-detector gatewidth: 125 ns. $\star$, second-order atomic carbon line. 51
4.16 Optical breakdown CN spectra in a 1:1 molar CO_2:N_2 flowing gas mixture for time delays of (**a**) 1200 ns, (**b**) 1450 ns, (**c**) 1700 ns, and (**d**) 1950 ns. Spectrometer-detector gatewidth: 125 ns. $\star$, second-order atomic carbon line. 52
4.17 Optical breakdown CN spectra in a 1:1 molar CO_2:N_2 flowing gas mixture for time delays of (**a**) 2200 ns, (**b**) 2450 ns, (**c**) 2700 ns, and (**d**) 2950 ns. Spectrometer-detector gatewidth: 125 ns. $\star$, second-order atomic carbon line. 53

4.18 Optical breakdown CN spectra in a 1:1 molar CO_2:N_2 flowing gas mixture for time delays of (**a**) 200 ns, (**b**) 450 ns, (**c**) 700 ns, and (**d**) 950 ns, recorded with 309 nm cut-on wavelength filter for suppression of 193.09 nm second order atomic carbon line. 54
4.19 Optical breakdown CN spectra in a 1:1 molar CO_2:N_2 flowing gas mixture for time delays of (**a**) 1200 ns, (**b**) 1450 ns, (**c**) 1700 ns, and (**d**) 1950 ns, recorded with 309 nm cut-on wavelength filter for suppression of 193.09 nm second order atomic carbon line. 55
4.20 Optical breakdown CN spectra in a 1:1 molar CO_2:N_2 flowing gas mixture for time delays of (**a**) 2200 ns, (**b**) 2450 ns, (**c**) 2700 ns, and (**d**) 2950 ns, recorded with 309 nm cut-on wavelength filter for suppression of 193.09 nm second order atomic carbon line. 56
4.21 Temperature vs. slit height for filtered line-of-sight CN spectra for fixed volume of 1:1 molar CO_2:N_2 gaseous mixture held at atmospheric pressure with 450 ns (left) and 700 ns (right) time delay [70 ,71]. 58
4.22 Temperature vs. slit height for filtered line-of-sight CN spectra for fixed volume of 1:1 molar CO_2:N_2 gaseous mixture held at atmospheric pressure with 950 ns (left) and 1200 ns (right) time delay [70 ,71]. 58
4.23 Temperature vs. slit height for filtered line-of-sight CN spectra for fixed volume of 1:1 molar CO_2:N_2 gaseous mixture held at atmospheric pressure with 1450 ns (left) and 1700 ns (right) time delay. 59
4.24 Temperature vs. slit height for filtered line-of-sight CN spectra for fixed volume of 1:1 molar CO_2:N_2 gaseous mixture held at atmospheric pressure with 1950 ns (left) and 2200 ns (right) time delay. 59
4.25 Temperature vs. slit height for filtered line-of-sight CN spectra for fixed volume of 1:1 molar CO_2:N_2 gaseous mixture held at 276 kPa (2070 Torr) with 450 ns (left) and 700 ns (right) time delay. 60
4.26 Temperature vs. slit height for filtered line-of-sight CN spectra for fixed volume of 1:1 molar CO_2:N_2 gaseous mixture held at 276 kPa (2070 Torr) with 950 ns (left) and 1200 ns (right) time delay. 60

4.27 Temperature vs. slit height for filtered line-of-sight CN spectra for fixed volume of 1:1 molar CO_2:N_2 gaseous mixture held at 276 kPa (2070 Torr) with 1450 ns (left) and 1700 ns (right) time delay. 61
4.28 Temperature vs. slit height for filtered line-of-sight CN spectra for fixed volume of 1:1 molar CO_2:N_2 gaseous mixture held at 276 kPa (2070 Torr) with 1950 ns (left) and 2200 ns (right) time delay. 61
4.29 Temperature vs. slit height for filtered line-of-sight CN spectra for a flowing 1:1 molar CO_2:N_2 gaseous mixture with 450 ns (left) and 700 ns (right) time delay [70]. 63
4.30 Temperature vs. slit height for filtered line-of-sight CN spectra for a flowing 1:1 molar CO_2:N_2 gaseous mixture with 950 ns (left) and 1200 ns (right) time delay [70]. 63
4.31 Temperature vs. slit height for filtered line-of-sight CN spectra for a flowing 1:1 molar CO_2:N_2 gaseous mixture with 1450 ns (left) and 1700 ns (right) time delay. 64
4.32 Temperature vs. slit height for filtered line-of-sight CN spectra for a flowing 1:1 molar CO_2:N_2 gaseous mixture with 1950 ns (left) and 2200 ns (right) time delay. 64
4.33 Inferred widths (top) and calculated electron densities (bottom) of CI 193.09 nm atmoic carbon line in second order vs. slit height for the 1:1 molar CO_2:N_2 gaseous mixture held at atmospheric pressure with 450 ns time delay. 66
4.34 Inferred widths (top) and calculated electron densities (bottom) of CI 193.09 nm atmoic carbon line in second order vs. slit height for the 1:1 molar CO_2:N_2 gaseous mixture held at atmospheric pressure with 700 ns time delay [70 ,71]. 66
4.35 Inferred widths (top) and calculated electron densities (bottom) of CI 193.09 nm atmoic carbon line in second order vs. slit height for the 1:1 molar CO_2:N_2 gaseous mixture held at atmospheric pressure with 950 ns time delay [70 ,71]. 67
4.36 Inferred widths (top) and calculated electron densities (bottom) of CI 193.09 nm atmoic carbon line in second order vs. slit height for the 1:1 molar CO_2:N_2 gaseous mixture held at atmospheric pressure with 1200 ns time delay. . . . 67

4.37 Inferred widths (top) and calculated electron densities (bottom) of CI 193.09 nm atmoic carbon line in second order vs. slit height for the 1:1 molar CO_2:N_2 gaseous mixture held at atmospheric pressure with 1450 ns time delay. . . . 68
4.38 Inferred widths (top) and calculated electron densities (bottom) of CI 193.09 nm atmoic carbon line in second order vs. slit height for the 1:1 molar CO_2:N_2 gaseous mixture held at atmospheric pressure with 1700 ns time delay. . . . 68
4.39 Inferred widths (top) and calculated electron densities (bottom) of CI 193.09 nm atmoic carbon line in second order vs. slit height for the 1:1 molar CO_2:N_2 gaseous mixture held at atmospheric pressure with 1950 ns time delay. . . . 69
4.40 Inferred widths (top) and calculated electron densities (bottom) of CI 193.09 nm atmoic carbon line in second order vs. slit height for the 1:1 molar CO_2:N_2 gaseous mixture held at atmospheric pressure with 2200 ns time delay. . . . 69
4.41 Inferred shifts (top) and calculated electron densities (bottom) of CI 193.09 nm atmoic carbon line in second order vs. slit height for the 1:1 molar CO_2:N_2 gaseous mixture held at atmospheric pressure with 450 ns time delay. 72
4.42 Inferred shifts (top) and calculated electron densities (bottom) of CI 193.09 nm atmoic carbon line in second order vs. slit height for the 1:1 molar CO_2:N_2 gaseous mixture held at atmospheric pressure with 700 ns time delay. 72
4.43 Inferred shifts (top) and calculated electron densities (bottom) of CI 193.09 nm atmoic carbon line in second order vs. slit height for the 1:1 molar CO_2:N_2 gaseous mixture held at atmospheric pressure with 950 ns time delay. 73
4.44 Inferred shifts (top) and calculated electron densities (bottom) of CI 193.09 nm atmoic carbon line in second order vs. slit height for the 1:1 molar CO_2:N_2 gaseous mixture held at atmospheric pressure with 1200 ns time delay. . . . 73
4.45 Inferred shifts (top) and calculated electron densities (bottom) of CI 193.09 nm atmoic carbon line in second order vs. slit height for the 1:1 molar CO_2:N_2 gaseous mixture held at atmospheric pressure with 1450 ns time delay. . . . 74
4.46 Inferred shifts (top) and calculated electron densities (bottom) of CI 193.09 nm atmoic carbon line in second order vs. slit height for the 1:1 molar CO_2:N_2 gaseous mixture held at atmospheric pressure with 1700 ns time delay. . . . 74

4.47 Inferred shifts (top) and calculated electron densities (bottom) of CI 193.09 nm atmoic carbon line in second order vs. slit height for the 1:1 molar CO_2:N_2 gaseous mixture held at atmospheric pressure with 1950 ns time delay. . . . 75
4.48 Inferred shifts (top) and calculated electron densities (bottom) of CI 193.09 nm atmoic carbon line in second order vs. slit height for the 1:1 molar CO_2:N_2 gaseous mixture held at atmospheric pressure with 2200 ns time delay. . . . 75
4.49 Inferred shifts (top) and calculated electron densities (bottom) of CI 193.09 nm atmoic carbon line in second order vs. slit height for the 1:1 molar CO_2:N_2 gaseous mixture held at 276 kPa (2070 Torr) with 450 ns time delay. 77
4.50 Inferred shifts (top) and calculated electron densities (bottom) of CI 193.09 nm atmoic carbon line in second order vs. slit height for the 1:1 molar CO_2:N_2 gaseous mixture held at 276 kPa (2070 Torr) with 700 ns time delay. 77
4.51 Inferred shifts (top) and calculated electron densities (bottom) of CI 193.09 nm atmoic carbon line in second order vs. slit height for the 1:1 molar CO_2:N_2 gaseous mixture held at 276 kPa (2070 Torr) with 950 ns time delay. 78
4.52 Inferred shifts (top) and calculated electron densities (bottom) of CI 193.09 nm atmoic carbon line in second order vs. slit height for the 1:1 molar CO_2:N_2 gaseous mixture held at 276 kPa (2070 Torr) with 1200 ns time delay. 78
4.53 Inferred shifts (top) and calculated electron densities (bottom) of CI 193.09 nm atmoic carbon line in second order vs. slit height for the 1:1 molar CO_2:N_2 gaseous mixture held at 276 kPa (2070 Torr) with 1450 ns time delay. 79
4.54 Inferred shifts (top) and calculated electron densities (bottom) of CI 193.09 nm atmoic carbon line in second order vs. slit height for the 1:1 molar CO_2:N_2 gaseous mixture held at 276 kPa (2070 Torr) with 1700 ns time delay. 79
4.55 Inferred shifts (top) and calculated electron densities (bottom) of CI 193.09 nm atmoic carbon line in second order vs. slit height for the 1:1 molar CO_2:N_2 gaseous mixture held at 276 kPa (2070 Torr) with 1950 ns time delay. 80
4.56 Inferred shifts (top) and calculated electron densities (bottom) of CI 193.09 nm atmoic carbon line in second order vs. slit height for the 1:1 molar CO_2:N_2 gaseous mixture held at 276 kPa (2070 Torr) with 2200 ns time delay. 80

4.57 Inferred widths (top) and calculated electron densities (bottom) of CI 193.09 nm atmoic carbon line in second order vs. slit height for the 1:1 molar CO_2:N_2 flowing gaseous mixture with 450 ns time delay. 82
4.58 Inferred widths (top) and calculated electron densities (bottom) of CI 193.09 nm atmoic carbon line in second order vs. slit height for the 1:1 molar CO_2:N_2 flowing gaseous mixture with 700 ns time delay [70]. 82
4.59 Inferred widths (top) and calculated electron densities (bottom) of CI 193.09 nm atmoic carbon line in second order vs. slit height for the 1:1 molar CO_2:N_2 flowing gaseous mixture with 950 ns time delay [70]. 83
4.60 Inferred widths (top) and calculated electron densities (bottom) of CI 193.09 nm atmoic carbon line in second order vs. slit height for the 1:1 molar CO_2:N_2 flowing gaseous mixture with 1200 ns time delay. 83
4.61 Inferred widths (top) and calculated electron densities (bottom) of CI 193.09 nm atmoic carbon line in second order vs. slit height for the 1:1 molar CO_2:N_2 flowing gaseous mixture with 1450 ns time delay. 84
4.62 Inferred widths (top) and calculated electron densities (bottom) of CI 193.09 nm atmoic carbon line in second order vs. slit height for the 1:1 molar CO_2:N_2 flowing gaseous mixture with 1700 ns time delay. 84
4.63 Inferred widths (top) and calculated electron densities (bottom) of CI 193.09 nm atmoic carbon line in second order vs. slit height for the 1:1 molar CO_2:N_2 flowing gaseous mixture with 1950 ns time delay. 85
4.64 Inferred widths (top) and calculated electron densities (bottom) of CI 193.09 nm atmoic carbon line in second order vs. slit height for the 1:1 molar CO_2:N_2 flowing gaseous mixture with 2200 ns time delay. 85
4.65 Inferred shifts (top) and calculated electron densities (bottom) of CI 193.09 nm atmoic carbon line in second order vs. slit height for the 1:1 molar CO_2:N_2 flowing gaseous mixture with 450 ns time delay. 88
4.66 Inferred shifts (top) and calculated electron densities (bottom) of CI 193.09 nm atmoic carbon line in second order vs. slit height for the 1:1 molar CO_2:N_2 flowing gaseous mixture with 700 ns time delay. 88

4.67 Inferred shifts (top) and calculated electron densities (bottom) of CI 193.09 nm atmoic carbon line in second order vs. slit height for the 1:1 molar CO_2:N_2 flowing gaseous mixture with 950 ns time delay. 89
4.68 Inferred shifts (top) and calculated electron densities (bottom) of CI 193.09 nm atmoic carbon line in second order vs. slit height for the 1:1 molar CO_2:N_2 flowing gaseous mixture with 1200 ns time delay. 89
4.69 Inferred shifts (top) and calculated electron densities (bottom) of CI 193.09 nm atmoic carbon line in second order vs. slit height for the 1:1 molar CO_2:N_2 flowing gaseous mixture with 1450 ns time delay. 90
4.70 Inferred shifts (top) and calculated electron densities (bottom) of CI 193.09 nm atmoic carbon line in second order vs. slit height for the 1:1 molar CO_2:N_2 flowing gaseous mixture with 1700 ns time delay. 90
4.71 Inferred shifts (top) and calculated electron densities (bottom) of CI 193.09 nm atmoic carbon line in second order vs. slit height for the 1:1 molar CO_2:N_2 flowing gaseous mixture with 1950 ns time delay. 91
4.72 Inferred shifts (top) and calculated electron densities (bottom) of CI 193.09 nm atmoic carbon line in second order vs. slit height for the 1:1 molar CO_2:N_2 flowing gaseous mixture with 2200 ns time delay. 91
4.73 Abel inverted CN spectra 1:1 molar CO_2:N_2 gaseous mixture held at atmospheric pressure with 200 ns (top), 450 ns (center), and 700 ns (bottom) time delay [70, 71]. 93
4.74 Abel inverted CN spectra 1:1 molar CO_2:N_2 gaseous mixture held at atmospheric pressure with 950 ns (top), 1200 ns (center), and 1450 ns (bottom) time delay [70, 71]. 94
4.75 Abel inverted CN spectra 1:1 molar CO_2:N_2 gaseous mixture held at atmospheric pressure with 1700 ns (top), 1950 ns (center), and 2200 ns (bottom) time delay. 95
4.76 Abel inverted CN spectra 1:1 molar CO_2:N_2 gaseous mixture held at atmospheric pressure with 2450 ns (top), 2700 ns (center), and 2950 ns (bottom) time delay. 96

4.77 Abel inverted CN spectra 1:1 molar CO_2:N_2 gaseous mixture held at atmospheric pressure with 3200 ns (top), 3450 ns (center), and 3700 ns (bottom) time delay. 97
4.78 Abel inverted CN spectra 1:1 molar CO_2:N_2 gaseous mixture held at atmospheric pressure with 3950 ns (top), 4200 ns (center), and 4450 ns (bottom) time delay. 98
4.79 Abel inverted CN spectra 1:1 molar CO_2:N_2 gaseous mixture held at atmospheric pressure with 4700 ns (top), 4950 ns (center), and 5200 ns (bottom) time delay. 99
4.80 Abel inverted CN spectra 1:1 molar CO_2:N_2 gaseous mixture held at 276 kPa (2070 Torr) with 200 ns (top), 450 ns (center), and 700 ns (bottom) time delay. 100
4.81 Abel inverted CN spectra 1:1 molar CO_2:N_2 gaseous mixture held at 276 kPa (2070 Torr) with 950 ns (top), 1200 ns (center), and 1450 ns (bottom) time delay. 101
4.82 Abel inverted CN spectra 1:1 molar CO_2:N_2 gaseous mixture held at 276 kPa (2070 Torr) with 1700 ns (top), 1950 ns (center), and 2200 ns (bottom) time delay. 102
4.83 Abel inverted CN spectra 1:1 molar CO_2:N_2 gaseous mixture held at 276 kPa (2070 Torr) with 2450 ns (top), 2700 ns (center), and 2950 ns (bottom) time delay. 103
4.84 Abel inverted CN spectra 1:1 molar CO_2:N_2 gaseous mixture held at 276 kPa (2070 Torr) with 3200 ns (top), 3450 ns (center), and 3700 ns (bottom) time delay. 104
4.85 Abel inverted CN spectra 1:1 molar CO_2:N_2 gaseous mixture held at 276 kPa (2070 Torr) with 3950 ns (top), 4200 ns (center), and 4450 ns (bottom) time delay. 105
4.86 Abel inverted CN spectra 1:1 molar CO_2:N_2 gaseous mixture held at 276 kPa (2070 Torr) with 4700 ns (top), 4950 ns (center), and 5200 ns (bottom) time delay. 107

4.87 Abel inverted CN spectra 1:1 molar CO_2:N_2 flowing gaseous mixture with 200 ns (top), 450 ns (center), and 700 ns (bottom) time delay. 108
4.88 Abel inverted CN spectra 1:1 molar CO_2:N_2 flowing gaseous mixture with 950 ns (top), 1200 ns (center), and 1450 ns (bottom) time delay. 109
4.89 Abel inverted CN spectra 1:1 molar CO_2:N_2 flowing gaseous mixture with 1700 ns (top), 1950 ns (center), and 2200 ns (bottom) time delay. 110
4.90 Abel inverted CN spectra 1:1 molar CO_2:N_2 flowing gaseous mixture with 2450 ns (top), 2700 ns (center), and 2950 ns (bottom) time delay. 111
4.91 Abel inverted CN spectra 1:1 molar CO_2:N_2 flowing gaseous mixture with 3200 ns (top), 3450 ns (center), and 3700 ns (bottom) time delay. 112
4.92 Abel inverted CN spectra 1:1 molar CO_2:N_2 flowing gaseous mixture with 3950 ns (top), 4200 ns (center), and 4450 ns (bottom) time delay. 113
4.93 Abel inverted CN spectra 1:1 molar CO_2:N_2 flowing gaseous mixture with 4700 ns (top), 4950 ns (center), and 5200 ns (bottom) time delay. 114

5.1 Single-shot shadowgraph of laser-induced plasma initiated with 90-mJ and 110-mJ, 5-ns, 532-nm focused beams, and imaged using two 5-ns, 532-nm back lights that are time-delayed by 0.03 μs, 0.45 μs, and 0.48 μs [70, 71]. . . 116

D.1 CN air at 1 atm versus temperature in chemical equilibirum. 152
D.2 CN 1:1 mole ratio CO_2:N_2 mixture at 1 atm versus temperature in chemical equilibirum. 153
D.3 Computed mole fractions of serveral species versus temperature for CN 1:1 mole ratio CO_2:N_2 mixture at 1 atm in chemical equilibirum. 153

Chapter 1

Introduction

1.1 Motivation

Cyanide (CN) has been of interest in a variety of research areas due to its existence in many forms in nature. CN is an integral part of amino acid, lipid, membrane, nucleotide, and protein production. Living organisms use cyanides as a source of nitrogen and a range of species can use cyanides as a mechanism for self-defense [1, 2, 3, 4]. Certain bacteria, fungi, and algae produce CN, and substantial amounts of CN are found in certain seeds and fruit stones, for example bitter almonds, apricots, apples, and peaches [5, 6]. CN is also found in interstellar space [7] and can be produced in oxygen-deficient conditions by combustion or pyrolysis of plastics derived from acrylonitrile [8]. Furthermore, cyanides can be instrumental in human applications such as copper, gold, silver, and zinc extraction due to its availability, effectiveness, and cost efficiency [9, 10]. Lastly, cyanides are a byproduct of many industrial processes, such as chemical and drug production, cosmetic manufacturing, electroplating, fiber synthesis, iron and steel production, and pesticide and plastic manufacturing [5, 11, 12]. Cyanides are linked to many organisms and produced through man-made processes, but they are highly toxic and can be lethal to humans.

Human intakes of cyanide (CN) can occur via ingestion, inhalation, or absorption through the skin. Humans can experience these intakes via consumption of foods containing cyanides, exposures to illicit use, smoke inhalation from building fires or cigarettes, or occupational hazards [13, 14, 15, 16]. Individuals experiencing acute intakes of CN, known as CN

poisoning, can display symptoms including shortness of breath, headache, dizziness, fast heart rate, vomiting, low blood pressure, seizures, loss of consciousness, and cardiac arrest [17]. CN poisoning is difficult to diagnosis due to the six biochemical abnormalities and 55 signs and symptoms that can occur in an exposed individual [17, 18]. Additionally, symptoms of CN poisoning are remarkably similar to symptoms of carbon monoxide poisoning, which can present challenges when treating fire victims [19]. Therefore, the best means of diagnosing CN poisoning is through the evaluation of CN blood concentration levels [19, 20, 21, 22]. CN blood concentration levels are categorized as mild when levels are 0.5–1 mg/L, moderate when levels are 1–2 mg/L, severe when levels are 2–3 mg/L, and lethal when levels are greater than 3 mg/L [17, 23, 24]. One issue that arises with the testing of CN blood concentration levels is that CN has a blood elimination half-life of about 1 hour due to the molecular instability of CN [25, 26]. Due to the poor stability [23] and short half-life of CN in blood, rapid sampling and analysis is necessary to assess CN poisonings especially in emergency settings [19, 22]. Treatment of cyanide (CN) poisoning is performed using antidotes such as hydroxocobalamin, methemoglobin inducers (including amyl nitrite, sodium nitrite, and 4-dimethylaminophenol), sodium thiosulfate, and dicobalt edetate (EDTA). Hydroxocobalamin is the preferred antidote due to its minimal side effects, but in rare occasions it can cause anaphylactic shock. Therefore, in cases where hydroxocobalamin is not available or cannot be used, methemoglobin inducers and dicobalt EDTA can serve as replacements. Caution must be used when using methemoglobin inducers and dicobalt EDTA as antidotes due to the cardiovascular side effects if CN is not present within individual being treated [27, 28]. Therefore, adequate diagnosis of CN poisoning is necessary before administering any antidote.

In order to diagnose cyanide (CN) poisonings and administer proper antidotes, detection methods must have a good limit of detection to distinguish between exposures and background concentrations, be accurate and precise, be handheld or portable, require minimal sample preparation, and have relative quick sample analysis [22]. Current detection methods include optical methods, electrochemical methods, mass spectrometry, gas chromatography, and quartz crystal mass monitors [29]. Although these methods are sufficient in detection of cyanides, they lack crucial requirements for diagnosis and treatment

of CN poisonings, with only 2,3-naphthalene dialdehyde (NDA), hydroxocyanocobinamide, and 2-nitro-5a-(2-(4-dimethylaminophenyl)-ethylene)-6,6-dimethyl-5a,6-dihydro-12H-indolo [2,1b] [1,3]benzoxazine (NDIB) most likely to produce a functional cyanide diagnostic [22]. Although there are potential detection methods that could be used for CN poisoning diagnosis, laser-induced breakdown spectroscopy can meet the requirements to properly identify CN in samples for diagnosis, due to its minimally invasive approach, short measurement acquisitions (on the order of microseconds), lack of sample preparation, and portability [30, 31, 32, 33, 34, 35, 36].

In addition to cyanide (CN) poisoning diagnosis, the detection of CN can be used for other medical applications such as the diagnosis of bacterial infections and forensic applications. For example, HCN can be produced by bacteria such as Pseudomonas aeruginosa, which can cause increased morbidity and mortality in immune-compromised patients, such as those with cystic fibrosis [37]. Detection of bacterial-produced HCN in the airways leads to earlier treatment of the immune-compromised infected with these bacteria. Forensic investigations also require an efficient means of detecting CN concentrations, which laser induced breakdown spectroscopy could provide. As time elapses, bacteriological activity in the blood causes CN instability [38, 39, 40]. Additionally, analysis of mouth and nose samples must be evaluated in a couple days, otherwise the elevated cyanide levels will be non-detectable using current toxicological testing [41].

1.2 Laser-Induced Breakdown Spectroscopy

Lasers are valuable in many applications and are an essential device for many fields of research which include biology, chemistry, and physics. Laser is an acronym for light amplification by stimulated emission radiation. Its theoretical groundwork was developed by Einstein through the re-derivation of Plank's radiation law using probability coefficients, known as the Einstein Coefficients, for stimulated emission of electromagnetic radiation [42]. After contributions from Landenberg in 1928 for the existence of stimulated emission, Fabrikant in 1939 for the predicted use of stimulated emission to amplify waves, Lamb in 1947 for experimentally demonstrating stimulated emission, and Kastler in 1950 for proposed method of optical pumping, which was experimentally demonstrated two years later, Maiman was

able to develop the first ruby laser in 1960 [43]. Shortly following, researchers around the world started performing experiments utilizing lasers. Experiments by Brech and Cross in 1962 of measured spectrum from laser-induced plasma and laser ablation experiments by Runge in 1964 were the beginning of the field of study known as Laser-Induced Breakdown Spectroscopy (LIBS) [44, 45]. Over time, LIBS has been utilized for the analysis of materials in solid, liquid, and gaseous forms to determine elemental composition. LIBS is used in numerous applications such as detection of hazardous contaminants in the environment [46], identification of hazardous materials of explosives and chemical and biological warfare agent surrogates [47, 48, 49, 50], glass discrimination in forensics [51], and gallstone evaluation in medicine [52]. LIBS is an advantageous technique due to being minimally destructive, not requiring sample preparation, in situ detection capabilities, and a straightforward experimental setup [53, 54, 55, 56, 57, 58, 59].

Typical LIBS experiments use focused light from a pulsed laser device to create a micro-plasma on a target surface. Plasma produced light emissions are imaged directly onto the entrance slit of a spectrometer, dispersion of light occurs and subsequently a distinctive spectrum is captured. Intensified charged couple devices (ICCD) are recording devices typically used in LIBS. Coupling an ICCD with a Czerny-Turner type spectrometer allows one to achieve temporal resolutions in the nanoscale range and spectral resolution on the order of 10^{-10} m; nevertheless, resolving small spectrum characteristics requires large spectrometers with long focal lengths, which are not ideal for in situ measurements. Therefore, using an Echelle type spectrometer, which can achieve resolutions on the order of 0.1 nm, may be an alternative for LIBS applications requiring smaller instrumentation.

Observing plasma spectroscopically greatly depends on the experimental conditions for the formation of plasma and the temporal resolution. Nanosecond pulsed lasers are used in laboratory settings for plasma initiation. A variety of phenomena occur as time elapses after plasma initiation. Ionization is occurring as the laser radiation is incident on the material, which causes continuum emissions to dominate. The duration of the continuum emission is determined by the pulse characteristics of the laser. Continuum emissions produced by nanosecond laser pulse durations typically last on the order of 100 ns. As the continuum diminishes, free electrons radiate energy causing recombination of free electrons and nuclei.

Due to this recombination, the atomic ion emissions are recognizable from the continuum. Following ionic emissions, atomic emissions become distinguishable and dominate until 1 µs after plasma formation. As the plasma cools, atomic and ionic emissions begin to weaken, and molecular emissions become visible, due to molecular bonding being stable. Molecular emissions are detectable on the order of microseconds following plasma formation and can even last on the order of hundreds of microseconds depending on the plasma conditions and molecule. In this dissertation molecular emission spectroscopy is of interest.

1.3 Molecular Spectroscopy

The molecular Hamiltonian determines the overall framework of the molecular emissions. The Hamiltonian accounts for electronic, vibrational, and rotational components due to vibrations and rotations associated with molecules. Additionally, the total molecular Hamiltonian contains influences due to molecular nuclei motion and nucleonic spins. This Hamiltonian consists of quantized rotations and vibrations. Spectral lines produced by vibrations and rotations correlate to transitions between quantum numbers associated with vibrations and rotations. The principal idea of a molecular emission is that there is a separate potential energy curve for each electronic state. Quantized vibrations represent splitting of these potentials and rotational splitting of these vibrations occur. Figure 1.1 shows the plotting of the potentials, V, versus the internuclear separation coordinate R. The potentials shown in Figure 1.1 are known as Morse potentials, which results from the work of P.M. Morse [60]. Electronic transitions, vibrational transitions, and rotational transitions represent the organizational structure of the spectral emission, respectively. Due to vibrational transitions being similar in electronic position, band like structures are formed.

Cyanide (CN) is a diatomic molecule and has two characteristic electronic systems. These two systems are the violet ($B^2\Sigma^+$–$X^2\Sigma^+$, 344–460 nm) and the red ($A^2\Pi$–$X^2\Sigma^+$, 437–1500 nm), where $X^2\Sigma^+$ state represents the ground state [61]. In this notation A, B, and X represent the potential curves, 2 represents the spin of +1/2 (doublet), Σ and Π represent the angular or orbital quantum number l=0, 1 respectively, and + represents the unchanged symmetry. For this dissertation the CN violet-band Δv=0 system is of interest and these emissions represent vibrational transitions from a higher energy potential ($B^2\Sigma^+$) to the

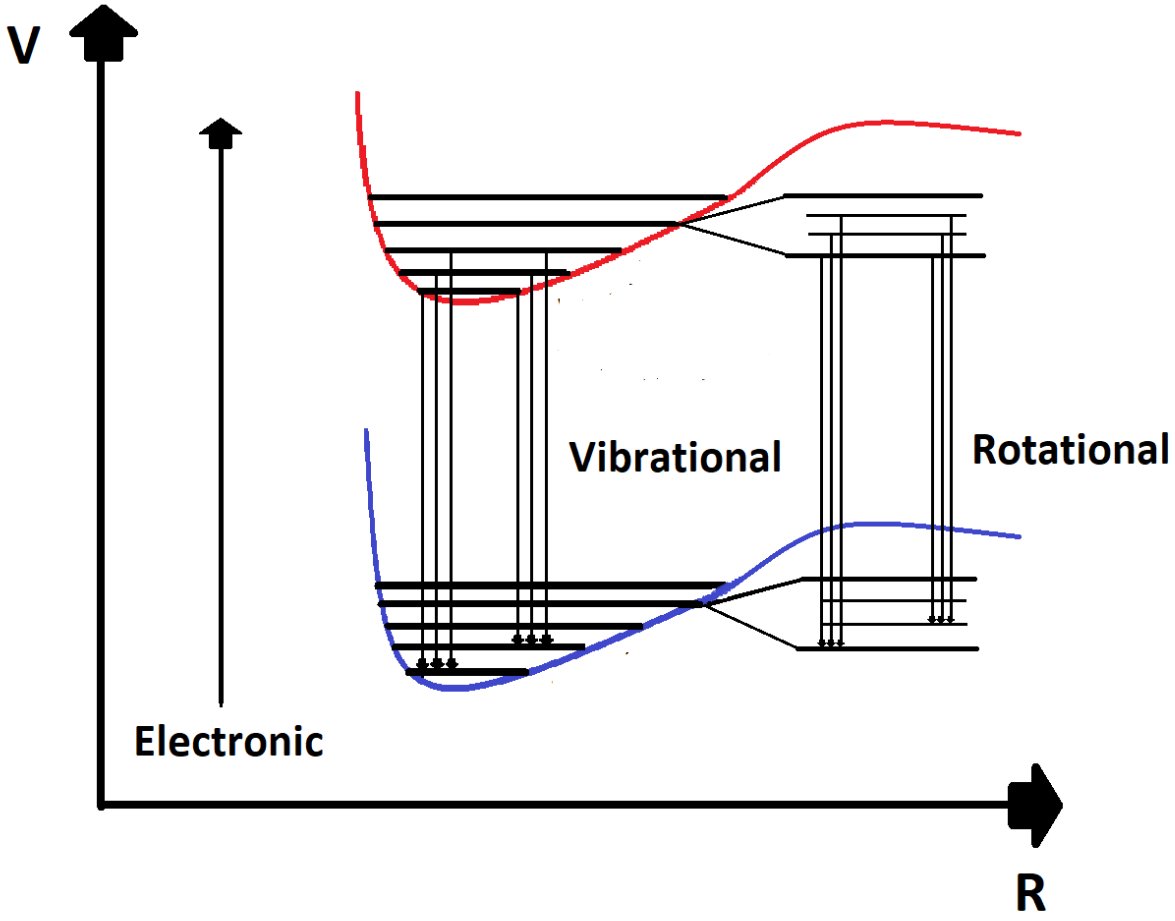

Figure 1.1: Electronic, vibrational, and rotational spectra as a result of molecular potentials between two electronic levels.

ground state, where Δv=0 means the difference between the vibrational quantum numbers is 0. As shown in Figure 1.2, if the CN molecule is in a vibrational state in the higher potential represented by vibrational quantum number v=1, it can only transition to the vibrational state in the ground state also represented by quantum number v=1, which would result in the (1,1) band. The CN violet system consists of vibrational bands (0,0), (1,1), (2,2), (3,3) and (4,4), which are 388.34 nm, 387.14 nm, 386.19 nm, 385.47 nm, and 385.09 nm respectively. In addition to the vibrational states, rotational states exist for the CN violet system which give the system its fine structure.

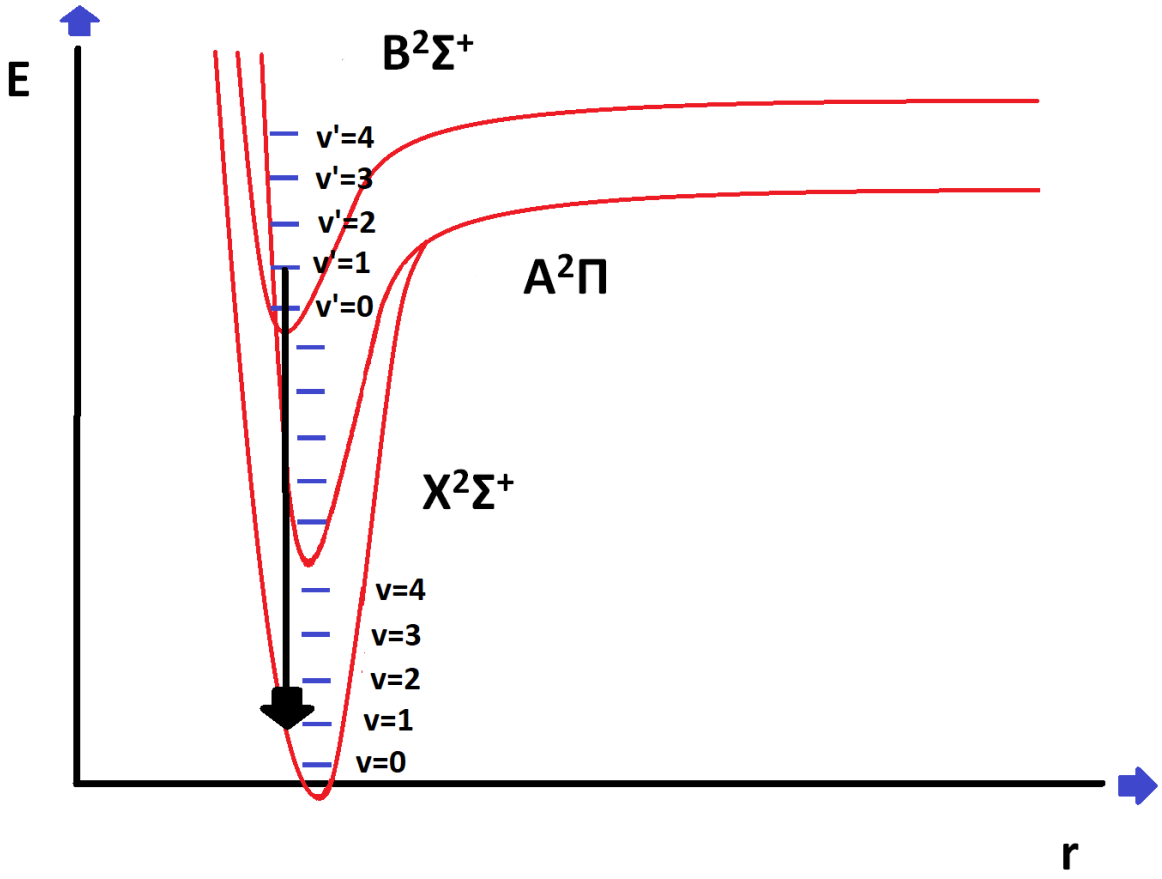

Figure 1.2: Potential curves of CN.

Chapter 2

Experimental Details

2.1 Experimental Details of Shadowgraph Imaging

Shadowgraphs of breakdown plasma are used to visualize plasma expansion [62]. It is imperative to capture shadowgraphs for plasma-excitation energies that were used for time-resolved spectroscopy. A Q-Switched neodymium-doped yttrium aluminum garnet Nd:$Y_3Al_5O_{12}$ (Nd:YAG) laser (Quantel model Q-smart 850, USA) is operated at fundamental wavelength of 1064 nm and a 10 Hz repetition rate to deliver full-width-at-half-maximum (FWHM) 6 ns laser radiation with an energy of 850 mJ per pulse. Beam splitters and apertures were used to attenuate laser-pulse energy from 850 to 170 mJ per pulse. Additionally, another Q-Switched Nd:YAG laser (Continuum Surelite model SL I-10, USA) was frequency-doubled to operate at its second harmonic wavelength, 532 nm, with 5 ns pulses.

A 100 mm plano-convex lens, f/10 focusing, is used to focus the 1064 nm IR beam. The 532-nm green laser beam is reflected by two prisms and three mirrors to produce a shadowgraph of the plasma. A beam expander and reflections by the prisms and mirrors caused the beam to become wide enough to cover the entire plasma volume for shadowgraph imaging. Figure 2.1 shows a schematic of the experimental setup.

Synchronization of the lasers and camera (Silicon Video Color Camera model 9C10) were performed to ensure precise temporal measurements of shadowgraphs. A control box (TSI Incorporated model 610032, USA), a Digital Delay Generator (Stanford Research System

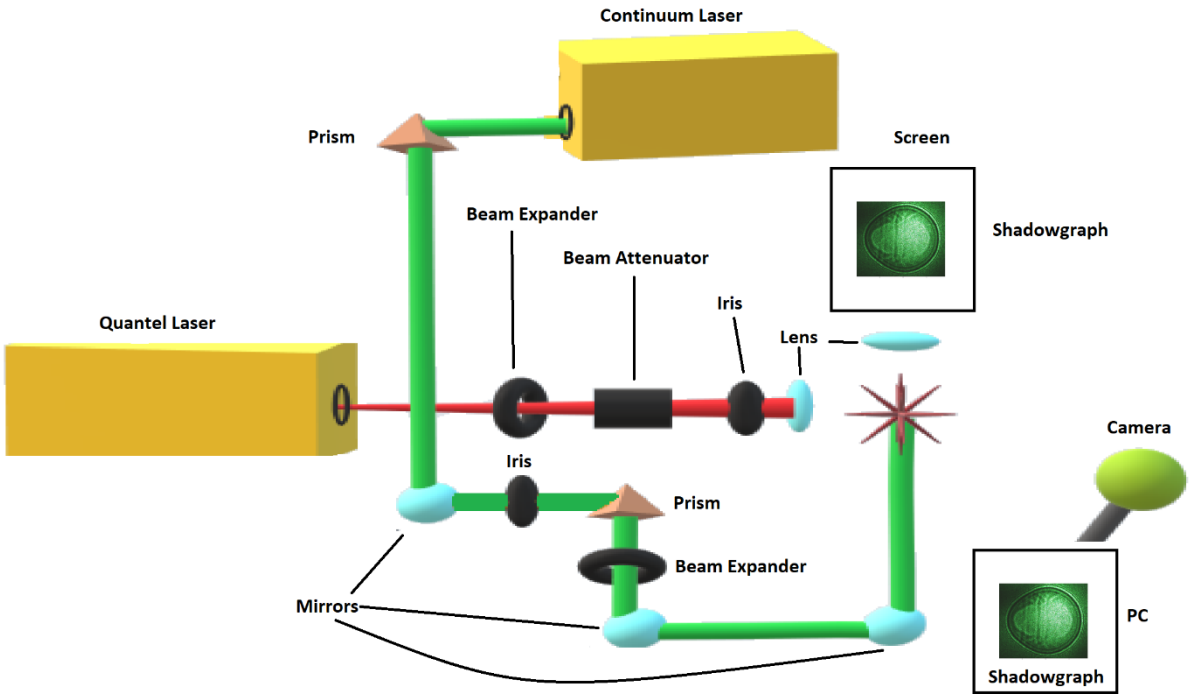

Figure 2.1: Schematic of the apparatus used for the shadowgraph experiments.

model DG535, USA), and two oscilloscopes were utilized in externally triggering the Surelite laser, Quantel laser, and camera to capture desired shadowgraphs. The externally triggered laser devices had 1 ns RMS amplitude trigger jitter.

Shadowgraphs were recorded using the silicon video camera equipped with a Nikon lens of 50 mm focal length and the silicon video camera was controlled by XCAP imaging software with a PIXCI image capture board. The silicon video camera is equipped with a sensitive area of 6.1 mm×4.58 mm with a resolution of 3488 horizontal × 2616 vertical pixels or with square 1.75 μm x 1.75 μm pixels image resolution of 512 x 512 pixels was used to capture images by 4 x 4 grouping.

2.2 Laser-Induced Breakdown in a Fixed Volume of Gas

A set of typical components for nanosecond laser-induced breakdown spectroscopy (LIBS) or time-resolved laser-induced optical emission spectroscopy was used in the experimental arrangement [54]. A Q-Switched neodymium-doped yttrium aluminum garnet, Nd:$Y_3Al_5O_{12}$ (Nd:YAG) laser (Quantel model Q-smart 850, USA) is operated at fundamental wavelength of 1064 nm and a 10 Hz repetition rate to deliver full-width-at-half-maximum (FWHM) 6 ns laser radiation with an energy of 850 mJ per pulse. Beam splitters and apertures were used to attenuate laser-pulse energy from 850 to 170 mJ per pulse. Energy per pulse is measured using the energy and optical power meter (Thorlabs model PM100USB, USA). A silicon photodiode detector (Thorlabs model DET10A/M, USA) is connected to a four-channel oscilloscope (Tektronix model TDS 3054, USA) to measure optical pulses from scattered laser radiation. Alignment of the laser beam is done with three IR reflective mirrors (Thorlabs model NB1-K13, USA) to ensure the laser beam is parallel to the spectrometer slit. A singlet lens (Thorlabs model LA-1509-C, USA) was used to produce optical-breakdown microplasma. A fused silica planoconvex lens (Thorlabs model LA4545, USA) was used for 1:1 imaging of the plasma onto the 100 μm slit of a Czerny-Turner type spectrometer (Jobin Yvon model HR 640, Fr) with a focal length of 0.64 nm. The Czerny-Turner type spectrometer has a spectral resolution of 0.1 nm and is equipped with a 1200 groove/mm

grating to disperse the radiation from the plasma into numerous wavelengths. A schematic of the experimental setup can be seen in Figure 2.2.

Laser-induced breakdown was created in a controlled gas chamber. The chamber consists of six 0.5-inch diameter and 1 cm thick uncoated uv-fs glass optical windows, two gas inlets, and one gas outlet. The gas inlets were used to mix Airgas ultra-high purity N_2 and research-grade CO_2 via partial pressure addition. Chamber evacuation was performed before and after experimentation via the gas outlet. A mechanical pump was connected to the gas outlet so the chamber could be evacuated as needed. To minimize contamination, the chamber was evacuated with a mechanical pump to bring the system pressure down to 1 Pa (10 mTorr). Chamber monitoring was performed using a differential pressure gauge. The gauge was operated as an absolute pressure gauge by evacuating the gauge casing volume via the vacuum pump. Figure 2.3 shows the chamber, mechanical pump, and pressure gauge. For these set of experiments the chamber consisted of a 1:1 CO_2:N_2 molar gas mixture held at 101 kPa (760 Torr). Measurements were performed with and without an Order-Sorting Filter (Oriel model 51250, USA) with a cut-on wavelength of 309 nm and transmittance range of 325 nm, to evaluate the CI 193.09 nm atomic carbon line interference [63]. Another set of measurements were performed with the chamber consisting of a 1:1 CO_2:N_2 molar gas mixture held at a pressure at 276 kPa (2070 Torr) without the use of the Order-Sorting filter.

Spatially resolved images were recorded with a 2-dimensional intensified charge coupled device (ICCD; Andor Technology model iStarDH334T-25U-04, USA) along the slit height. The ICCD is mounted to the spectrometer, connected to a computer by USB cable, and run by the Andor Solis 64-bit Acquisition and Analysis software. The ICCD has an array of 1024 x 1024 pixels, which coincide with horizontal-spectral and vertical-spatial variations along the slit height. The pixels are binned in four-pixel tracks along the slit direction, resulting in 256 spectra for each time delay. Recording of measurements with and without the Order-Sorting filter consist of 100 accumulations collected for 21 time delays at 250 ns steps.

Synchronization of plasma generating instrumentation and data collection equipment was accomplished by using a Function Generator (Wavetek model FG3C, USA), a Digital Delay Generator (Stanford Research System model DG535, USA), a custom-built divide by five

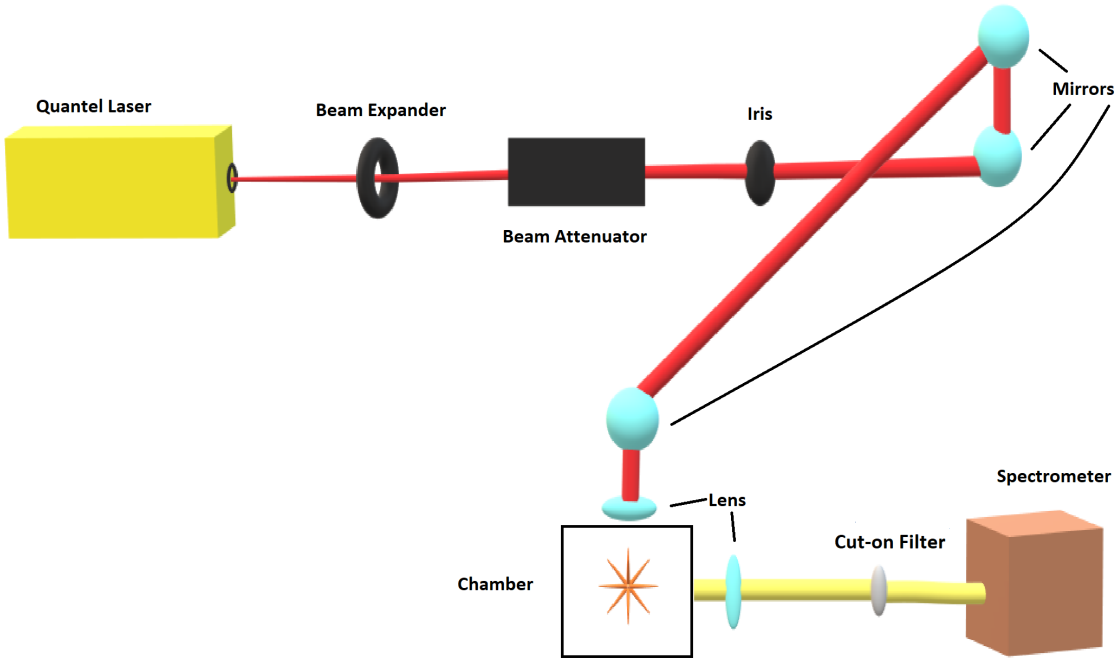

Figure 2.2: Schematic of the apparatus used for the laser-induced breakdown experiments.

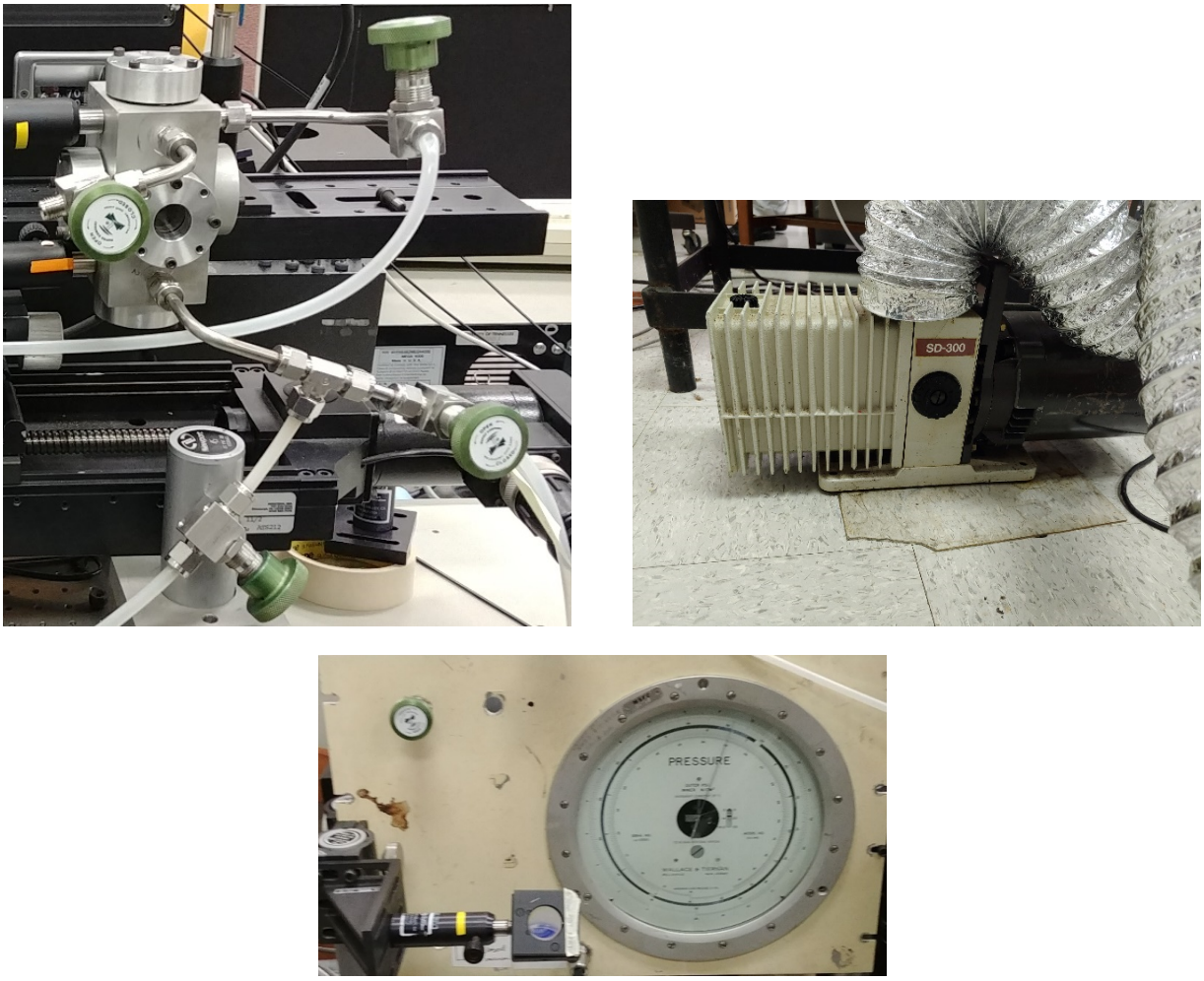

Figure 2.3: Pictures of the gas chamber (top left), the mechanical vacuum pumps connected to the pressure system (top right), and the differential pressure gauge (bottom).

circuit, and the previously mentioned four-channel oscilloscope. 50 Hz triangular waves are produced by the wave generator and the divide by fivecircuit, and the previously mentioned four-channel oscilloscope. 50 Hz triangular waves are produced by the wave generator and the divide by five circuit box yields a 10 Hz wave. The digital delay generator and production of 10 Hz wave are used to trigger the flashlamp of the laser and synchronize all other equipment.

2.3 Laser-Induced Breakdown in a Flowing Gas

A set of flowing gas mixture measurements were performed using an experimental setup similar to that of a fixed gas mixture. A flowmeter (Cole-Parmer Instrument Company model FM112-02ST, USA) was connected to the gas outlet instead of the differential pressure gauge as mentioned in the fixed gas mixture experimental setup. The chamber was supplied with a constant flow of ultrahigh purity N_2 and research-grade CO_2 gas mixture. A flow rate of 100 mL per min of the mixture entered and left the cell, which was monitored by the flowmeter as seen in Figure 2.4. Inside the chamber, optical breakdown was created at a rate of 10 Hz using a laser beam focused with f/5 optics from the top or parallel to the slit. Pixels of the ICCD were binned in four-pixel tracks along the slit direction, resulting in the production of 256 spectra for each time delay. Recordings of spectra were performed with and without the Order-Sorting Filter consisting of 100 accumulations collected for 21 time delays at 250 ns steps.

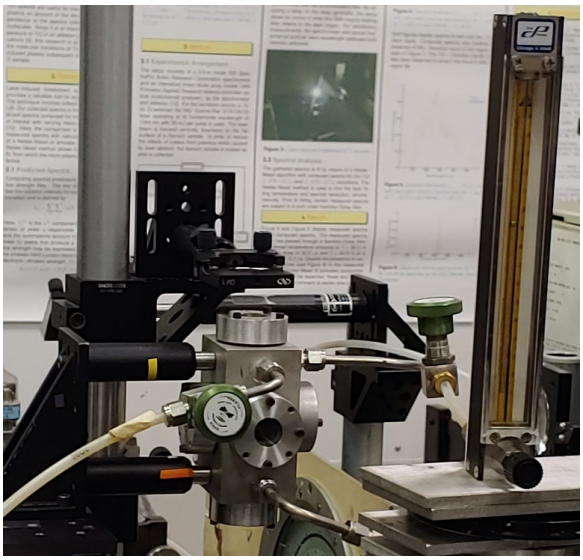

Figure 2.4: Picture of the gas chamber and flowmeter.

Chapter 3

Theoretical Basis

3.1 Laser-Induced Shockwave

Laser-induced breakdown performed on solid, liquid or gaseous materials produces a small explosion. This explosion, together with the excitation, plasma formation and ablation of material, is accompanied by the surrounding material being fiercely displaced and the production of a shockwave. The geometry and the evolvement over time of a laser-induced shockwave are dependent on the energy of the laser and the shape of plasma produced.

Blast waves due to nuclear explosions set the foundation for the study of shockwave production and propagation. The vast amounts of energy released in a fixed volume by nuclear explosions compared to normal explosions were examined by Bethe et al. [64] at Los Alamos in 1941 and Taylor [65] in the United Kingdom in 1950 yielding the theory of a point strong explosion. Studies by John von Neumann [64] and L.I. Sedov [66, 67], which assumed an adiabatic expansion and a sudden release of energy, E, in negligible volume and time, lead to the development of the expansion law of the shock wave:

$$R(\tau) = \frac{(E\,\tau^2)^{1/5}}{\rho\,K} \tag{3.1}$$

where R(τ) is the radius of the shockwave at time τ, K is a constant dependent on the adiabatic coefficient of the gas, and ρ is the density of the gas. For studies performed in standard ambient temperature and pressure (SATP) air, K $\approx$ 1, which is consistent with

shadowgraph studies performed by Gautam et. al [62]. Allowing K = 1, simplifies equation (3.1) to:

$$R(\tau) = \frac{(E\,\tau^2)^{1/5}}{\rho} \tag{3.2}$$

Energies for laser-induced breakdown for this dissertation fall within the range of 160-200 mJ. Comparisons of computed blast-wave radii, using equation (3.2), for SATP air and molar cyanide (CN) mixture are seen in Tables 3.1 and 3.2. There is minimal variation in shockwave expansion in SATP air versus CN mixture, which would indicate that measured shadowgraphs in air provide an acceptable guide for the CN gaseous mixture.

Another important characteristic of the shockwave is the expansion velocity. The shockwave expansion velocity indicates whether the approximation used in the shockwave expansion law is accurate. Shock wave expansion velocity, $v(\tau)$, assuming K $\approx$ 1, is determined by:

$$v(\tau) = \frac{2}{5}\,\tau^{-3/5}\,\left(\frac{E}{\rho}\right)^{1/5} \tag{3.3}$$

Studies by Harith et. al [68] verify that the shockwave expansion law is a great approximation when the shockwave expansion velocity is around Mach numbers M $\approx$ 2. Mach numbers, M, are calculated using:

$$M = \frac{v(\tau)}{c} \tag{3.4}$$

where c is the speed of sound in SATP, 343 m/s. Comparisons of computed shock wave expansion velocities and Mach numbers for energies 160 mJ and 200 mJ, using equation (3.3) and (3.4), for SATP air and molar cyanide (CN) mixture are seen in Tables 3.3, 3.4, 3.5, and 3.6. Shockwave expansion velocities in air for early time delays (450 ns or less) move at hypersonic speeds (Mach numbers 5 or greater), while at later time delays (greater than 450 ns) the shock wave expansion velocities move at supersonic speeds (Mach numbers 1.3 to 5, inclusive). For the CN mixture, the shockwave expansion velocities move at supersonic speeds except for early time delays of 200 ns or less where they move at hypersonic speeds.

Table 3.1: Computed shockwave radii for SATP air and for molar CN mixture, 160 mJ

τ (ns)	R(mm) for Air [$\rho = 1.2\ kg/m^3$]	R(mm) for CN [$\rho = 1.63\ kg/m^3$]
200	1.40	1.31
450	1.93	1.82
700	2.31	2.17
950	2.61	2.45
1200	2.86	2.69
1450	3.09	2.90

Table 3.2: Computed shockwave radii for SATP air and for molar CN mixture, 200 mJ

τ (ns)	R(mm) for Air [$\rho = 1.2\ kg/m^3$]	R(mm) for CN [$\rho = 1.63\ kg/m^3$]
200	1.46	1.37
450	2.02	1.90
700	2.41	2.27
950	2.73	2.56
1200	2.99	2.81
1450	3.23	3.04

Table 3.3: Computed shockwave velocity for SATP air and for molar CN mixture, 160 mJ

τ (ns)	v(km/s) for Air [$\rho = 1.2\ kg/m^3$]	v(km/s) for CN [$\rho = 1.63\ kg/m^3$]
200	2.80	2.63
450	1.72	1.62
700	1.32	1.24
950	1.10	1.03
1200	0.95	0.90
1450	0.85	0.80

Table 3.4: Computed shockwave velocity for SATP air and for molar CN mixture, 200 mJ

τ (ns)	v(km/s) for Air [$\rho = 1.2\ kg/m^3$]	v(km/s) for CN [$\rho = 1.63\ kg/m^3$]
200	2.92	2.75
450	1.80	1.69
700	1.38	1.30
950	1.15	1.08
1200	1.00	0.94
1450	0.89	0.84

Table 3.5: Computed shockwave Mach numbers for SATP air and for molar CN mixture, 160 mJ

τ (ns)	M for Air [$\rho = 1.2\ kg/m^3$]	M for CN [$\rho = 1.63\ kg/m^3$]
200	8.15	7.67
450	5.01	4.71
700	3.84	3.61
950	3.20	3.01
1200	2.78	2.62
1450	2.48	2.34

Table 3.6: Computed shockwave Mach numbers for SATP air and for molar CN mixture, 200 mJ

τ (ns)	M for Air [$\rho = 1.2\ kg/m^3$]	M for CN [$\rho = 1.63\ kg/m^3$]
200	8.52	8.02
450	5.24	4.93
700	4.02	3.78
950	3.35	3.15
1200	2.91	2.74
1450	2.60	2.44

Therefore, as time elapses the shockwave expansion law approximation improves as Mach numbers approach $M \approx 2$ and slower.

3.2 Electron Density

3.2.1 Atomic Carbon Line Interference

Laser-induced breakdown performed on the carbon dioxide and nitrogen gaseous mixture produces a variety of species, which includes C, C^+, C^-, CN+, CN-, CNN, CO, CO+, CO_2, $CO_2{}^+$, C_2, C_2+, C_2-, CCN, CNC, C_2O, C_3, N, N^+, N^-, NCO, NO, NO^+, NO_2, N_2, $N_2{}^+$, $N_2{}^-$, NCN, N_2O, N_3, O, O^+, O^-, O_2, and $O_2{}^+$ [69]. This dissertation is focused on the analysis of the CN violet-band Δv=0 system that has vibrational bands (0, 0), (1, 1), (2, 2), (3, 3) and (4, 4), which are 388.34 nm, 387.14 nm, 386.19 nm, 385.47 nm, and 385.09 nm respectively. The Czerny-Turner spectrometer equipped with 1200 groove/mm grating is adjusted to the region of interest of 370 nm to 393.5 nm to observe the CN violet band Δv=0 system via the Andor Solis software as seen in Figure 3.1 [63].

In LIBS, first order lines ($m = 1$) are of interest when performing analysis of LIBS produced spectra, but spectral lines have different orders or modes due to the use of diffraction gratings which follow the equation:

$$d\ sin(\theta) = m\lambda \tag{3.5}$$

where d is the distance between the center of two adjacent slits, θ is the angle at which maxima occur, m is the propagation mode of interest, and λ wavelength of monochromatic light. For example, if a first order ($m = 1$) spectral line has a wavelength, λ, equivalent to 193 nm, then its wavelength, λ, measured in second order ($m = 2$) would be 386 nm when using equation (3.5). Eventhough the spectrometer is set for the desired region of interest and the CN band heads are well defined as seen in Figure 3.1, there can be interference from the other species' spectral lines in higher order that are produced by the laser-induced breakdown (LIBS). In this work there is overlap of the CI 193.09 nm atomic carbon line in second order and the vibrational band (2, 2) of 386.19 nm for time delays up to 2.5 µs as seen in Figure 3.2 [63, 69, 70, 71].

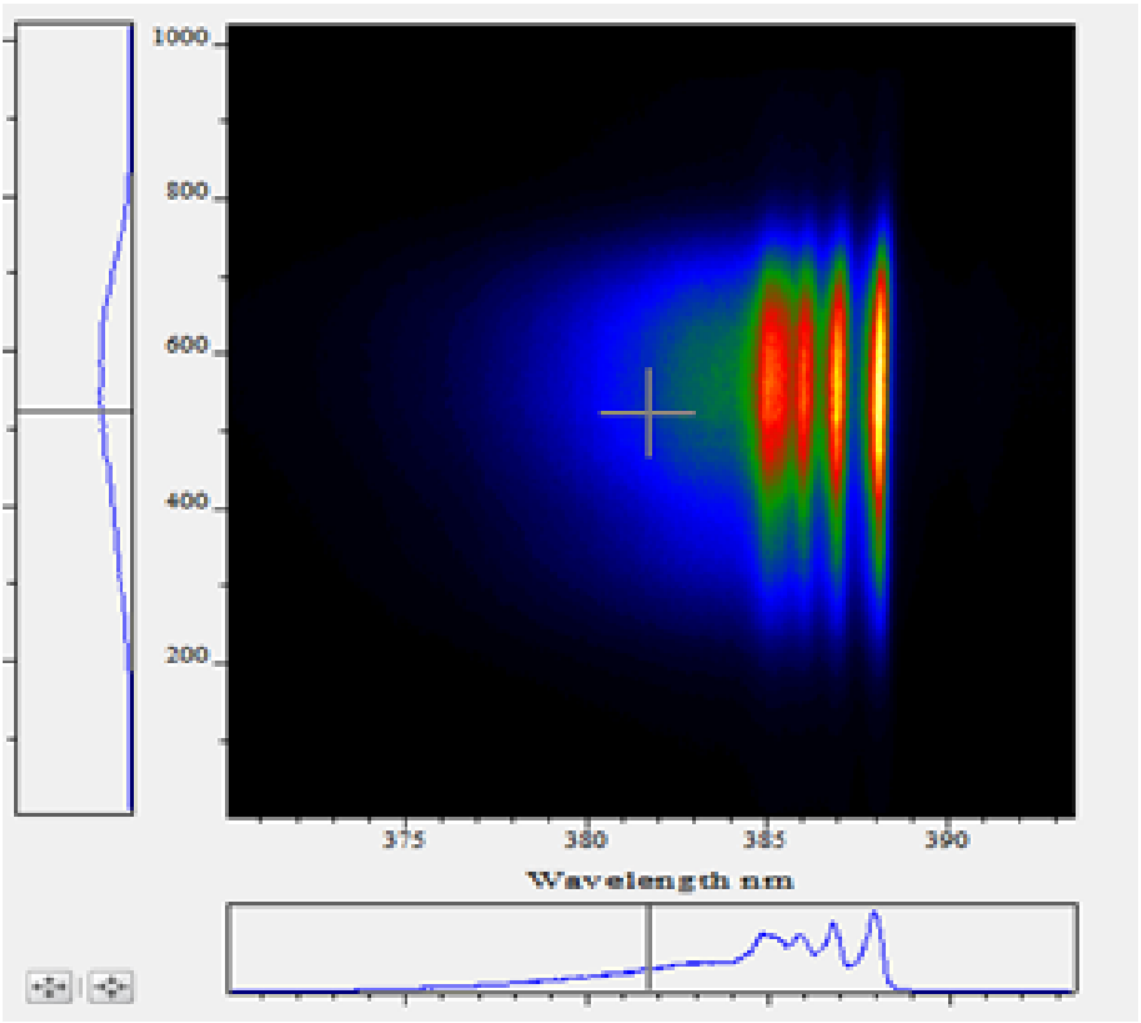

Figure 3.1: Recorded raw spectra 3.7 µs after optical breakdown in a 1:1 CO_2:N_2 atmospheric gas mixture [69].

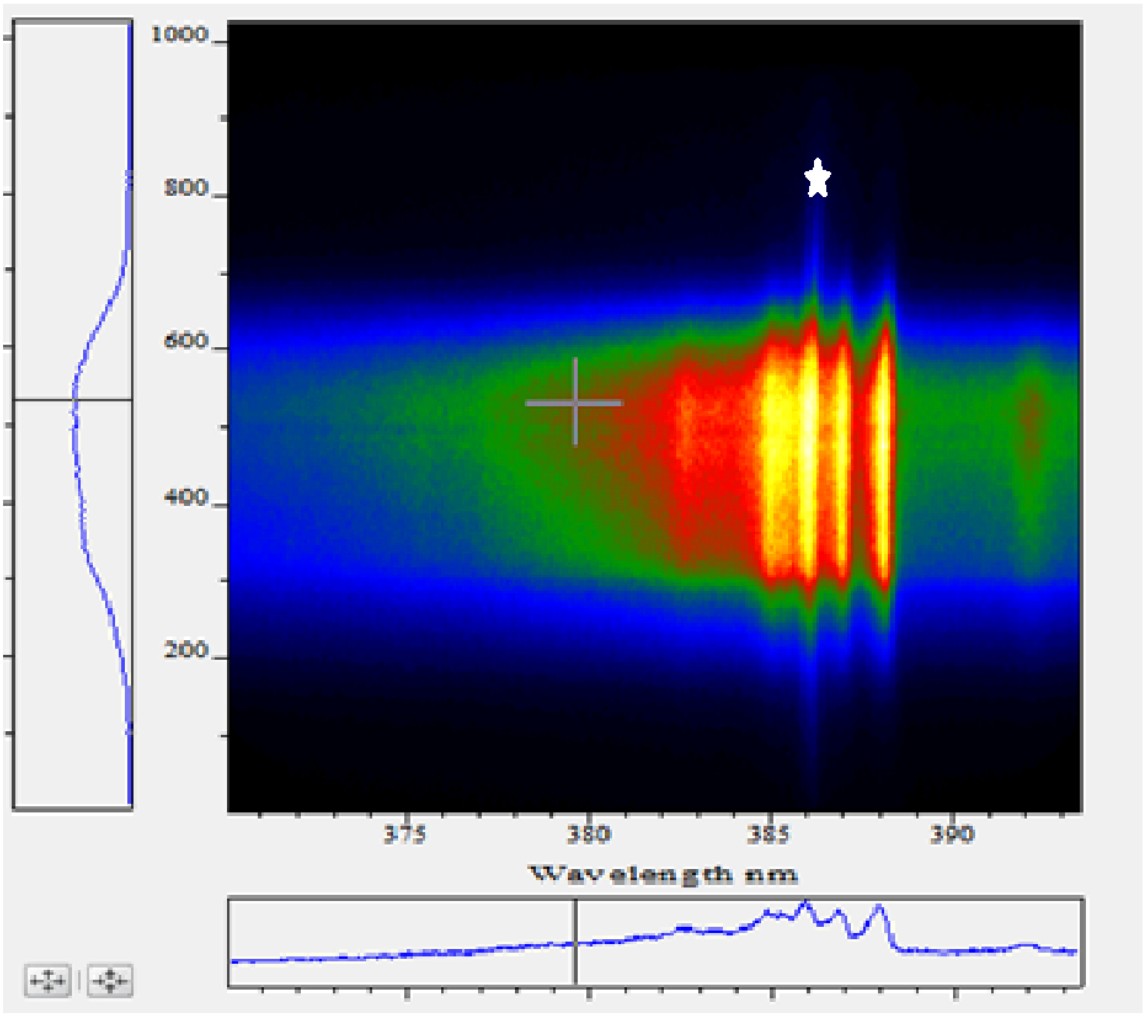

Figure 3.2: Recorded raw spectra 0.45 µs after optical breakdown in a 1:1 CO_2:N_2 atmospheric gas mixture. The * near 386.2 nm represents the atomic carbon line measured in second order [63, 69].

3.2.2 Line Broadening and Deconvolution

Spectral line broadening of observed plasma is caused by the effect of ions and electrons. Local conditions such as local thermodynamic equilibrium and extended conditions such as the plasma radiation's traversed path as viewed by an observer cause the spectral lines to broaden. Doppler or thermal broadening, natural broadening, and pressure broadening are different types of local effect broadening. Doppler broadening is characterized as a Gaussian profile and is due to the position of the detector or observer relative to the velocity of the atoms or ions within a gas or plasma. Natural broadening is characterized as a Lorentzian profile and occurs due to the uncertainty associated with the lifetime of the excited states and its energy. Lastly, pressure broadening is characterized as a Lorentzian profile and is caused by atoms or other ions neighboring the emitter atom or ion. One example of pressure broadening is Stark broadening, which is caused by the shifting and splitting of spectral lines due to the presence of an external electric field, known as the Stark effect.

Electron number density, n_e, can be determined from the full-width at half maximum (FWHM), $\Delta\lambda_{Stark}$, of the stark-broadened CI 193.09 nm atomic carbon line [72], measured in second order,

$$\Delta\lambda_{Stark}\ (nm) = 2w\ (nm) * n_e\ (10^{17}\ cm^{-3}) \tag{3.6}$$

where width parameter, w, was extrapolated [72, 73] to be $w \approx 0.0029$ nm or by the Stark shift of the CI 193.09 nm atomic carbon line [72],

$$\delta\lambda_{Stark}\ (nm) = d\ (nm) * n_e\ (10^{17}\ cm^{-3}) \tag{3.7}$$

where shift parameter, d, was extrapolated [72, 73] to be d ≈ 0.0029 nm. In order to use equations (3.6) and (3.7) to determine n_e, deconvolution of measured Stark FWHM and Stark shifts must be performed. This is due to the line broadening being largely influenced by Stark broadening, which is typically approximated using a Voigt profile [74]. The convolution of Gaussian and Lorentzian line profiles results in the Voigt profile, therefore using a rough approximation between Gaussian, Lorentzian, and Voigt profile widths:

$$f_V = \frac{f_L}{2} + \sqrt{\frac{{f_L}^2}{4} + {f_G}^2} \tag{3.8}$$

where f_V is the FWHM of the Voigt profile, f_L is the FWHM of the Lorentzian profile, and f_G is the FWHM of the Gaussian profile, can be used to apply deconvolution to the measured line profile. In this dissertation, f_V represents the measured spectral line, f_L represents the Stark FWHM or Stark shift, and f_G represents the spectral resolution of the spectrometer. Therefore, rearranging equation (3.8) to determine f_L yields:

$$f_L = f_V + \frac{{f_G}^2}{f_V} \tag{3.9}$$

which can be used in conjunction with equations (3.6) and (3.7) to determine n_e of the CI 193.09 nm atomic carbon line in second order.

3.2.3 Method for Calculating Electron Density

Spectra that were unfiltered had an overlap of the (2, 2) CN band head of 386.19 nm and the second order CI 193.09 nm atomic carbon line, where spectra filtered with the cut-on filter only had the (2, 2) CN band head of 386.19 nm. A peak-fitting Matlab® script [75] was applied to filtered and unfiltered spectra to evaluate CI 193.09 nm atomic carbon line in second-order Stark widths and shifts as seen in Figure 3.3. Equation (3.9) was used on the extracted Stark full-width at half maximum (FWHM) and Stark shifts to apply deconvolution. The difference between deconvoluted Stark FWHM from unfiltered spectra and deconvoluted Stark FWHM from filtered spectra was performed to determine the FWHM contribution of the CI 193.09 nm atomic carbon line in second order only. The FWHM contribution of the CI 193.09 nm atomic carbon line in second order only was used in conjunction with equation (3.6) to determine n_e, where deconvoluted Stark shifts were used in conjunction with equation (3.7) to determine n_e.

3.3 Nelder-Mead Temperature Fitting

Plasma temperature from molecular spectra is dependent on vibrational and rotational elements of the molecular spectrum. Due to this dependence, temperature from molecular

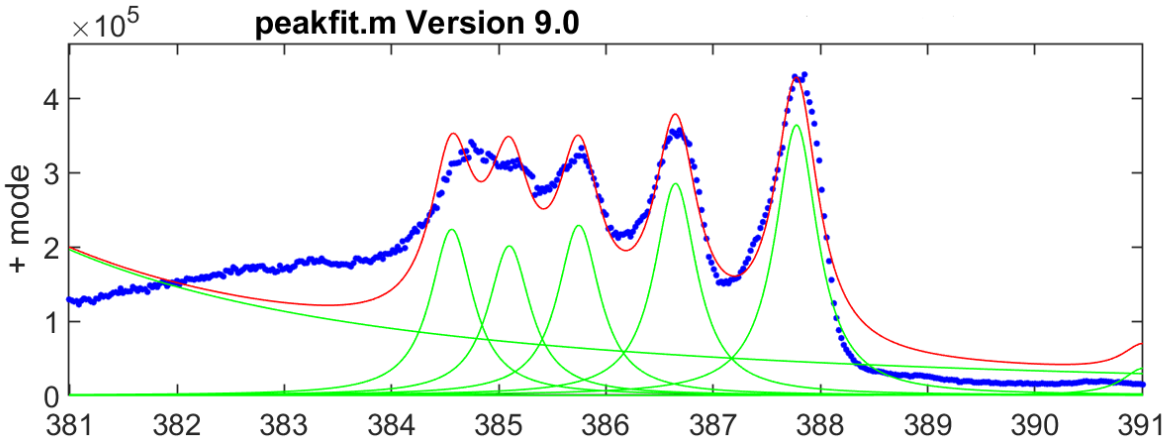

Figure 3.3: Peakfit script applied to a measured line-of-sight CN spectra.

spectrum. Due to this dependence, temperature from molecular spectra can be used to evaluate the condition of the plasma. Temperature determination can be performed by fitting measured spectra to calculated theoretical diatomic spectrum. Diatomic line strength is used to calculate the needed theoretical diatomic spectrum for appropriate fitting. Diatomic line strength calculations are rather cumbersome to perform due to spectral line position requirements and the need for very accurate molecular rotational constants. Parigger and Hornkohl [76] describe the theoretical background and development of diatomic line strength tables necessary for temperature evaluation. Therefore, cyanide (CN) line strength tables reported by Parigger et. al [77] are used for the calculation of theoretical CN spectrum.

The Nelder-Mead temperature (NMT) program [74] was used to fit measured CN spectral data. The NMT program utilizes the Nelder-Mead method [78], which is a numerical method used to find the minimum or maximum of an objective function in a multidimensional space. The NMT program requires initial fit parameter assumptions, which consist of the temperature of the molecular spectra, the line width of the molecular spectral line, and a linear baseline offset. Specifically, the Nelder-Mead algorithm creates a simplex established on the initial given fit parameters. Each vertex of the simplex represents a fit parameter and the size of the simplex is reduced by changing the vertex arrangement until the tolerance is achieved. During minimization, the first local minimum identified represents the minimum and the best fit parameters are established on final location of the simplex's vertices.

A typically fit to CN spectra collected at time delay 1.2 µs and slit height of 6.9 mm is shown in Figure 3.4. The inferred temperature is 8748 Kelvin using a fit with a spectral resolution of 0.1 nm. The spectral resolution causes a reduced signal to noise ratio of the collected spectra, which can be seen when comparing the resolution between the measured spectra and the fitted spectra. Additionally, the image displays CN spectra having noise present where rotational lines are anticipated to be. Most likely the noise seen is actually rotational lines which cannot be differentiated due to the spectral resolution.

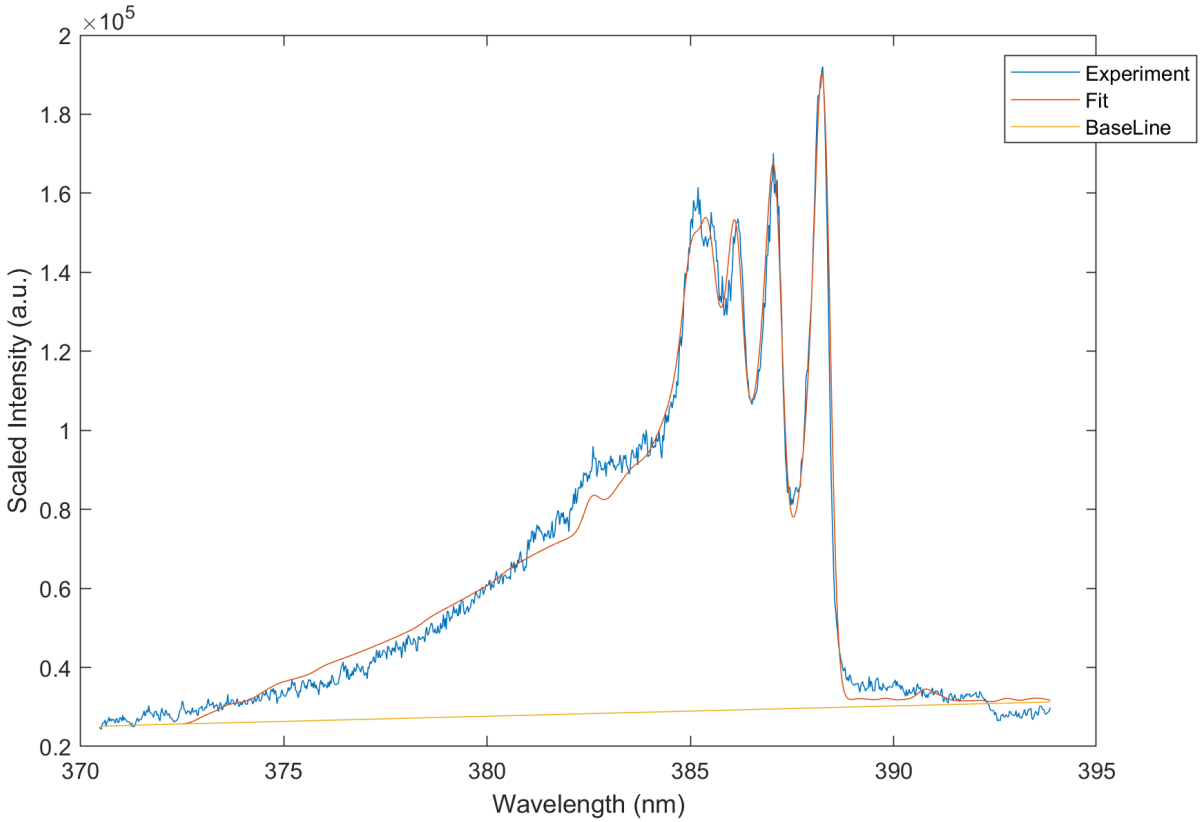

Figure 3.4: Fit to measured CN spectra at a slit height of 6.9 mm at a time delay of 1.2 µs, Temperature = 8748 K, fit FWHM = 0.39 nm

3.4 Abel Inversion

Determining the information across a plasma allows one to analyze the radial/spatial intensity distribution. Unfortunately, the radial intensity cannot be directly measured from recorded line-of-sight data. The use of an Abel transform, which analyzes spherically symmetric functions, can be applied to evaluate line of-sight measurements from close to spherically symmetric plasmas. Specifically, the Abel inversion [79, 80, 81, 82, 83] technique allows one to extract the radial distributions of electron densities of a close to spherically symmetric plasma directly from the recorded line-of-sight data. Letting $\varepsilon(r, \lambda)$ represent a spherically symmetric plasma's radial distribution intensity, the Abel transform of $\varepsilon(r, \lambda)$ is shown to be [63, 69, 70, 71, 84, 85, 86, 87],

$$I(z, \lambda) = 2 \int_z^{\rho} \varepsilon(r, \lambda) \frac{r}{\sqrt{r^2 - z^2}} dr \tag{3.10}$$

where z is the perpendicular distance from the origin of the line-of-sight, r is the radial distance from the center of the observed plasma at which electron density will be evaluated, R is the radius of the spherical object and ρ is the upper integration limit which is established as being much greater than R, $\rho >> R$.

An intensified charge coupling device (ICCD) attached to a spectrometer is used to collect spatial data of the emitted intensity. An emission intensity map with a function of spatial location and wavelength are displayed by recorded images. Abel inversion is performed on measured line-of-sight data of the emitted spectral intensity and a determination of radial variations is accomplished. The emission intensity has subtle asymmetry along the direction perpendicular to the laser beam which may be a result of laser-plasma interaction that normally takes place in nanosecond laser-induced plasmas or may be a result of variations of the laser pulse profile. Figure 3.5 displays the geometry of the line-of-sight measurements utilized in this work, where line-of-sight measurements are along the x-axis, the direction of the laser beam is along the y-axis, and the z-axis is perpendicular to the x and y axes. Abel inversion is used to obtain radial dimension measurements of the plasma, which allows for

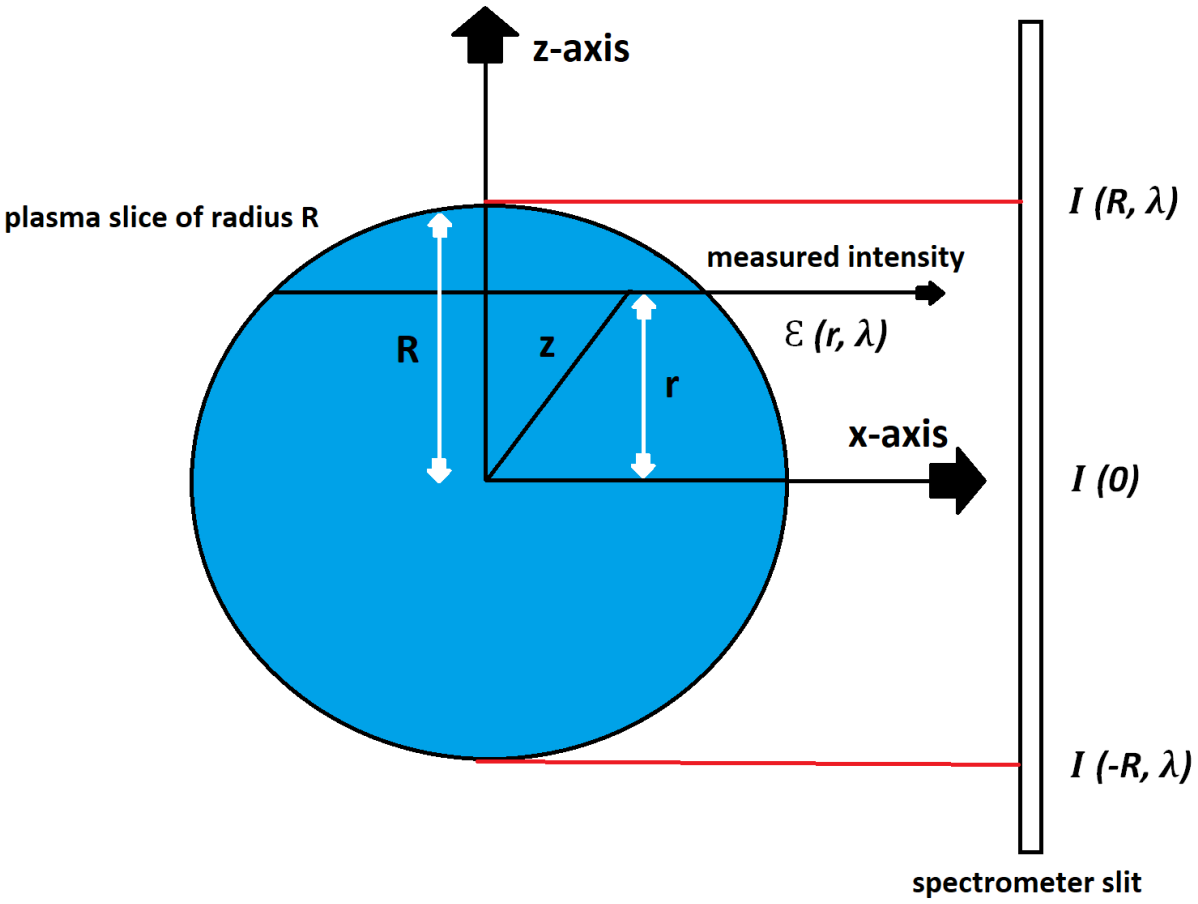

Figure 3.5: Line-of-sight geometry and Abel inversion method.

the extraction of plasma radial information. Using the top half and bottom half of line-of-sight profiles subtle asymmetric data points are averaged utilizing the same symmetrization method for atomic hydrogen spectra [84, 86, 87] and application of Abel inversion is used.

Shadowgraph measurements of plasma kernels in hydrogen and hydrogen-nitrogen gaseous mixtures show a close to cylindrical symmetry or prolate spheroidal symmetry as compared to the close to spherically symmetric plasma kernels in standard ambient temperature and pressure in laboratory air for time delays of 100 to 10,000 ns [62, 85, 86, 87, 88, 89]. The deviation from close to spherically symmetric plasma kernels may be due to the laser energy employed for laser-induced breakdown, therefore as discussed in this dissertation, shadowgraph measurements in standard ambient temperature and pressure are performed at laser energies observed in the carbon dioxide and nitrogen gaseous mixture, which are seen to be close to spherically symmetric [70, 71]. Due to the spherically symmetric plasma requirement of the Abel inversion technique, collected line-of-sight data is adjusted to allow subtle deviations from circular symmetry and modeled to be spherically symmetric [84, 86, 87]. Figure 3.5 shows the Abel inversion method of measured line-of-sight spectra for a single slice of the plasma created in the carbon dioxide and nitrogen gaseous mixture. The y-direction, i.e., into the page of Figure 3.5, represents the focused laser beam. Abel inversion of each wavelength determines the spatial distribution and subtle asymmetries present in the captured data are kept by applying an asymmetric factor, which then establish the asymmetric radial distributions [84, 86, 87]. Pre-treatment of the captured data is not required when using the derivative free Abel inverse transform method [79]. Inversion of equation (3.10) can be accomplished using an analytical method with derivatives, known as the Abel inverse transform. Differentiation of spectra is rather challenging; therefore, coefficients are determined by developing the measured line-of-sight signal in a complete set of orthogonal polynomials that are similar to a Fourier-series, Chebyshev polynomials, and then using a minimization method, which applies least-square fitting for the selected number of polynomials. The use of Chebyshev polynomials in conjunction with the available Matlab® script [79, 83] for Abel inversion of equation (3.10), allows the direct inversion of measured data. For this dissertation, inversion was accomplished by choosing 15 polynomials [79, 80], which maintained fidelity of the spectra and was comparable to the use of a digital

filter resulting in computed radial spectra. Smaller spectral resolution would occur with the selection of a smaller number of polynomials. Line-of-sight data along the spectrometer slit were captured and inverted for each wavelength to get the radial intensity distribution. Calibration and correction for system sensitivity using standard lamps is required for recorded data to undergo Abel inversion.

Chapter 4

Results and Discussion

4.1 Shadowgraphs

Shadowgraphs of plasma in standard ambient air and temperature (SATP) produced by infrared (IR) 1064 nm radiation with excitation energy of 170 mJ and 6 ns pulse-width are shown below. A single 5 ns pulse-width 532 nm laser beam was used to capture the shadowgraphs. Shadowgraphs were taken at 0.2 μs, 1 μs, 1.2 μs, 2.2 μs, and 4.2 μs time delays and the IR 1064 nm laser beam is along the z axis and moving from the right to left as shown in Figures 4.1, 4.2, 4.3, 4.4, and 4.5, respectively.

As seen in Figures 4.1 to 4.5 the expanding shockwave and plasma kernel are clearly visible. At 0.2 μs delay, as shown in Figure 4.1, the plasma kernel appears cylindrical and the expanding shockwave has a prolate spheroidal shape. As time delays approach 1 μs the plasma kernel and expanding shockwave become nearly spherical as seen in Figure 4.2. As time elapses further the plasma kernel and expanding shockwave continue to become close to spherical. The expanding shockwave radii results are shown in Table 4.1, computed shockwave velocities results are shown in Table 4.2, and measured plasma kernel radii are shown in Table 4.3. The expanding shockwave radius for 0.2 μs delay is not consistent with the previously discussed shockwave expansion law, equation (3.2), and this can be due to the velocity of the shockwave being greater than the Mach 2 maximum velocity requirement of the shockwave expansion law. For time delays approaching 1 μs and later, the expanding

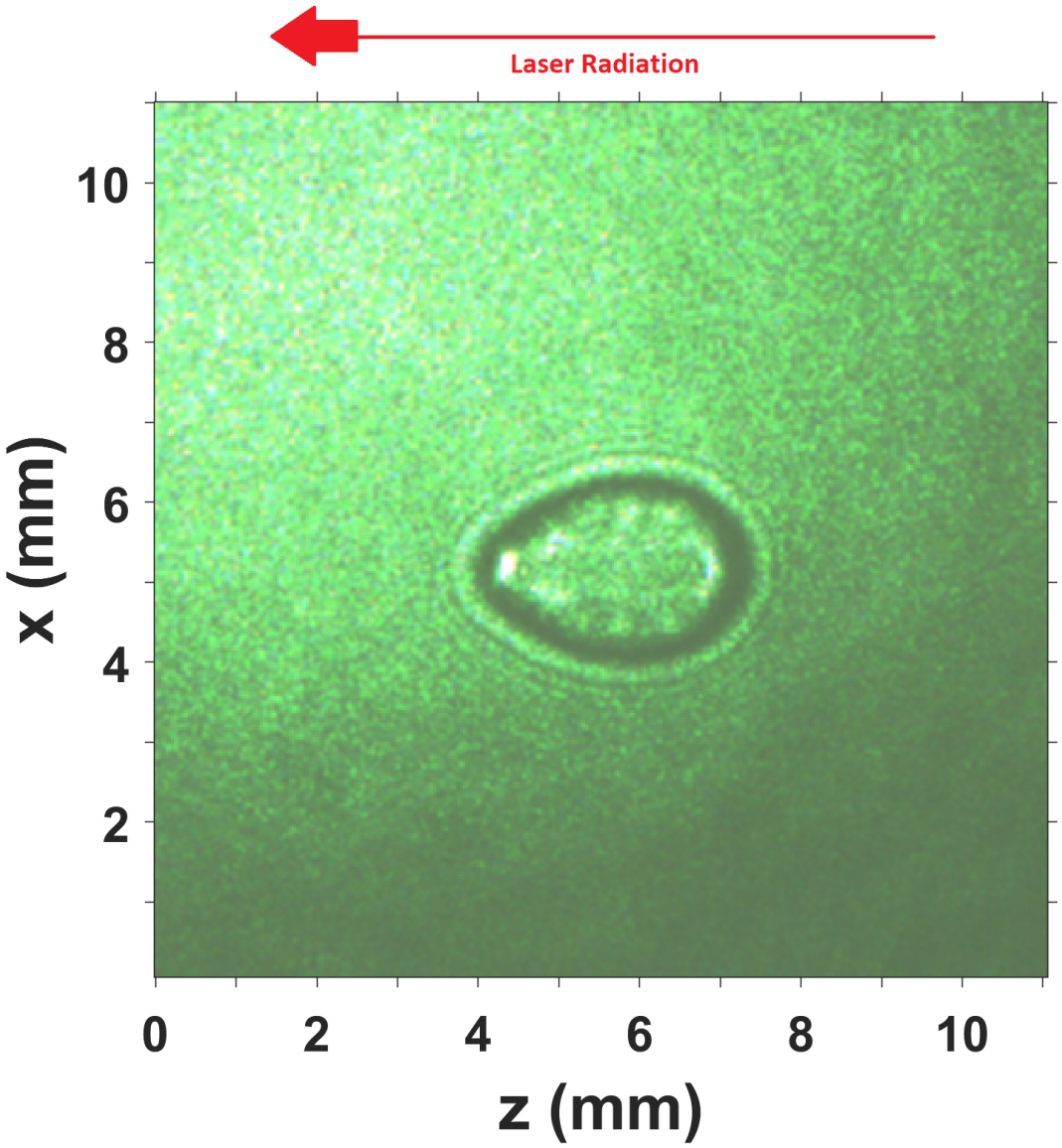

Figure 4.1: Single-shot shadowgraph of expanding laser-induced plasma initiated with a 170 mJ, 6 ns, 1064 nm focused beam, and imaged using a 5 ns, 532 nm backlight that was time-delayed by 0.20±0.05 µs.

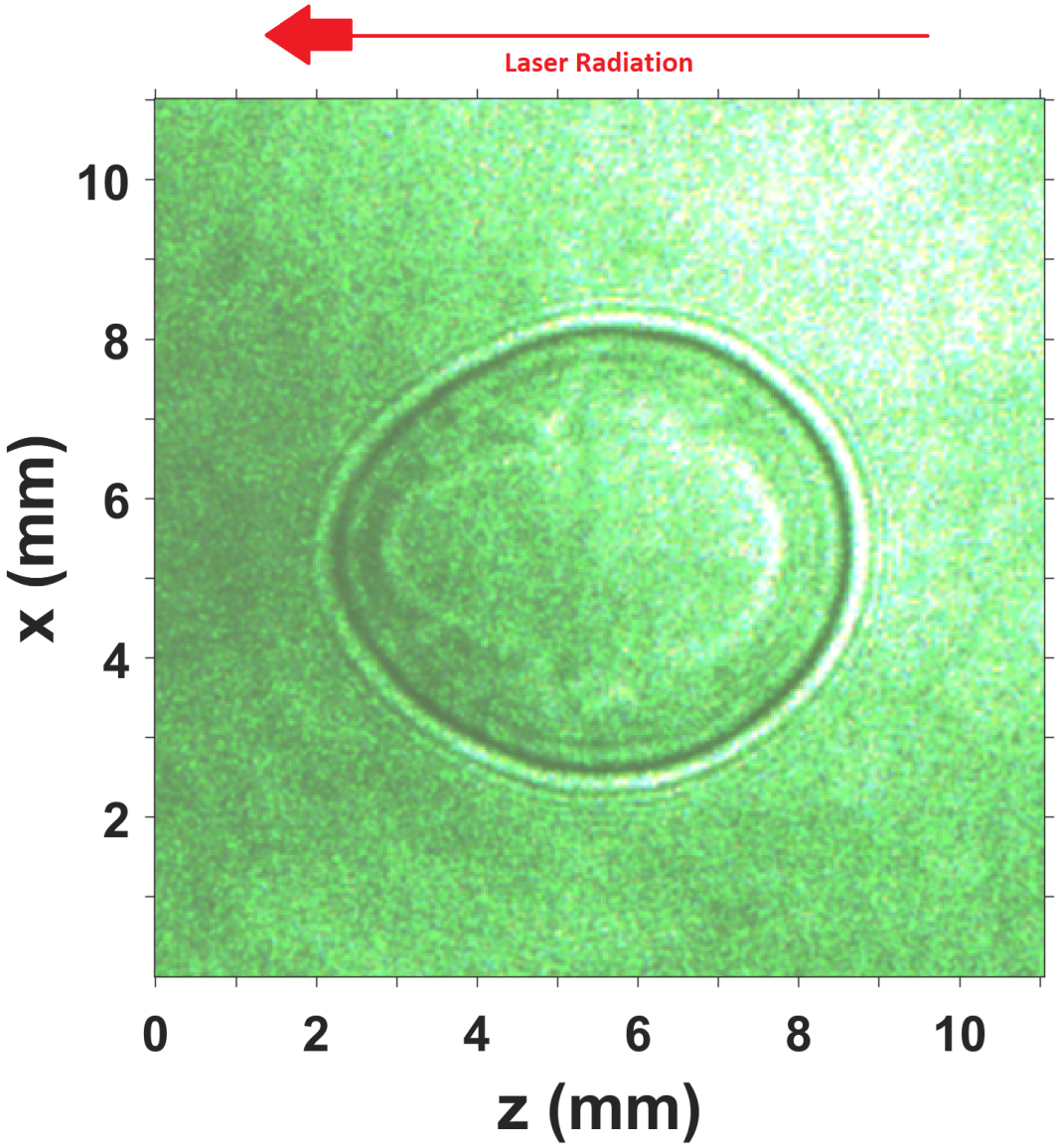

Figure 4.2: Single-shot shadowgraph of expanding laser-induced plasma initiated with a 170 mJ, 6 ns, 1064 nm focused beam, and imaged using a 5 ns, 532 nm backlight that was time-delayed by 1.00±0.05 µs.

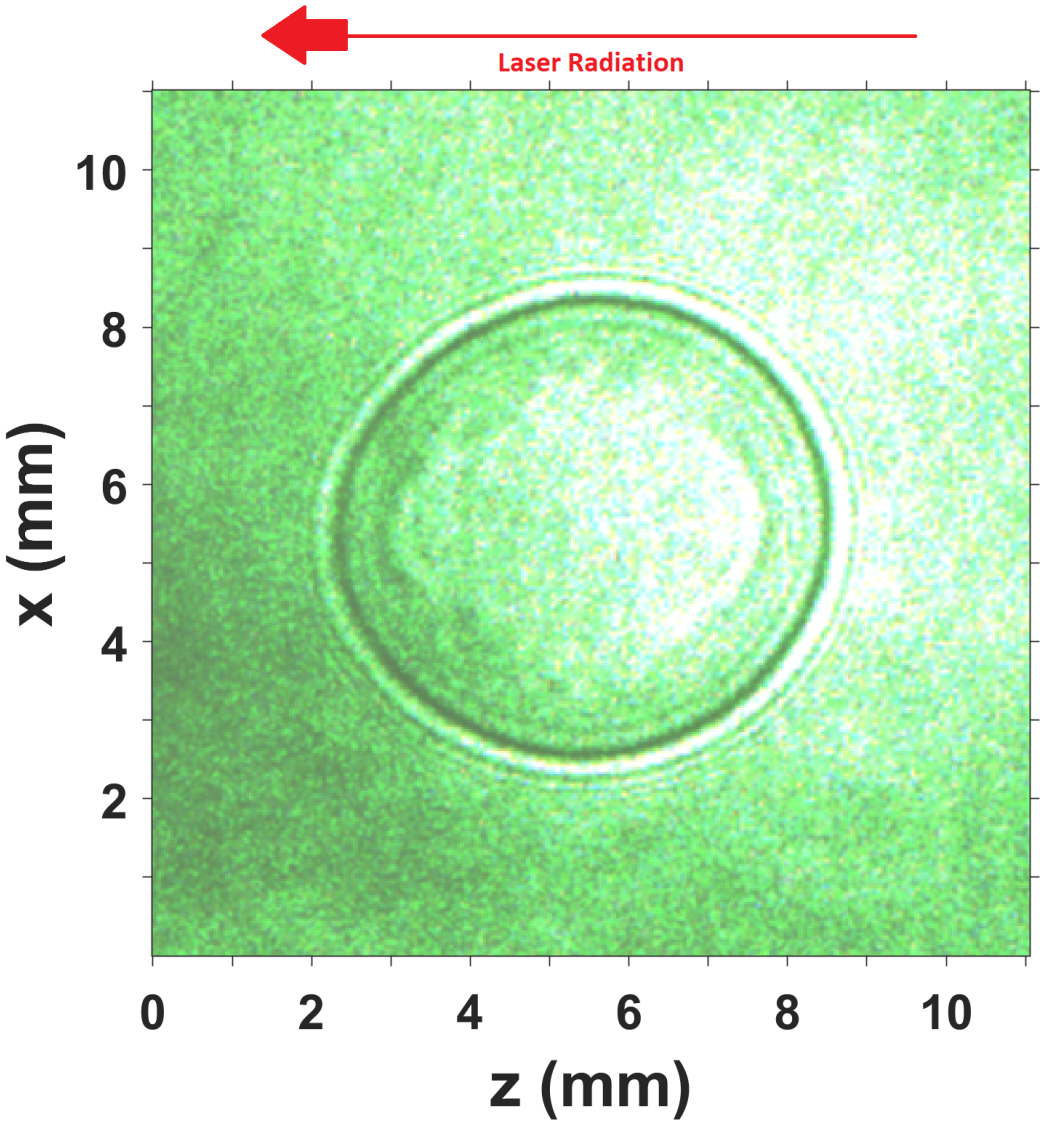

Figure 4.3: Single-shot shadowgraph of expanding laser-induced plasma initiated with a 170 mJ, 6 ns, 1064 nm focused beam, and imaged using a 5 ns, 532 nm backlight that was time-delayed by 1.20±0.05 µs.

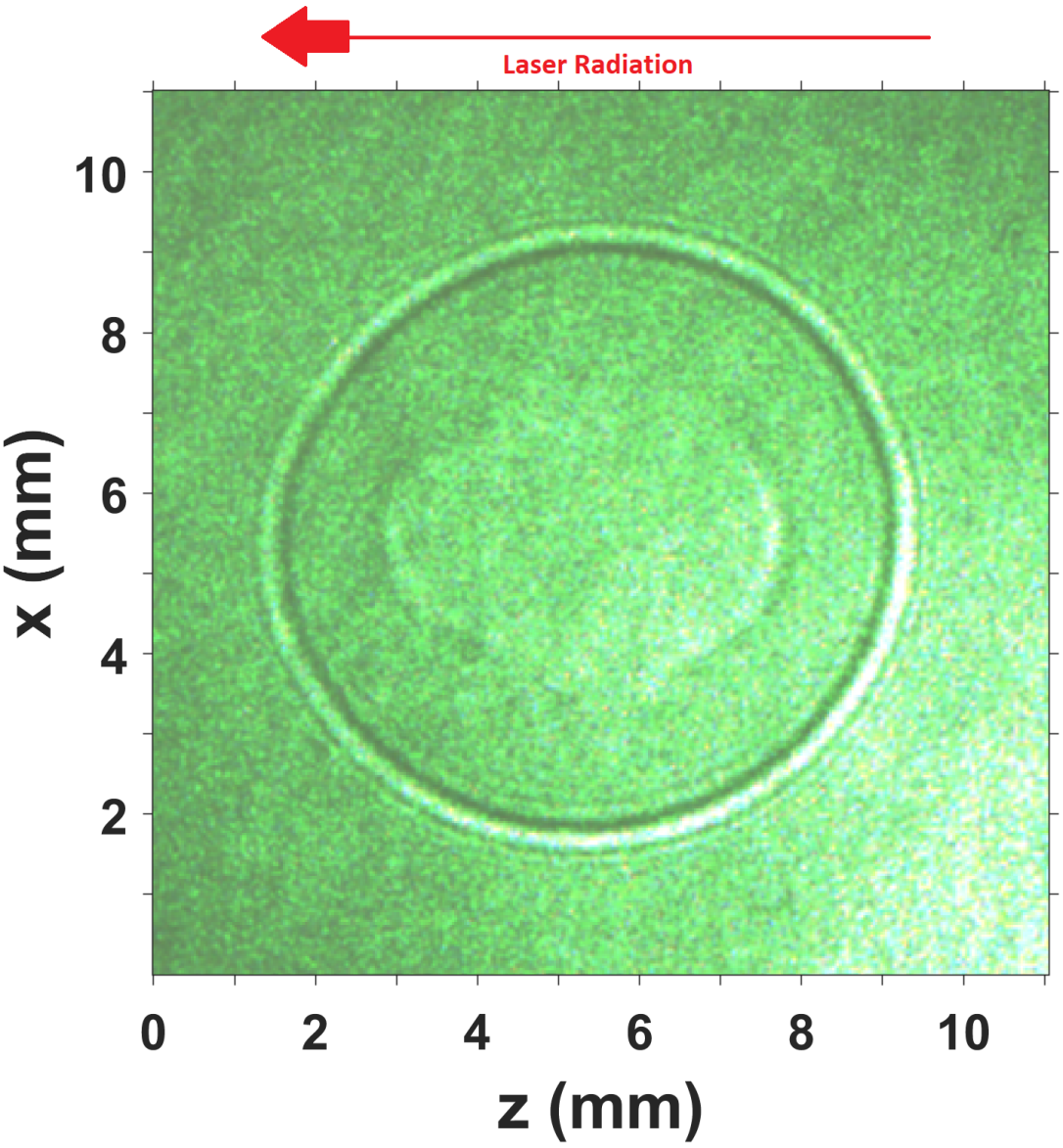

Figure 4.4: Single-shot shadowgraph of expanding laser-induced plasma initiated with a 170 mJ, 6 ns, 1064 nm focused beam, and imaged using a 5 ns, 532 nm backlight that was time-delayed by 2.20±0.05 µs.

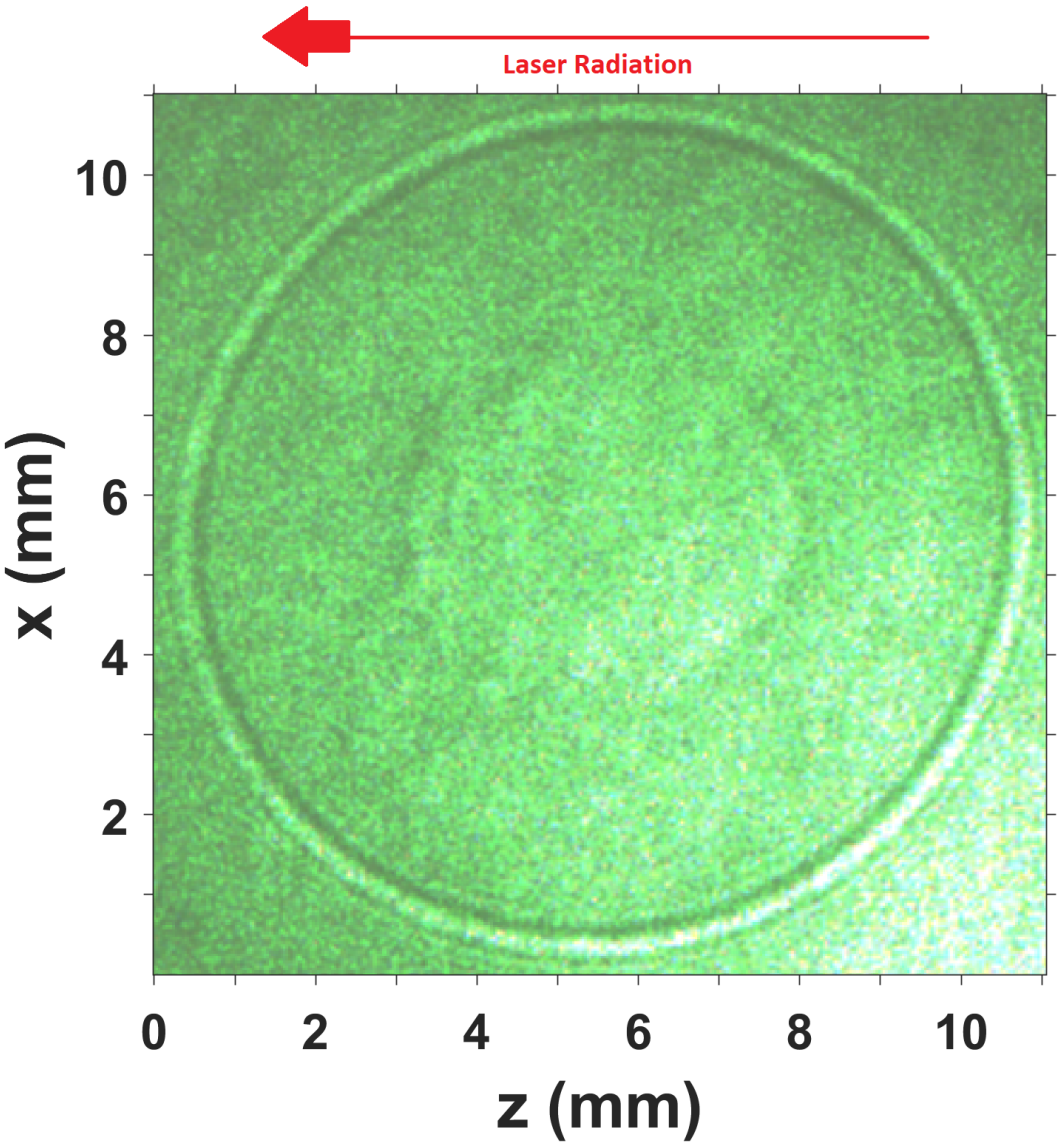

Figure 4.5: Single-shot shadowgraph of expanding laser-induced plasma initiated with a 170 mJ, 6 ns, 1064 nm focused beam, and imaged using a 5 ns, 532 nm backlight that was time-delayed by 4.20±0.05 µs.

Table 4.1: Computed shockwave radii versus measured shockwave radii for SATP air, 170 mJ

τ (ns)	Computed R(mm)	Measured R(mm)
200	1.41	1.00 ± 0.30
1000	2.69	2.67 ± 0.80
1200	2.90	2.83 ± 0.85
2200	3.69	3.57 ± 1.07
4200	4.78	4.95 ± 1.49

Table 4.2: Calculated shockwave velocities and Mach numbers for SATP air, 170 mJ

τ (ns)	v(km/s)	M
200	4.03 ± 1.21	11.76 ± 3.53
1000	1.31 ± 0.39	3.82 ± 1.15
1200	1.08 ± 0.32	3.15 ± 0.95
2200	0.58 ± 0.17	1.67 ± 0.50
4200	0.30 ± 0.09	0.87 ± 0.26

Table 4.3: Measured plasma kernel radii for SATP air, 170 mJ

τ (ns)	r(mm)
200	0.45 ± 0.13
1000	2.25 ± 0.67
1200	2.40 ± 0.72
2200	3.00 ± 0.90
4200	4.04 ± 1.21

shockwave radii are consistent with the shockwave expansion law, with their shockwave expansion velocities, $v(\tau)$, being closer to Mach 2 and slower.

As previously discussed, shockwave expansions in SATP are similar to the CN mixtures used in this dissertation. Therefore, the visualization of these shockwave expansions in SATP provide a good model to the shockwave expansion behavior and plasma kernel geometry in the CN mixtures.

4.2 Cyanide Spectra

4.2.1 CO_2 and N_2 Gaseous Mixture of Fixed Volume

The cyanide (CN) spectra captured by the spectrometer and 2-dimensional intensified charge coupled device for a fixed volume of the 1:1 molar CO_2:N_2 gas mixture held at atmospheric pressure are shown in Figures 4.6 to 4.8. As seen in Figures 4.6 to 4.8 the CN violet system $B^2\Sigma^+$–$X^2\Sigma^+$ vibrational bands of (0,0), (1,1), (2,2), (3,3) and (4,4) are clearly visible. The overlap of the CI 193.09 nm atomic carbon line in second order and the (2,2) CN band head is also seen in Figures 4.6 to 4.8. At time delays greater than 2.5 μs, the CI 193.09 nm atomic carbon line in second order appears to dissipate and does not overlap the (2,2) CN band head as seen in Figure 4.8.

Figures 4.9 to 4.11 are captured CN spectra for a fixed volume of the 1:1 molar CO_2:N_2 gas mixture held at atmospheric pressure with the use of a 309 nm cut-on wavelength filter. The 309 nm cut-on wavelength filter allows for the suppression of the CI 193.09 nm atomic carbon line in second order, which is clearly seen when comparing filtered CN spectra, Figures 4.9 to 4.11, and unfiltered CN spectra, Figures 4.6 to 4.8. Although it is advantageous to apply the 309 nm cut-on wavelength filter for the suppression of the CI 193.09 nm atomic carbon line in second order, the 309 nm cut-on wavelength filter causes a reduction in spectral intensity captured by the spectrometer and ICCD by $\approx$ 13%. Filtered and unfiltered spectra also show the CN plasma moving towards the laser as time elapses.

Figures 4.12 to 4.14 are captured CN spectra for a fixed volume of the 1:1 molar CO_2:N_2 gas mixture held at 276 kPa (2070 Torr). Similar to the gaseous mixture under atmospheric

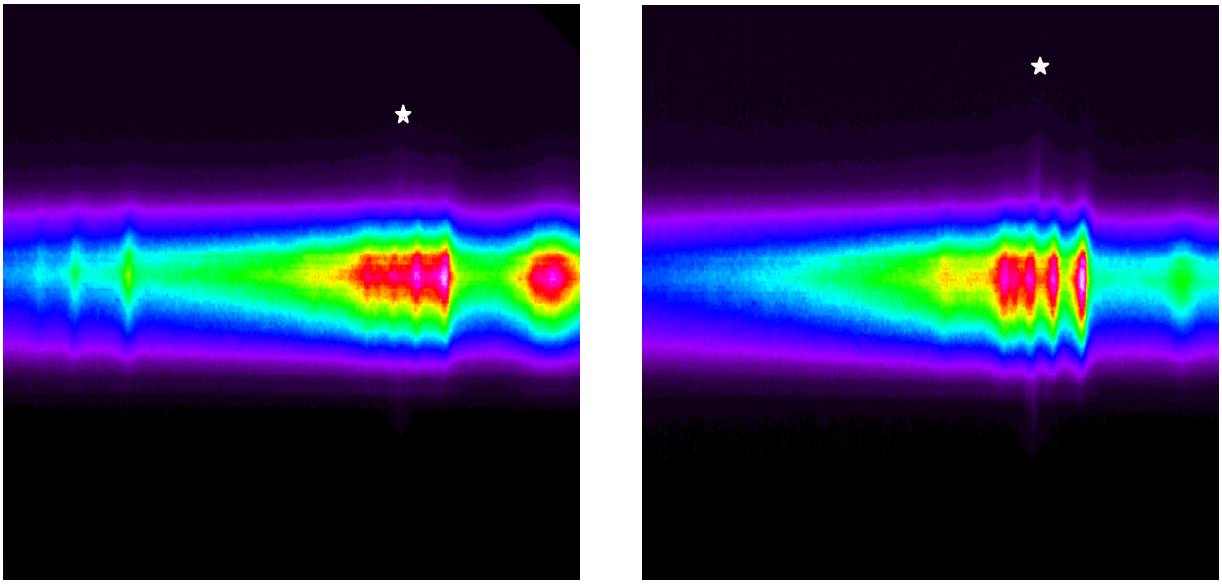

(a) 200 ns

(b) 450 ns

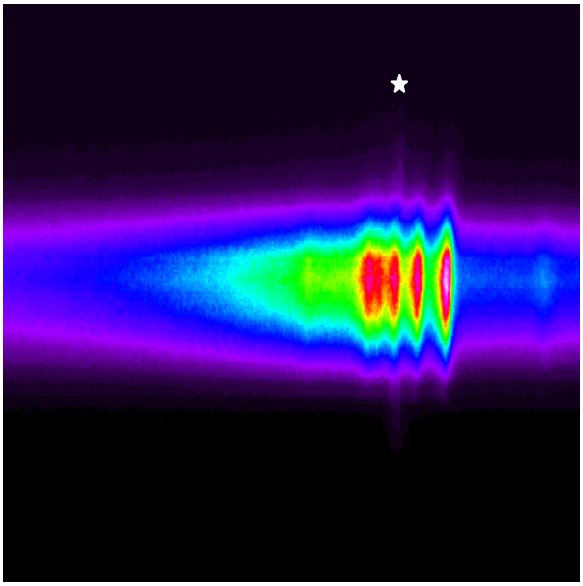

(c) 700 ns

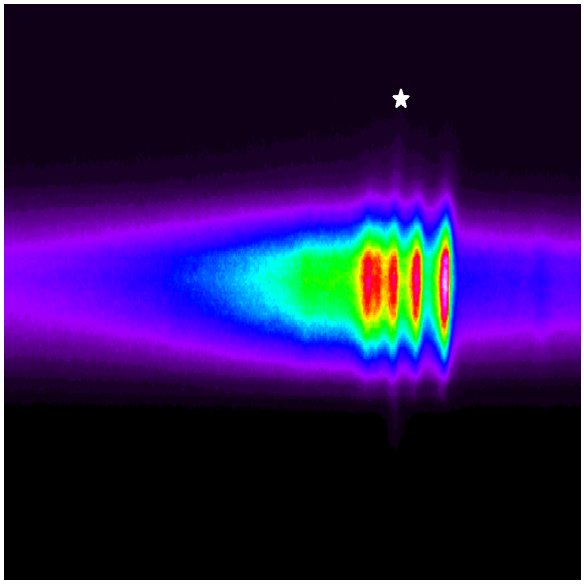

(d) 950 ns

Figure 4.6: Optical breakdown CN spectra in a 1:1 molar CO_2:N_2 gas mixture held at atmospheric pressure for time delays of (**a**) 200 ns, (**b**) 450 ns, (**c**) 700 ns, and (**d**) 950 ns. Spectrometer-detector gatewidth: 125 ns. $\star$, second-order atomic carbon line [70].

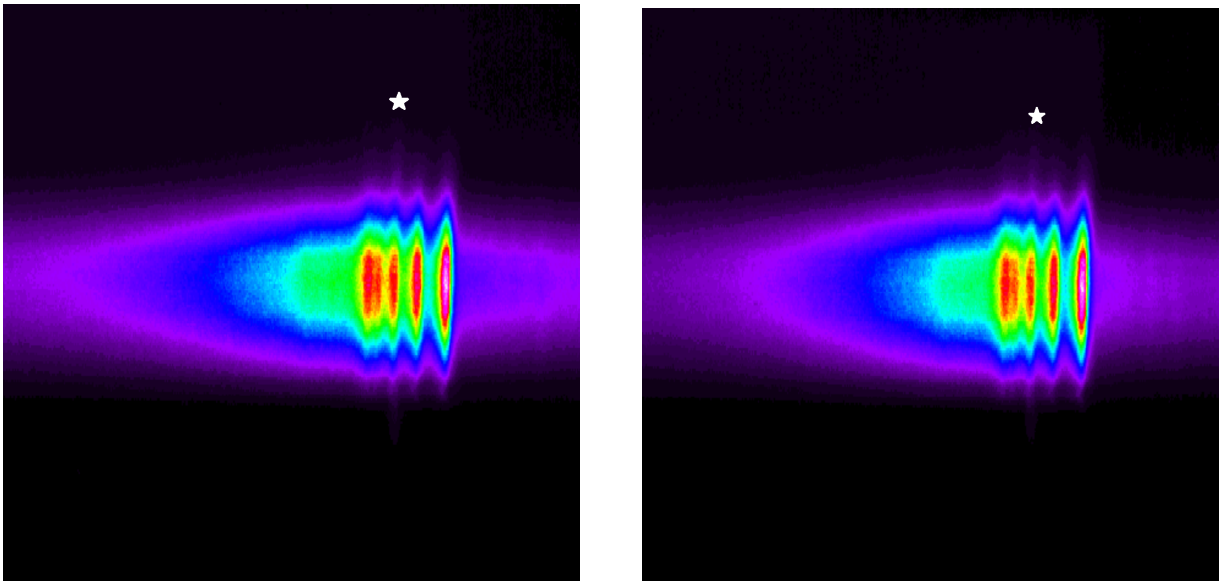

(a) 1200 ns

(b) 1450 ns

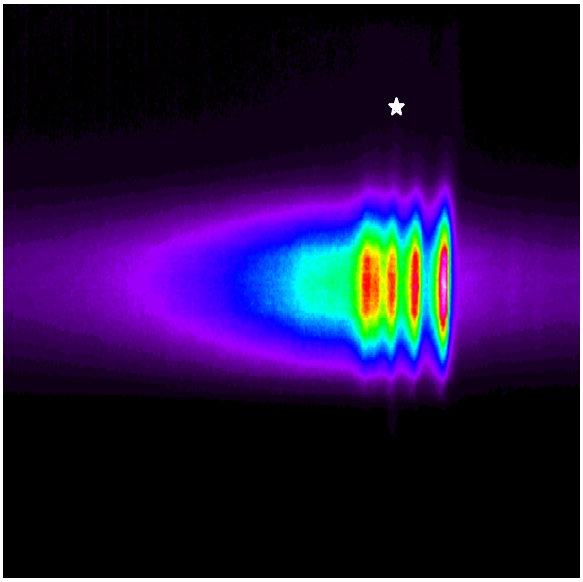

(c) 1700 ns

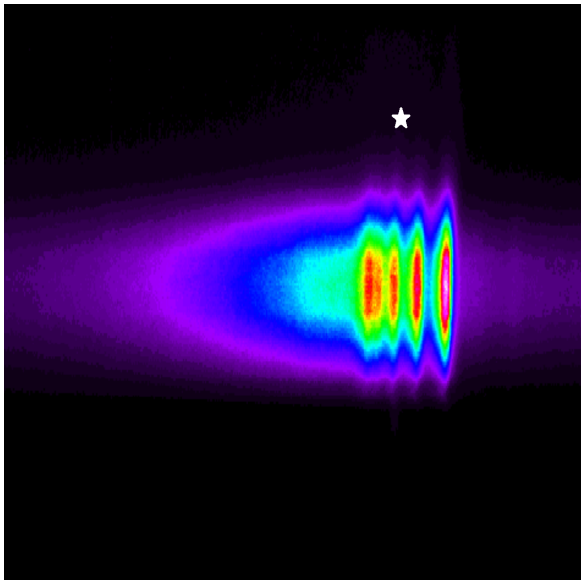

(d) 1950 ns

Figure 4.7: Optical breakdown CN spectra in a 1:1 molar CO_2:N_2 gas mixture held at atmospheric pressure for time delays of (**a**) 1200 ns, (**b**) 1450 ns, (**c**) 1700 ns, and (**d**) 1950 ns. Spectrometer-detector gatewidth: 125 ns. $\star$, second-order atomic carbon line.

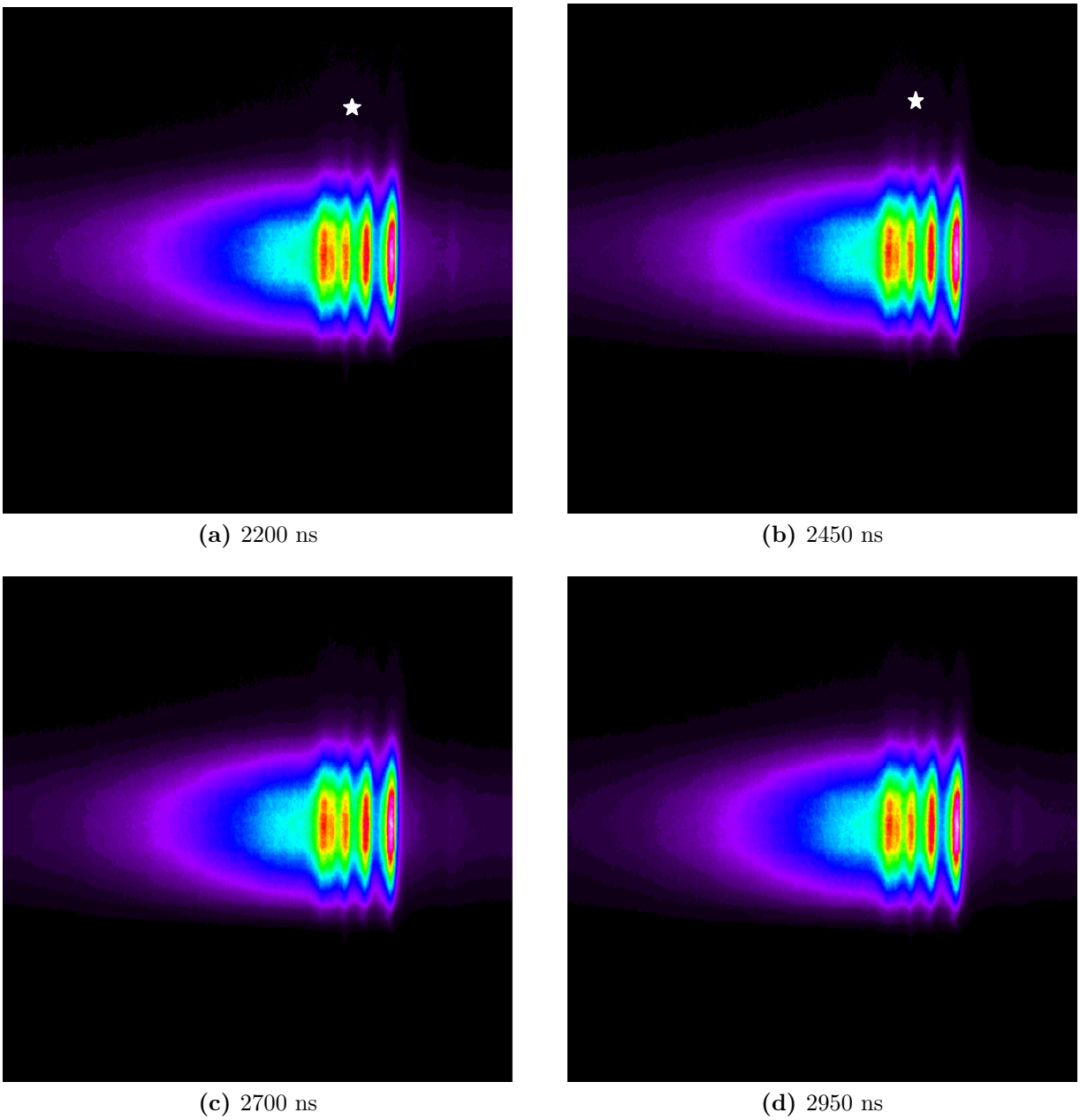

(a) 2200 ns

(b) 2450 ns

(c) 2700 ns

(d) 2950 ns

Figure 4.8: Optical breakdown CN spectra in a 1:1 molar CO_2:N_2 gas mixture held at atmorspheric pressure for time delays of (**a**) 2200 ns, (**b**) 2450 ns, (**c**) 2700 ns, and (**d**) 2950 ns. Spectrometer-detector gatewidth: 125 ns. $\star$, second-order atomic carbon line.

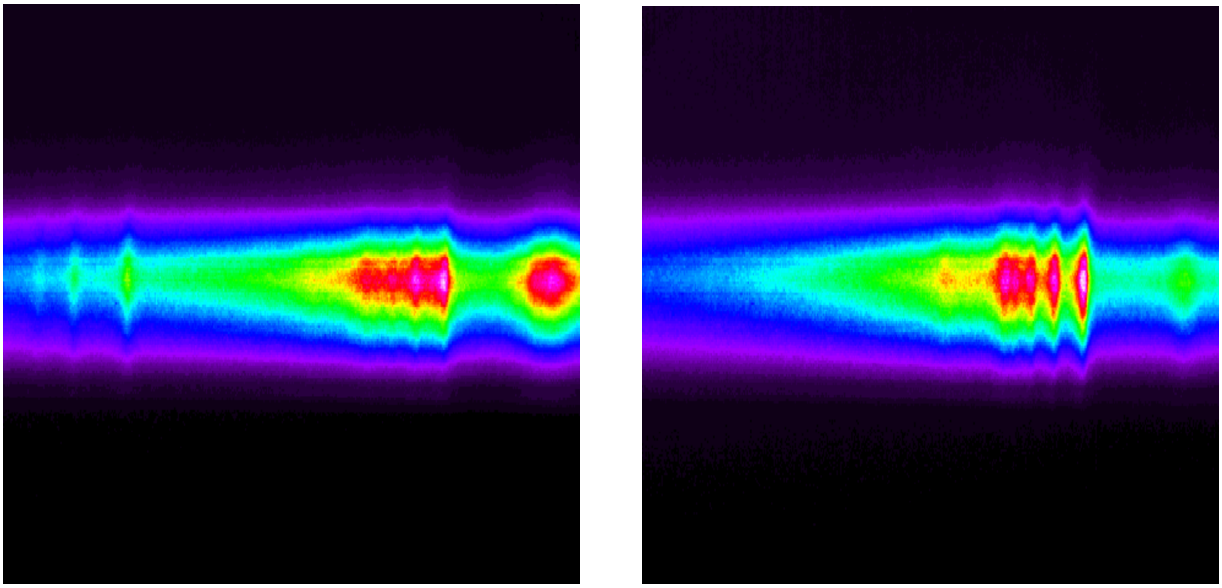

(a) 200 ns

(b) 450 ns

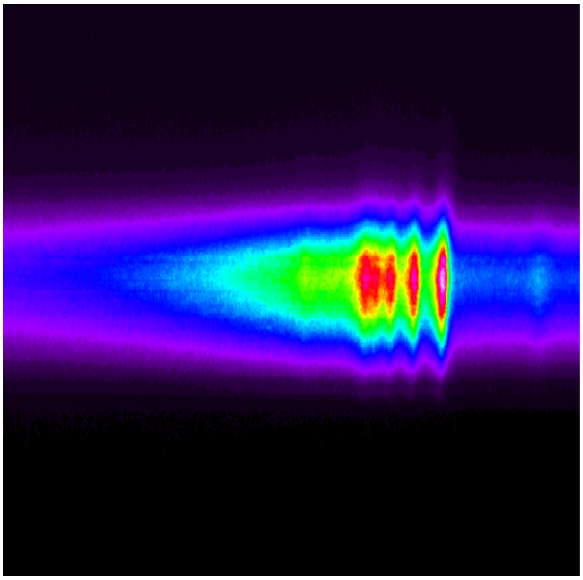

(c) 700 ns

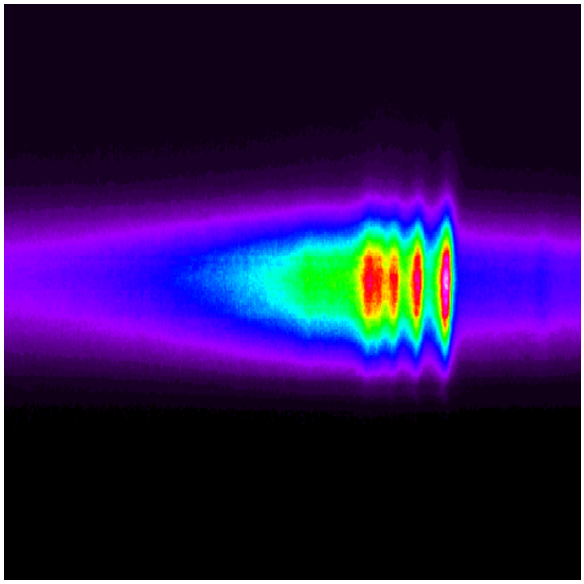

(d) 950 ns

Figure 4.9: Optical breakdown CN spectra in a 1:1 molar CO_2:N_2 gas mixture held at atmospheric pressure for time delays of (**a**) 200 ns, (**b**) 450 ns, (**c**) 700 ns, and (**d**) 950 ns, recorded with 309 nm cut-on wavelength filter for suppression of 193.09 nm second order atomic carbon line [70].

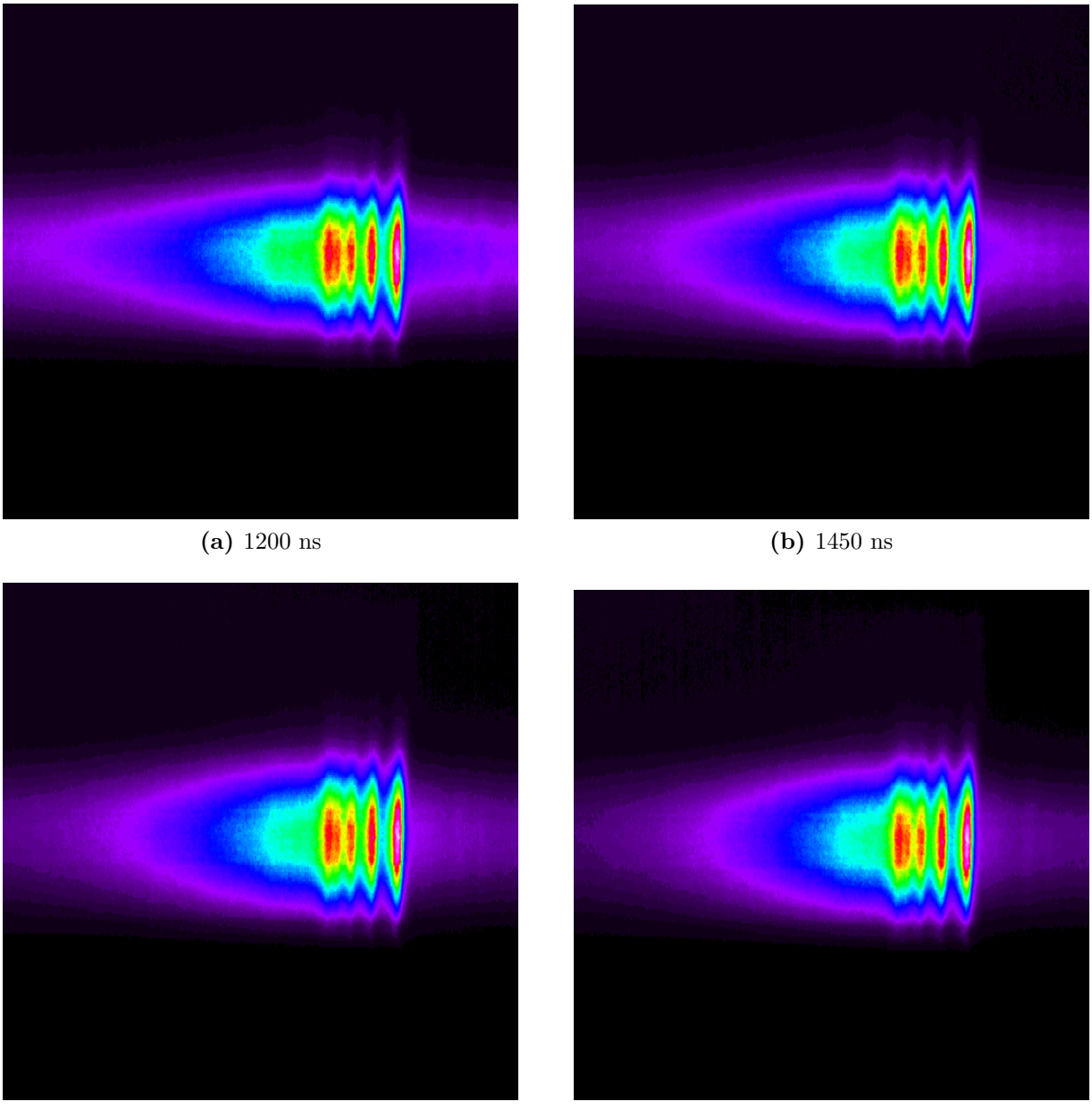

(a) 1200 ns

(b) 1450 ns

(c) 1700 ns

(d) 1950 ns

Figure 4.10: Optical breakdown CN spectra in a 1:1 molar CO_2:N_2 gas mixture held at atmospheric pressure for time delays of (**a**) 1200 ns, (**b**) 1450 ns, (**c**) 1700 ns, and (**d**) 1950 ns, recorded with 309 nm cut-on wavelength filter for suppression of 193.09 nm second order atomic carbon line.

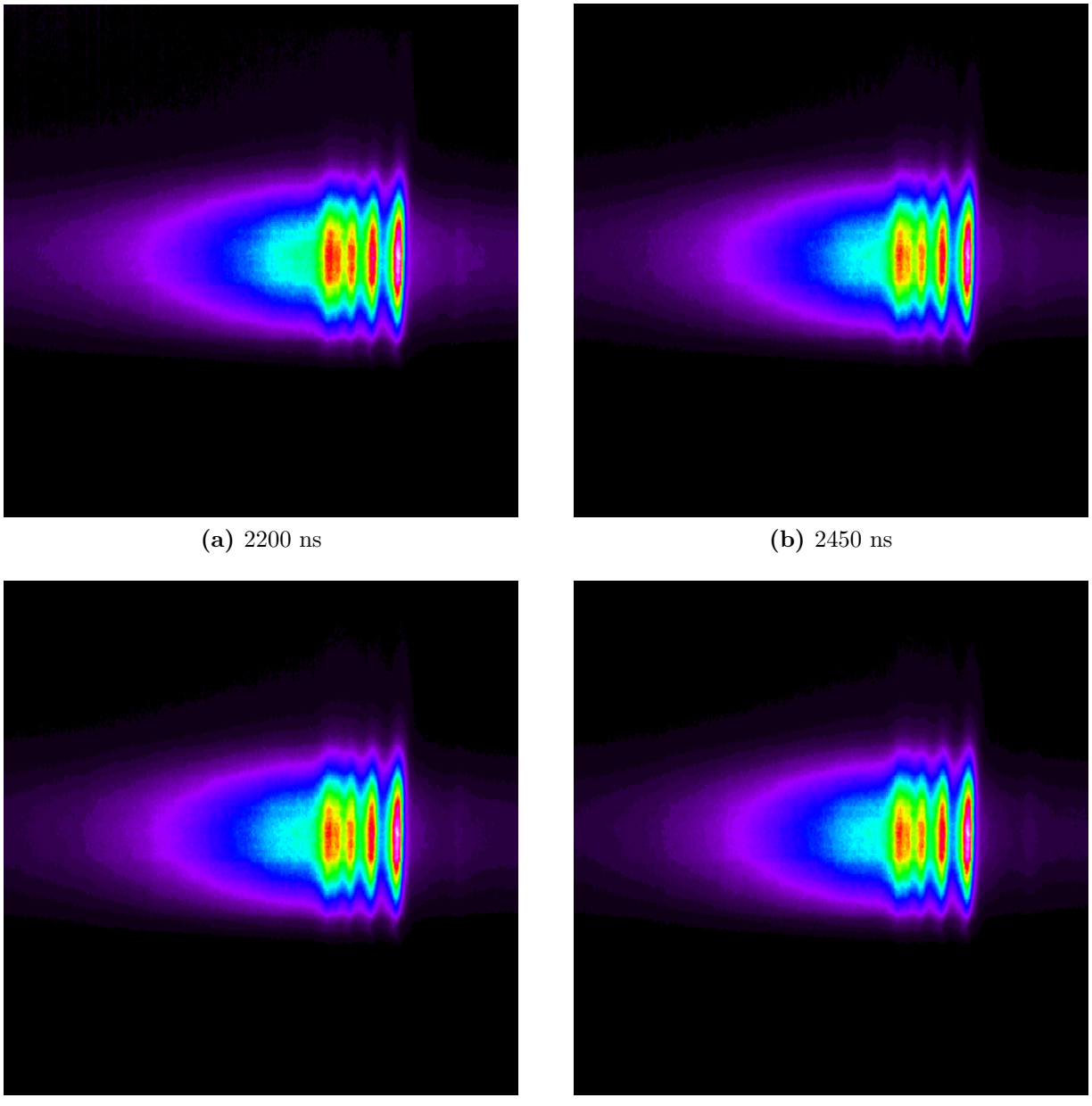

(a) 2200 ns

(b) 2450 ns

(c) 2700 ns

(d) 2950 ns

Figure 4.11: Optical breakdown CN spectra in a 1:1 molar CO_2:N_2 gas mixture held at atmospheric pressure for time delays of (**a**) 2200 ns, (**b**) 2450 ns, (**c**) 2700 ns, and (**d**) 2950 ns, recorded with 309 nm cut-on wavelength filter for suppression of 193.09 nm second order atomic carbon line.

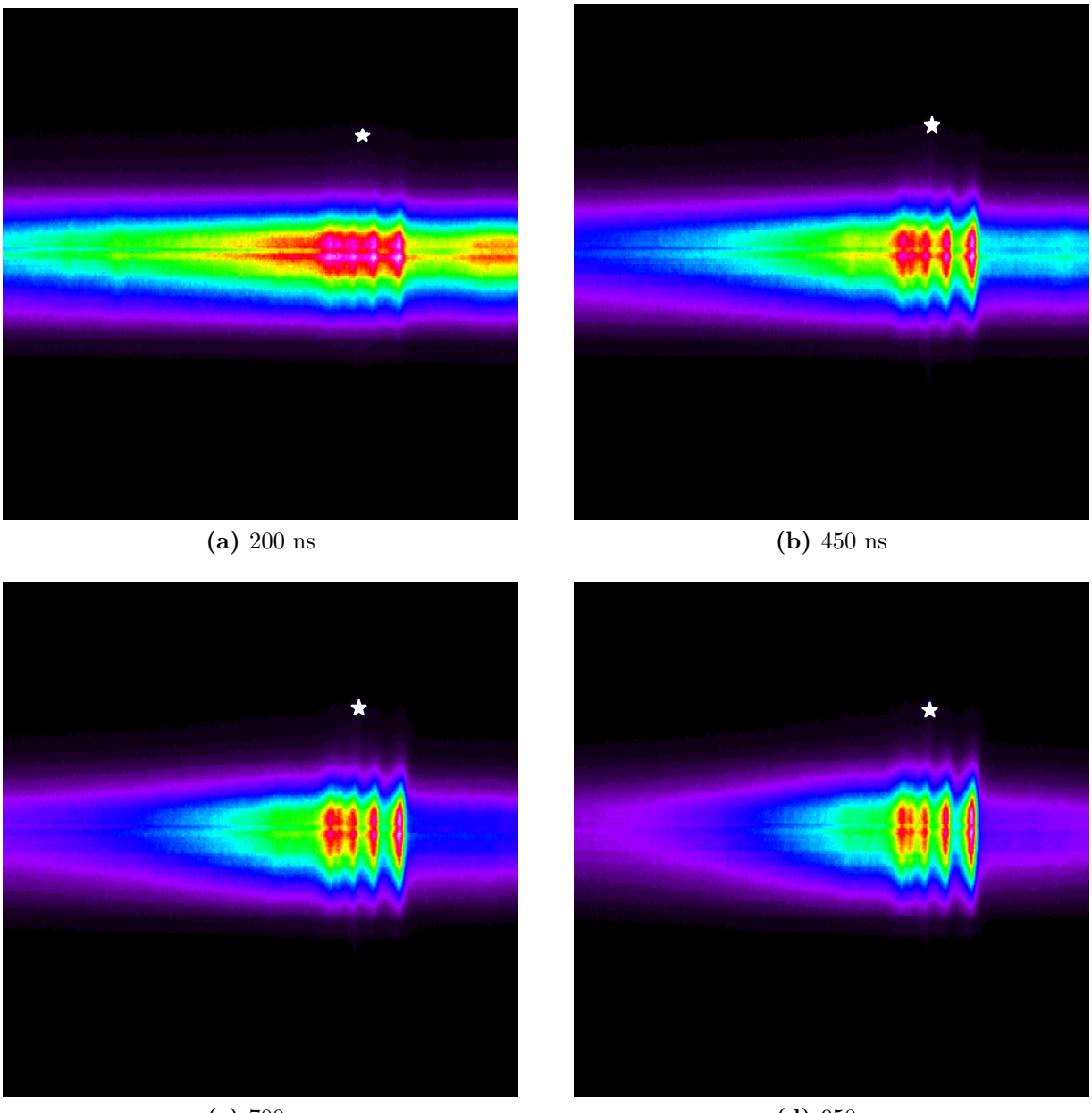

(a) 200 ns **(b)** 450 ns

(c) 700 ns **(d)** 950 ns

Figure 4.12: Optical breakdown CN spectra in a 1:1 molar CO_2:N_2 gas mixture held at 276 kPa (2070 Torr) for time delays of (**a**) 200 ns, (**b**) 450 ns, (**c**) 700 ns, and (**d**) 950 ns. Spectrometer-detector gatewidth: 125 ns. $\star$, second-order atomic carbon line.

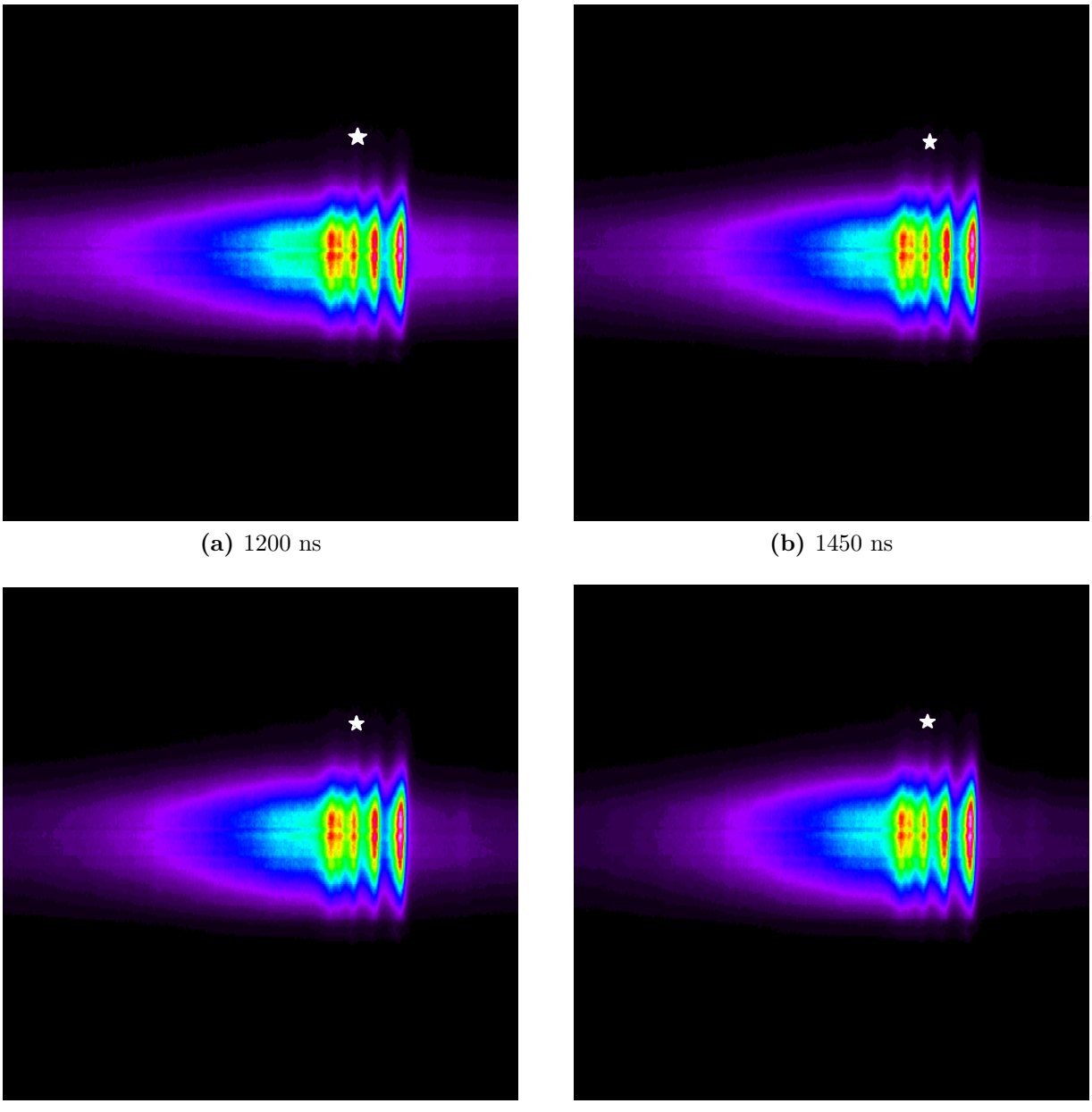

(a) 1200 ns

(b) 1450 ns

(c) 1700 ns

(d) 1950 ns

Figure 4.13: Optical breakdown CN spectra in a 1:1 molar CO_2:N_2 gas mixture held at 276 kPa (2070 Torr) for time delays of (**a**) 1200 ns, (**b**) 1450 ns, (**c**) 1700 ns, and (**d**) 1950 ns. Spectrometer-detector gatewidth: 125 ns. $\star$, second-order atomic carbon line.

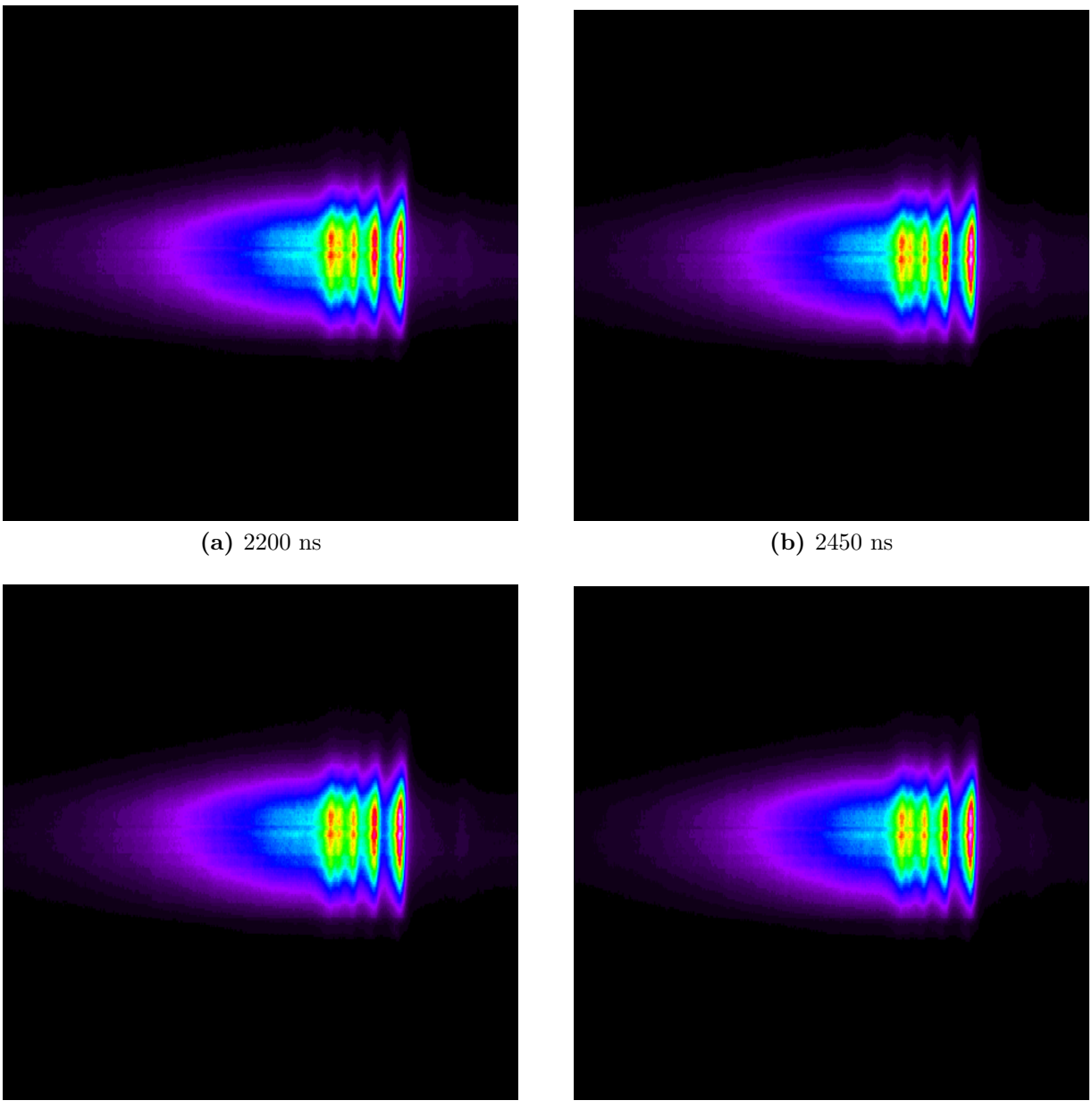

(a) 2200 ns

(b) 2450 ns

(c) 2700 ns

(d) 2950 ns

Figure 4.14: Optical breakdown CN spectra in a 1:1 molar CO_2:N_2 gas mixture held at 276 kPa (2070 Torr) for time delays of (**a**) 2200 ns, (**b**) 2450 ns, (**c**) 2700 ns, and (**d**) 2950 ns. Spectrometer-detector gatewidth: 125 ns.

pressure, the CN violet system $B^2\Sigma^+$–$X^2\Sigma^+$ vibrational bands of (0,0), (1,1), (2,2), (3,3) and (4,4) are clearly visible. Additionally, the overlap of the CI 193.09 nm atomic carbon line in second order and the (2,2) band head is present as in the gaseous mixture under atmospheric pressure. Lastly, it appears the CI 193.09 nm atomic carbon line in second order dissipates away around time delays of 2.2 μs and later, which occurs earlier than what was observed in the gaseous mixture under atmospheric pressure as seen in Figure 4.14.

4.2.2 Flowing CO_2 and N_2 Gaseous Mixture

Figures 4.15 to 4.17 are captured CN spectra for a 1:1 molar CO_2:N_2 flowing gas mixture with a flow rate of 100 mL/min. Similar to the gaseous mixture of fixed volume, the CN violet system $B^2\Sigma^+$–$X^2\Sigma^+$ vibrational bands of (0,0), (1,1), (2,2), (3,3) and (4,4) are clearly visible. Additionally, the overlap of the CI 193.09 nm atomic carbon line in second order and the (2,2) band head is present as in the gaseous mixture of fixed volume. At time delays greater than 2.2 μs, the CI 193.09 nm atomic carbon line in second order appears to dissipate away, which was observed in the gaseous mixture of fixed volume held at 276 kPa (2070 Torr).

Figures 4.18 to 4.20 are captured CN spectra for a 1:1 molar CO_2:N_2 flowing gas mixture with a flow rate of 100 mL/min using a 309 nm cut-on wavelength filter. As in the gaseous mixtures with fixed volumes, the 309 nm cut-on wavelength filter suppresses the CI 193.09 nm atomic carbon line in second order, which is clearly seen when comparing filtered CN spectra, Figures 4.18 to 4.20, and unfiltered CN spectra, Figures 4.15 to 4.17. The 309 nm cut-on wavelength filter causes a reduction in spectral intensity captured by the spectrometer and ICCD by $\approx 10\%$. Filtered and unfiltered CN spectra also show the CN plasma moving towards the laser similar to that of the gaseous mixture of fixed volume.

4.3 Cyanide Temperature

4.3.1 CO_2 and N_2 Gaseous Mixture of Fixed Volume at Atmospheric Pressure

Inferred temperatures of filtered line-of-sight CN spectra in the 1:1 molar CO_2:N_2 gaseous mixture held at atmospheric pressure are plotted versus slit height of the spectrometer as

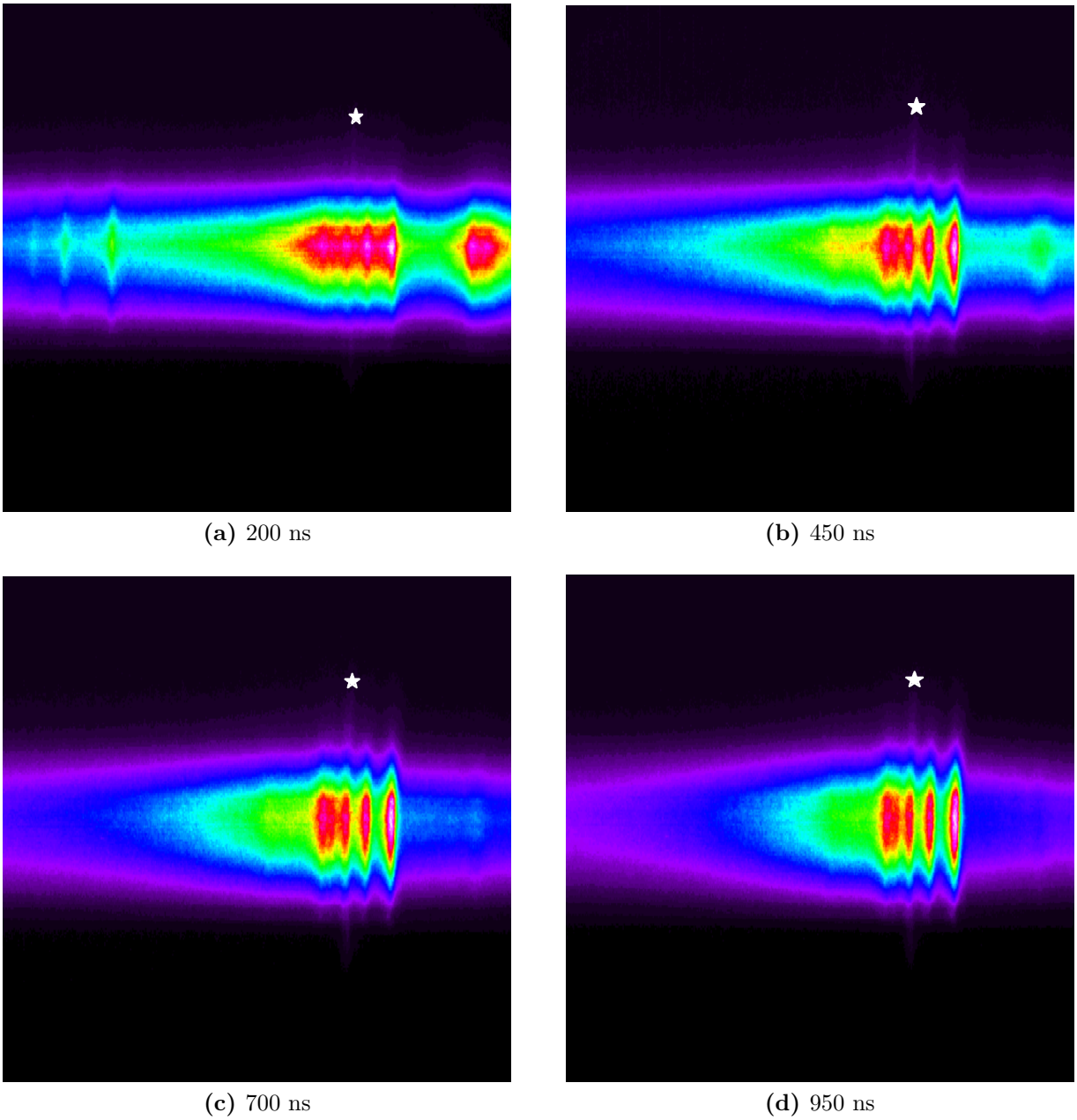

(a) 200 ns **(b)** 450 ns

(c) 700 ns **(d)** 950 ns

Figure 4.15: Optical breakdown CN spectra in a 1:1 molar CO_2:N_2 flowing gas mixture for time delays of (**a**) 200 ns, (**b**) 450 ns, (**c**) 700 ns, and (**d**) 950 ns. Spectrometer-detector gatewidth: 125 ns. $\star$, second-order atomic carbon line.

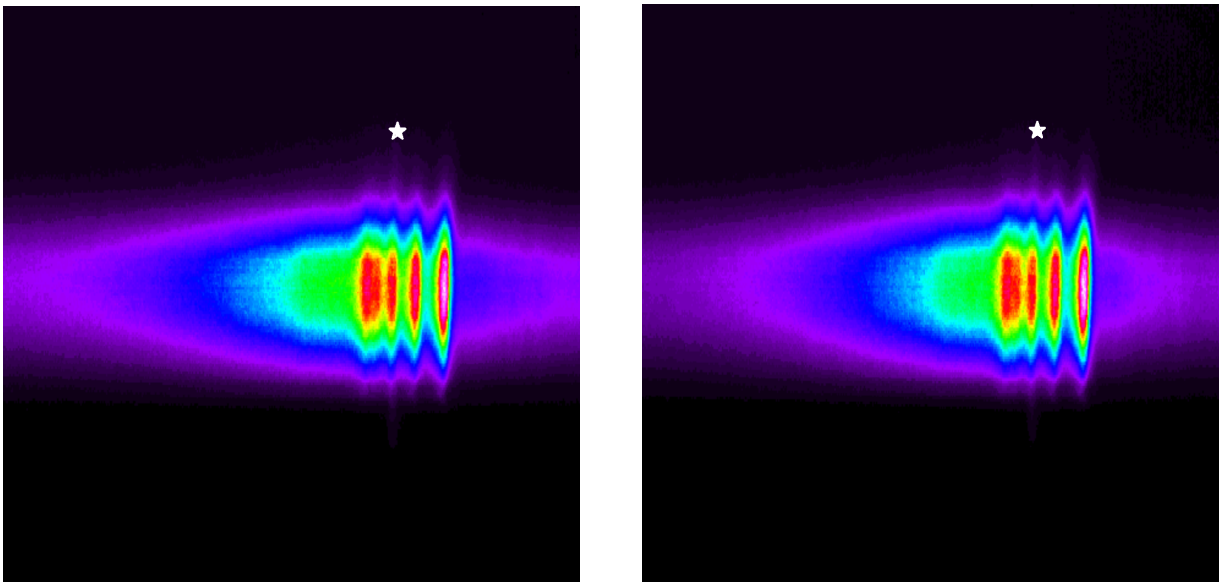

(a) 1200 ns

(b) 1450 ns

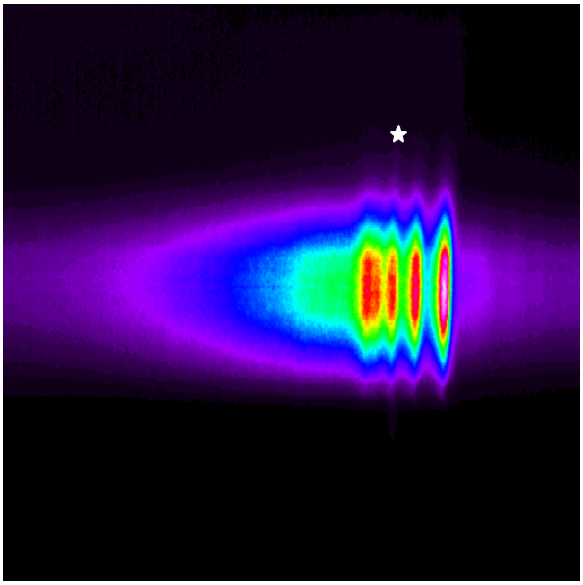

(c) 1700 ns

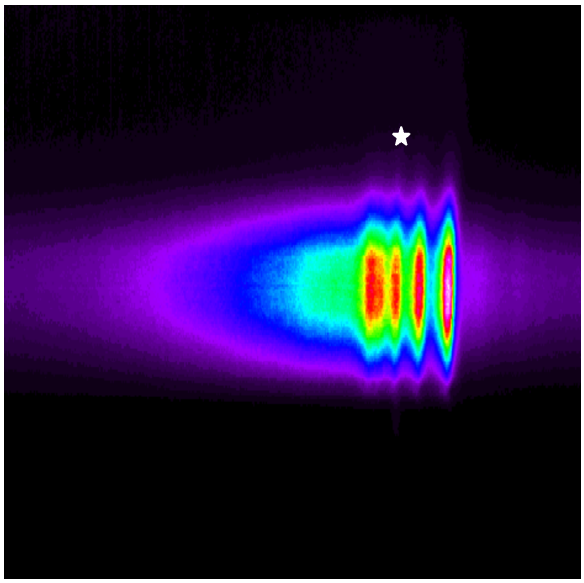

(d) 1950 ns

Figure 4.16: Optical breakdown CN spectra in a 1:1 molar CO_2:N_2 flowing gas mixture for time delays of (**a**) 1200 ns, (**b**) 1450 ns, (**c**) 1700 ns, and (**d**) 1950 ns. Spectrometer-detector gatewidth: 125 ns. $\star$, second-order atomic carbon line.

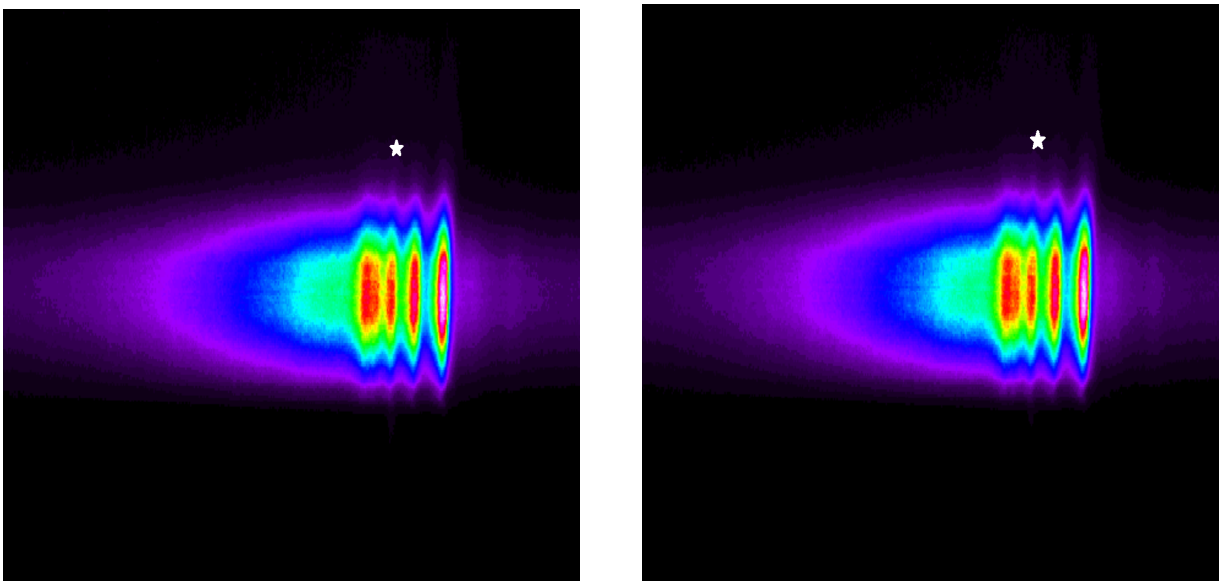

(a) 2200 ns

(b) 2450 ns

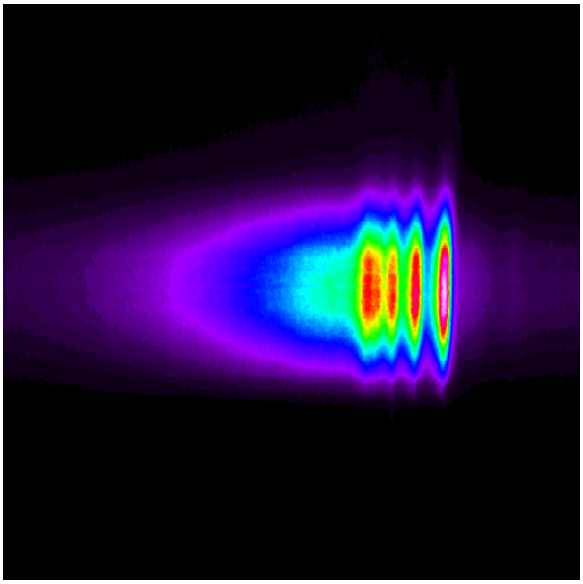

(c) 2700 ns

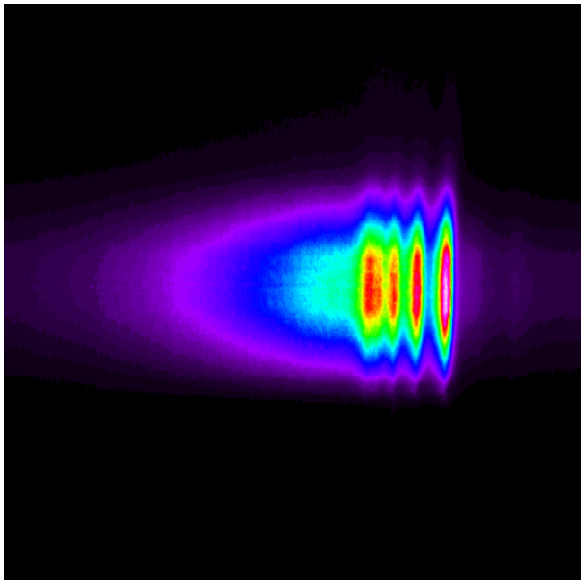

(d) 2950 ns

Figure 4.17: Optical breakdown CN spectra in a 1:1 molar CO_2:N_2 flowing gas mixture for time delays of (**a**) 2200 ns, (**b**) 2450 ns, (**c**) 2700 ns, and (**d**) 2950 ns. Spectrometer-detector gatewidth: 125 ns. $\star$, second-order atomic carbon line.

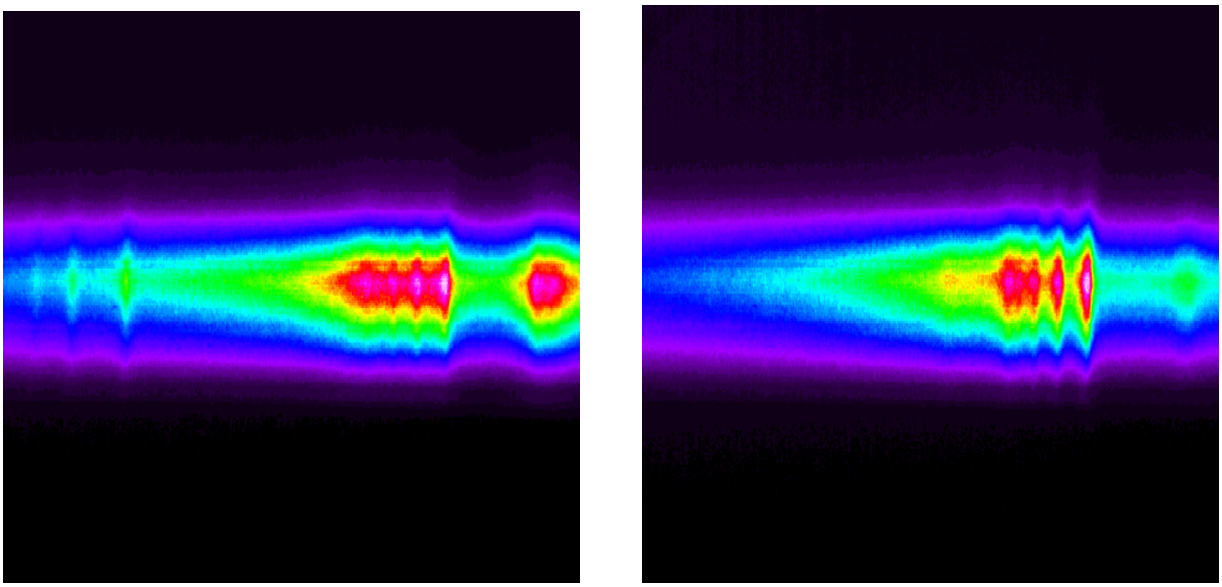

(a) 200 ns

(b) 450 ns

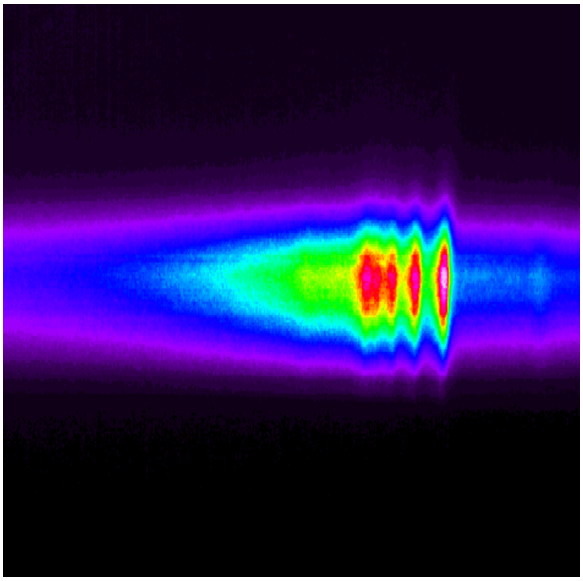

(c) 700 ns

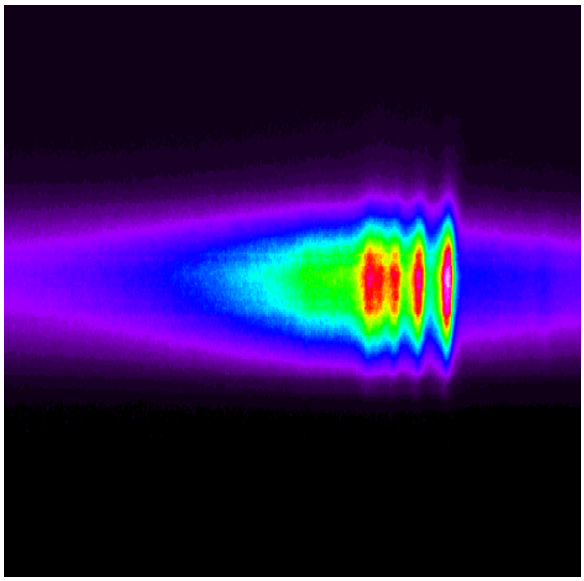

(d) 950 ns

Figure 4.18: Optical breakdown CN spectra in a 1:1 molar CO_2:N_2 flowing gas mixture for time delays of (**a**) 200 ns, (**b**) 450 ns, (**c**) 700 ns, and (**d**) 950 ns, recorded with 309 nm cut-on wavelength filter for suppression of 193.09 nm second order atomic carbon line.

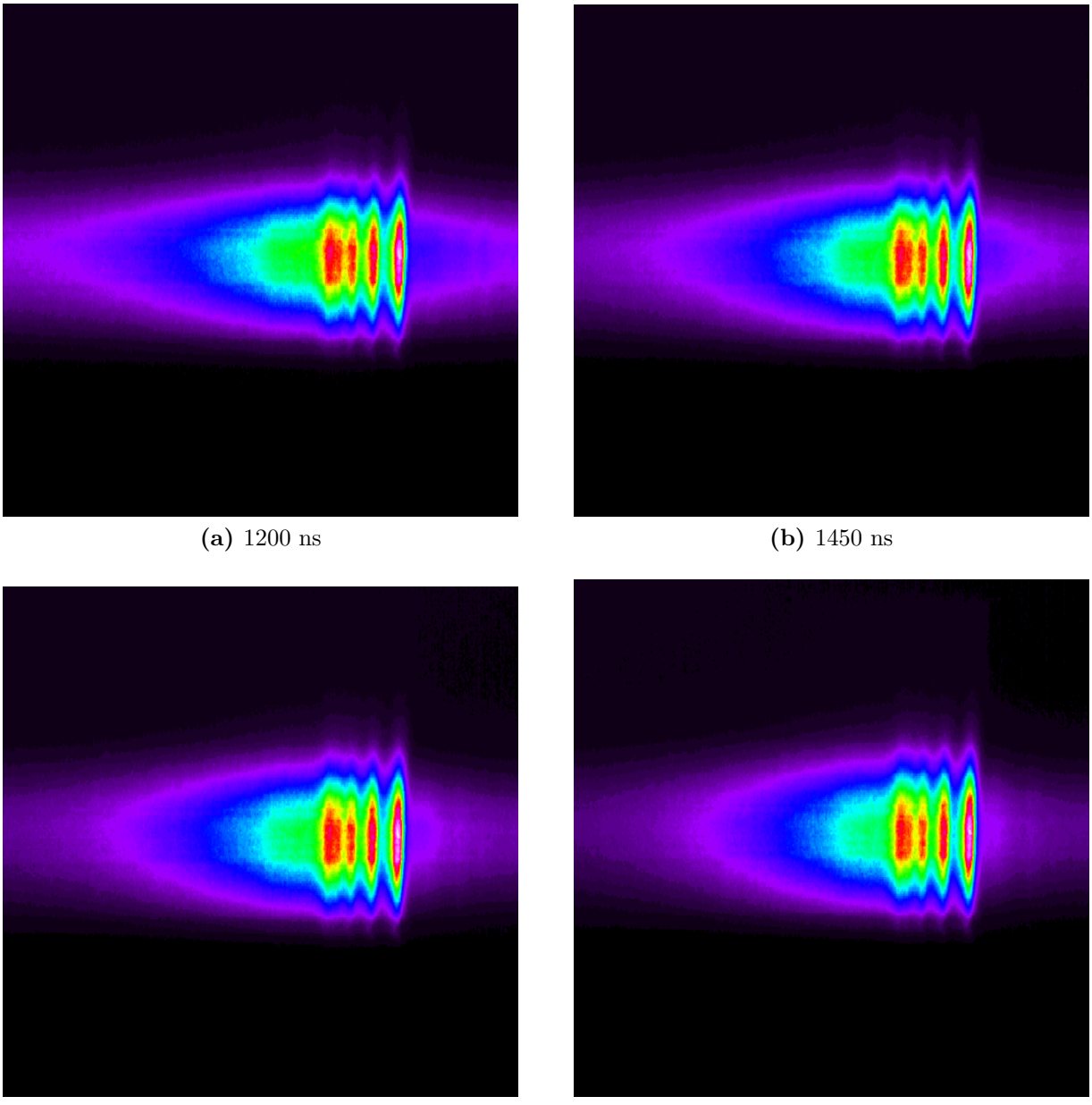

(a) 1200 ns

(b) 1450 ns

(c) 1700 ns

(d) 1950 ns

Figure 4.19: Optical breakdown CN spectra in a 1:1 molar CO_2:N_2 flowing gas mixture for time delays of (**a**) 1200 ns, (**b**) 1450 ns, (**c**) 1700 ns, and (**d**) 1950 ns, recorded with 309 nm cut-on wavelength filter for suppression of 193.09 nm second order atomic carbon line.

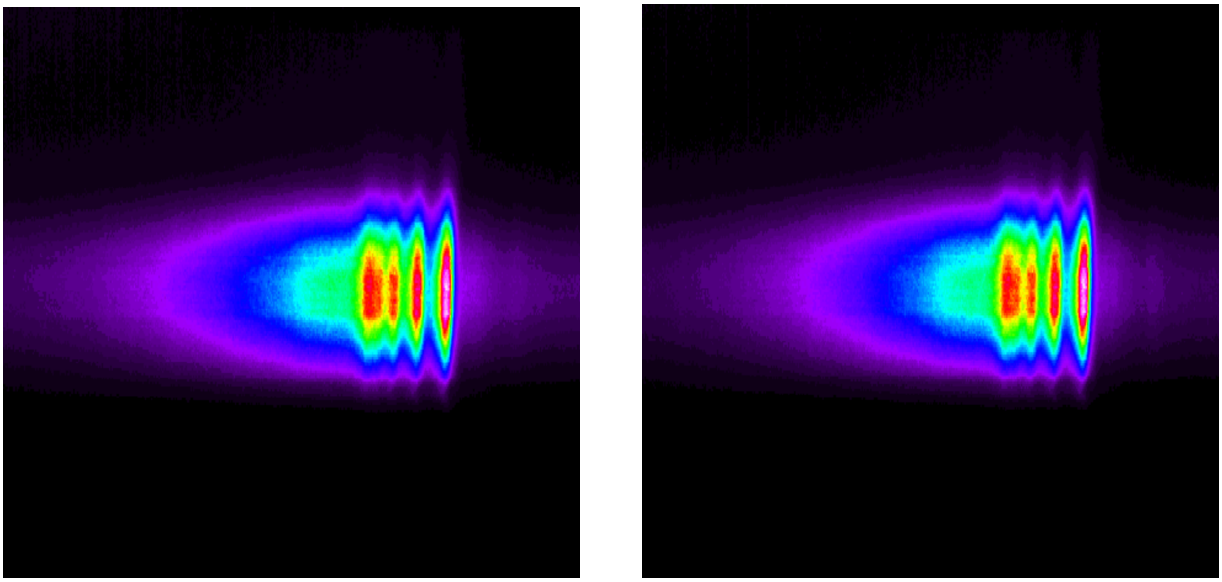

(a) 2200 ns

(b) 2450 ns

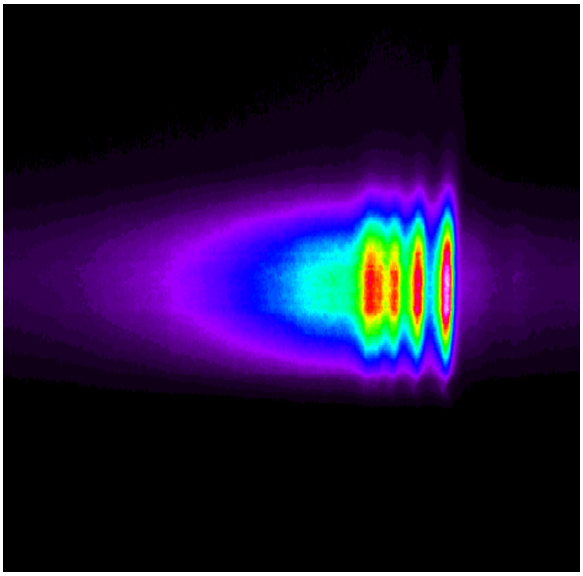

(c) 2700 ns

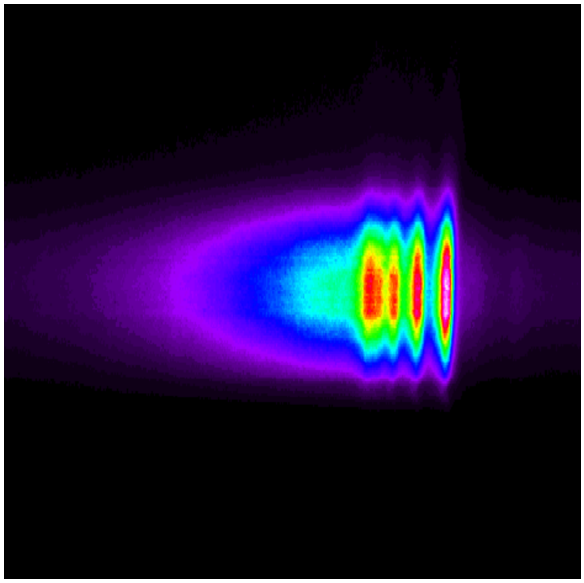

(d) 2950 ns

Figure 4.20: Optical breakdown CN spectra in a 1:1 molar CO_2:N_2 flowing gas mixture for time delays of (**a**) 2200 ns, (**b**) 2450 ns, (**c**) 2700 ns, and (**d**) 2950 ns, recorded with 309 nm cut-on wavelength filter for suppression of 193.09 nm second order atomic carbon line.

as shown in Figures 4.21 to 4.24. The outgoing shockwave can be seen from time delays of 450 ns to 950 ns. As can be seen in Figures 4.21 to 4.24, temperature variations occur in the central region, while increased temperatures are shown at the edges of the plasma. Higher temperatures are seen on the edge of the plasma towards the top of slit or towards the laser side. At a time delay of 450 ns, Figure 4.21, the temperatures in the central region of the plasma are between 9,500 K to 10,000 K, while the temperatures at the edges of the plasma are more than 10,000 K. At time delays of 700 ns and 950 ns, Figures 4.21 and 4.22, the temperatures in the central region of the plasma cool to a range of 9,000 K to 9,500 K, while temperatures at the edges of the plasma are between 9,500 K to 10,000 K. As time elapses further the plasma central region temperatures cool even further to a range of 8,500 K to 9,000 K for time delays of 1.2 μs to 1.7 μs, while the edges of the plasma maintain a temperature range of 9,500 K to 10,000 K as seen in Figures 4.22 to 4.23. From time delays of 1.95 μs to 2.2 μs, Figure 4.24, the central region of the plasma sustains temperatures of 8,500 K to 9,000 K and temperatures near the edge of plasma towards the bottom of the slit are around 9,000 K, while temperatures near the edge of the plasma towards the top of the slit increase to greater than 11,000 K.

4.3.2 CO_2 and N_2 Gaseous Mixture of Fixed Volume at 276 kPa (2070 Torr)

Inferred temperatures of filtered line-of-sight CN spectra in the 1:1 molar CO_2:N_2 gaseous mixture held at 276 kPa (2070 Torr) are plotted versus slit height of the spectrometer as shown in Figures 4.25 to 4.28. The outgoing shockwave can be seen from time delays of 450 ns to 950 ns. As can be seen in Figures 4.25 to 4.28, temperature variations occur in the central region, while increased temperatures are shown at the edges of the plasma. Higher temperatures are seen on the edge of the plasma towards the top of slit or towards the laser side. Unlike the 1:1 molar CO_2:N_2 gaseous mixture held at atmospheric pressure at a time delay of 450 ns, Figure 4.25, the temperatures in the central region of the plasma and at the edges are the plasma are between 9,500 K to 10,000 K, showing no increase of temperature at the edges. This absence of temperature increase near the edges may be caused by the CI 193.09 nm atomic carbon line in second order interference, due to the lack of filtering of 1:1

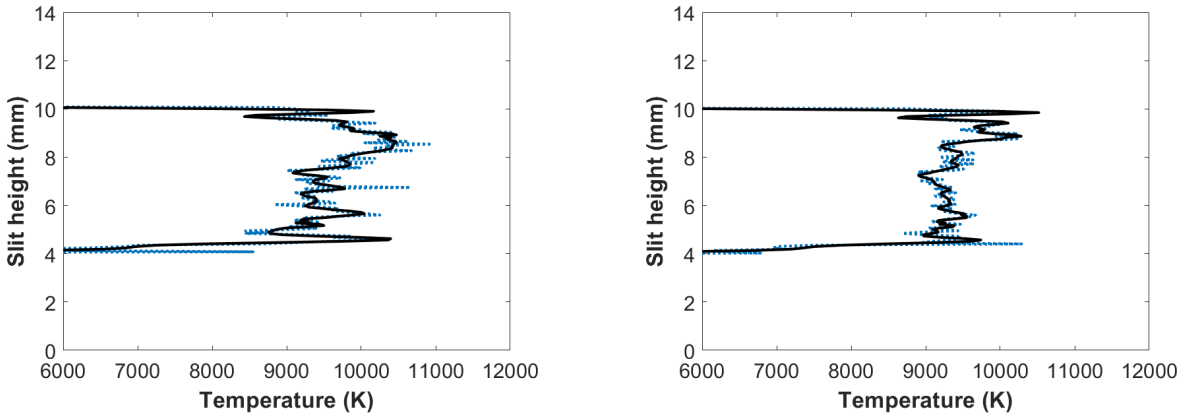

Figure 4.21: Temperature vs. slit height for filtered line-of-sight CN spectra for fixed volume of 1:1 molar CO_2:N_2 gaseous mixture held at atmospheric pressure with 450 ns (left) and 700 ns (right) time delay [70 ,71].

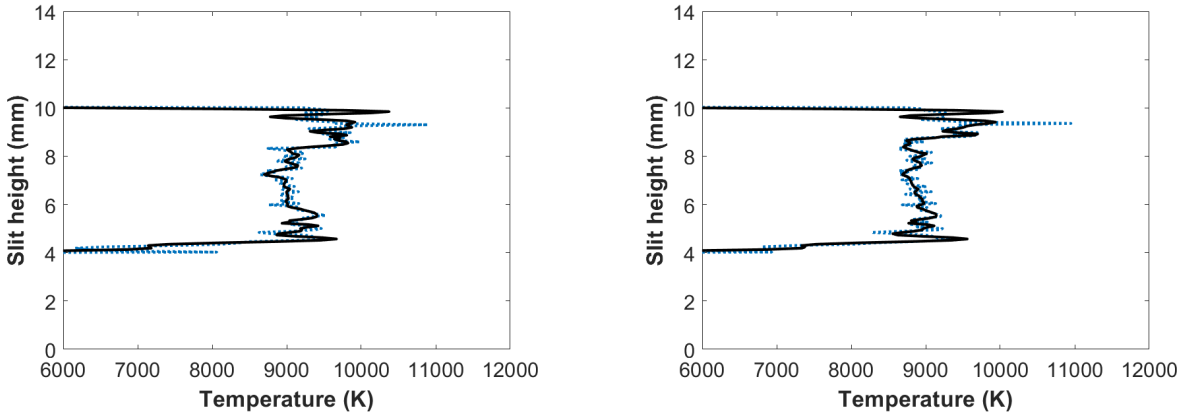

Figure 4.22: Temperature vs. slit height for filtered line-of-sight CN spectra for fixed volume of 1:1 molar CO_2:N_2 gaseous mixture held at atmospheric pressure with 950 ns (left) and 1200 ns (right) time delay [70 ,71].

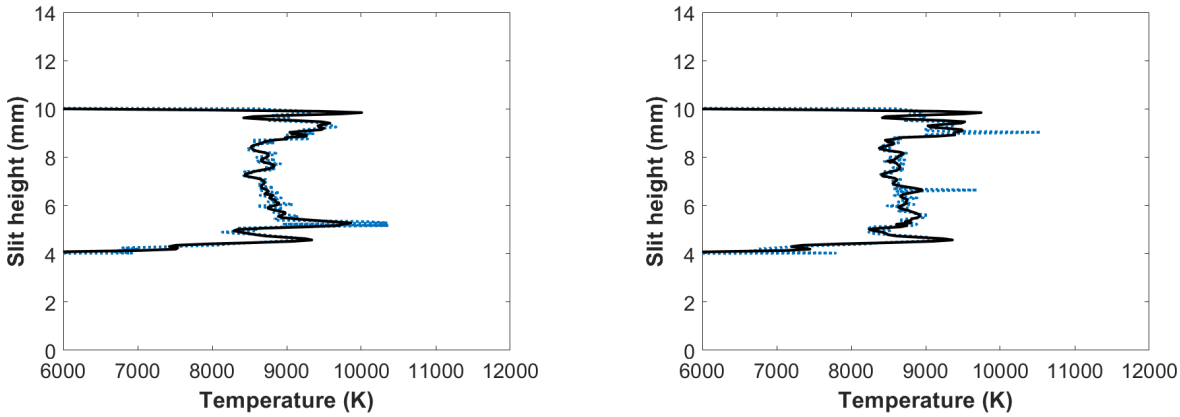

Figure 4.23: Temperature vs. slit height for filtered line-of-sight CN spectra for fixed volume of 1:1 molar CO_2:N_2 gaseous mixture held at atmospheric pressure with 1450 ns (left) and 1700 ns (right) time delay.

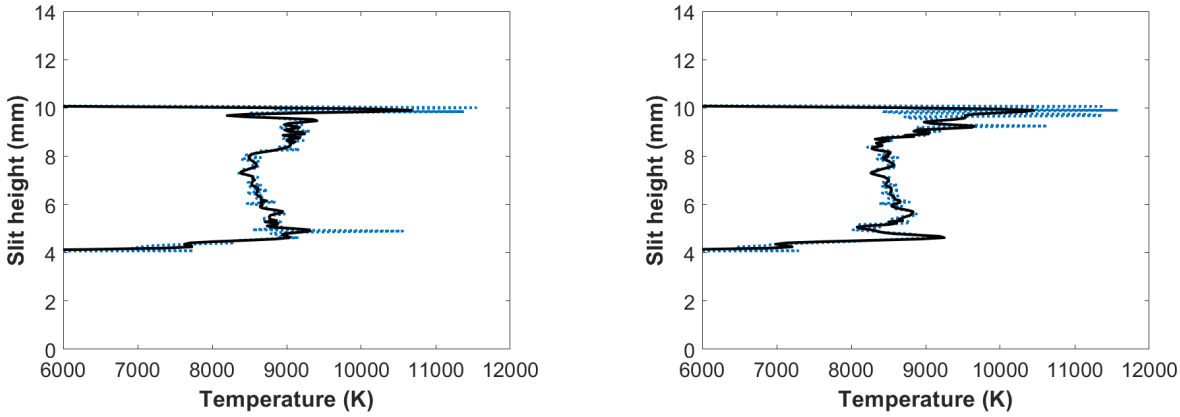

Figure 4.24: Temperature vs. slit height for filtered line-of-sight CN spectra for fixed volume of 1:1 molar CO_2:N_2 gaseous mixture held at atmospheric pressure with 1950 ns (left) and 2200 ns (right) time delay.

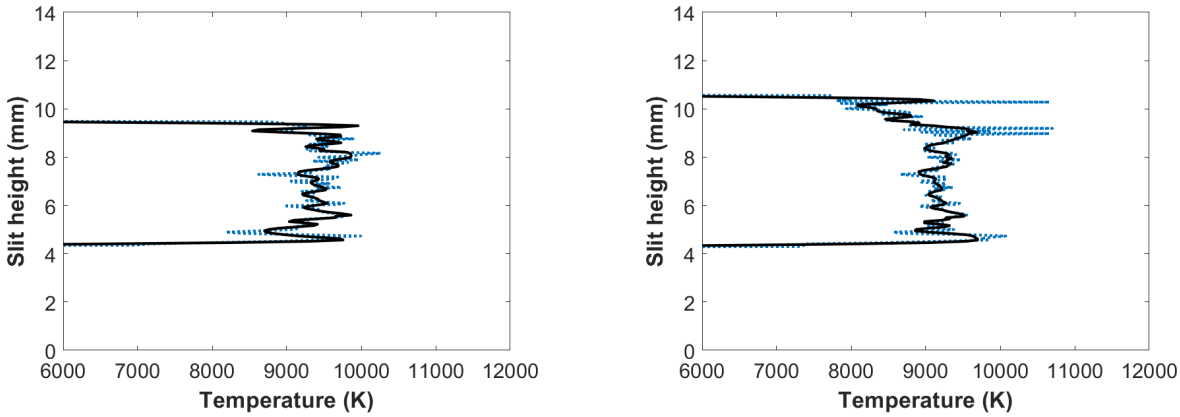

Figure 4.25: Temperature vs. slit height for filtered line-of-sight CN spectra for fixed volume of 1:1 molar CO_2:N_2 gaseous mixture held at 276 kPa (2070 Torr) with 450 ns (left) and 700 ns (right) time delay.

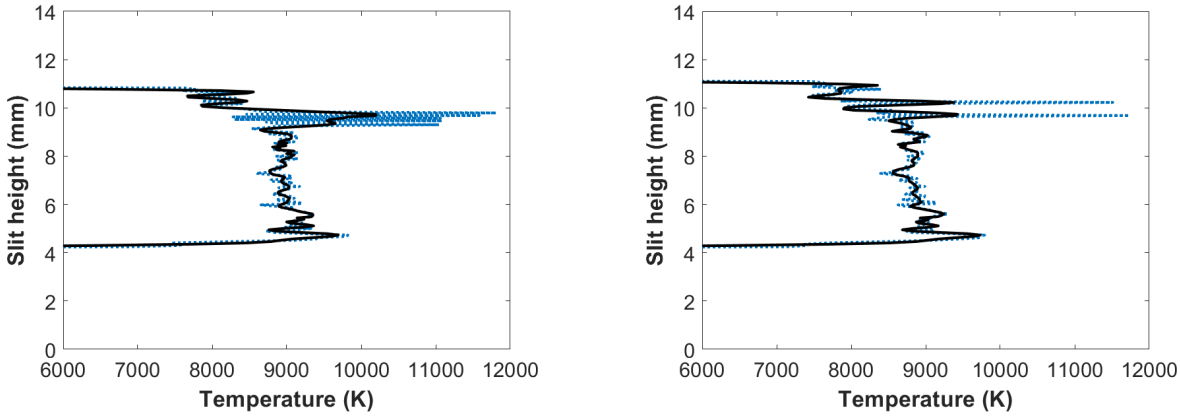

Figure 4.26: Temperature vs. slit height for filtered line-of-sight CN spectra for fixed volume of 1:1 molar CO_2:N_2 gaseous mixture held at 276 kPa (2070 Torr) with 950 ns (left) and 1200 ns (right) time delay.

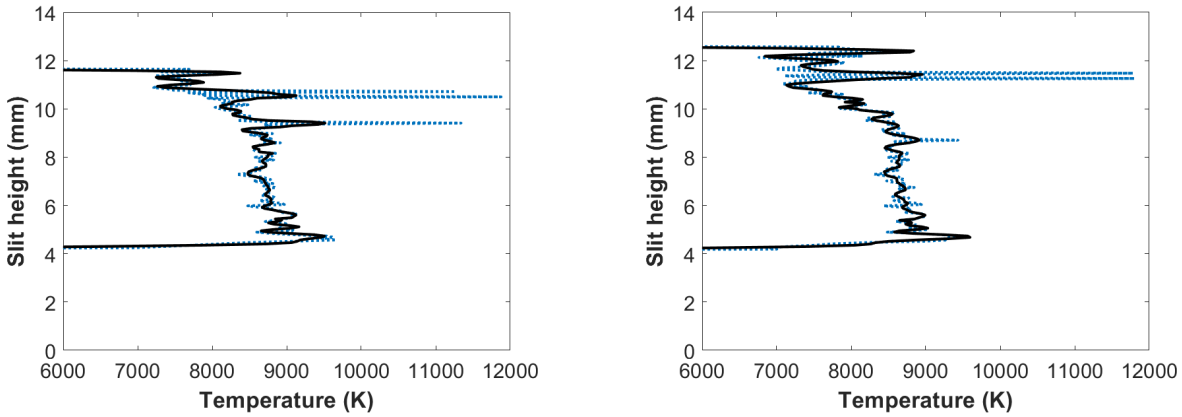

Figure 4.27: Temperature vs. slit height for filtered line-of-sight CN spectra for fixed volume of 1:1 molar CO_2:N_2 gaseous mixture held at 276 kPa (2070 Torr) with 1450 ns (left) and 1700 ns (right) time delay.

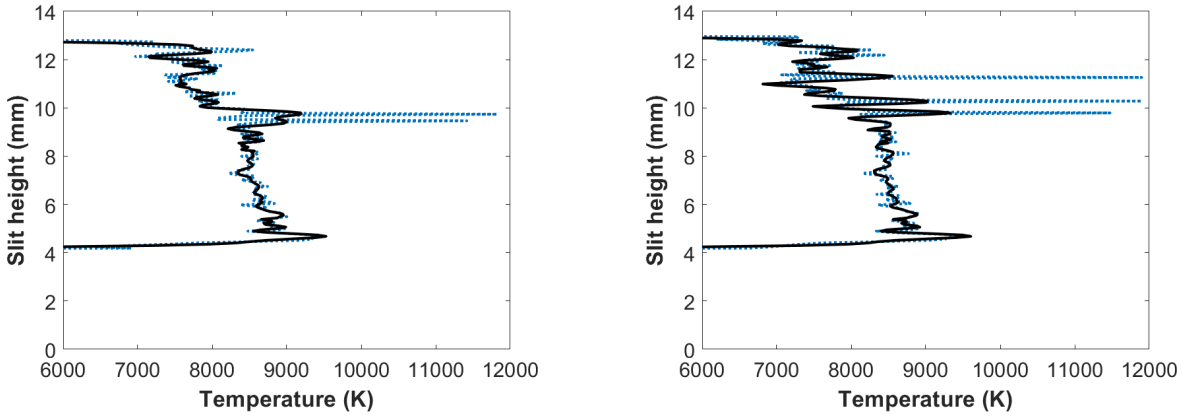

Figure 4.28: Temperature vs. slit height for filtered line-of-sight CN spectra for fixed volume of 1:1 molar CO_2:N_2 gaseous mixture held at 276 kPa (2070 Torr) with 1950 ns (left) and 2200 ns (right) time delay.

molar CO_2:N_2 gaseous mixture held at 276 kPa (2070 Torr). At a time delay of 700 ns time delay, Figure 4.25, the temperatures in the central region of the plasma cool to a range of 9,000 K to 9,500 K, while temperatures at the edges of the plasma increase to an excess of 10,000 K. At the 950 ns time delay, Figure 4.26, the temperatures in the central region of the plasma remain in a range of 9,000 K to 9,500 K, while the temperatures at the edge of the plasma towards the top of the slit increase to greater than 11,000 K. At a time delays of 1.2 μs to 1.7 μs the plasma central region temperatures cool even further to a range of 8,500 K to 9,000 K, while the edge of the plasma towards the top of the slit maintain temperatures in excess of 11,000 K as seen in Figures 4.26 to 4.27. From time delays of 1.95 μs to 2.2 μs, Figure 4.28, the central region of the plasma sustains temperatures of 8,500 K to 9,000 K and temperatures near the edge of the plasma towards the top of slit continue to be greater than 11,000 K. Also seen in Figure 4.28 is the plasma temperatures in excess of 11,000 K are near the edge of the plasma towards the top of the slit, but are closer to the center plasma, which does not occur in the CO_2:N_2 gaseous mixture held at atmospheric pressure.

4.3.3 CO_2 and N_2 Flowing Gaseous Mixture

Inferred temperatures of filtered line-of-sight CN spectra in the 1:1 molar CO_2:N_2 flowing gaseous mixture are plotted versus slit height of the spectrometer as shown in Figures 4.29 to 4.32. The outgoing shockwave can be seen from time delays of 450 ns to 950 ns as with the 1:1 molar CO_2:N_2 gaseous mixture held at atmospheric pressure and 276 kPa (2070 Torr). As can be seen in Figures 4.29 to 4.32, temperature variations occur in the central region, while increased temperatures are shown at the edges of the plasma similar to the 1:1 molar CO_2:N_2 gaseous mixture held at atmospheric pressure and 276 kPa (2070 Torr). Identical to the 1:1 molar CO_2:N_2 gaseous mixture held at atmospheric pressure and 276 kPa (2070 Torr), higher temperatures are seen on the edge of the plasma towards the top of slit or towards the laser side. At a time delay of 450 ns, Figure 4.29, the temperatures in the central region of the plasma are between 9,500 K to 10,000 K, while the temperatures at the edges of the plasma are more than 10,000 K. At a time delay of 700 ns time delay, Figure 4.29, the temperatures in the central region of the plasma cool to a range of 9,000 K to 9,500 K, while temperatures at the edges of the plasma are between 9,500 K to 10,000 K.

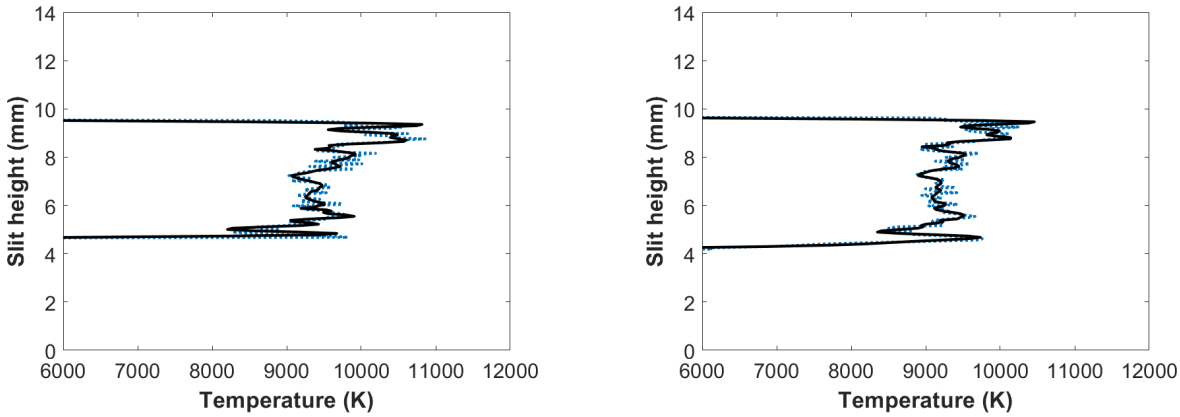

Figure 4.29: Temperature vs. slit height for filtered line-of-sight CN spectra for a flowing 1:1 molar CO_2:N_2 gaseous mixture with 450 ns (left) and 700 ns (right) time delay [70].

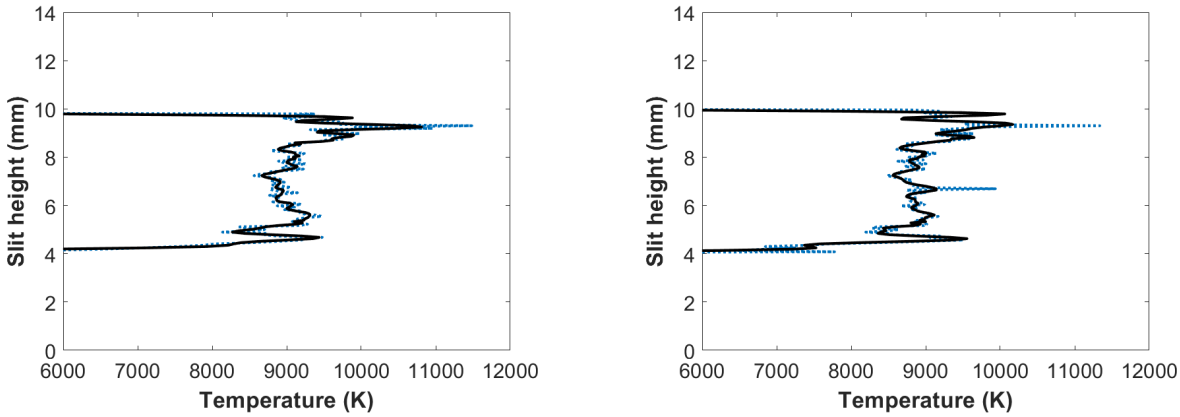

Figure 4.30: Temperature vs. slit height for filtered line-of-sight CN spectra for a flowing 1:1 molar CO_2:N_2 gaseous mixture with 950 ns (left) and 1200 ns (right) time delay [70].

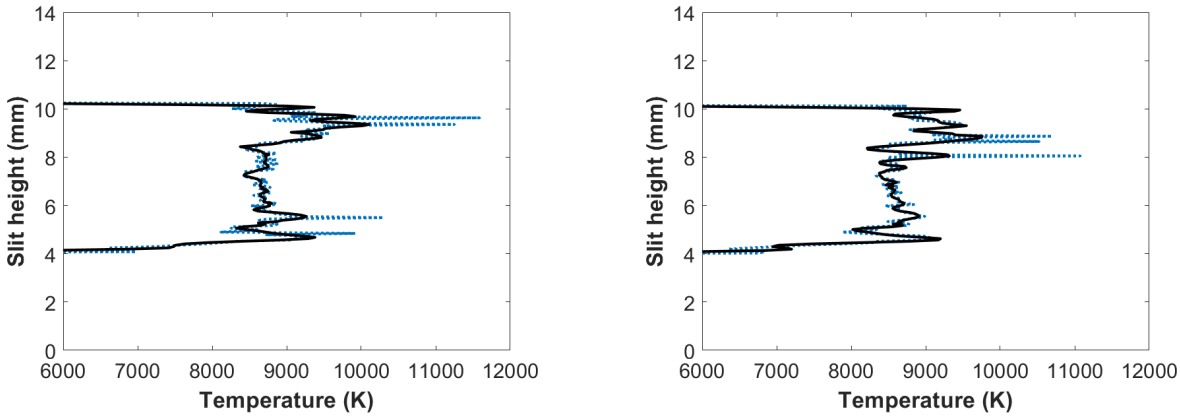

Figure 4.31: Temperature vs. slit height for filtered line-of-sight CN spectra for a flowing 1:1 molar CO_2:N_2 gaseous mixture with 1450 ns (left) and 1700 ns (right) time delay.

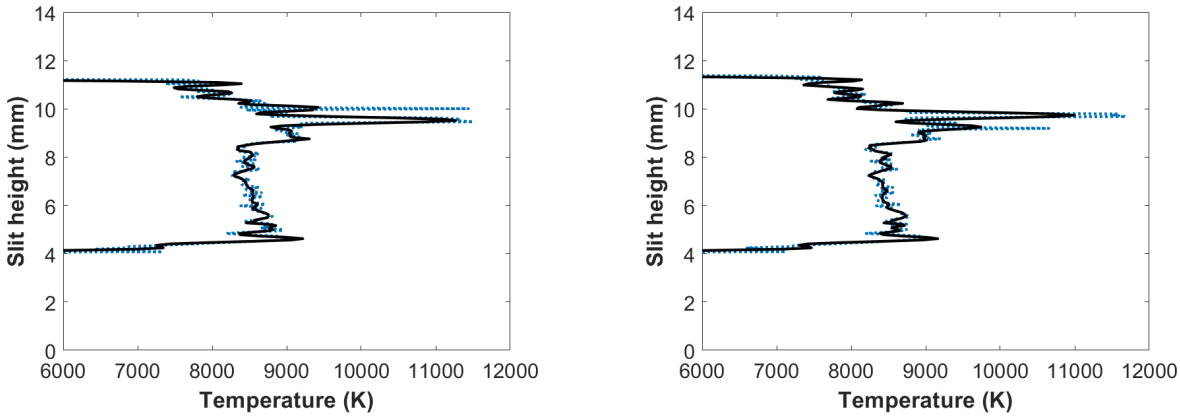

Figure 4.32: Temperature vs. slit height for filtered line-of-sight CN spectra for a flowing 1:1 molar CO_2:N_2 gaseous mixture with 1950 ns (left) and 2200 ns (right) time delay.

At the 950 ns time delay, Figure 4.30, the temperatures in the central region of the plasma remain in a range of 9,000 K to 9,500 K, while the temperatures at the edge of the plasma towards the top of the slit increase to greater than 11,000 K. At a time delays of 1.2 μs to 1.7 μs the plasma central region temperatures cool even further to a range of 8,500 K to 9,000 K, while the edge of the plasma towards the top of the slit maintain temperatures in excess of 11,000 K as seen in Figures 4.30 to 4.31. From time delays of 1.95 μs to 2.2 μs, Figure 4.32, the central region of the plasma sustains temperatures of 8,500 K to 9,000 K and temperatures near the edge of plasma towards the bottom of the slit are around 9,000 K, while temperatures near the edge of the plasma towards the top of slit increase to greater than 11,000 K. Also seen in Figure 4.32 is the plasma temperatures in excess of 11,000 K are near the edge of the plasma towards the top of the slit, but are closer to the center plasma as seen in the 1:1 molar CO_2:N_2 gaseous mixture held at 276 kPa (2070 Torr).

4.4 Calculated Electron Densities

4.4.1 Stark Widths and Stark Shifts in the CO_2 and N_2 Gaseous Mixture of Fixed Volume at Atmospheric Pressure

Inferred Stark widths of the CI 193.09 nm carbon line in second order for the 1:1 molar CO_2:N_2 gaseous mixture held at atmospheric pressure were determined using the previously discussed peak-fitting Matlab® script [75], deconvolution of the filtered and unfiltered measured peaks, and taking the difference between the filtered and unfiltered deconvoluted peaks. The inferred Stark widths are plotted versus the slit height of the spectrometer, which can be seen in Figures 4.33 to 4.40. Larger Stark widths are seen towards the edges of the plasma, while smaller Stark widths are seen in the center of the plasma. For time delays of 450 ns to 1700 ns, Figures 4.33 to 4.38, the Stark widths are between 0.4 to 0.5 nm and located towards the edges of the plasma. At a time delay of 1950 ns, Figure 4.39, the Stark widths increase to a range of 0.6 to 0.7 nm located towards the edges of the plasma. As time elapses further to a time delay of 2200 ns, Figure 4.40, the Stark widths range from 0.4 to 0.7 nm towards the edge located at the top of the slit, while the Stark widths decrease to a range of 0.4 to 0.5 nm towards the edge located at the bottom of the slit.

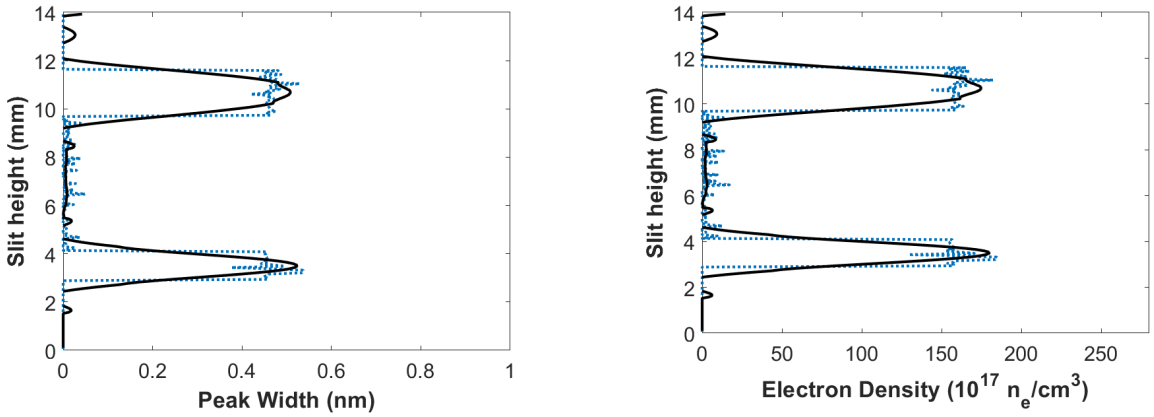

Figure 4.33: Inferred widths (top) and calculated electron densities (bottom) of CI 193.09 nm atmoic carbon line in second order vs. slit height for the 1:1 molar CO_2:N_2 gaseous mixture held at atmospheric pressure with 450 ns time delay.

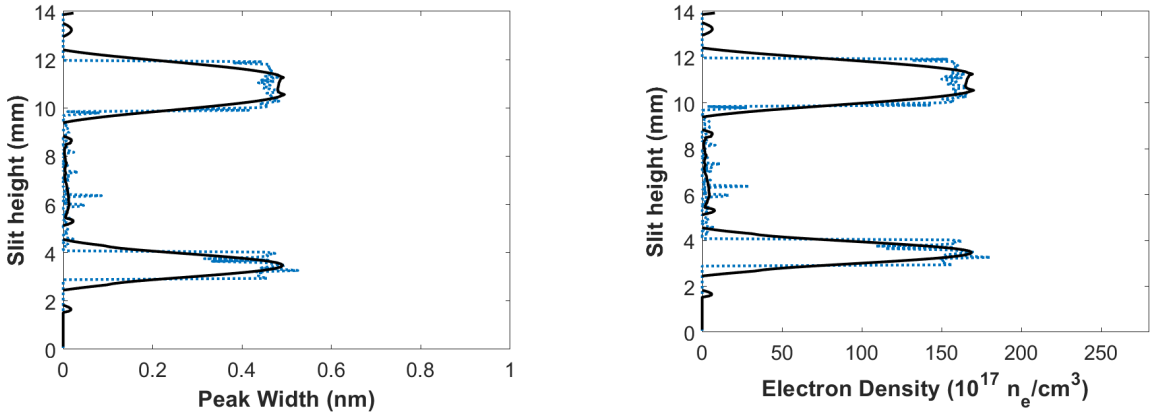

Figure 4.34: Inferred widths (top) and calculated electron densities (bottom) of CI 193.09 nm atmoic carbon line in second order vs. slit height for the 1:1 molar CO_2:N_2 gaseous mixture held at atmospheric pressure with 700 ns time delay [70 ,71].

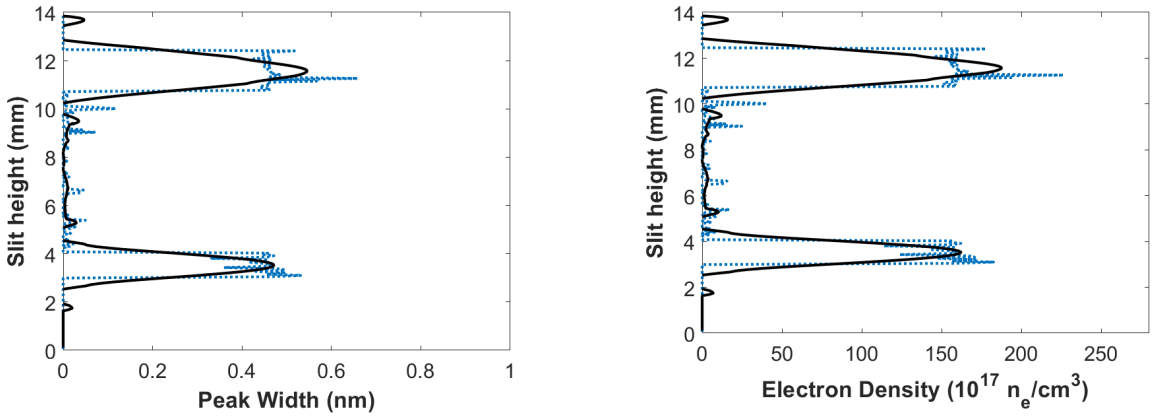

Figure 4.35: Inferred widths (top) and calculated electron densities (bottom) of CI 193.09 nm atmoic carbon line in second order vs. slit height for the 1:1 molar CO_2:N_2 gaseous mixture held at atmospheric pressure with 950 ns time delay [70 ,71].

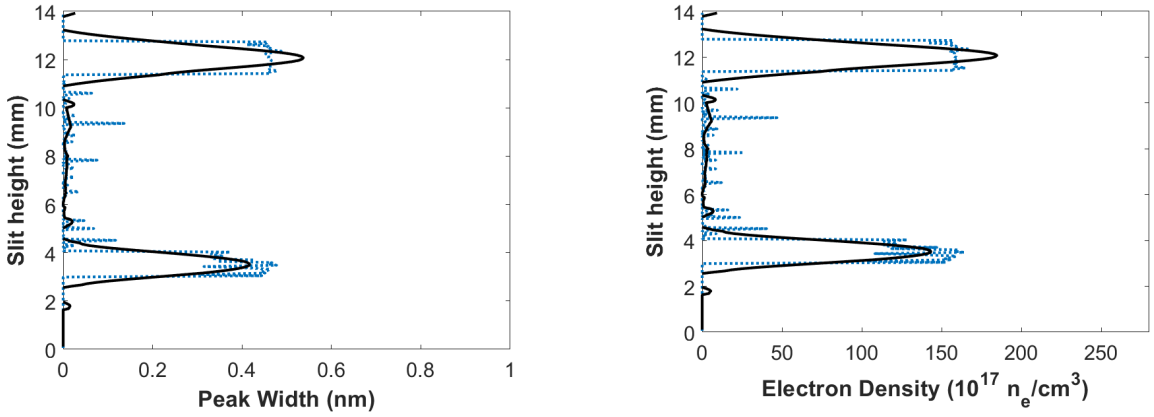

Figure 4.36: Inferred widths (top) and calculated electron densities (bottom) of CI 193.09 nm atmoic carbon line in second order vs. slit height for the 1:1 molar CO_2:N_2 gaseous mixture held at atmospheric pressure with 1200 ns time delay.

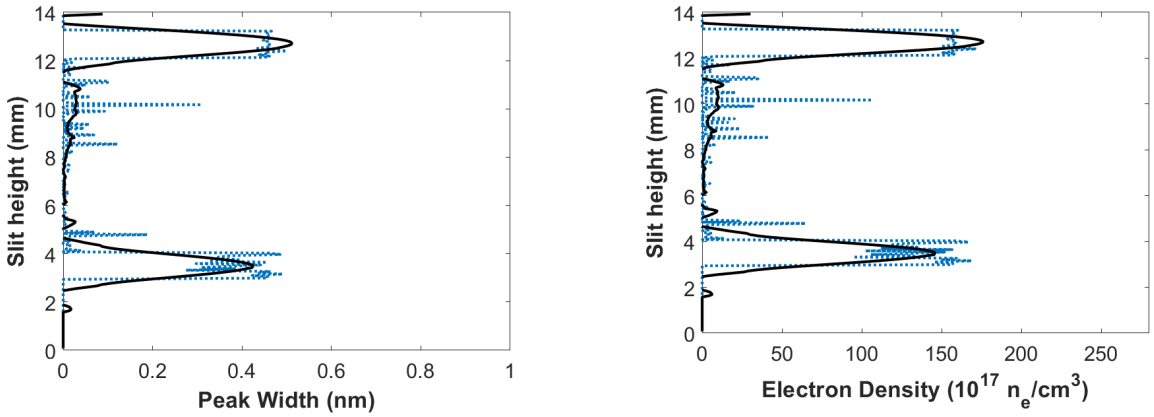

Figure 4.37: Inferred widths (top) and calculated electron densities (bottom) of CI 193.09 nm atmoic carbon line in second order vs. slit height for the 1:1 molar CO_2:N_2 gaseous mixture held at atmospheric pressure with 1450 ns time delay.

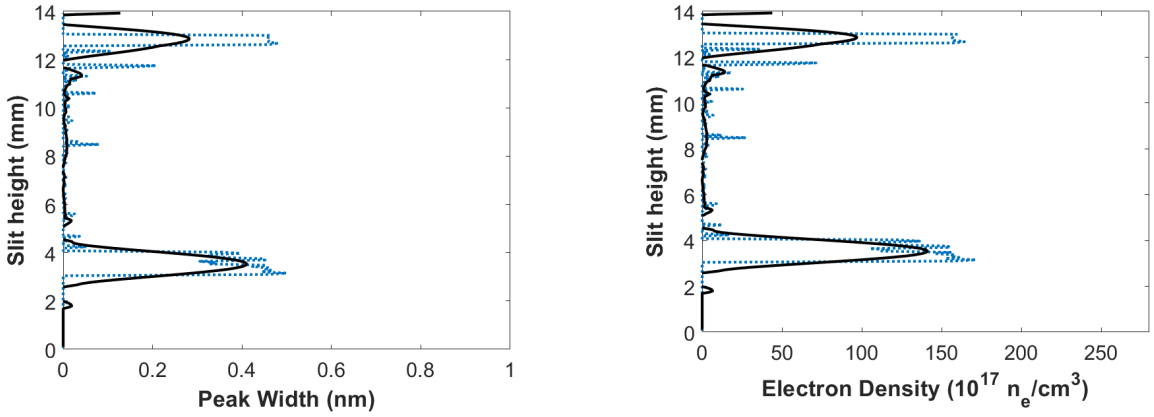

Figure 4.38: Inferred widths (top) and calculated electron densities (bottom) of CI 193.09 nm atmoic carbon line in second order vs. slit height for the 1:1 molar CO_2:N_2 gaseous mixture held at atmospheric pressure with 1700 ns time delay.

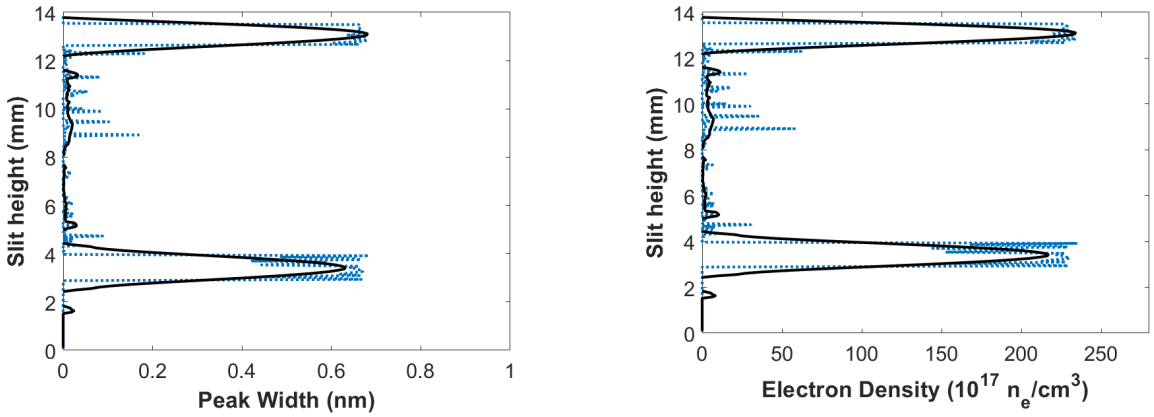

Figure 4.39: Inferred widths (top) and calculated electron densities (bottom) of CI 193.09 nm atmoic carbon line in second order vs. slit height for the 1:1 molar CO_2:N_2 gaseous mixture held at atmospheric pressure with 1950 ns time delay.

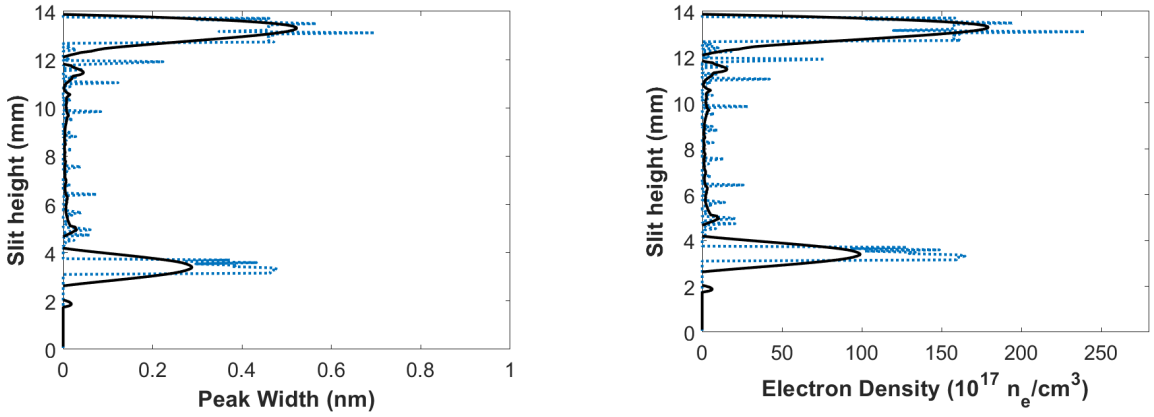

Figure 4.40: Inferred widths (top) and calculated electron densities (bottom) of CI 193.09 nm atmoic carbon line in second order vs. slit height for the 1:1 molar CO_2:N_2 gaseous mixture held at atmospheric pressure with 2200 ns time delay.

The Stark widths are used to calculate electron number density, n_e. The calculated n_e is plotted versus the slit height of the spectrometer, which can be seen in Figures 4.33 to 4.40. Calculated electron densities are on the order of $n_e \approx 10^{17}\text{cm}^{-3}$. Since n_e is directly proportional to the Stark width of the 193.09 nm carbon line in second order as previously shown in equation (3.6), n_e plots mimic the same behavior as the previously mentioned Stark width plots, where higher n_e is seen towards the edges of the plasma and lower n_e is towards the center of the plasma. The higher electron densities toward the edges of the plasma appear to follow the previously discussed shockwave expansion law, equation (3.2), with the exception of the 450 ns and 700 ns time delays, which can be seen in Table 4.4. This inconsistency can be due to the velocity of the shockwave being greater than Mach 2 for early time delays as discussed in the previously mentioned shadowgraphs.

Inferred Stark shifts of the CI 193.09 nm carbon line in second order for the 1:1 molar CO_2:N_2 gaseous mixture held at atmospheric pressure were also determined using the peak-fitting Matlab® script [75]. The inferred Stark shifts are plotted versus the slit height of the spectrometer, which can be seen in Figures 4.41 to 4.48. Larger Stark shifts are seen towards the edges of the plasma, while smaller Stark widths are seen in the center of the plasma. At 450 ns time delay, Figure 4.41, the Stark shifts across the plasma are mostly within the range of 0.5 to 0.6 nm. As the time delay reaches 700 ns, Figure 4.42, the Stark shifts towards the edge of the plasma located at the top of the slit stay within the range of 0.5 to 0.6 nm, while across the rest of the plasma the Stark shifts decrease to a range of 0.4 to 0.5 nm. At times delays of 950 ns to 1450 ns, Figures 4.43 to 4.45, the Stark shifts towards the edge of the plasma located at the top of the slit decrease to a range of 0.4 to 0.5 nm, the Stark shifts in the center of the plasma decrease to a range of 0.3 to 0.4 nm, and the Stark shifts towards the edge of plasma located at the bottom of the slit increase to a range of 0.5 to 0.6 nm. As time elapses further to a time delay of 1700 ns to 2200 ns, Figures 4.46 to 4.48, the Stark shifts towards the edge of the plasma located at the top and bottom of the slit increase to a range of 0.5 to 0.7 nm and the Stark shifts in the center of the plasma increase to a range of 0.4 to 0.5 nm. Larger Stark shifts are seen towards the edges of the plasma, while smaller Stark widths are seen in the center of the plasma.

Table 4.4: Computed shockwave radii versus plasma radius for 1:1 molar CO_2:N_2 gaseous mixture held at atmospheric pressure, 170 mJ

τ (ns)	Computed R(mm)	Measured R_{Plasma}(mm)
450	1.84	2.90 ± 0.87
700	2.20	3.00 ± 0.90
950	2.48	3.30 ± 0.99
1200	2.72	3.35 ± 1.01
1450	2.94	4.00 ± 1.20
1700	3.13	4.30 ± 1.29
1950	3.31	4.40 ± 1.32
2200	3.47	4.30 ± 1.29

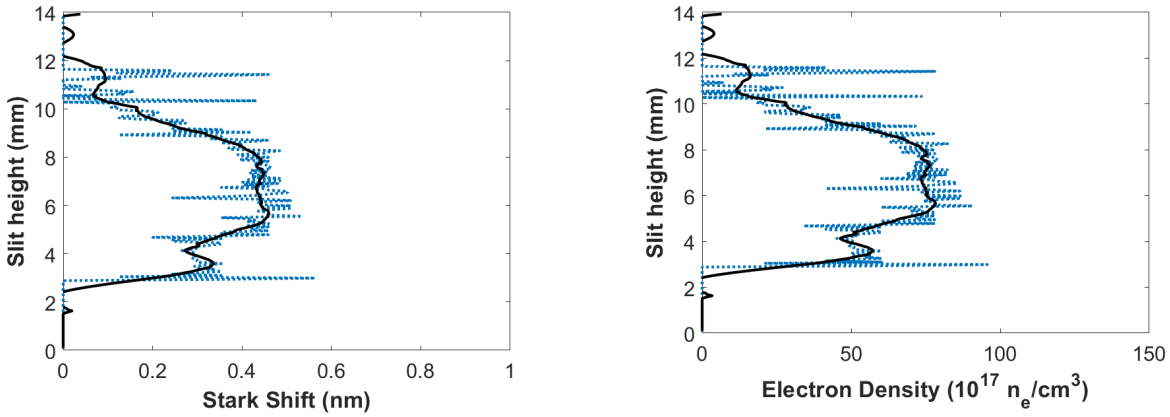

Figure 4.41: Inferred shifts (top) and calculated electron densities (bottom) of CI 193.09 nm atmoic carbon line in second order vs. slit height for the 1:1 molar CO_2:N_2 gaseous mixture held at atmospheric pressure with 450 ns time delay.

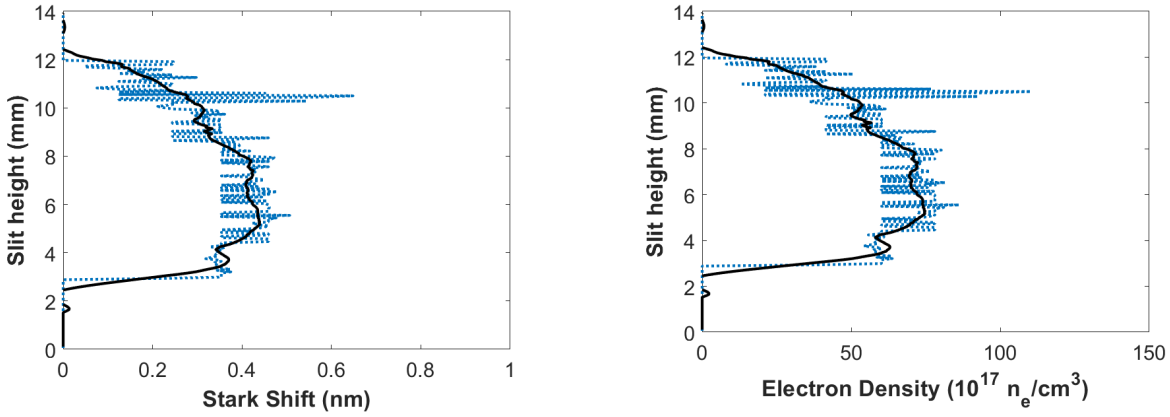

Figure 4.42: Inferred shifts (top) and calculated electron densities (bottom) of CI 193.09 nm atmoic carbon line in second order vs. slit height for the 1:1 molar CO_2:N_2 gaseous mixture held at atmospheric pressure with 700 ns time delay.

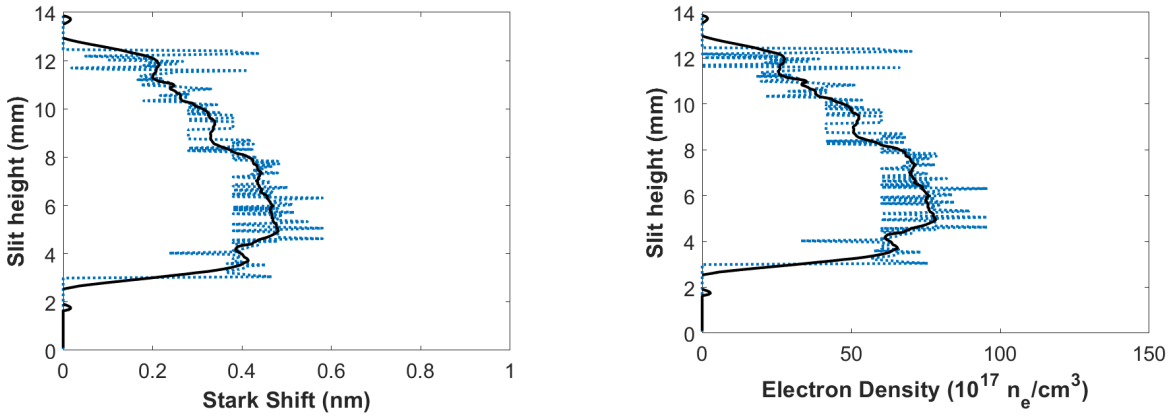

Figure 4.43: Inferred shifts (top) and calculated electron densities (bottom) of CI 193.09 nm atmoic carbon line in second order vs. slit height for the 1:1 molar CO_2:N_2 gaseous mixture held at atmospheric pressure with 950 ns time delay.

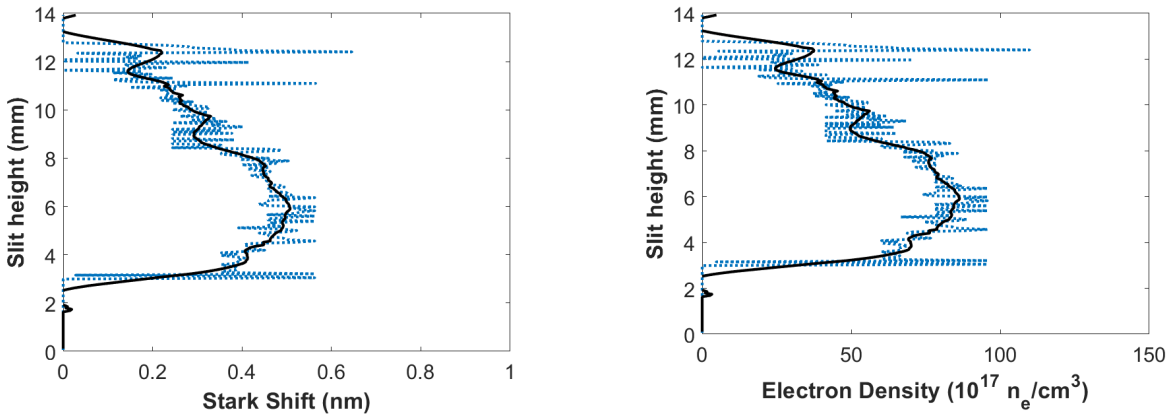

Figure 4.44: Inferred shifts (top) and calculated electron densities (bottom) of CI 193.09 nm atmoic carbon line in second order vs. slit height for the 1:1 molar CO_2:N_2 gaseous mixture held at atmospheric pressure with 1200 ns time delay.

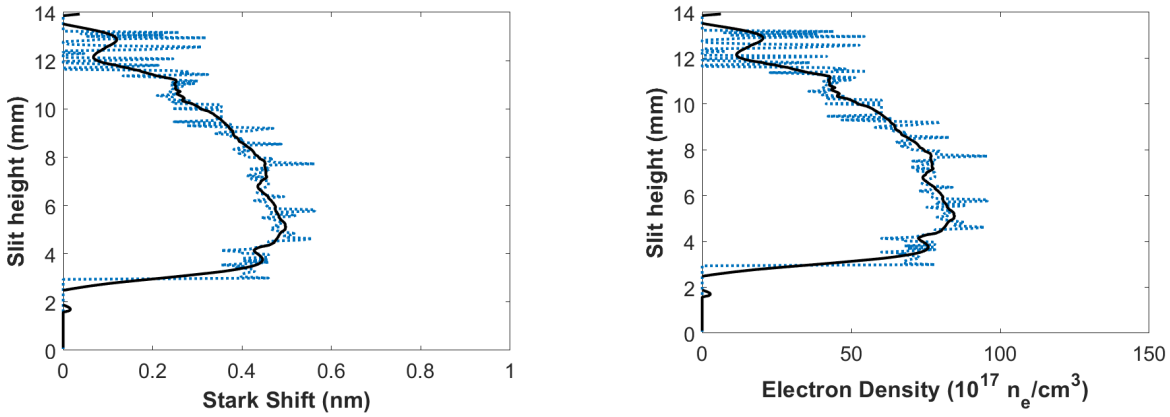

Figure 4.45: Inferred shifts (top) and calculated electron densities (bottom) of CI 193.09 nm atmoic carbon line in second order vs. slit height for the 1:1 molar CO_2:N_2 gaseous mixture held at atmospheric pressure with 1450 ns time delay.

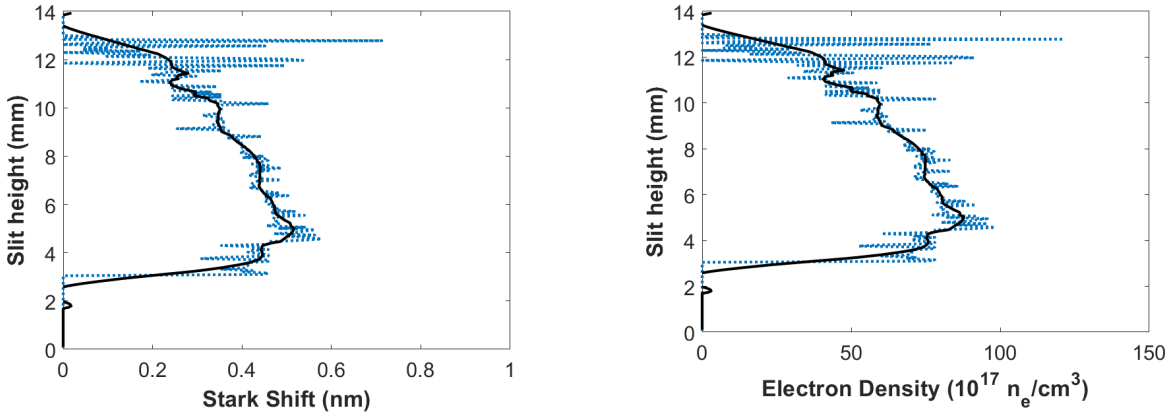

Figure 4.46: Inferred shifts (top) and calculated electron densities (bottom) of CI 193.09 nm atmoic carbon line in second order vs. slit height for the 1:1 molar CO_2:N_2 gaseous mixture held at atmospheric pressure with 1700 ns time delay.

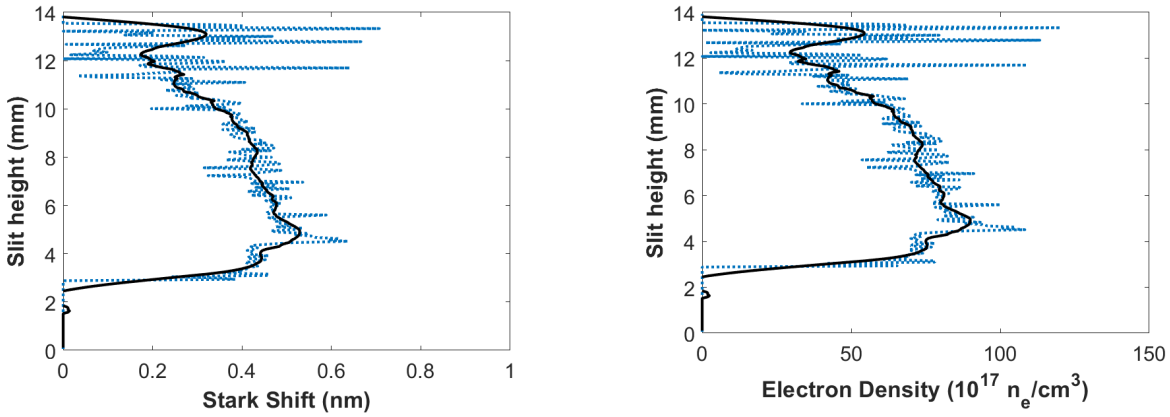

Figure 4.47: Inferred shifts (top) and calculated electron densities (bottom) of CI 193.09 nm atmoic carbon line in second order vs. slit height for the 1:1 molar CO_2:N_2 gaseous mixture held at atmospheric pressure with 1950 ns time delay.

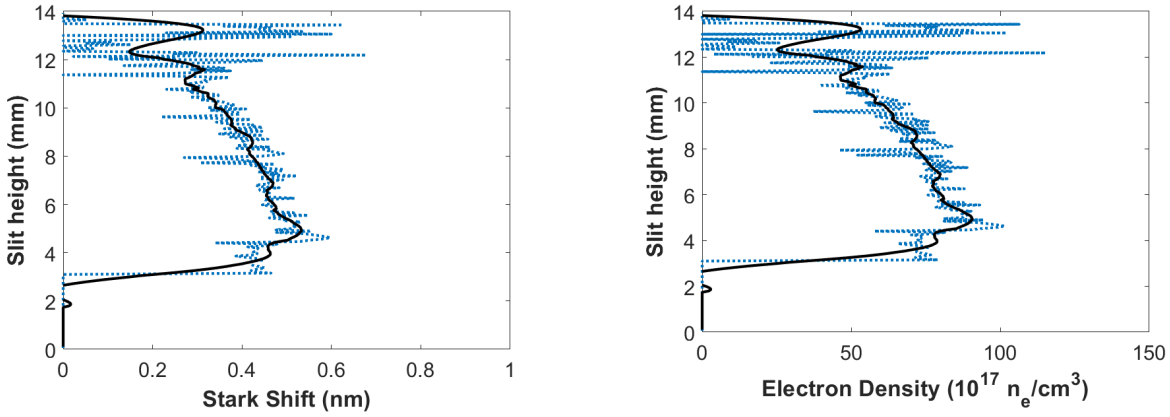

Figure 4.48: Inferred shifts (top) and calculated electron densities (bottom) of CI 193.09 nm atmoic carbon line in second order vs. slit height for the 1:1 molar CO_2:N_2 gaseous mixture held at atmospheric pressure with 2200 ns time delay.

The Stark shifts are used to calculate electron number density, n_e. The calculated n_e is plotted versus the slit height of the spectrometer, which can be seen in Figures 4.41 to 4.48. Calculated electron densities are on the order of $n_e \approx 10^{17}\text{cm}^{-3}$ similar to the electron densities determined from Stark widths. Since n_e is directly proportional to the Stark shift of the 193.09 nm carbon line in second order as previously shown in equation (3.7), n_e plots mimic the same behavior as the previously mentioned Stark shift plots, where higher n_e is seen towards the edges of the plasma and lower n_e is towards the center of the plasma. Although Stark shifts can be used to determine n_e, the Stark width method appears to be a superior technique when plotting n_e versus slit height.

4.4.2 Stark Shifts in the CO_2 and N_2 Gaseous Mixture of Fixed Volume at 276 kPa (2070 Torr)

Inferred Stark shifts of the CI 193.09 nm carbon line in second order for the 1:1 molar CO_2:N_2 gaseous mixture held at 276 kPa (2070 Torr) were also determined using the same method as previously discussed. The inferred Stark shifts are plotted versus the slit height of the spectrometer, which can be seen in Figures 4.49 to 4.56. Larger Stark shifts are seen towards the edges of the plasma, while smaller Stark widths are seen in the center of the plasma similar to the gaseous mixture held at atmospheric pressure. For time delays of 450 ns to 1200 ns, Figures 4.49 to 4.52, the Stark shifts towards the edge of the plasma located at the top and bottom of the slit are within the range of 0.5 to 0.6 nm, while the Stark shifts in the central region of the plasma are within the range of 0.3 to 0.4 nm. For time delays of 1450 ns to 1700 ns, Figures 4.53 and 4.54, the Stark shifts towards the edge of the plasma located at the top of the slit increase to a range of 0.6 to 0.7 nm, the Stark shifts towards the edge of the plasma located at the bottom of the slit sustain a range of 0.5 to 0.6 nm, and the Stark shifts in the central region sustain a range of 0.3 to 0.4 nm. At 1950 ns and 2200 ns time delays, Figures 4.55 and 4.56, the Stark shifts towards the edges are within a range 0.4 to 0.5 nm and the Stark shifts in the central region continue to maintain a range of 0.3 to 0.4 nm.

The Stark shifts are used to calculate electron number density, n_e, just like the gaseous mixture held at atmospheric pressure. The calculated n_e is plotted versus the slit height of

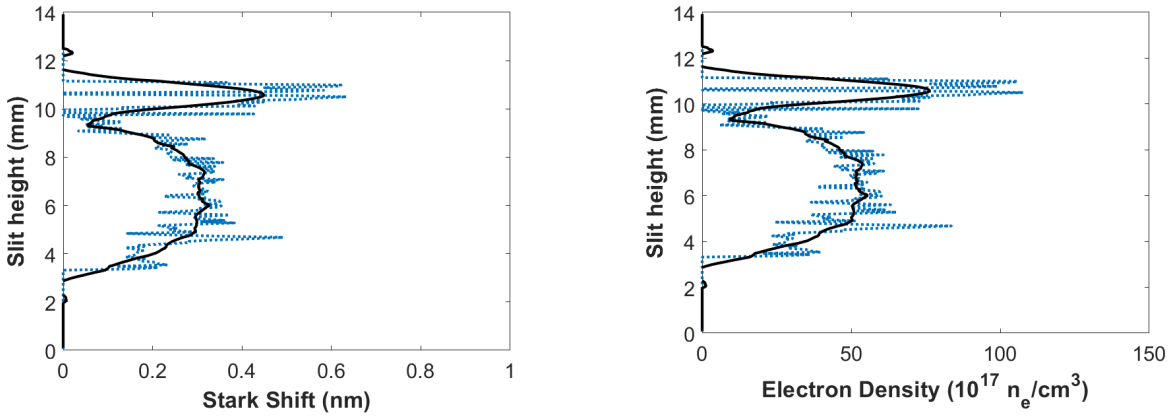

Figure 4.49: Inferred shifts (top) and calculated electron densities (bottom) of CI 193.09 nm atmoic carbon line in second order vs. slit height for the 1:1 molar CO_2:N_2 gaseous mixture held at 276 kPa (2070 Torr) with 450 ns time delay.

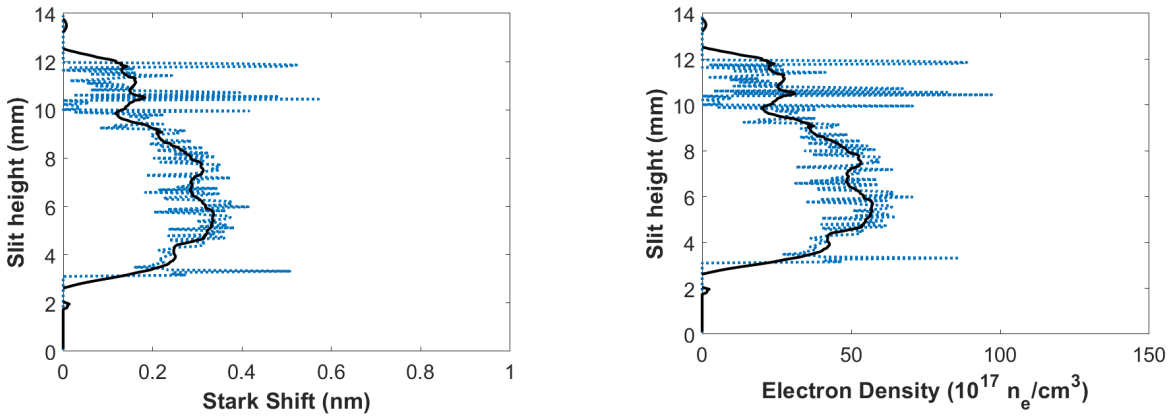

Figure 4.50: Inferred shifts (top) and calculated electron densities (bottom) of CI 193.09 nm atmoic carbon line in second order vs. slit height for the 1:1 molar CO_2:N_2 gaseous mixture held at 276 kPa (2070 Torr) with 700 ns time delay.

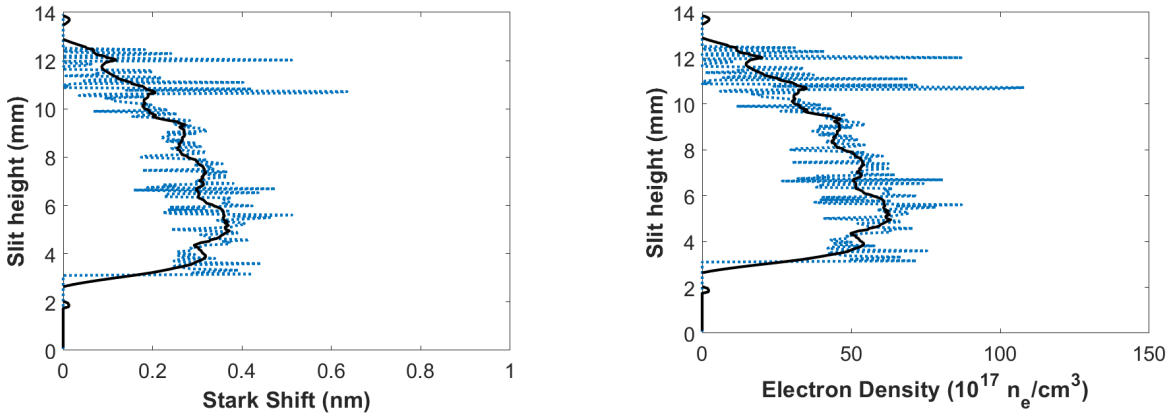

Figure 4.51: Inferred shifts (top) and calculated electron densities (bottom) of CI 193.09 nm atmoic carbon line in second order vs. slit height for the 1:1 molar CO_2:N_2 gaseous mixture held at 276 kPa (2070 Torr) with 950 ns time delay.

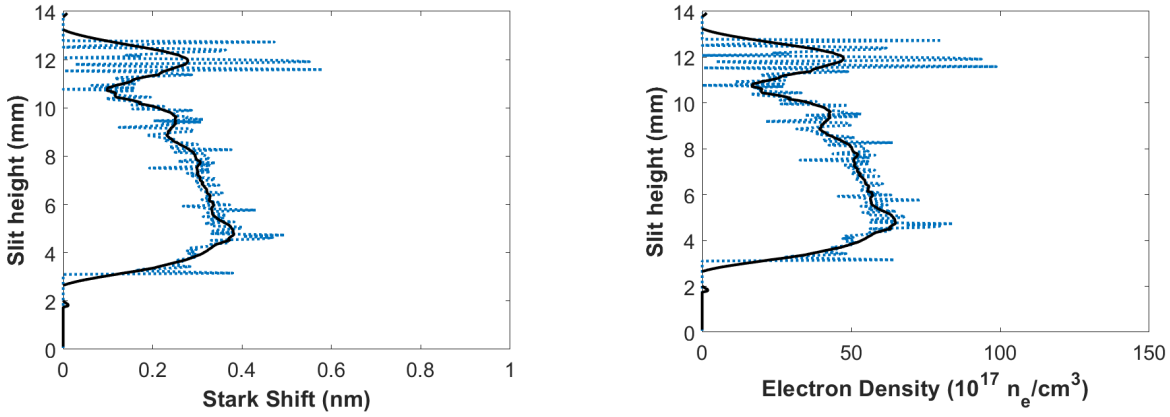

Figure 4.52: Inferred shifts (top) and calculated electron densities (bottom) of CI 193.09 nm atmoic carbon line in second order vs. slit height for the 1:1 molar CO_2:N_2 gaseous mixture held at 276 kPa (2070 Torr) with 1200 ns time delay.

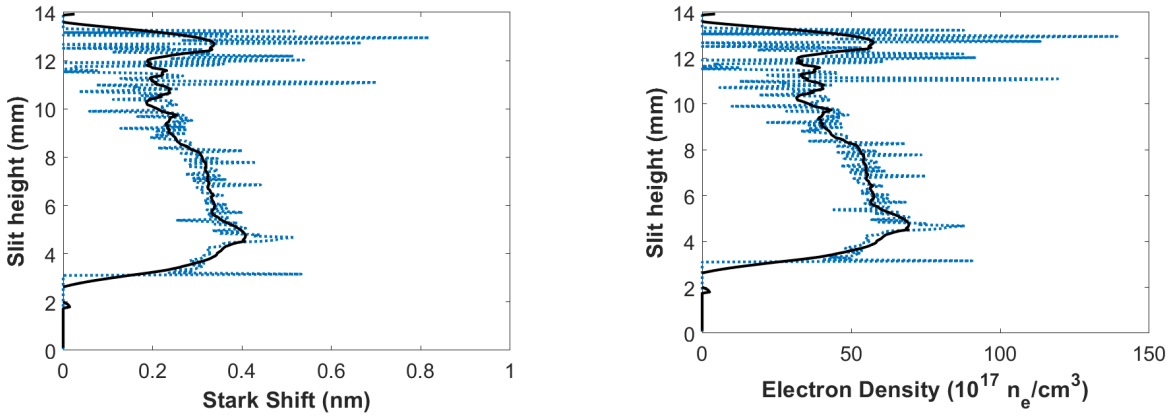

Figure 4.53: Inferred shifts (top) and calculated electron densities (bottom) of CI 193.09 nm atmoic carbon line in second order vs. slit height for the 1:1 molar CO_2:N_2 gaseous mixture held at 276 kPa (2070 Torr) with 1450 ns time delay.

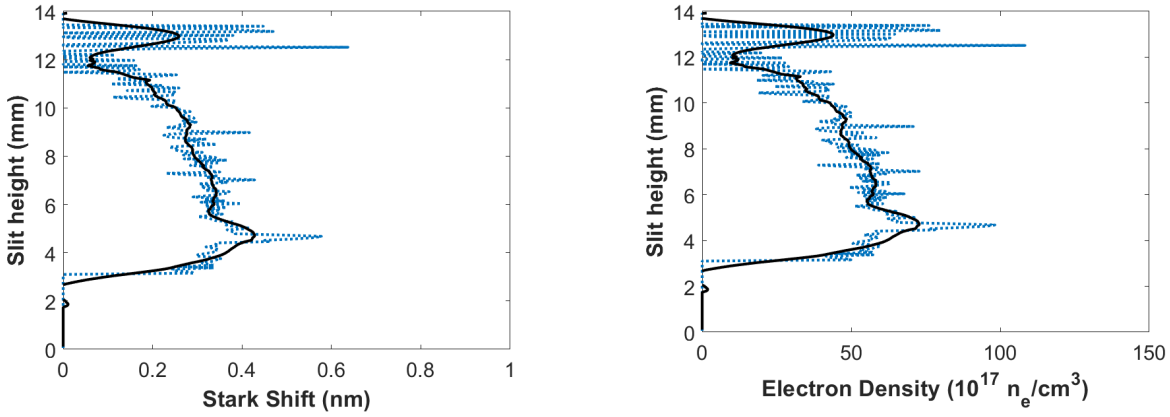

Figure 4.54: Inferred shifts (top) and calculated electron densities (bottom) of CI 193.09 nm atmoic carbon line in second order vs. slit height for the 1:1 molar CO_2:N_2 gaseous mixture held at 276 kPa (2070 Torr) with 1700 ns time delay.

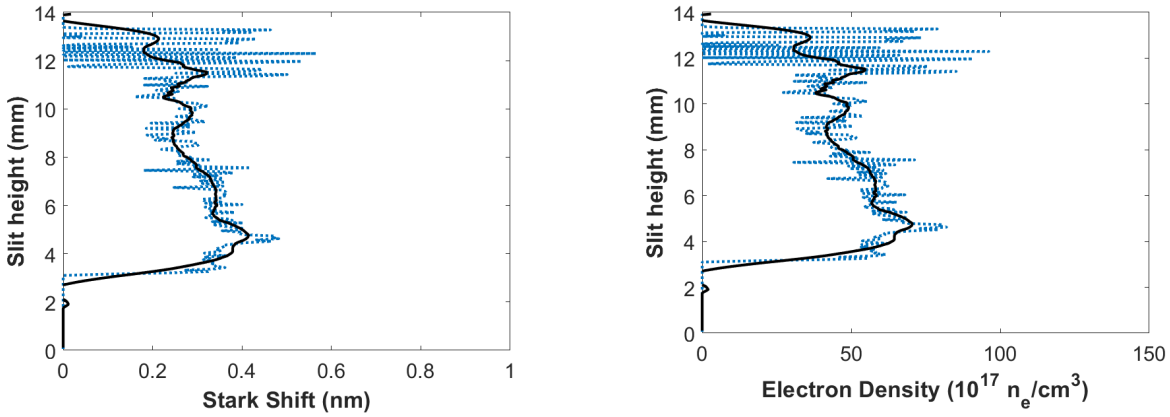

Figure 4.55: Inferred shifts (top) and calculated electron densities (bottom) of CI 193.09 nm atmoic carbon line in second order vs. slit height for the 1:1 molar CO_2:N_2 gaseous mixture held at 276 kPa (2070 Torr) with 1950 ns time delay.

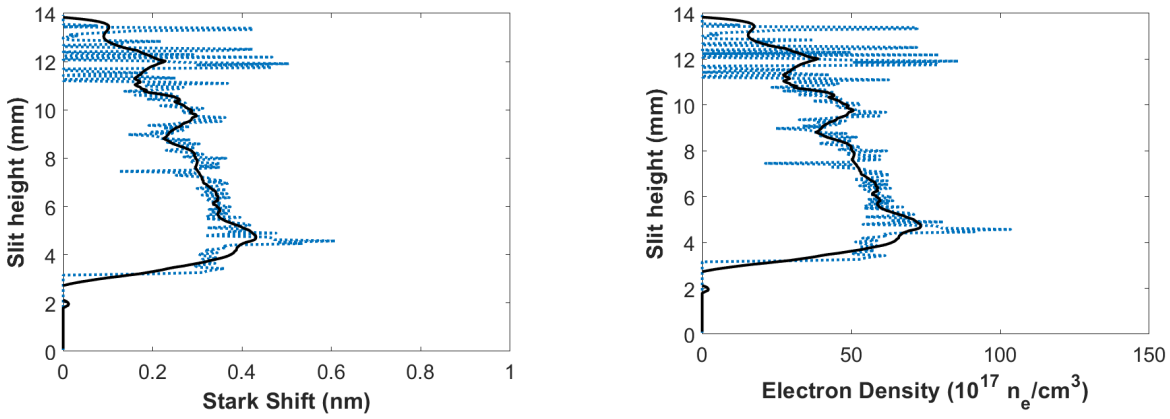

Figure 4.56: Inferred shifts (top) and calculated electron densities (bottom) of CI 193.09 nm atmoic carbon line in second order vs. slit height for the 1:1 molar CO_2:N_2 gaseous mixture held at 276 kPa (2070 Torr) with 2200 ns time delay.

the spectrometer, which can be seen in Figures 4.49 to 4.56. Calculated electron densities are on the order of $n_e \approx 10^{17}$cm^{-3} similar to the electron densities in the gaseous mixture held at atmospheric pressure. Electron density plots mimic the same behavior as the previously mentioned Stark shift plots, where higher n_e is seen towards the edges of the plasma and lower n_e is towards the center of the plasma.

4.4.3 Stark Widths and Stark Shifts in the CO_2 and N_2 Flowing Gaseous Mixture

Inferred Stark widths of the CI 193.09 nm carbon line in second order for the 1:1 molar CO_2:N_2 flowing gaseous mixture were determined using the same technique as the gaseous mixture held at atmospheric pressure. The inferred Stark widths are plotted versus the slit height of the spectrometer, which can be seen in Figures 4.57 to 4.64. Larger Stark widths are seen towards the edges of the plasma, while smaller Stark widths are seen in the center of the plasma similar to the gaseous mixture held at atmospheric pressure. For time delays of 450 ns to 2200 ns, Figures 4.57 to 4.64, the Stark widths are between 0.4 to 0.5 nm and located towards the edges of the plasma.

The Stark widths are used to calculate electron number density, n_e similar to the gaseous mixture held at atmospheric pressure. The calculated n_e is plotted versus the slit height of the spectrometer, which can be seen in Figures 4.57 to 4.64. Calculated electron densities are on the order of $n_e \approx 10^{17}$cm^{-3} similar to the electron densities in the gaseous mixture held at atmospheric pressure. Electron density plots mimic the same behavior as the previously mentioned Stark width plots for the flowing gaseous mixture, where higher n_e is seen towards the edges of the plasma and lower n_e is towards the center of the plasma similar to the gaseous mixture held at atmospheric pressure. The higher electron densities toward the edges of the plasma appear to follow the shockwave expansion law, equation (3.2), which can be seen in Table 4.5. These shockwave radii of the flowing gaseous mixture are much closer to the predicted shockwave radii than the shockwave radii of the gaseous mixture held at atmospheric pressure.

Inferred Stark shifts of the CI 193.09 nm carbon line in second order for the 1:1 molar CO_2:N_2 flowing gaseous mixture were determined using the same technique applied to

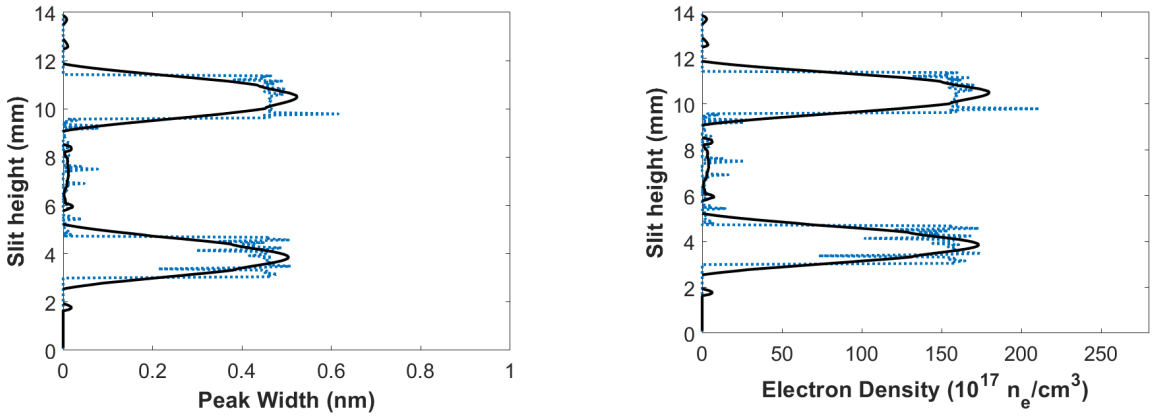

Figure 4.57: Inferred widths (top) and calculated electron densities (bottom) of CI 193.09 nm atmoic carbon line in second order vs. slit height for the 1:1 molar CO_2:N_2 flowing gaseous mixture with 450 ns time delay.

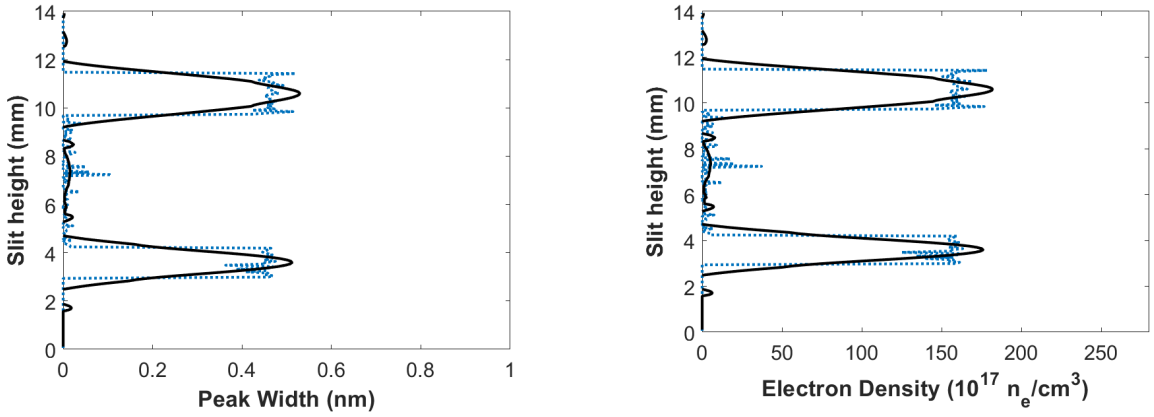

Figure 4.58: Inferred widths (top) and calculated electron densities (bottom) of CI 193.09 nm atmoic carbon line in second order vs. slit height for the 1:1 molar CO_2:N_2 flowing gaseous mixture with 700 ns time delay [70].

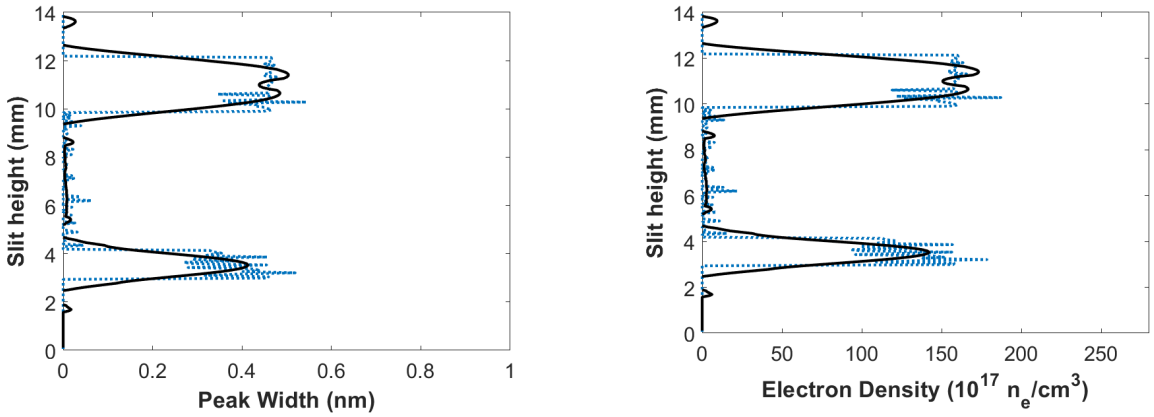

Figure 4.59: Inferred widths (top) and calculated electron densities (bottom) of CI 193.09 nm atmoic carbon line in second order vs. slit height for the 1:1 molar CO_2:N_2 flowing gaseous mixture with 950 ns time delay [70].

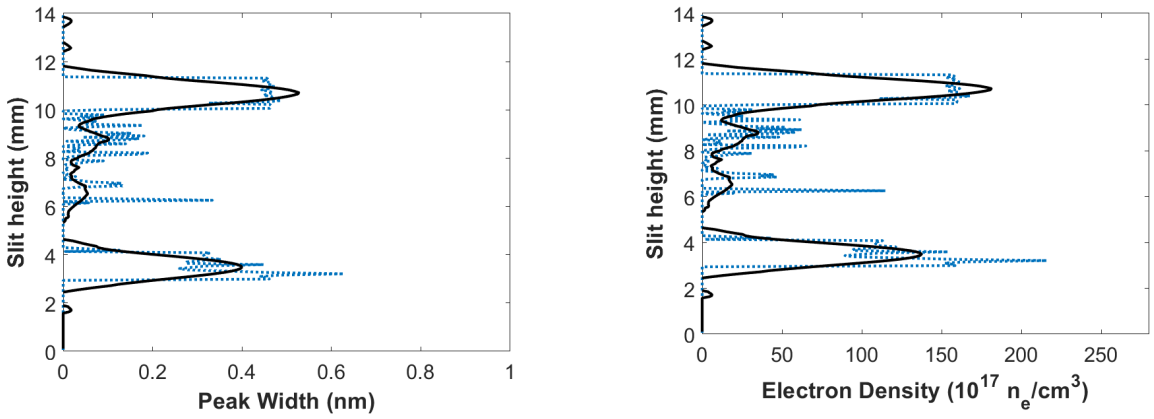

Figure 4.60: Inferred widths (top) and calculated electron densities (bottom) of CI 193.09 nm atmoic carbon line in second order vs. slit height for the 1:1 molar CO_2:N_2 flowing gaseous mixture with 1200 ns time delay.

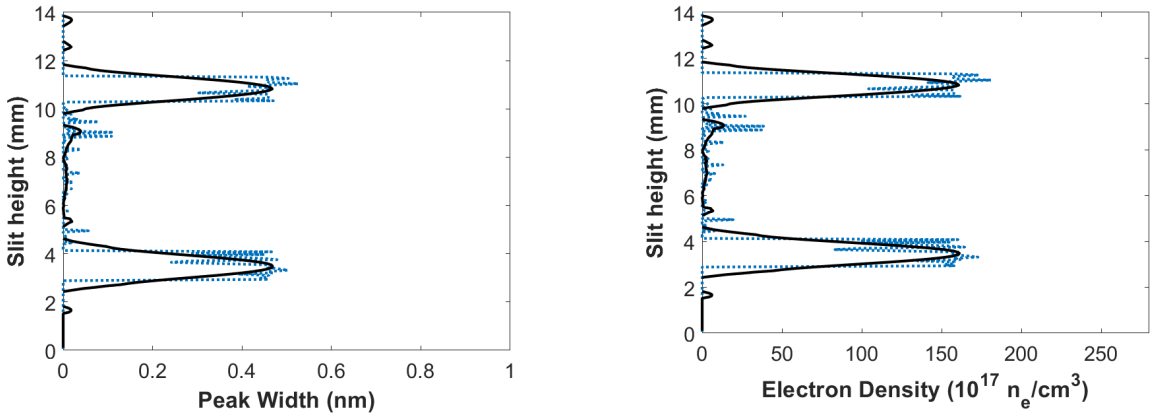

Figure 4.61: Inferred widths (top) and calculated electron densities (bottom) of CI 193.09 nm atmoic carbon line in second order vs. slit height for the 1:1 molar CO_2:N_2 flowing gaseous mixture with 1450 ns time delay.

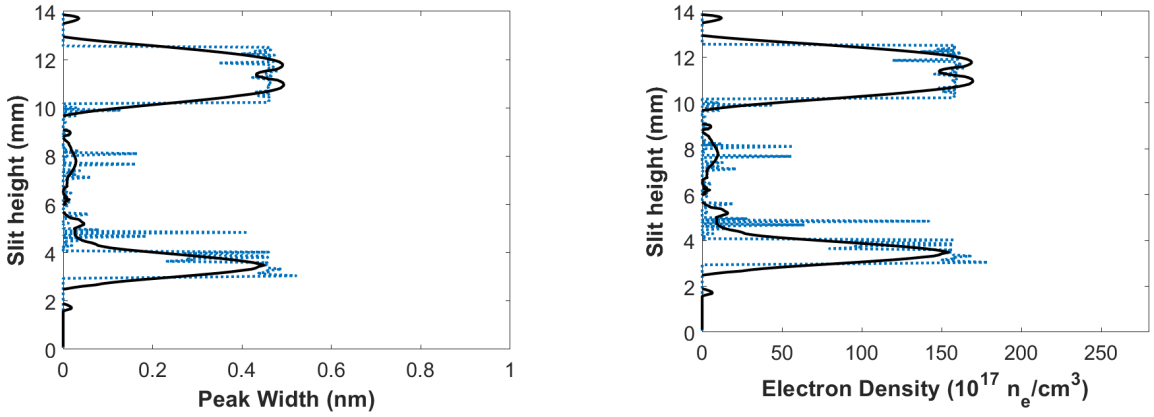

Figure 4.62: Inferred widths (top) and calculated electron densities (bottom) of CI 193.09 nm atmoic carbon line in second order vs. slit height for the 1:1 molar CO_2:N_2 flowing gaseous mixture with 1700 ns time delay.

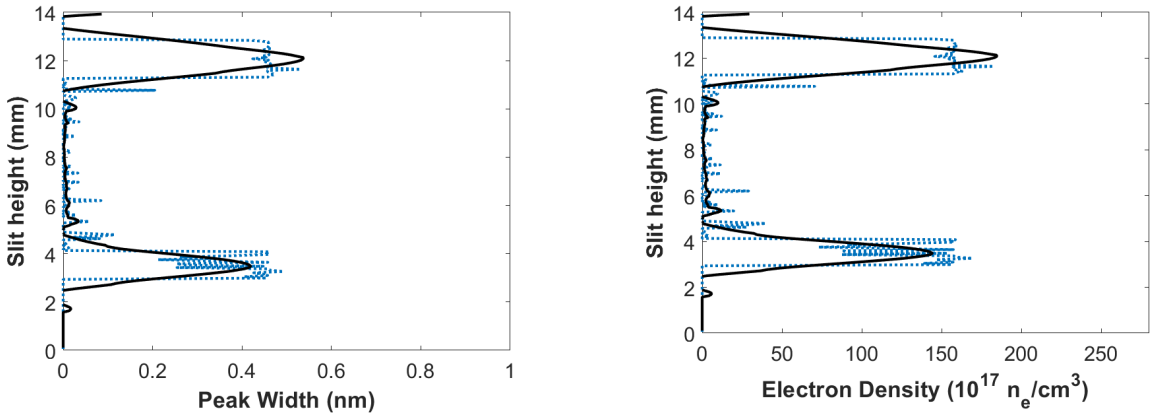

Figure 4.63: Inferred widths (top) and calculated electron densities (bottom) of CI 193.09 nm atmoic carbon line in second order vs. slit height for the 1:1 molar CO_2:N_2 flowing gaseous mixture with 1950 ns time delay.

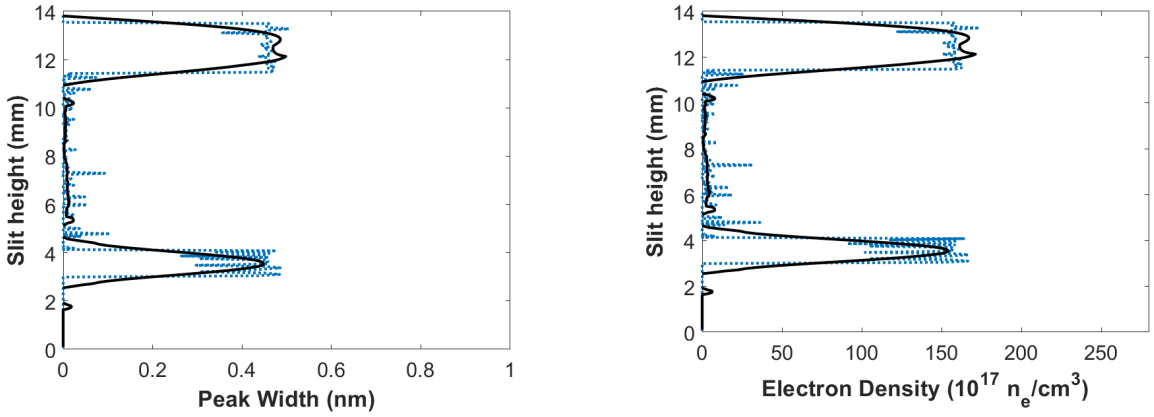

Figure 4.64: Inferred widths (top) and calculated electron densities (bottom) of CI 193.09 nm atmoic carbon line in second order vs. slit height for the 1:1 molar CO_2:N_2 flowing gaseous mixture with 2200 ns time delay.

Table 4.5: Computed shockwave radii versus plasma radius for the 1:1 molar CO_2:N_2 flowing gaseous mixture, 170 mJ

τ (ns)	Computed R(mm)	Measured R_{Plasma}(mm)
450	1.84	2.40 ± 0.72
700	2.20	2.70 ± 0.81
950	2.48	2.85 ± 0.86
1200	2.72	2.90 ± 0.87
1450	2.94	3.05 ± 0.92
1700	3.13	3.15 ± 0.95
1950	3.31	3.55 ± 1.07
2200	3.47	3.70 ± 1.11

the gaseous mixtures held at atmospheric pressure and 276 kPa (2070 Torr). The inferred Stark shifts are plotted versus the slit height of the spectrometer, which can be seen in Figures 4.65 to 4.72. Larger Stark shifts are seen towards the edges of the plasma, while smaller Stark widths are seen in the center of the plasma similar to both the gaseous mixture held at atmospheric pressure and 276 kPa (2070 Torr). At time delays of 450 ns to 950 ns, Figures 4.65 to 4.67, the Stark shifts across the plasma are mostly within the range of 0.4 to 0.5 nm. At time delays of 1200 ns to 2200 ns, Figures 4.68 and 4.72, the Stark shifts towards the edge of the plasma located at the bottom of the slit increase to a range of 0.5 to 0.6 nm, while across the rest of the plasma the Stark shifts sustain a range of 0.4 to 0.5 nm. Larger Stark shifts are seen towards the edges of the plasma, while smaller Stark widths are seen in the center of the plasma similar to the gaseous mixtures held at atmospheric pressure and 276 kPa (2070 Torr).

The Stark shifts are used to calculate electron number density, n_e, similar to the gaseous mixture held at atmospheric pressure and 276 kPa (2070 Torr). The calculated n_e is plotted versus the slit height of the spectrometer, which can be seen in Figures 4.65 to 4.72. Calculated electron densities are on the order of $n_e \approx 10^{17}\text{cm}^{-3}$ similar to the electron densities determined from flowing gas Stark widths. Electron density plots mimic the same behavior as the previously mentioned flowing gaseous mixture Stark shift plots, where higher n_e is seen towards the edges of the plasma and lower n_e is towards the center of the plasma. Although Stark shifts can be used to determine n_e, the Stark width method appears to be a superior technique when plotting n_e versus slit height similar to the gaseous mixture held at atmospheric pressure.

4.5 Abel Inverted Cyanide Spectra

4.5.1 Abel Inverted CN Spectra in a Fixed Volume of the 1:1 Molar CO_2 and N_2 Gaseous Mixture Held at Atmospheric Pressure

Abel inversion of the filtered 1:1 molar CO_2:N_2 gaseous mixture held at atmospheric pressure was performed by inverting measured line-of-sight data, $I(z, \lambda)$, for each wavelength, λ, to

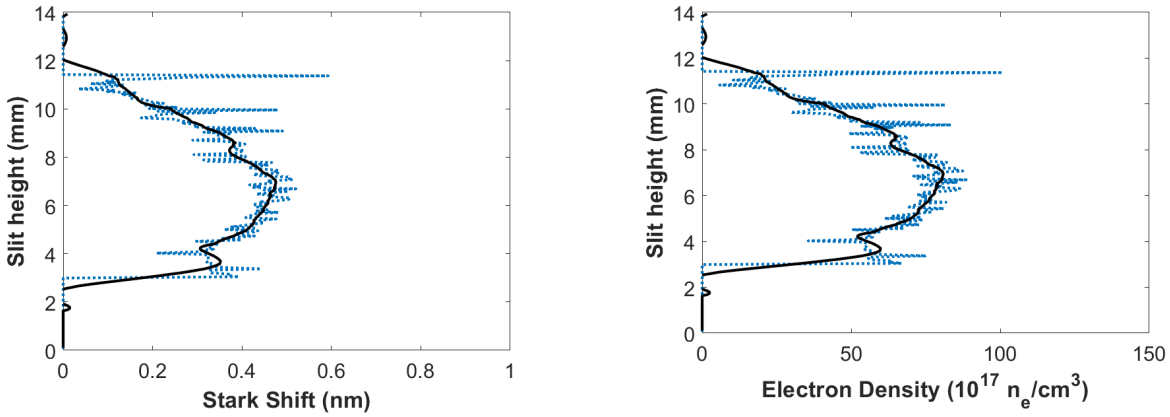

Figure 4.65: Inferred shifts (top) and calculated electron densities (bottom) of CI 193.09 nm atmoic carbon line in second order vs. slit height for the 1:1 molar CO_2:N_2 flowing gaseous mixture with 450 ns time delay.

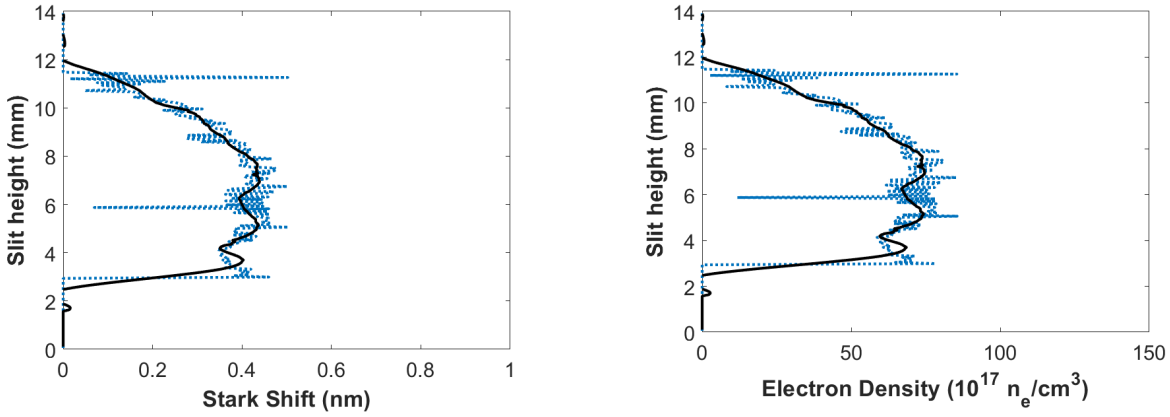

Figure 4.66: Inferred shifts (top) and calculated electron densities (bottom) of CI 193.09 nm atmoic carbon line in second order vs. slit height for the 1:1 molar CO_2:N_2 flowing gaseous mixture with 700 ns time delay.

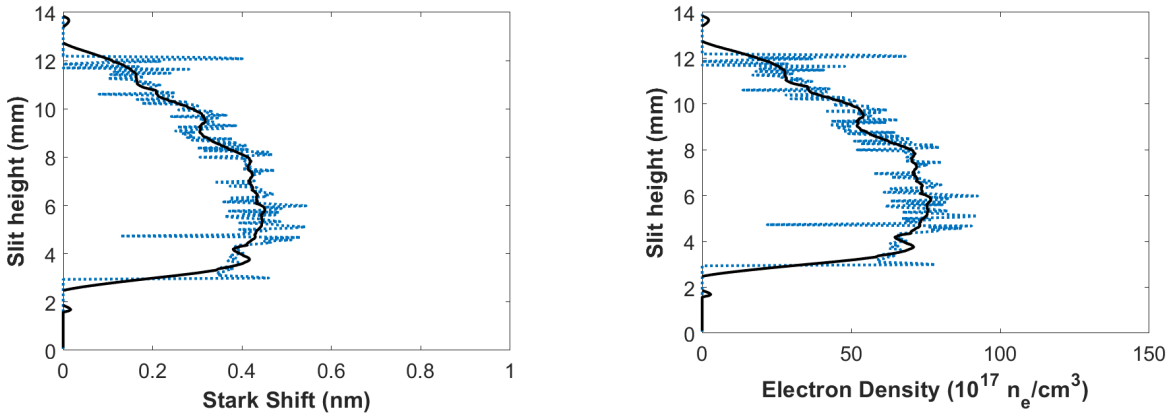

Figure 4.67: Inferred shifts (top) and calculated electron densities (bottom) of CI 193.09 nm atmoic carbon line in second order vs. slit height for the 1:1 molar CO_2:N_2 flowing gaseous mixture with 950 ns time delay.

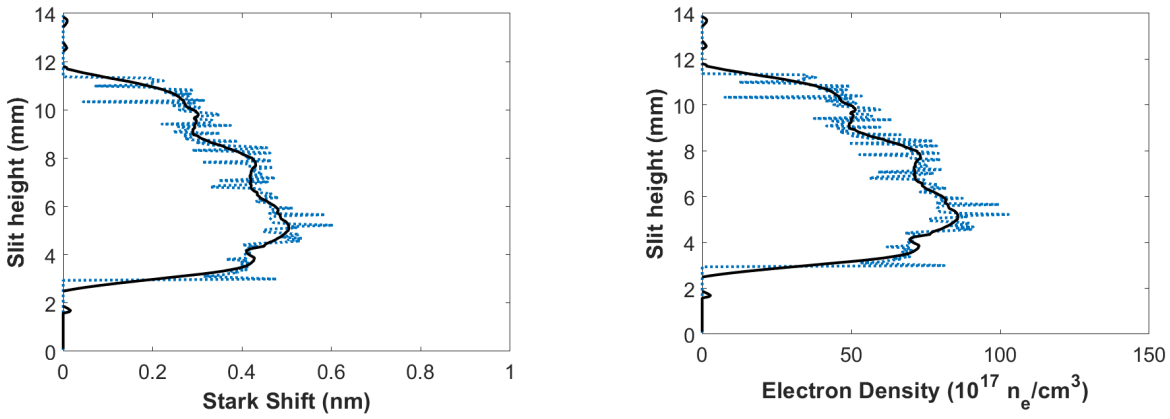

Figure 4.68: Inferred shifts (top) and calculated electron densities (bottom) of CI 193.09 nm atmoic carbon line in second order vs. slit height for the 1:1 molar CO_2:N_2 flowing gaseous mixture with 1200 ns time delay.

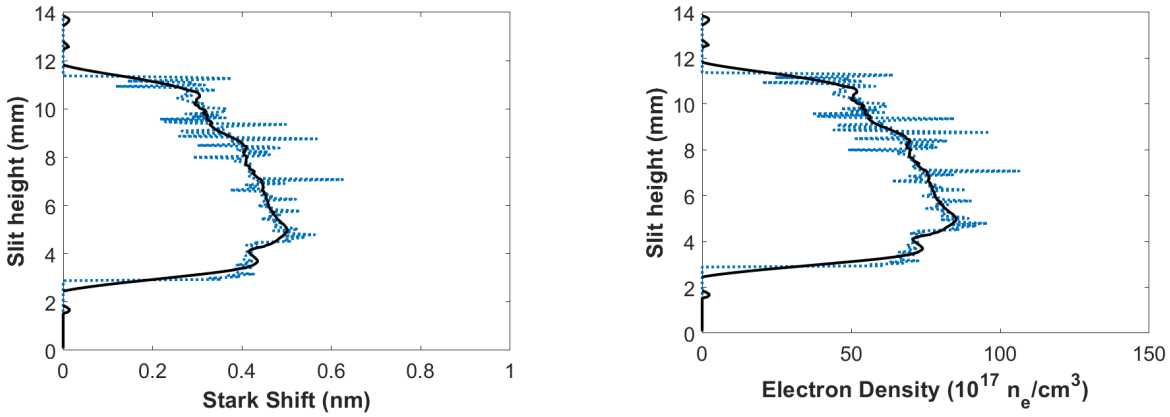

Figure 4.69: Inferred shifts (top) and calculated electron densities (bottom) of CI 193.09 nm atmoic carbon line in second order vs. slit height for the 1:1 molar CO_2:N_2 flowing gaseous mixture with 1450 ns time delay.

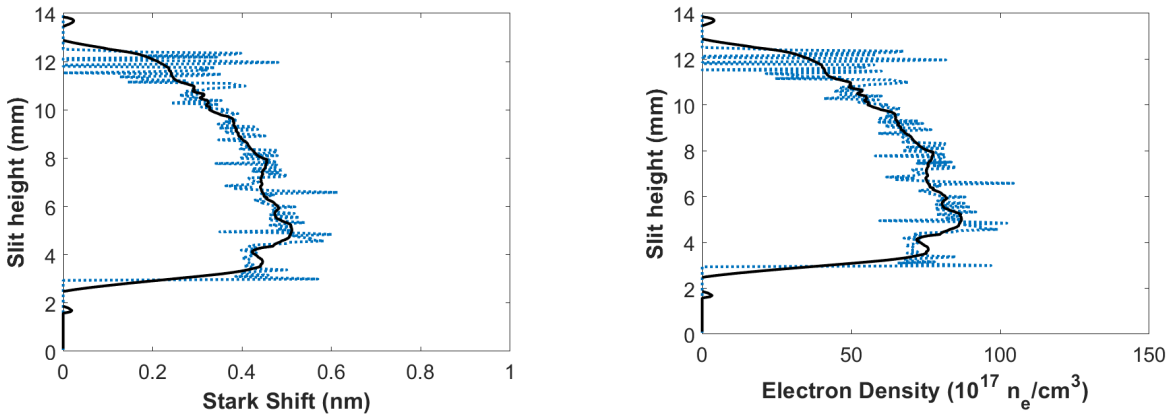

Figure 4.70: Inferred shifts (top) and calculated electron densities (bottom) of CI 193.09 nm atmoic carbon line in second order vs. slit height for the 1:1 molar CO_2:N_2 flowing gaseous mixture with 1700 ns time delay.

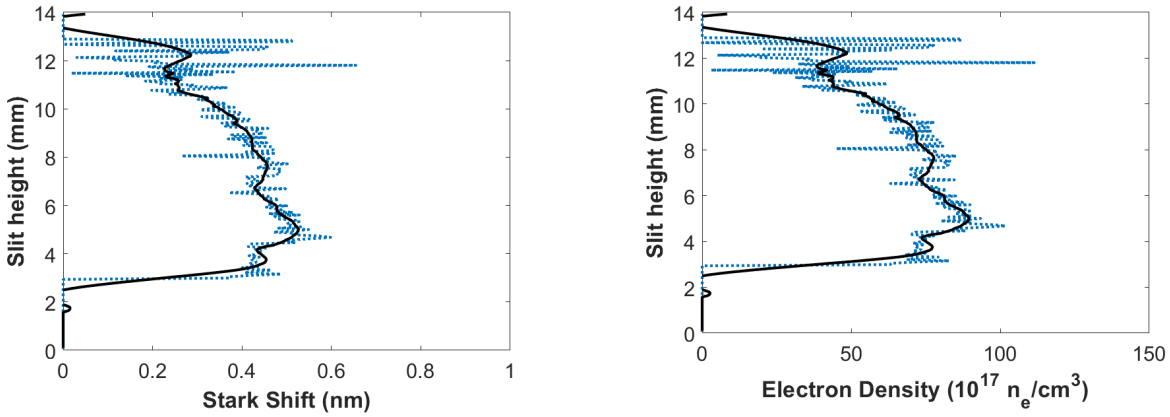

Figure 4.71: Inferred shifts (top) and calculated electron densities (bottom) of CI 193.09 nm atmoic carbon line in second order vs. slit height for the 1:1 molar CO_2:N_2 flowing gaseous mixture with 1950 ns time delay.

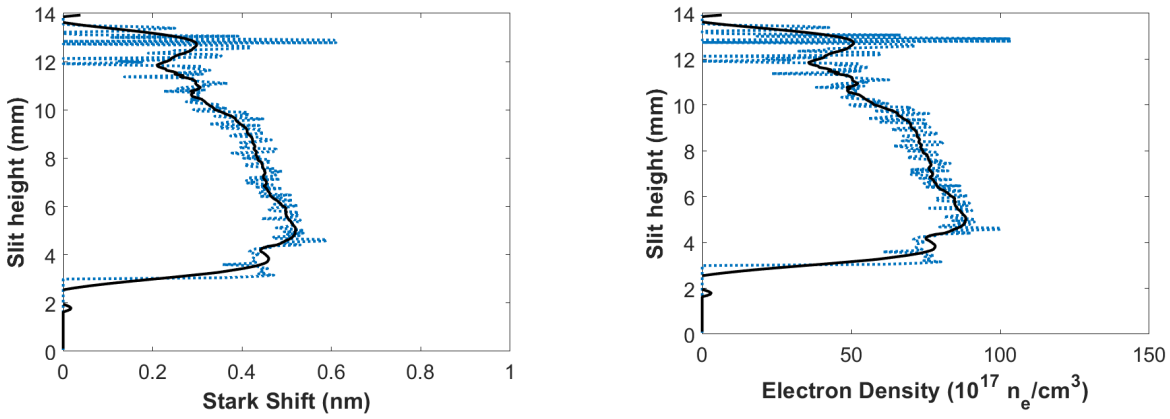

Figure 4.72: Inferred shifts (top) and calculated electron densities (bottom) of CI 193.09 nm atmoic carbon line in second order vs. slit height for the 1:1 molar CO_2:N_2 flowing gaseous mixture with 2200 ns time delay.

obtain the radial intensity distribution, $\varepsilon(r, \lambda)$. Previously measured shadowgraphs show the plasma generated in the 1:1 molar CO_2:N_2 gaseous mixture held at atmospheric pressure has a close to spherical shape, which would justify the use of Abel inversion. At a time delay of 200 ns, Figure 4.73, the CN distribution appears evenly distributed across the plasma. From time delays of 450 ns to 1950 ns, Figures 4.73 to 4.75, the CN signals begin to become stronger towards the edges of the plasma and weaker in the center of the plasma, which is consistent with the higher temperatures seen at the edges of the plasma as discussed previously. At 2200 ns time delay, Figure 4.75, it is clearly visible that there is a higher CN signal towards the edges of the plasma than in the center. This trend is maintained up to 5200 ns as can be seen in Figures 4.76 to 4.79. These results were projected to be similar to the shockwave results, but inside the plasma kernel and shockwave the variations of the CN distribution were expected.

4.5.2 Abel Inverted CN Spectra in a Fixed Volume of the 1:1 Molar CO_2 and N_2 Gaseous Mixture Held at 276 kPa (2070 Torr)

Abel inversion of the unfiltered 1:1 molar CO_2:N_2 gaseous mixture held at 276 kPa (2070 Torr) was performed by using the same technique as the gaseous mixture held at atmospheric pressure. At a time delay of 200 ns, Figure 4.80, the CN distribution appears largest in the center of the plasma. From time delays of 450 ns to 1950 ns, Figures 4.80 to 4.82, the CN signals begin to become stronger towards the edges of the plasma and weaker in the center of the plasma, which is consistent with the higher temperatures seen at the edges of the plasma as discussed previously. Although the CN signals become higher at the edges of the plasma for time delays of 450 ns to 1950 ns, Figures 4.80 to 4.82, and weaker in the center of the plasma, it is much more subtle than in the gaseous mixture held at atmospheric pressure, which can be due to interference of the CI 193.09 nm atomic carbon line in second order. At time delays of 2200 ns to 3200 ns, Figures 4.82 to 4.84, the CN signals appear to be evenly distributed across the plasma. As time elapses to a time delay of 3450 ns, Figure 4.84 the CN distribution becomes weaker at the edges or the plasma and stronger towards the center of the plasma. This trend is maintained up to 5200 ns as can be seen in Figures 4.84 to

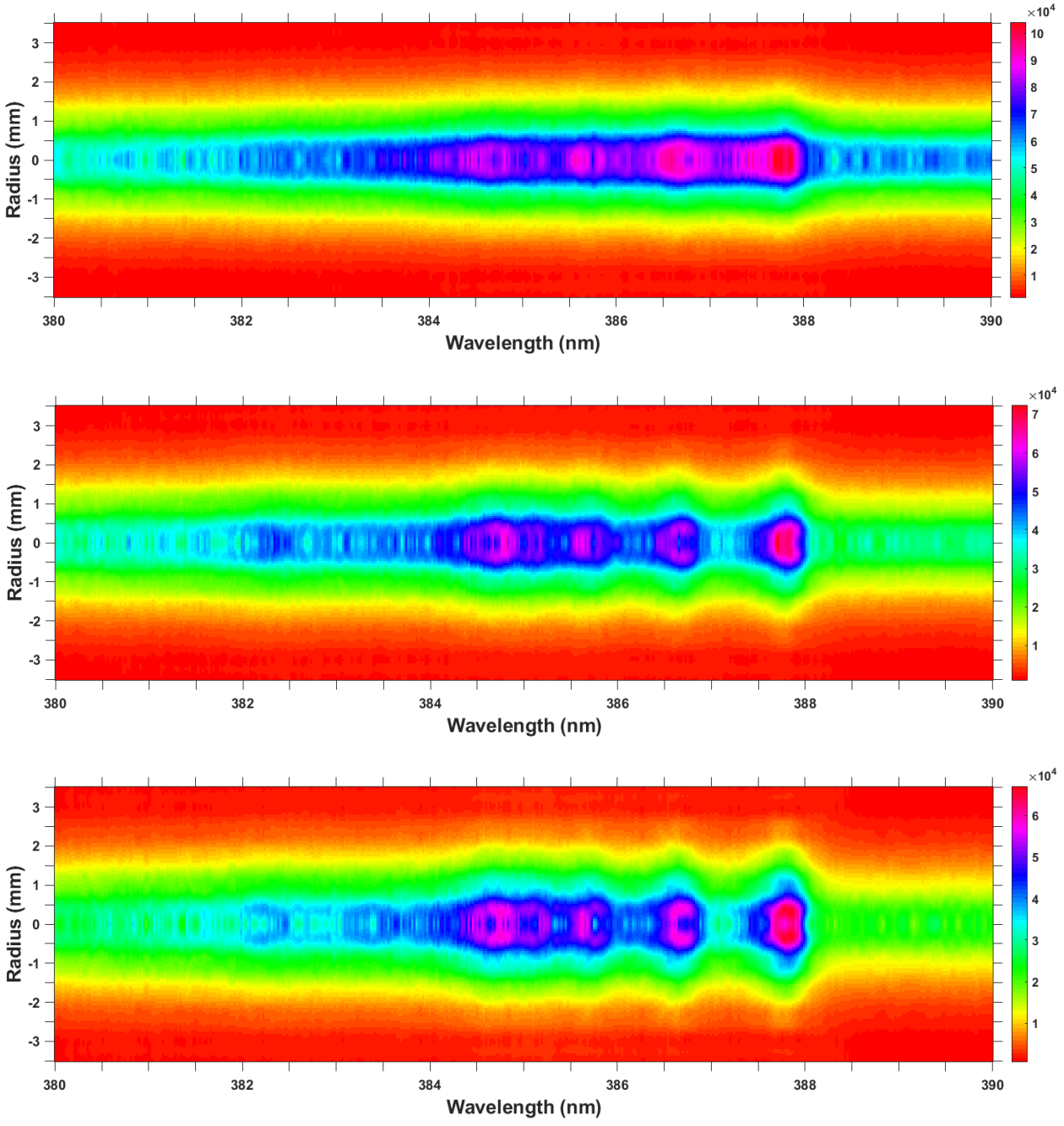

Figure 4.73: Abel inverted CN spectra 1:1 molar CO_2:N_2 gaseous mixture held at atmospheric pressure with 200 ns (top), 450 ns (center), and 700 ns (bottom) time delay [70, 71].

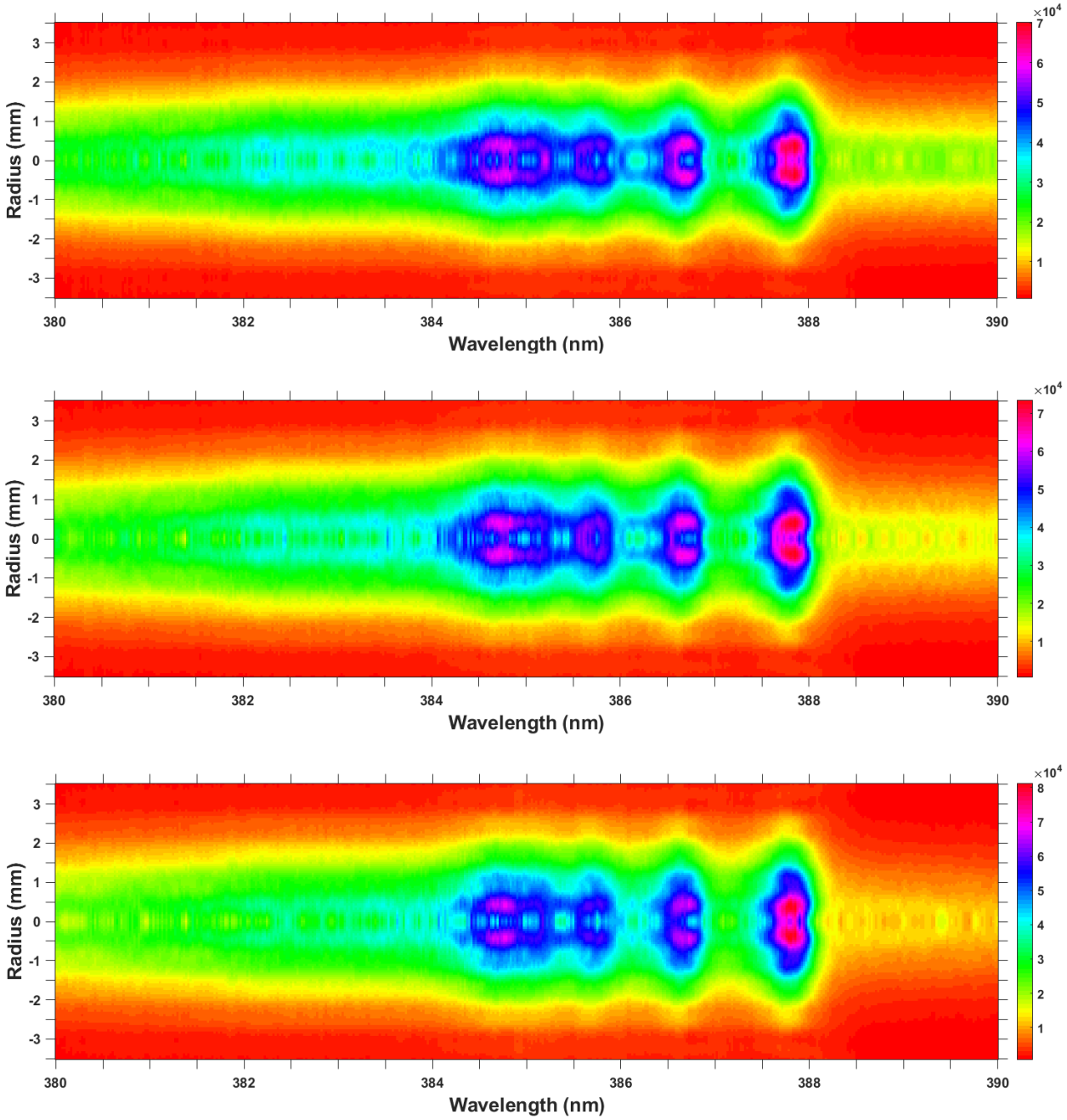

Figure 4.74: Abel inverted CN spectra 1:1 molar CO_2:N_2 gaseous mixture held at atmospheric pressure with 950 ns (top), 1200 ns (center), and 1450 ns (bottom) time delay [70, 71].

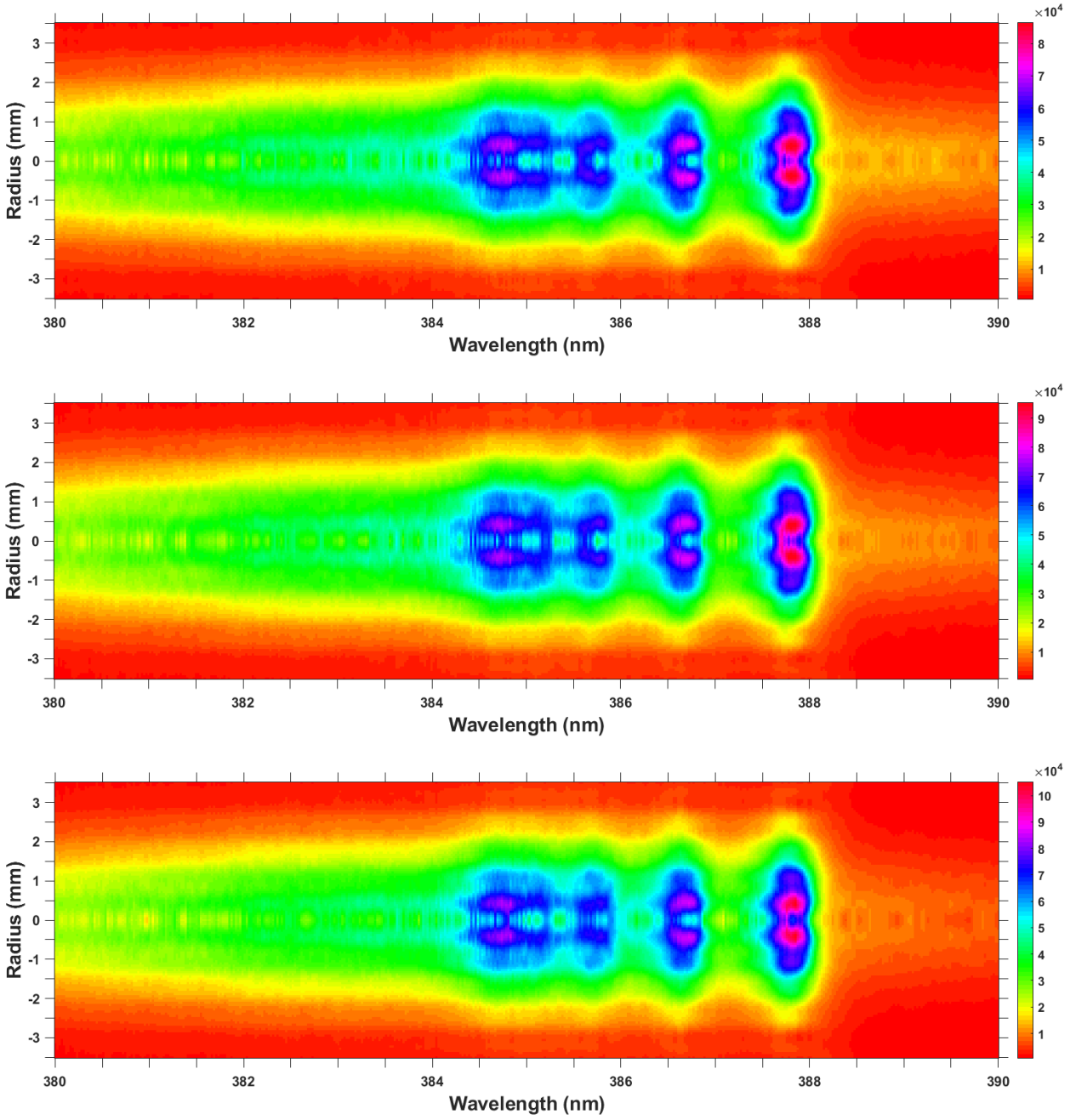

Figure 4.75: Abel inverted CN spectra 1:1 molar CO_2:N_2 gaseous mixture held at atmospheric pressure with 1700 ns (top), 1950 ns (center), and 2200 ns (bottom) time delay.

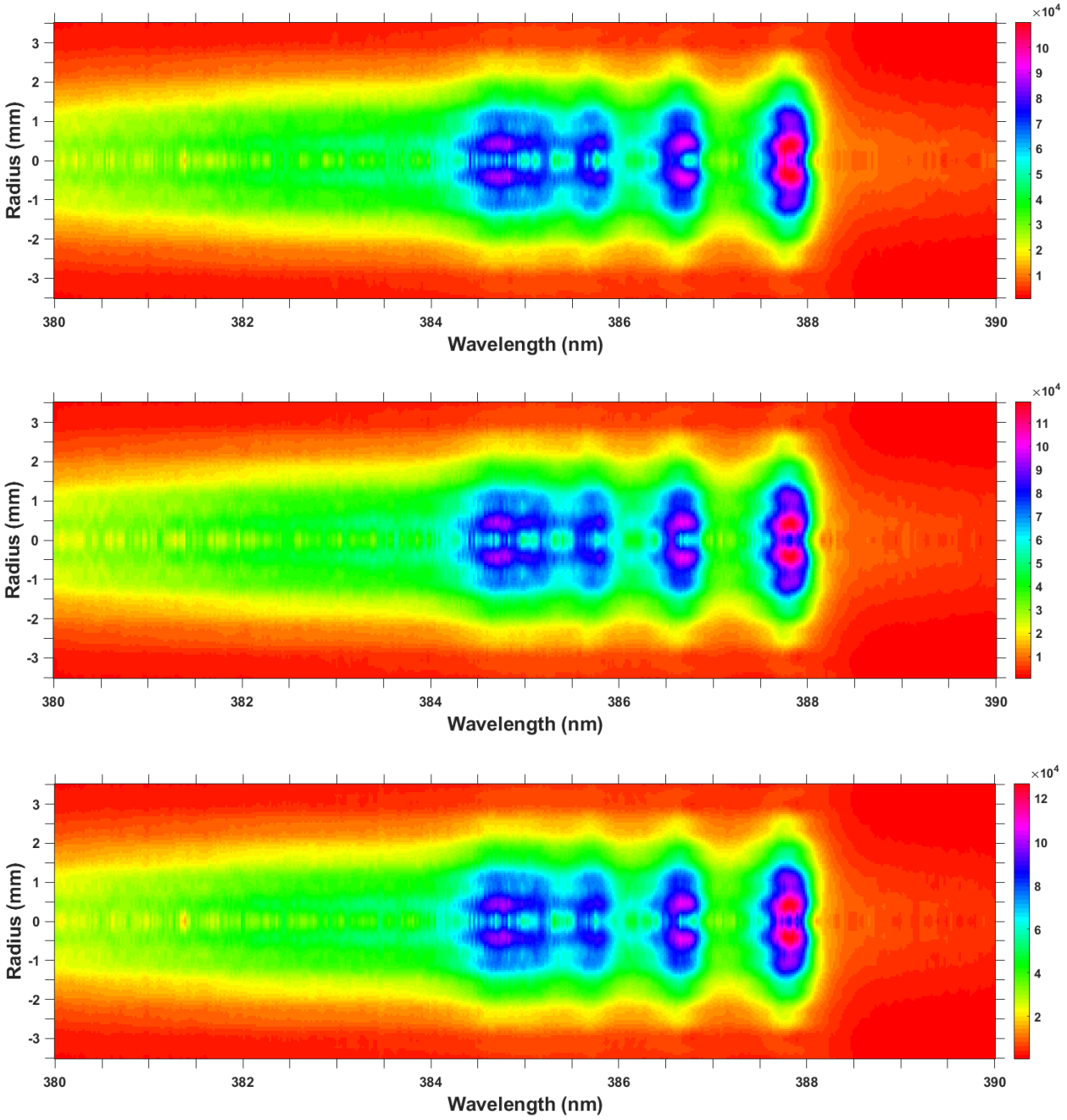

Figure 4.76: Abel inverted CN spectra 1:1 molar CO_2:N_2 gaseous mixture held at atmospheric pressure with 2450 ns (top), 2700 ns (center), and 2950 ns (bottom) time delay.

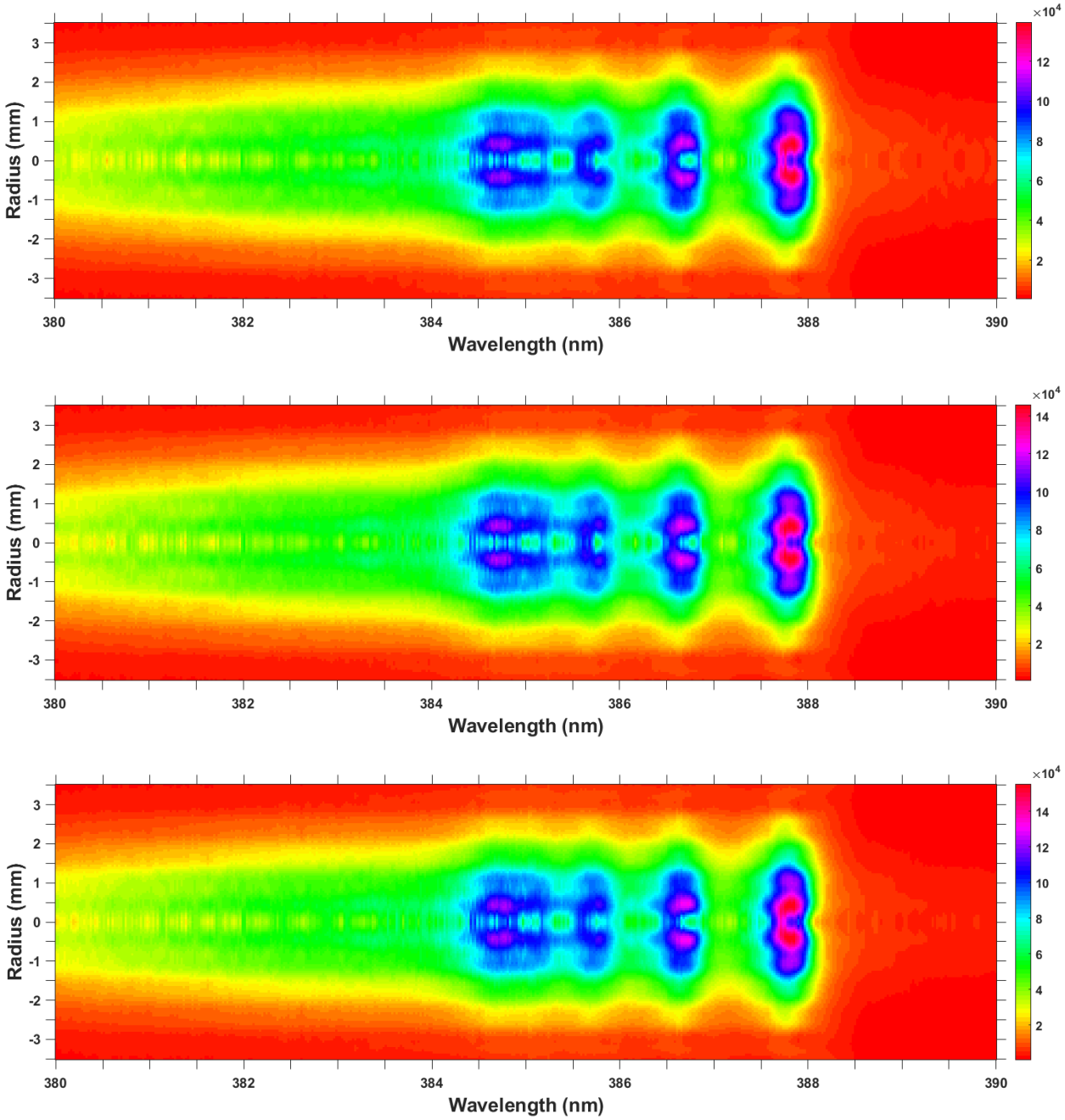

Figure 4.77: Abel inverted CN spectra 1:1 molar CO_2:N_2 gaseous mixture held at atmospheric pressure with 3200 ns (top), 3450 ns (center), and 3700 ns (bottom) time delay.

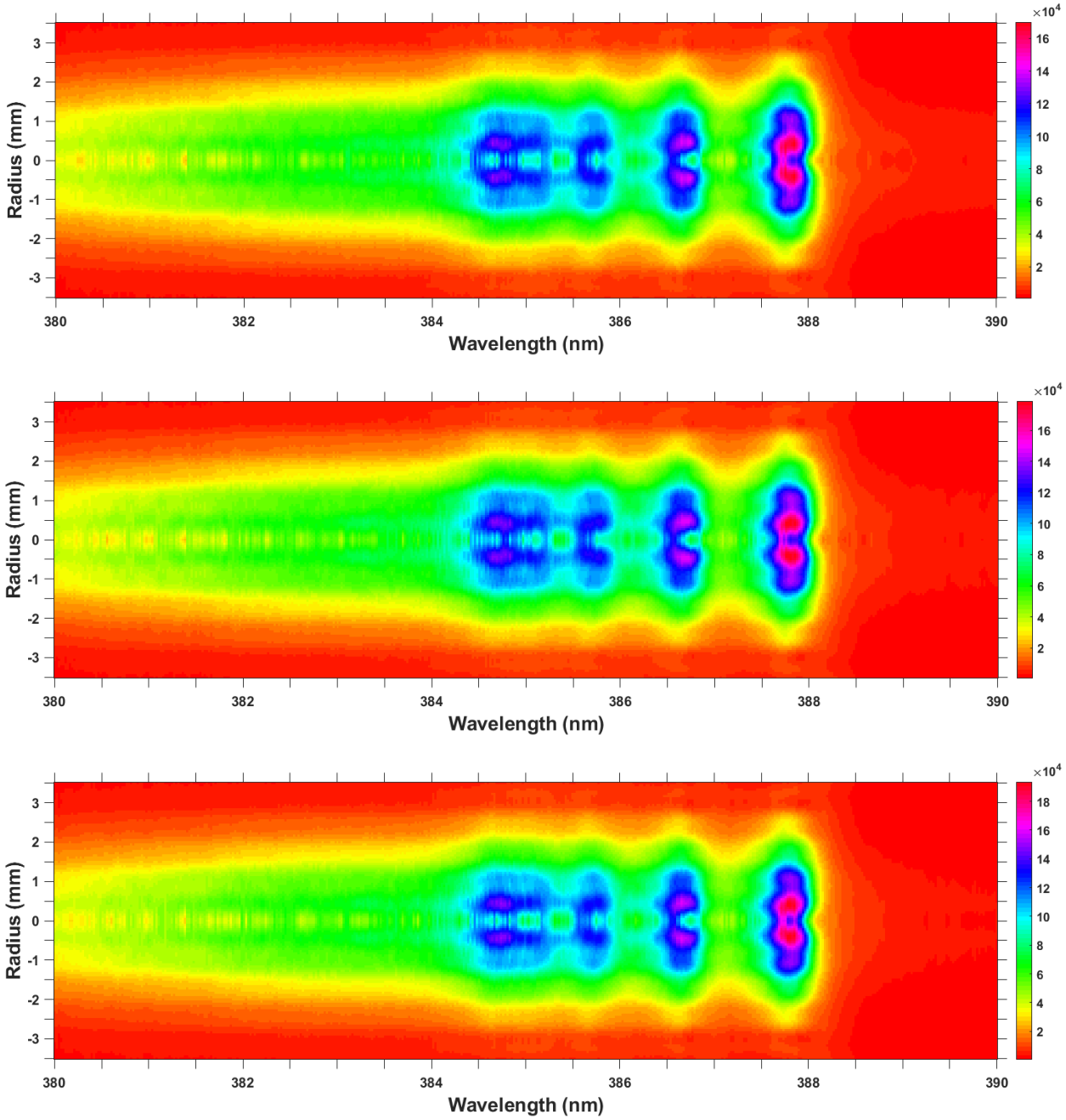

Figure 4.78: Abel inverted CN spectra 1:1 molar CO_2:N_2 gaseous mixture held at atmospheric pressure with 3950 ns (top), 4200 ns (center), and 4450 ns (bottom) time delay.

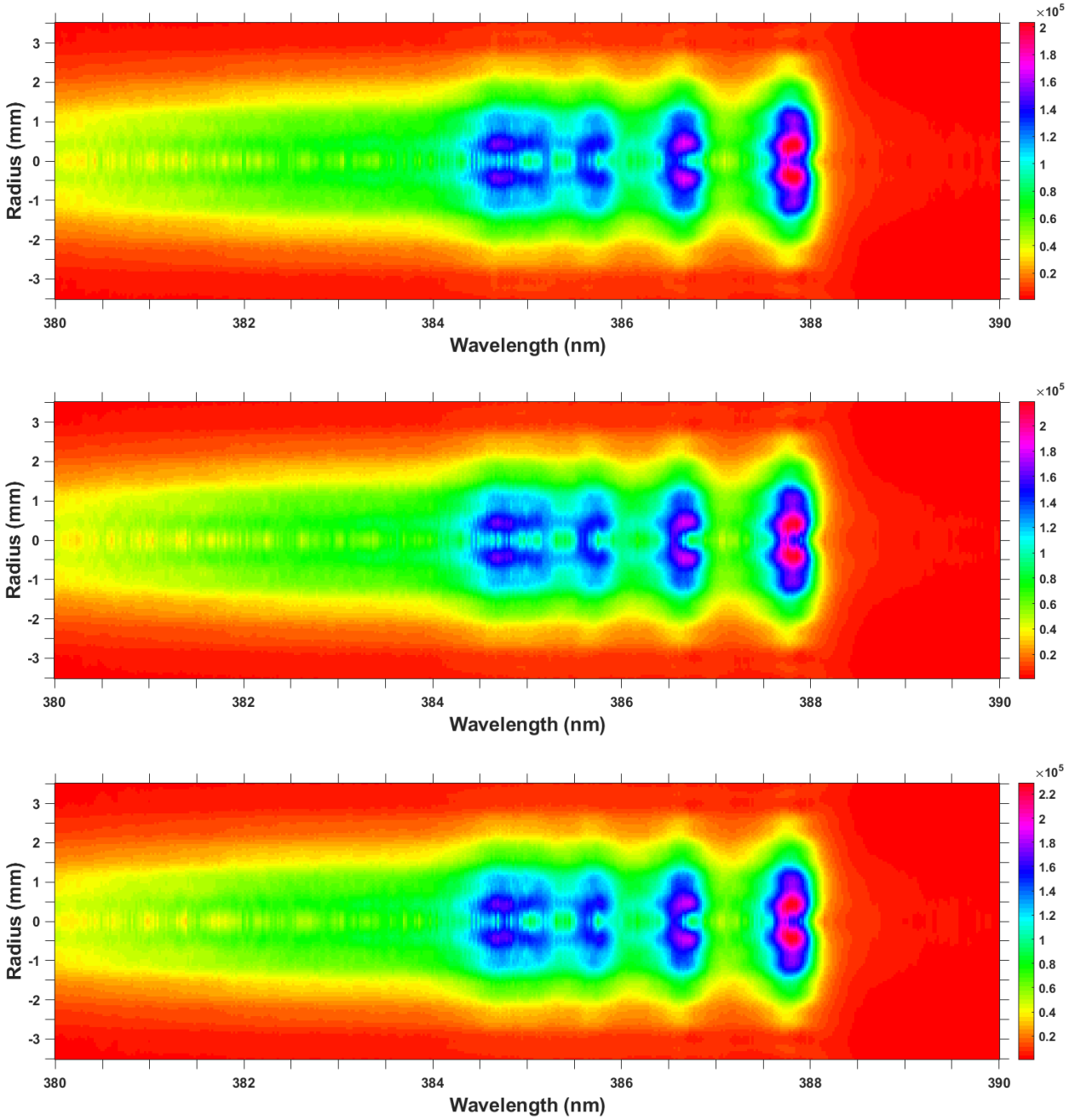

Figure 4.79: Abel inverted CN spectra 1:1 molar CO_2:N_2 gaseous mixture held at atmospheric pressure with 4700 ns (top), 4950 ns (center), and 5200 ns (bottom) time delay.

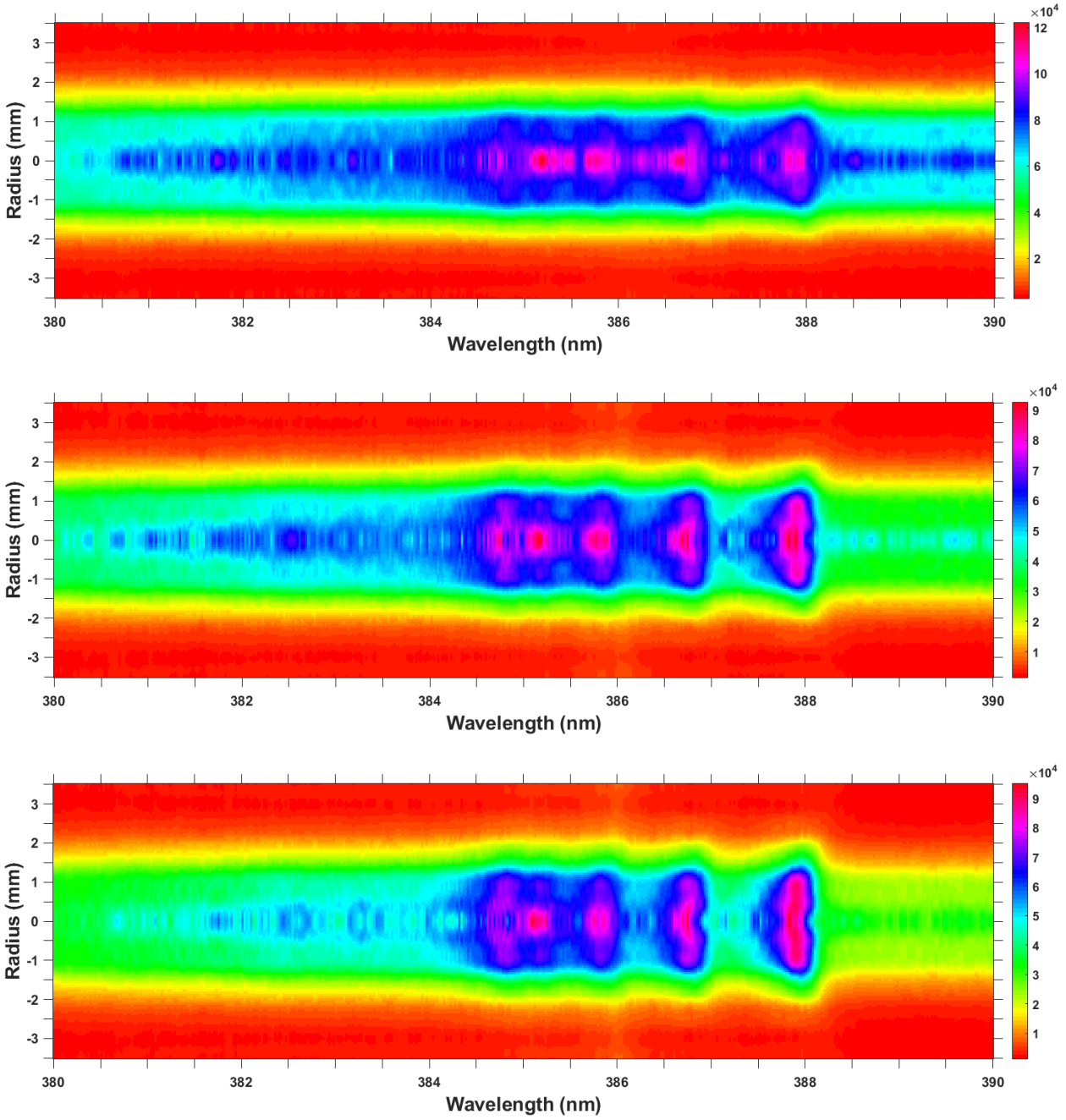

Figure 4.80: Abel inverted CN spectra 1:1 molar CO_2:N_2 gaseous mixture held at 276 kPa (2070 Torr) with 200 ns (top), 450 ns (center), and 700 ns (bottom) time delay.

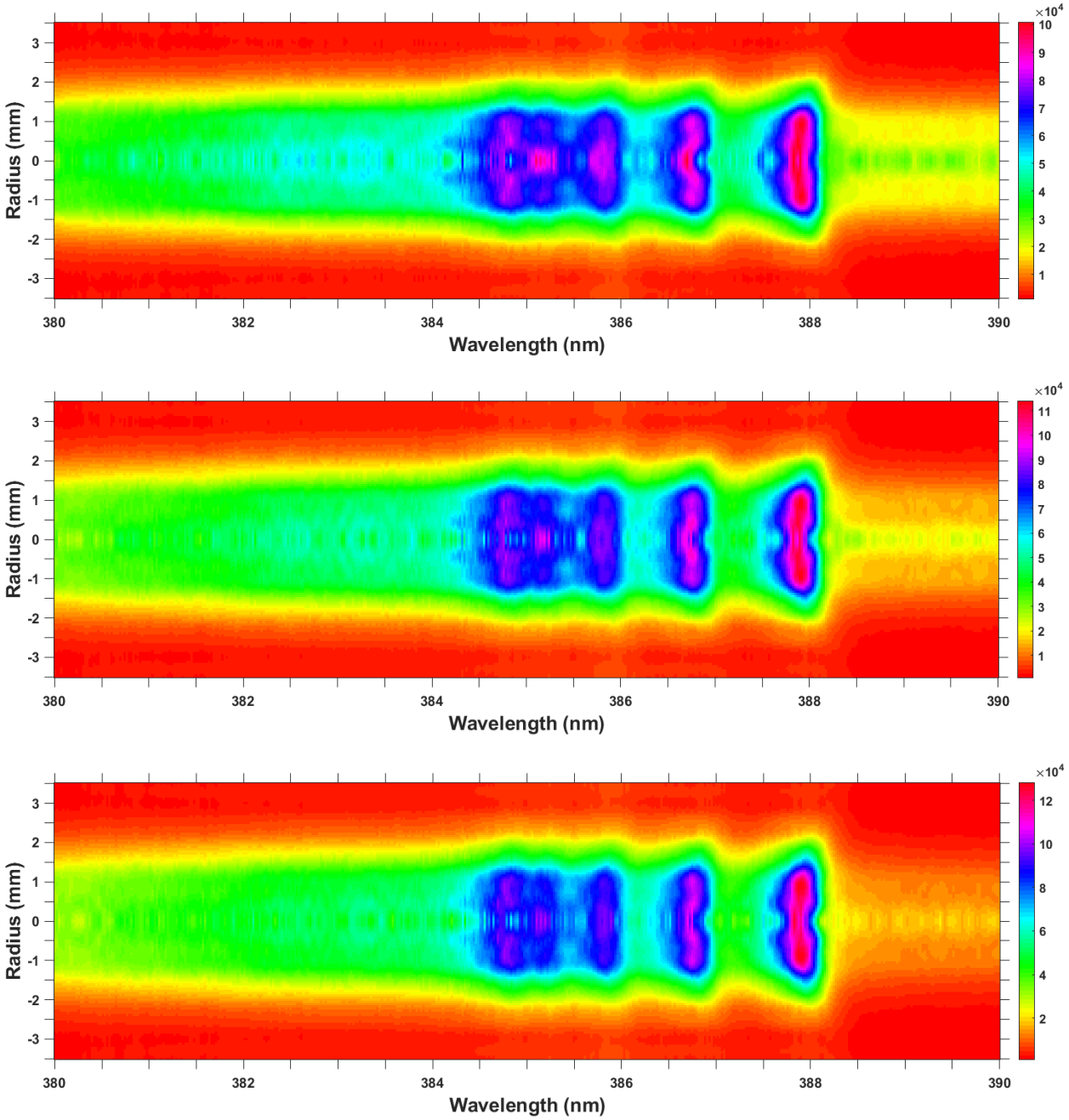

Figure 4.81: Abel inverted CN spectra 1:1 molar CO_2:N_2 gaseous mixture held at 276 kPa (2070 Torr) with 950 ns (top), 1200 ns (center), and 1450 ns (bottom) time delay.

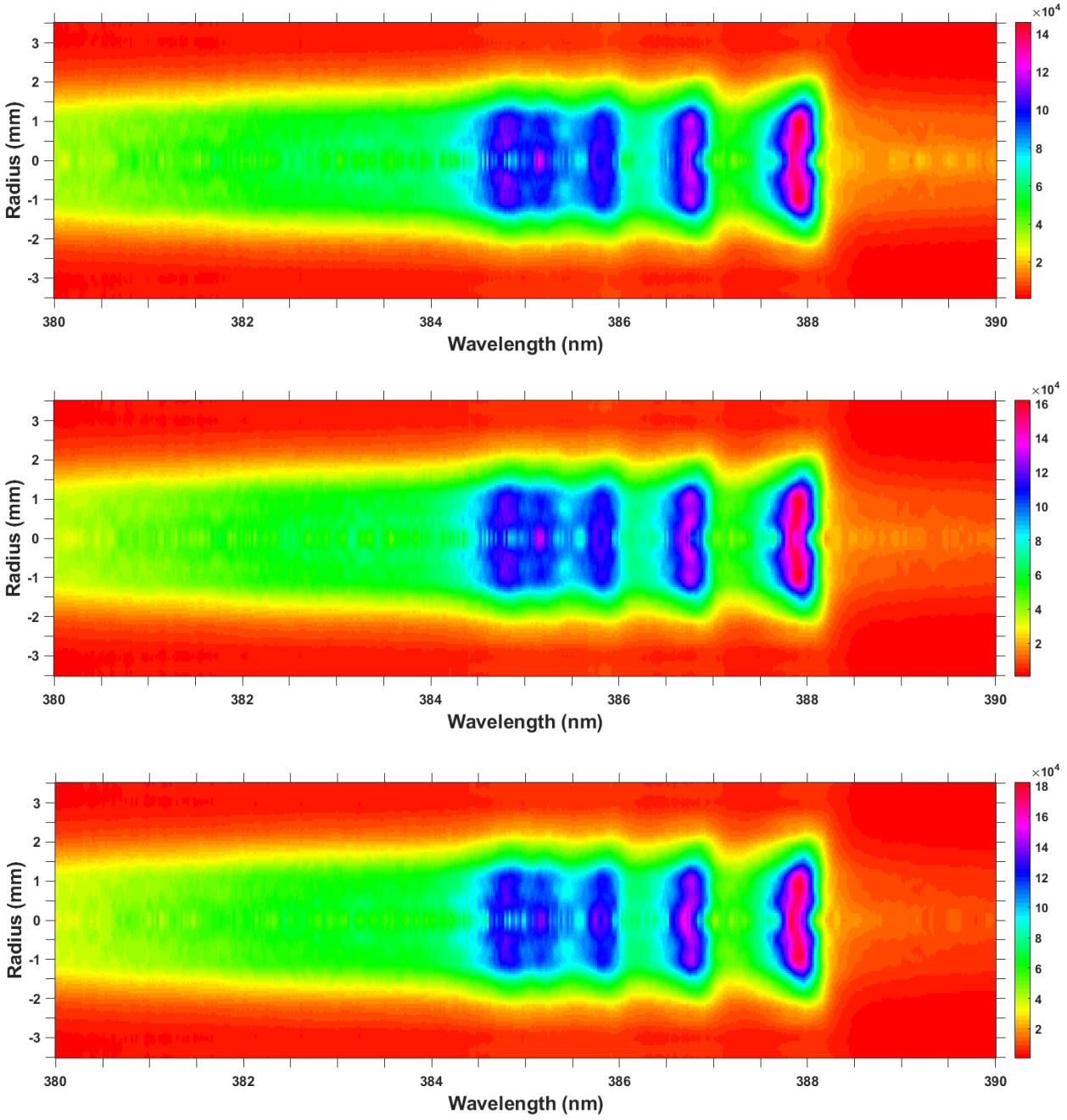

Figure 4.82: Abel inverted CN spectra 1:1 molar CO_2:N_2 gaseous mixture held at 276 kPa (2070 Torr) with 1700 ns (top), 1950 ns (center), and 2200 ns (bottom) time delay.

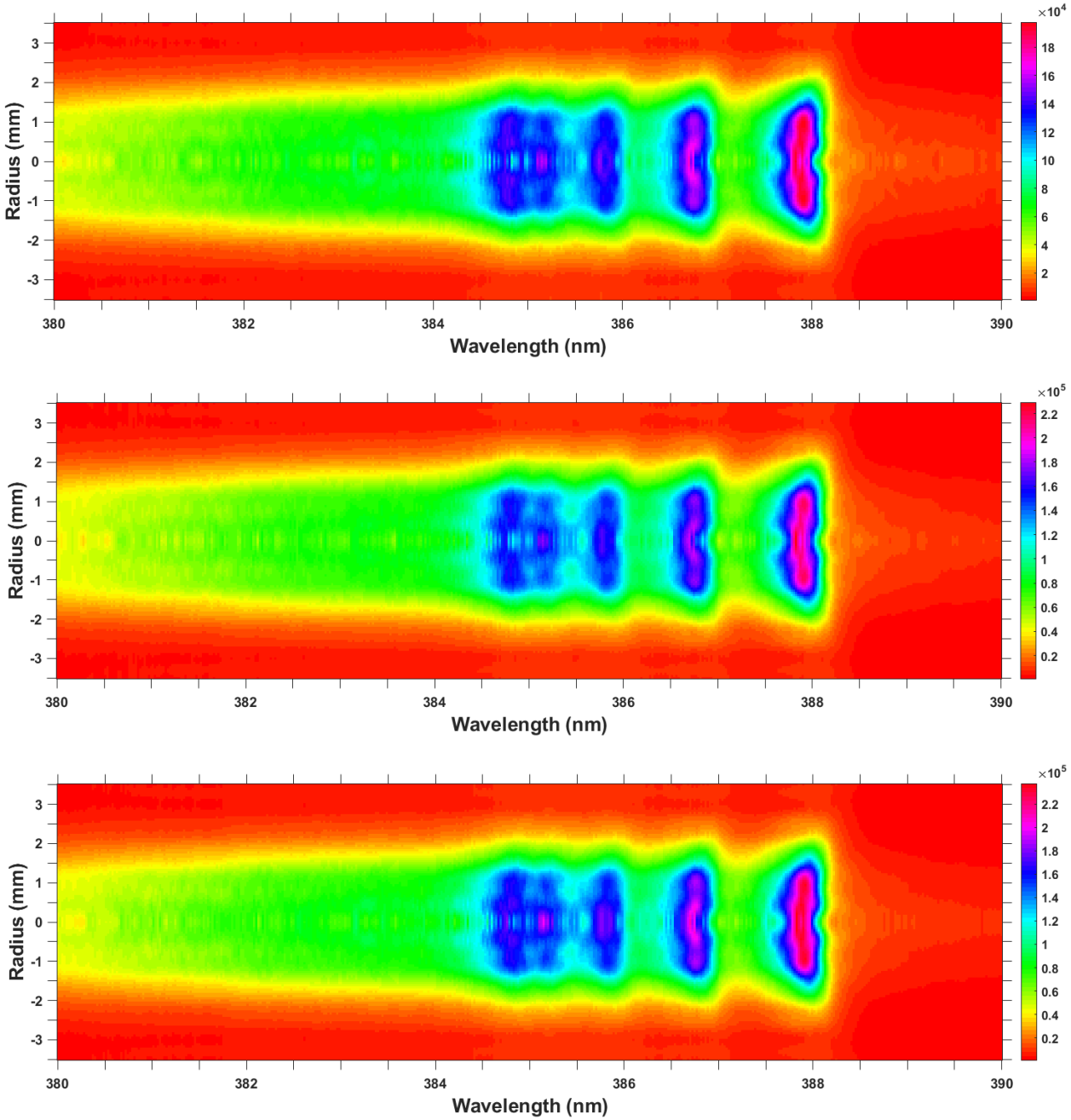

Figure 4.83: Abel inverted CN spectra 1:1 molar CO_2:N_2 gaseous mixture held at 276 kPa (2070 Torr) with 2450 ns (top), 2700 ns (center), and 2950 ns (bottom) time delay.

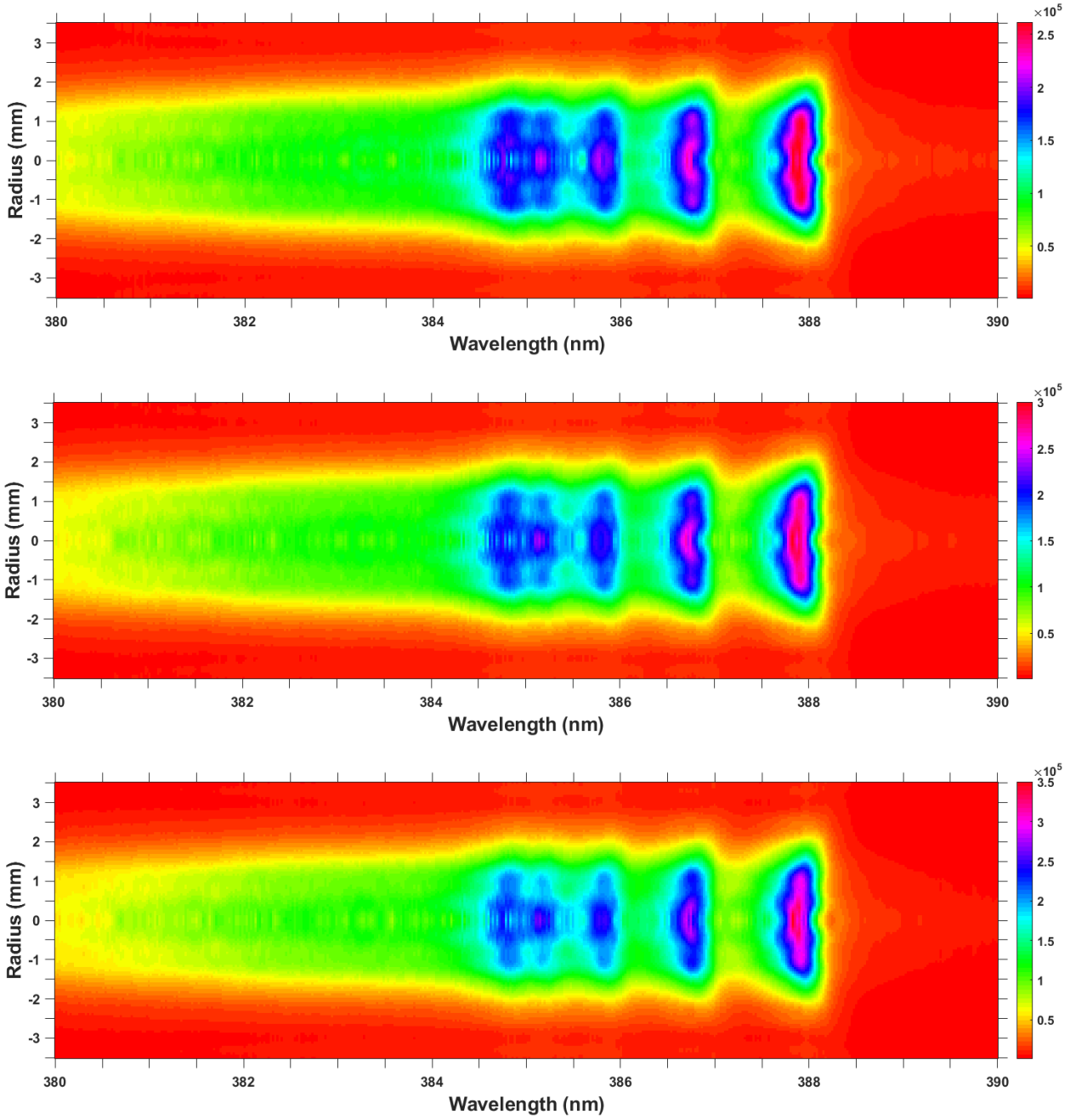

Figure 4.84: Abel inverted CN spectra 1:1 molar CO_2:N_2 gaseous mixture held at 276 kPa (2070 Torr) with 3200 ns (top), 3450 ns (center), and 3700 ns (bottom) time delay.

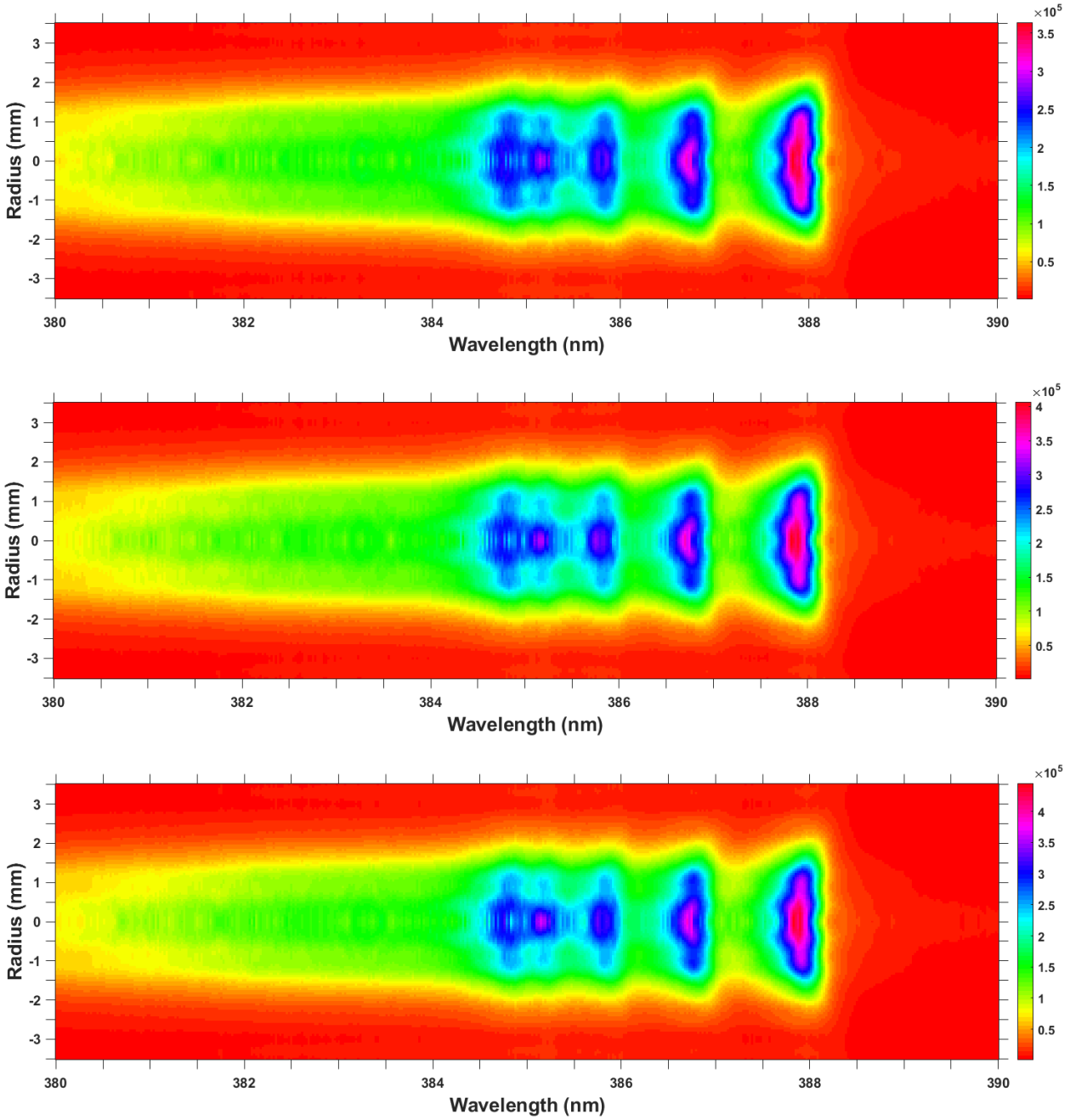

Figure 4.85: Abel inverted CN spectra 1:1 molar CO_2:N_2 gaseous mixture held at 276 kPa (2070 Torr) with 3950 ns (top), 4200 ns (center), and 4450 ns (bottom) time delay.

4.86. The predicted results were to be similar to the shockwave results, but the variations inside the plasma kernel and shockwave as seen in the gaseous mixture held at atmospheric pressure were also expected for the gaseous mixture held at 276 kPa (2070 Torr).

4.5.3 Abel Inverted CN Spectra in the 1:1 Molar CO_2 and N_2 Flowing Gaseous Mixture

Abel inversion of the filtered 1:1 molar CO_2:N_2 flowing gaseous mixture was performed using the same technique as the gaseous mixture held at atmospheric pressure and 276 kPa (2070 Torr). At a time delay of 200 ns, Figure 4.87, the CN distribution appears evenly distributed across the plasma similar to the gaseous mixture held at atmospheric pressure. From time delays of 450 ns to 2200 ns, Figures 4.87 to 4.89, the CN signals begin to become stronger towards the edges of the plasma and weaker in the center of the plasma similar to the gaseous mixture held at atmospheric pressure. The higher distributions of CN towards the edges is consistent with the higher temperatures seen at the edges of the plasma as discussed previously. At 2450 ns time delay, Figure 4.90, it is clearly visible that there is a higher CN signal towards the edges of the plasma than in the center. This trend is maintained up to 5200 ns as can be seen in Figures 4.91 to 4.93. The predicted results were to be similar to the shockwave results, but the variations inside the plasma kernel and shockwave as seen in the gaseous mixture held at atmospheric pressure and 276 kPa (2070 Torr) were also expected for the flowing gaseous mixture.

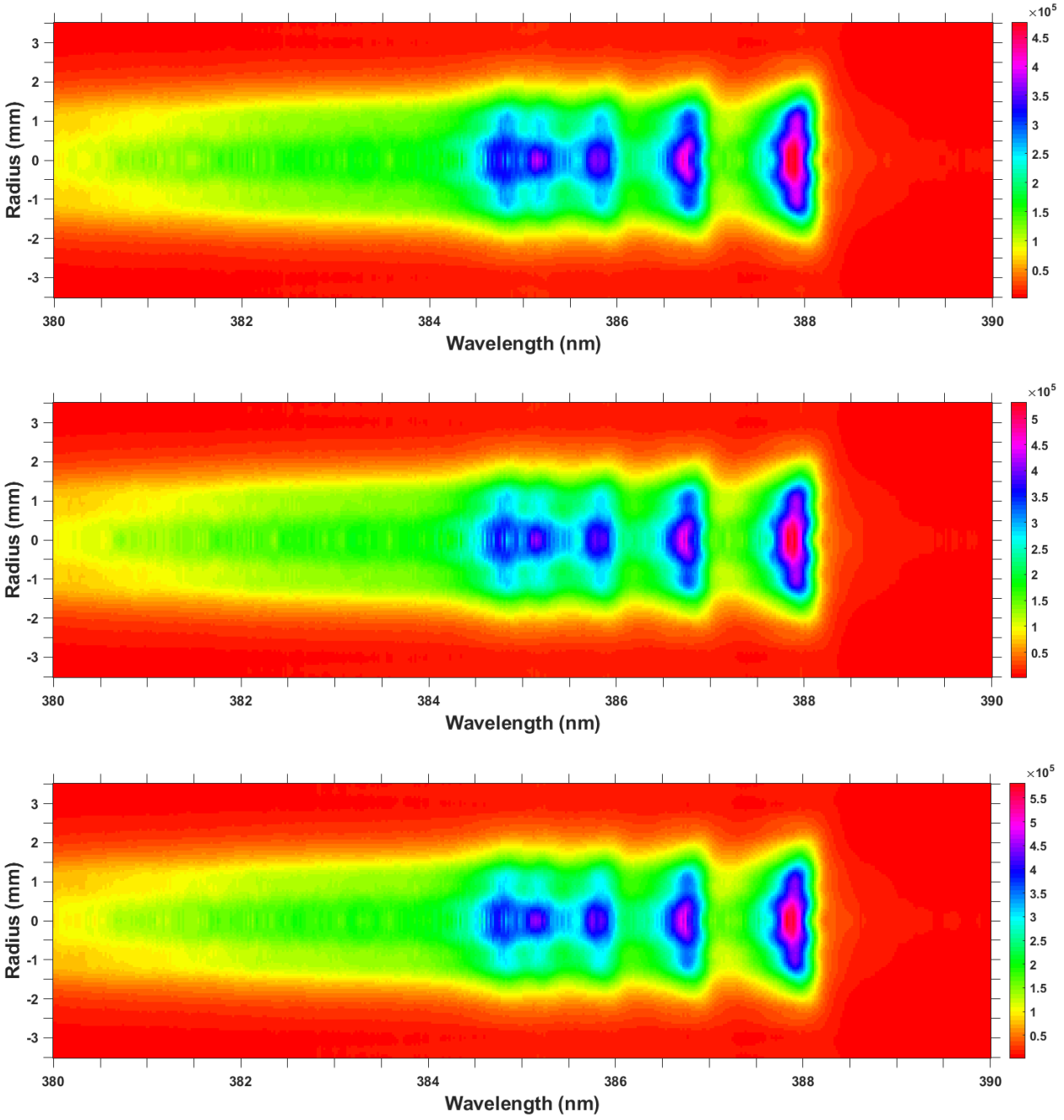

Figure 4.86: Abel inverted CN spectra 1:1 molar CO_2:N_2 gaseous mixture held at 276 kPa (2070 Torr) with 4700 ns (top), 4950 ns (center), and 5200 ns (bottom) time delay.

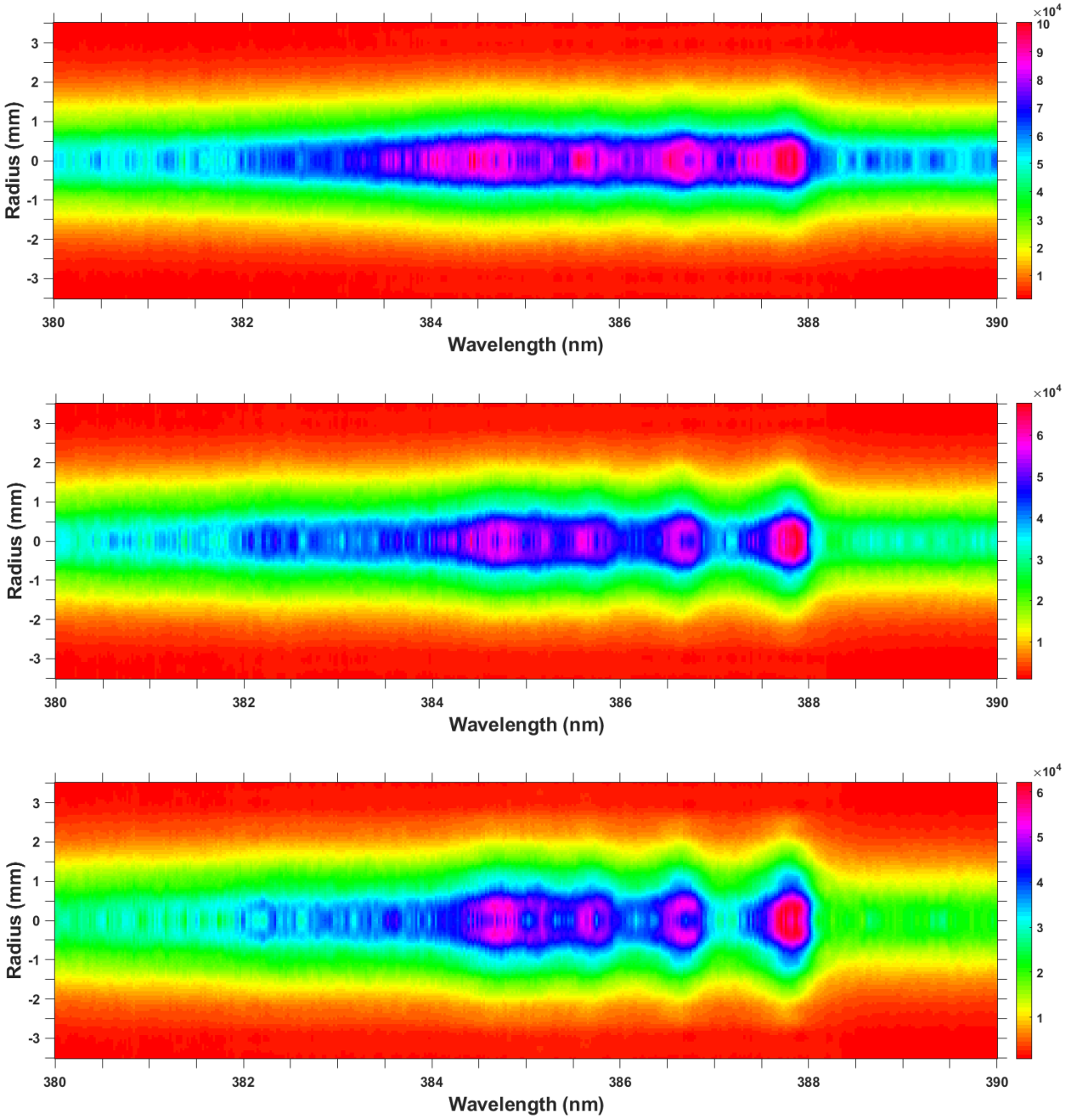

Figure 4.87: Abel inverted CN spectra 1:1 molar CO_2:N_2 flowing gaseous mixture with 200 ns (top), 450 ns (center), and 700 ns (bottom) time delay.

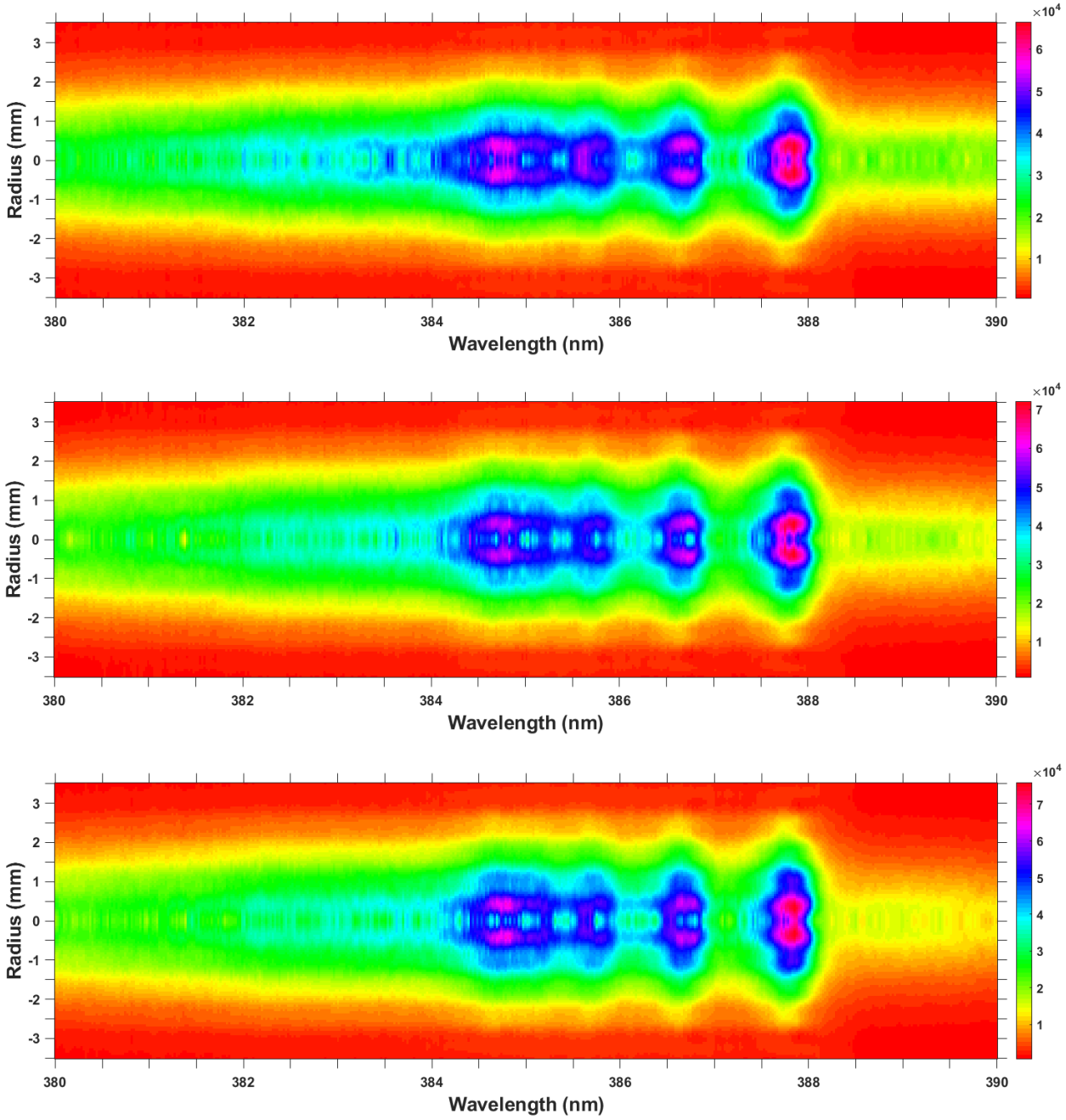

Figure 4.88: Abel inverted CN spectra 1:1 molar CO_2:N_2 flowing gaseous mixture with 950 ns (top), 1200 ns (center), and 1450 ns (bottom) time delay.

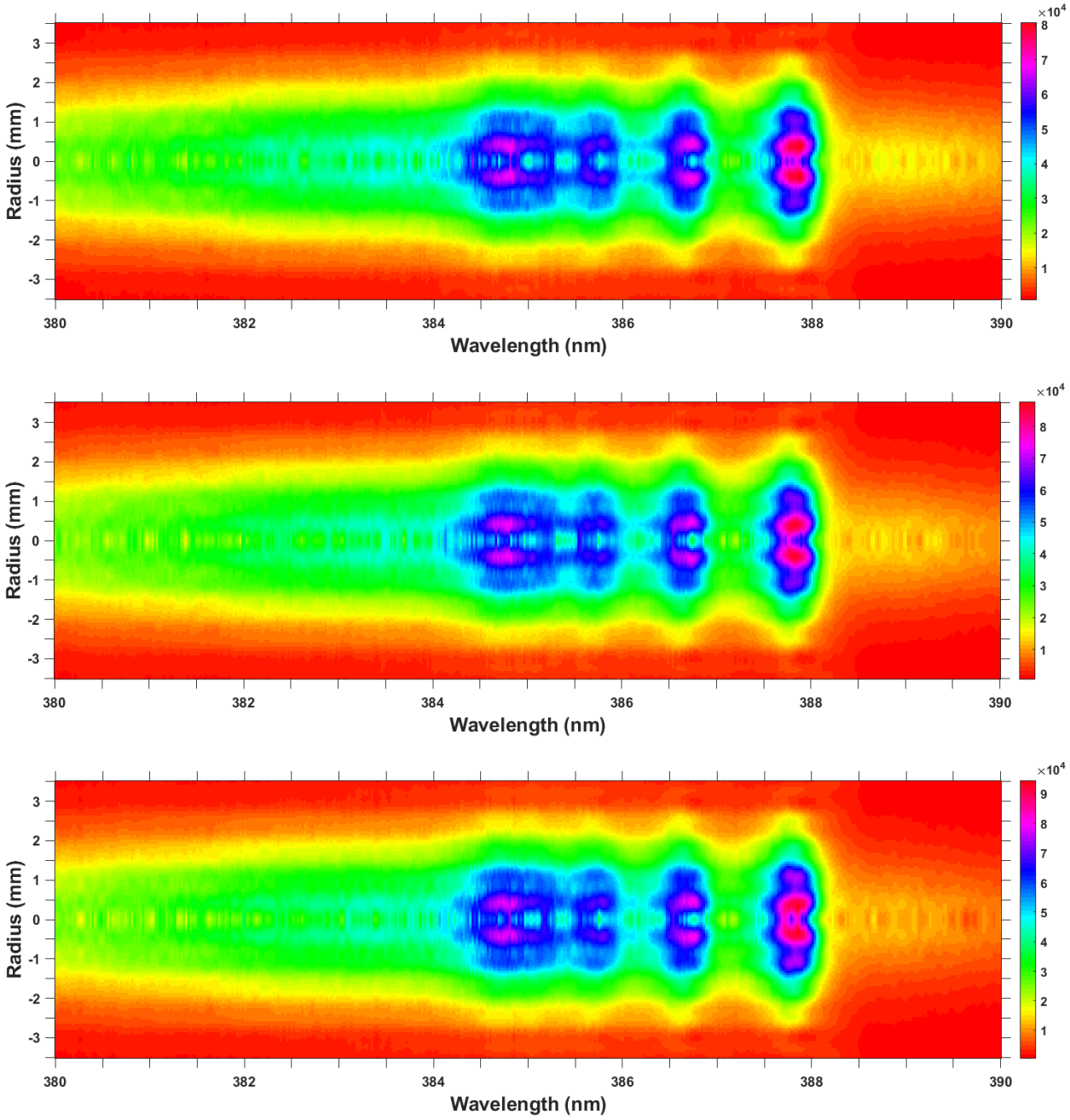

Figure 4.89: Abel inverted CN spectra 1:1 molar CO_2:N_2 flowing gaseous mixture with 1700 ns (top), 1950 ns (center), and 2200 ns (bottom) time delay.

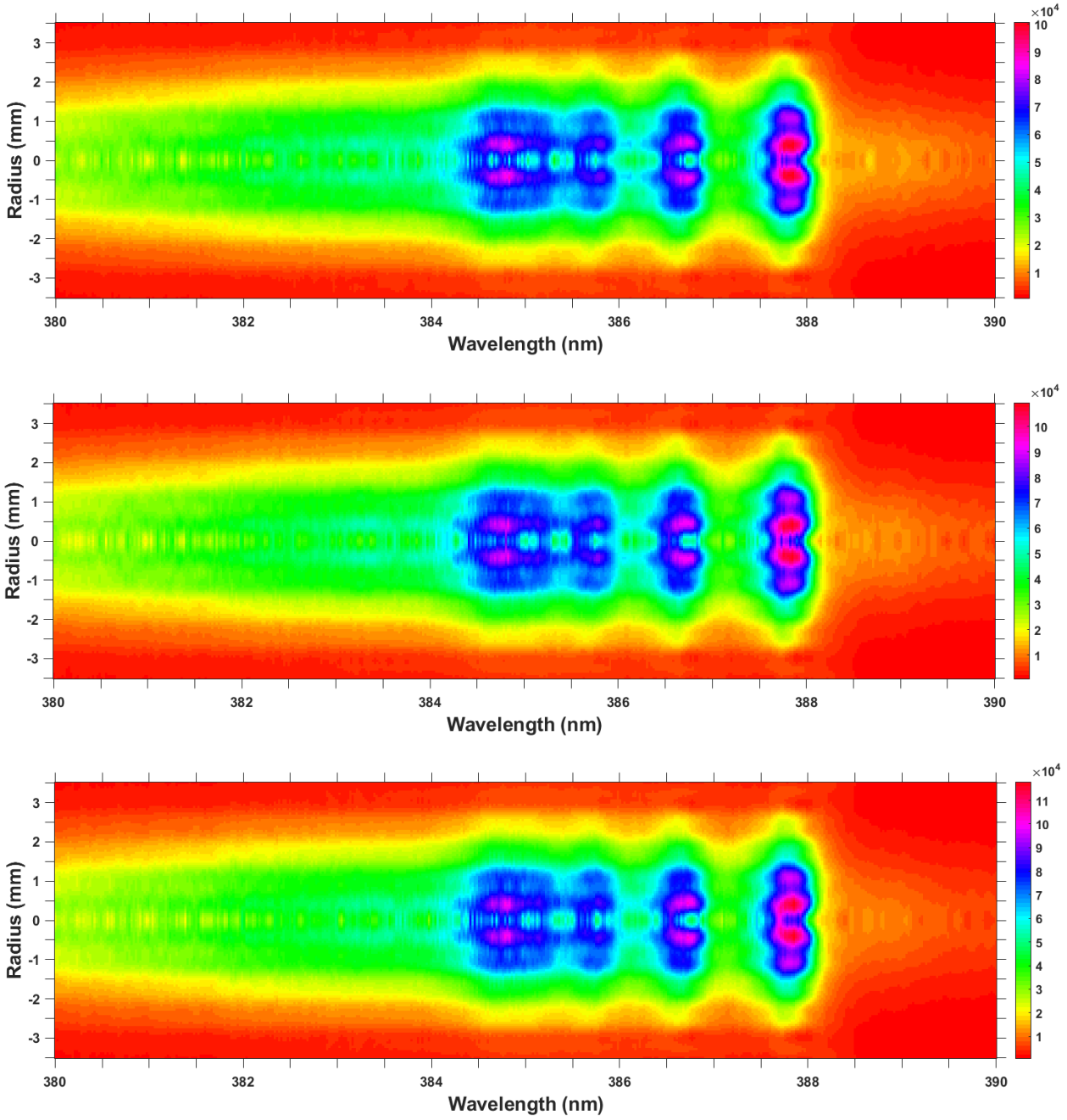

Figure 4.90: Abel inverted CN spectra 1:1 molar CO_2:N_2 flowing gaseous mixture with 2450 ns (top), 2700 ns (center), and 2950 ns (bottom) time delay.

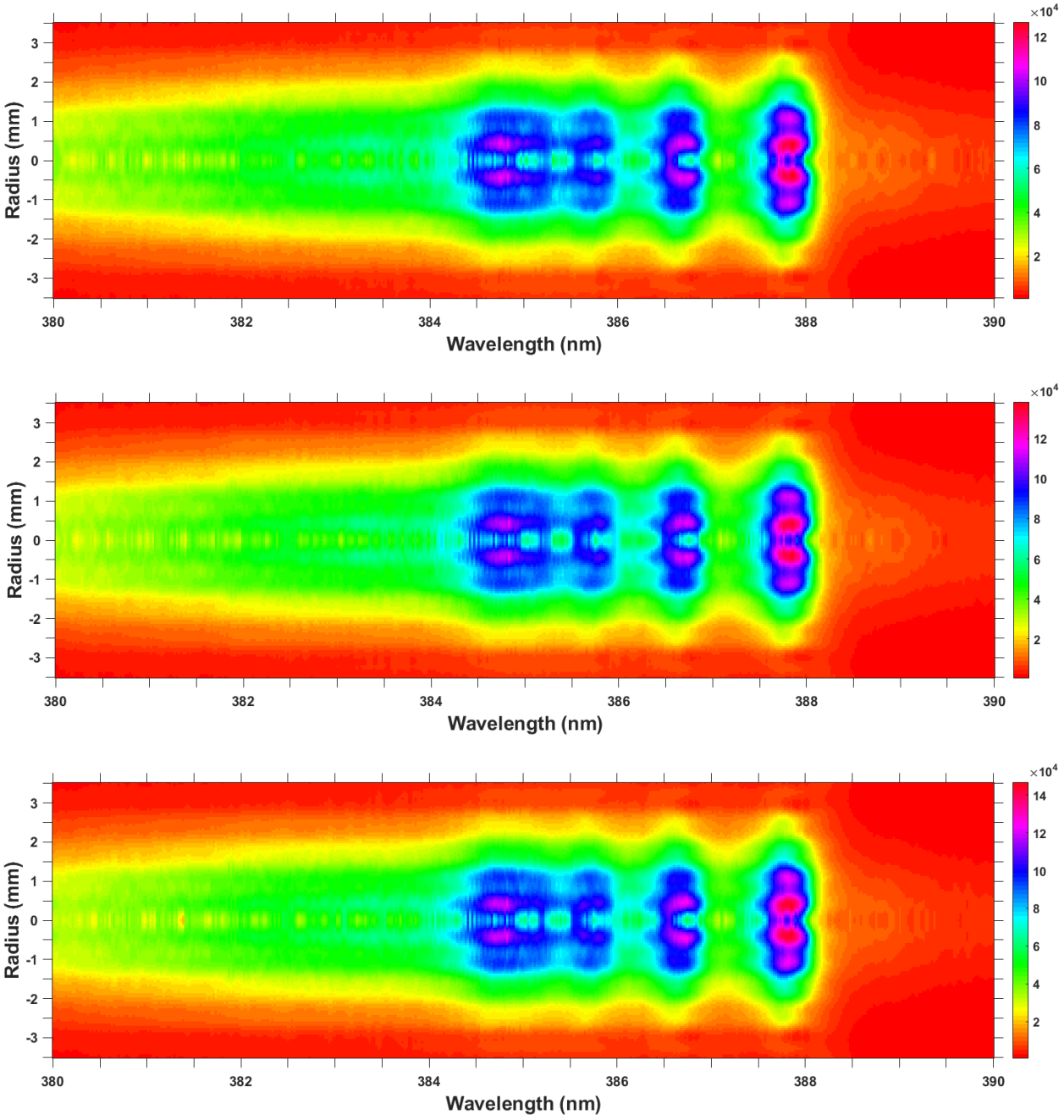

Figure 4.91: Abel inverted CN spectra 1:1 molar CO_2:N_2 flowing gaseous mixture with 3200 ns (top), 3450 ns (center), and 3700 ns (bottom) time delay.

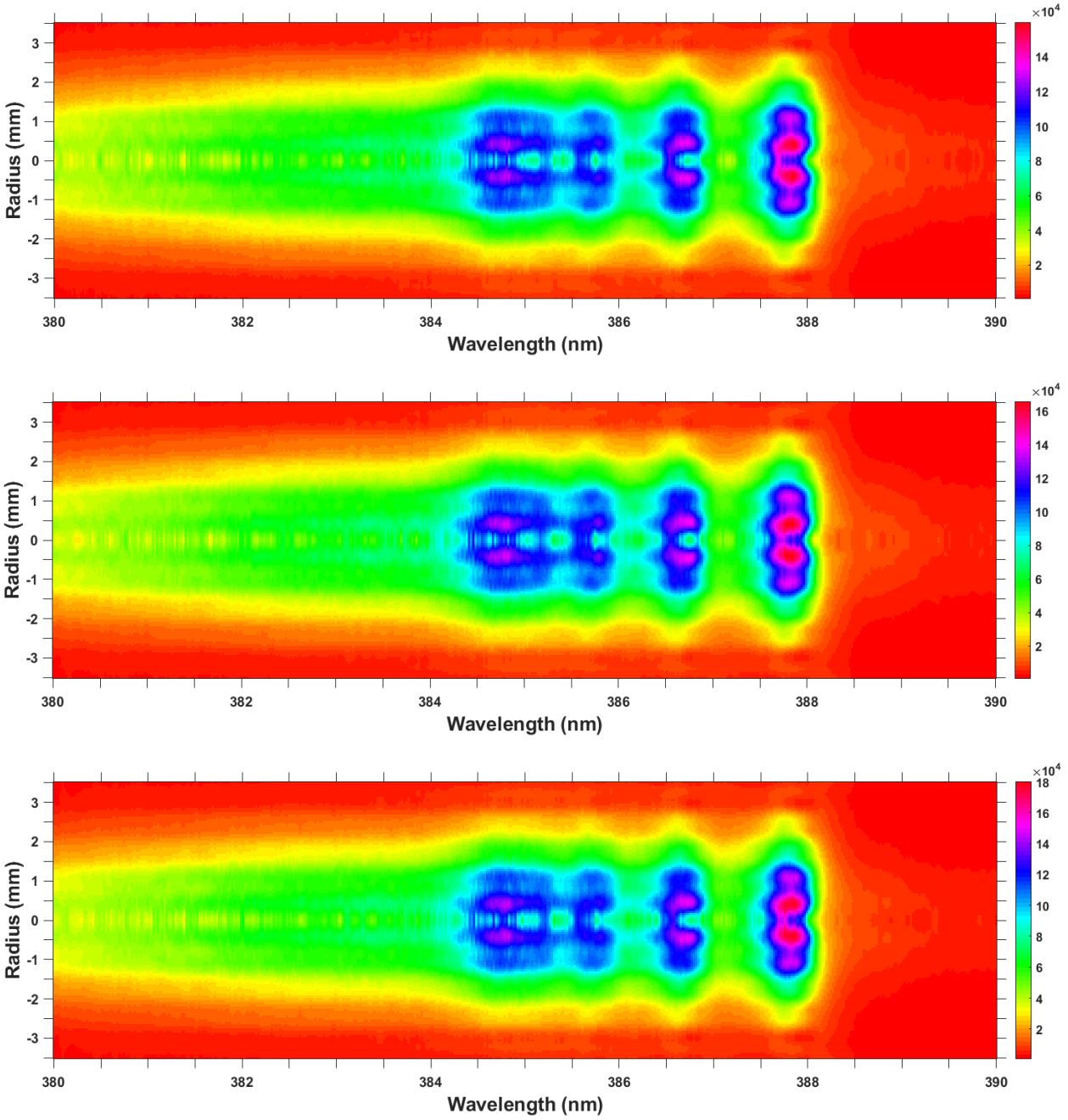

Figure 4.92: Abel inverted CN spectra 1:1 molar CO_2:N_2 flowing gaseous mixture with 3950 ns (top), 4200 ns (center), and 4450 ns (bottom) time delay.

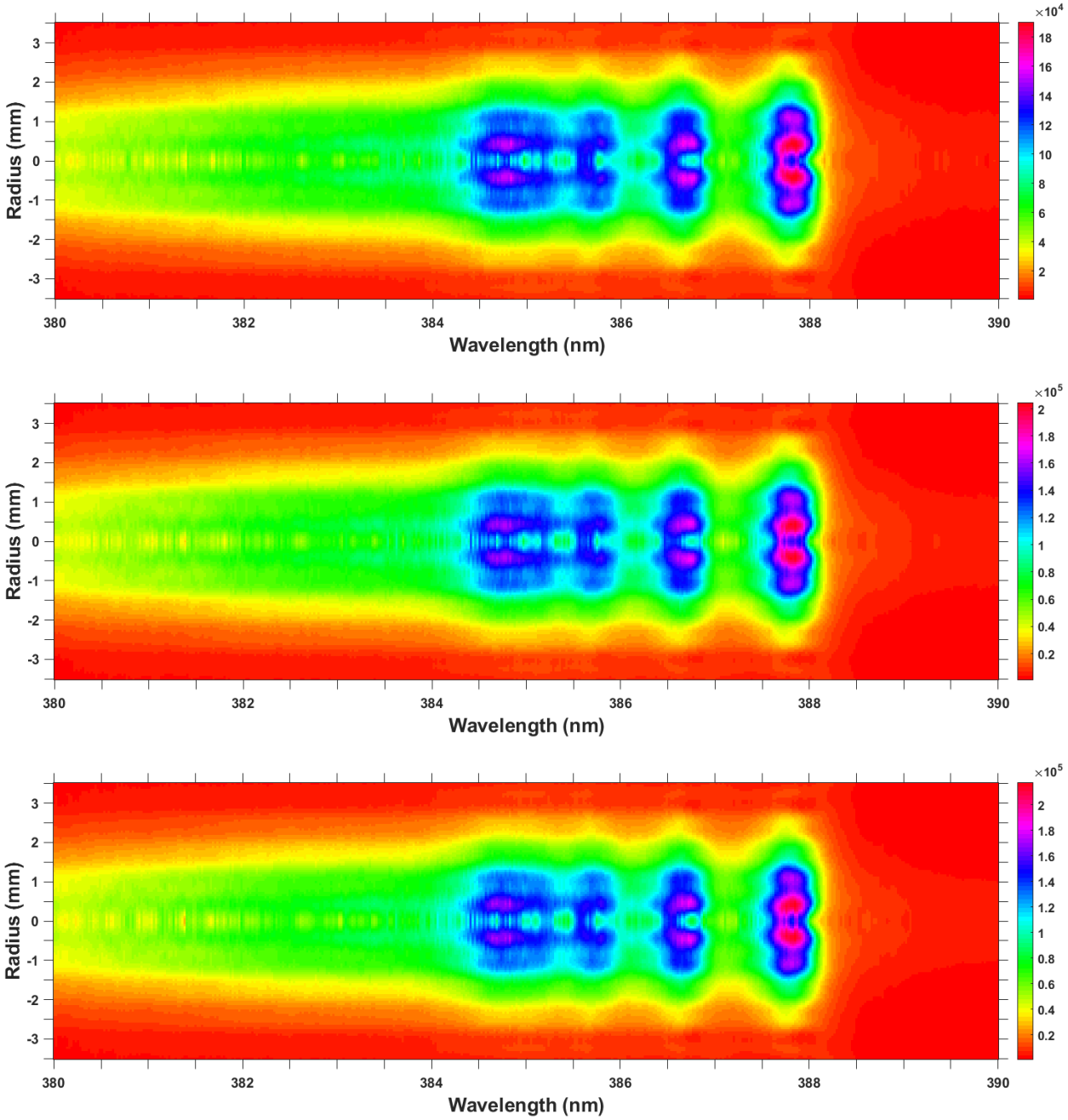

Figure 4.93: Abel inverted CN spectra 1:1 molar CO_2:N_2 flowing gaseous mixture with 4700 ns (top), 4950 ns (center), and 5200 ns (bottom) time delay.

Chapter 5

Conclusions

Laser-induced breakdown plasma is produced in a variety of different experimental arrangements such as ambient air and carbon dioxide and nitrogen gas mixtures. Laser-plasma expansion following optical breakdown occurs above hypersonic speed. Shadowgraphs of plasmas generated in air were performed to evaluate the shock front geometry and plasma shape, which both were determined to be nearly spherical. Theoretical comparison of shock-wave radii for ambient air and the carbon dioxide and nitrogen gaseous mixture for similar energy per pulse, showed the shadowgraphs in air provide an excellent guide for the shockwave effects in the carbon dioxide and nitrogen gaseous mixture. Investigation of the plasma dynamics for a range of absorbed energies starting with minimum energy required for optical breakdown to the maximum energy that can be absorbed would be of future interest. A composite shadowgraph produced by a green, 90 mJ/pulse, 5 ns beam for the initial generation of the plasma and a spatially overlapped 110 mJ/pulse, 5 ns beam generating laser plasma at the shockwave is seen in Figure 5.1. These composite shadowgraphs can also be evaluated to determine shockwave and plasma dynamics in air. Additionally, evaluation of shadowgraphs of shockwave dynamics in carbon dioxide and nitrogen gas mixtures would be of future interest to validate the use of shadowgraphs in air to predict shockwave dynamics.

Measurements of recombination cyanide (CN) spectra were performed in a fixed volume gaseous mixture held at atmospheric pressure, a fixed volume gaseous mixture held at 276 kPa (2070 Torr), and a flowing gaseous mixture with flowrate of 100 mL/min. Evaluation of Stark widths and Stark shifts of the overlapping CI 193.09 nm atomic carbon line in second order were performed using filtered and unfiltered CN spectra for each mixture. The Stark

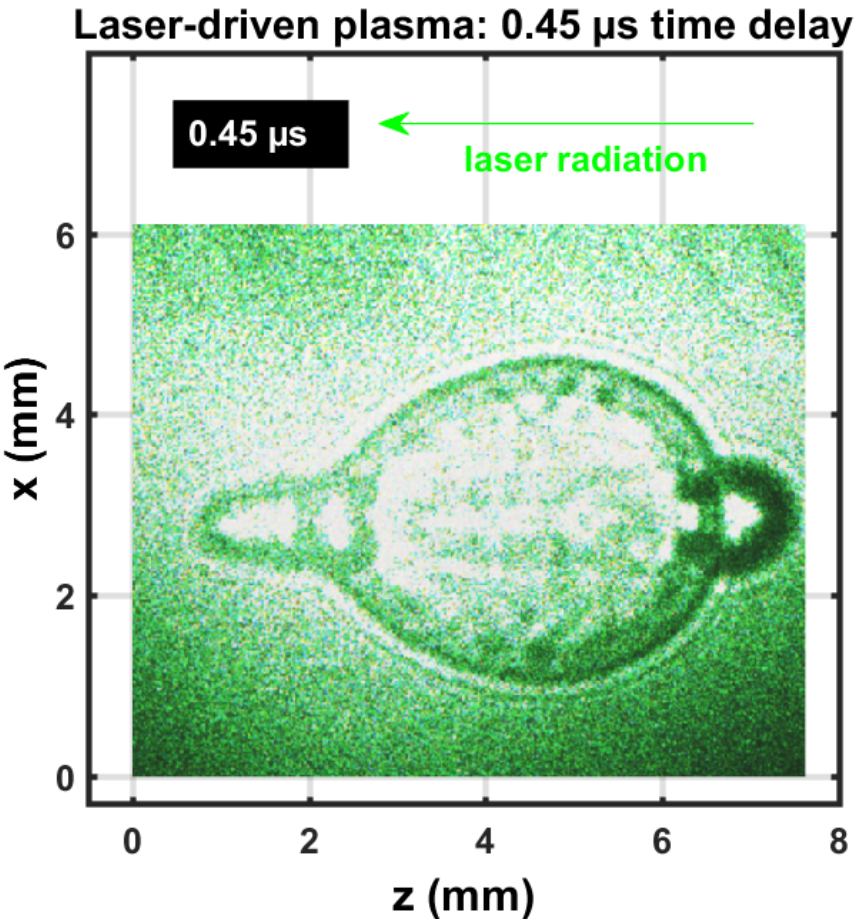

Figure 5.1: Single-shot shadowgraph of laser-induced plasma initiated with 90-mJ and 110-mJ, 5-ns, 532-nm focused beams, and imaged using two 5-ns, 532-nm back lights that are time-delayed by 0.03 μs, 0.45 μs, and 0.48 μs [70, 71].

widths and Stark shifts were used to determine electron densities, which were seen to be larger towards the edges of the plasma, near the shockwave, and smaller towards the center for time delays around 1 to 2 μs for all three mixtures. Higher spectral resolutions on the order of 0.02 nm would be necessary to determine more accurate atomic carbon line electron densities.

CN plasma excitation temperatures were evaluated using the application of the Nelder-Mead Temperature Program to filtered and unfiltered line-of-sight data, which yielded higher excitation temperatures towards the edges of the plasma, near the shockwave, and lower excitation temperatures towards to the center for time delays around 1 to 2 μs for all three mixtures. Spectral resolution better than 0.1 nm for CN spectra would yield an improved evaluation of excitation temperature. Both the calculated electron densities and inferred CN excitation temperatures indicate shockwave expansion affects the formation of CN molecules as the plasma expands in each mixture.

Abel inversion application on the measured line-of-sight was acceptable and validated by the shadowgraphs measured in air. Abel inverted CN spectra showed higher CN signals towards the edges of the plasma and lower CN signals in the center for time delays around 1 to 2 μs, which was consistent with the results of the electron densities and CN excitation temperatures. Radon transform techniques can be used to create computer tomography images to evaluate CN signals but would require the spectrometer with intensified charged couple device (ICCD) to be rotated around the sample or the use of multiple spectrometers with corresponding ICCDs.

Laser-induced breakdown spectroscopy can be used an effective technique to identify CN within samples. Due to the shockwave effects causing the CN to be more concentrated towards the edges of the plasma, slit size, energy per pulse, and measurment acquisition time would need to be considered when capturing data, especially for handheld designs. The use of a 309 nm cut-on filter is an effective way to filter out unwanted atomic carbon line contribution from CN recombination spectra but causes a 10% reduction in the signal captured, which can cause issues with possible quantification of CN for medical and forensic applications. Laser-induced breakdown spectroscopy (LIBS) in conjunction with univariate analysis and partial least square regression (PSLR) [90, 91, 92, 93, 94, 95, 96] can be

used to quantify elemental content within samples. Quantification of cyanide content in gaseous and liquid mixtures would be of future interest for the application of LIBS for medical applications such as cyanide poisoning diagnosis and forensic applications such as determination of cyanide concentrations in deceased victims. Lastly, LIBS performed on other molecular compounds such as carbon monoxide are of future interest to determine the applicability of LIBS for hazardous material identification.

Bibliography

[1] P.V. Minorsky. On the inside. *Plant Physiology*, 155(1):169–170, 2011. 1

[2] R. Eisler. *Cyanide Hazards to Fish, Wildlife and Invertebrates: A Synoptic Review*. Biological Report (Contaminant Hazards Review) 85 (1.23). U.S. Fish and Wildlife Service: Washington DC, United States of America, 1991. 1

[3] B.A. Logue, D.M. Hinkens, S.I. Baskin, and G.A. Rockwood. The analysis of cyanide and its breakdown products in biological samples. *Critical Reviews in Analytical Chemistry*, 40(2):122–147, 2010. 1

[4] C.J. Knowles. Microorganisms and cyanide. *Bacteriological Review*, 40(3):652–680, 1976. 1

[5] Agency for Toxic Substances and Disease Registry (ATSDR). *Toxicological Profile for Cyanide*, 2006 (accessed June 8, 2020). 1

[6] D.S. Seigler. Plants of the northeastern united states that produce cyanogenic glycosides. *Economic Botany*, 30:395–407, 1976. 1

[7] P.A. Pieniazek, S.E. Bradforth, and A.I. Krylov. Spectroscopy of the cyano radical in an aqeuous environment. *The Journal of Physical Chemistry A*, 110(14):4854–4865, 2006. 1

[8] Centers for Disease Control and Prevention (CDC). *Facts About Cyanide*, 2018 (accessed June 8, 2020). 1

[9] T. Mudder, M. Botz, and A. Smith. *Chemistry and Treatment of Cyanidation Wastes*. Second Edition. Mining Journal Books: London, United Kingdom, 2001. 1

[10] T.I. Mudder and M.M Botz. Cyanide and soceity: A critical review. *The European Journal of Mineral Processing and Environmental Protection*, 4:62–74, 2004. 1

[11] N. Gupta, C. Balomajumder, and V. K. Agarwal. Enzymatic mechanism and biochemistry for cyanide degradation: A review. *Journal of Hazardous Materials*, 176(1-3):1–13, 2010. 1

[12] C. Stewart. *Cyanide as a Chemical Weapon: a Review*, 2010 (accessed June 8, 2020). 1

[13] S.I. Baskin, J.B. Kelly, B.I. Maliner, G.A. Rockwood, and C.K. Zoltani. *Cyanide Poisoning in: S.D. Turonisky (Ed.) Medical Aspects of Chemical Warfare*, pages 371–410. Office of the Surgeon General, Department of the Army, United States of America, Falls Church, Virginia, 2008. 1

[14] S.I. Baskin and T. Brewer. *Cyanide Poisoning in: F. Sidell, E. Takafuji, D. Franz (Eds.), Medical Aspects of Chemical and Biological Warfare*, pages 271–286. Office of the Surgeon General, Department of the Army, United States of America, Falls Church, Virginia, 1997. 1

[15] F. Moriya and Y. Hashimoto. Potential for error when assessing blood cyanide concentrations in fire victims. *Journal of Forensic Sciences*, 46(6):1421–1425, 2001. 1

[16] K.W. Fent, D.E. Evans, K. Babik, C. Striley, S. Bertke, S. Kerber, D. Smith, and G.P. Horn. Airborne contaminants during controlled residential fires. *Journal of Occupational Environmental Hygiene*, 15(5):399–412, 2018. 1

[17] K. Anseeuw, N. Delvau, G. Burillo-Putze, F. De Iaco, G. Geldner, P. Holmström, Y. Lambert, and M. Sabbe. Cyanide poisoning by fire smoke inhalation: A european expert consensus. *European Journal of Emergency Medicine*, 20(1):2–9, 2013. 2

[18] A.H. Hall, B.H. Rumack, M.I. Schaffer, and C.H. Linden. *Clinical Toxicology of Cyanide: North American Clinical Experiences in: B. Ballantyne, T.C. Marrs (Eds.), Clinical and Experimental Toxicology of Cyanides*, pages 312–333. Wright, 1987. 2

[19] F.J. Baud. Cyanide: Critical issues in diagnosis and treatment. *Human and Experimental Toxicology*, 26(3):191–201, 2007. 2

[20] F.L. Rodkey and H.A. Collison. Determination of cyanide and nitroprusside in blood and plasma. *Clinical Chemsitry*, 23(11):1969–1975, 1977. 2

[21] P. Lundquist, H. Rosling, and B. Sorbo. Determination of cyanide in whole blood, erthrocytes, and plasma. *Clinical Chemsitry*, 31(4):591–595, 1985. 2

[22] R. Jackson and B. Logue. A review of rapid and field-portable analytical techniques for the diagnosis of cyanide exposure. *Analytica Chimica Acta*, 960:18–19, 2017. 2, 3

[23] B. Ballantyne and T. Marrs. *Post-Mortem Features and Criteria for the Diagnosis of Acute Lethal Cyanide Poisoning in: B. Ballantyne, T.C. Marrs (Eds.), Clinical and Experimental Toxicology of Cyanides*, pages 217–247. Wright, 1987. 2

[24] Y. Alarie. Toxicity of fire smoke. *Critical Reviews in Toxicology*, 32(4):259–289, 2002. 2

[25] F.J. Baud, P. Barriot, V. Toffis, B. Riou, E. Vicaut, Y. Lecarpentier, R. Bourdon, A. Astier, and C. Bismuth. Elevated blood cyanide concentrations in victims of smoke inhalation. *New England Journal of Medicine*, 325(25):1761–1766, 1991. 2

[26] F.J. Baud, B. Megarbane, H. Trout, F. Lapostolle, E. Vicaut, M. Debray, and C. Bismuth. Value of lactic acidosis in the assessment of the severity of acute cyanide poisoning. *Critical Care Medicine*, 30(9):2044–2050, 2002. 2

[27] T. Meredith, D. Jacobsen, J. Haines, and Berger J.C. *Antidotes to poisoning by cyanide in: T. Meredith, D. Jacobsen, J. Haines, J.C. Berger (Eds.), IPCS/CEC evaluation of antidotes series*, pages 1–26. Cambridge University Press: Cambridge, United Kingdom, 1992. 2

[28] S.I. Baskin, A.M. Horowitz, and E.W. Nealley. The antidotal action of sodium nitrite and sodium thiosulfate against cyanide poisoning. *Journal of Clinical Pharmacology*, 32(4):368–375, 1992. 2

[29] J. Ma and P.K. Dasgupta. Recent developments in cyanide detection: A review. *Analytica Chimica Acta*, 673(2):117–125, 2010. 2

[30] R. Noll. *Laser-Induced Breakdown Spectroscopy Fundamentals and Applications*. Springer, Heidelberg, Berlin, 2012. 3

[31] D. Hahn and N. Omenetto. Laser-induced breakdown spectroscopy (libs) part ii: Review of instrumental and methodological approaches to material analysis and applications to different fields. *Applied Spectroscopy*, 66(4):347–419, 2012. 3

[32] A. Pochon, A. Desaulty, and Bailly L. Handheld laser-induced breakdown spectroscopy (libs) as a fast and easy method to trace gold. *Journal of Analytical Atomic Spectrometry*, 35:254–264, 2020. 3

[33] R.A. Crocombe. Portable spectroscopy. *Applied Spectroscopy*, 72(12):1701–1751, 2018. 3

[34] Y. Foucaud, C. Fabre, B. Demeusy, I.V. Filippova, and L.O. Filippov. Optimisation of fast quantification of fluorine content using handheld laser induced breakdown spectroscopy. *Spectrochimica Acta Part B: Atomic Spectroscopy*, 158:105628, 2019. 3

[35] B.T Manard, M.F. Schappert, E.M. Wylie, and G.E. McMath. Investigation of handheld laser induced breakdown spectroscopy (hh libs) for the analysis of beryllium on swipe surfaces. *Analytical Methods*, 11(6):752–759, 2019. 3

[36] F.R. Doucet, G. Lithgow, R. Kosierb, P. Bouchard, and M. Sabsabi. Determination of isotope ratios using laser-induced breakdown spectroscopy in ambient air at atmospheric pressure for nuclear forensics. *Analytical Methods*, 26(3):536–541, 2011. 3

[37] D.D. Arslanov, M.P.P. Castro, N.A. Creemers, A.H. Neerincx, M. Spunei, J. Mandon, S.M. Cristescu, P. Merkus, and F.J.M. Harren. Optical parametric oscillator-based photoacoustic detection of hydrogen cyanide for biomedical applications. *Journal of Biomedical Optics*, 18(10):107002, 2013. 3

[38] A. Surleva, R. Gradinaru, and G. Drochioiu. Cyanide poisoning: From physiology to forensic analytical chemistry. *International Journal of Criminial Investigation*, 2(2):79–101, 2012. 3

[39] J.L. McAllister, R.J. Roby, B. Levine, and D. Purser. Stability of cyanide in cadavers and in postmortem stored tissue specimens: A review. *Journal of Analytical Toxicology*, 32(8):612–620, 2008. 3

[40] S.B. Peddy, M.R. Rigby, and D.H. Shaffner. Acute cyanide poisoning. *Pediatric Critical Care Medicine*, 7(1):79–82, 2006. 3

[41] S.Y. Li, I. Petrikovics, and J. Yu. The potential use of 2-aminothiazoline-4-carboxylic acid (atca) as a forensic marker for cyanide exposure in medicolegal death investigation: A review. *Forensic Science Review*, 31(1):45–58, 2019. 3

[42] A. Einstein. Zur quantentheorie der strahlung. *Physikalisch Zeitschrift*, 18:121–128, 1917. 3

[43] W. Steen. *Laser Material Processing*. Springer, 1998. 4

[44] F. Brech and L. Cross. Optical microemission stimulated by a ruby laser. *Applied Spectroscopy*, 16(2):59, 1962. 4

[45] E.F. Runge, R.W. Minck, and Bryan F.R. Spectrochemical analysis using a pulsed laser source. *Spectroachimica Acta*, 20:733–736, 1964. 4

[46] T. Keyata, H. Tiedje, and R. Fedosejevs. Application of laser induced breakdown spectroscopy (libs) for detection of lead contaminants in water using wood sample substrates. *2016 IEEE International Conference on Plasma Science (ICOPS), Banff, Alberta, Canada June 19-23, 2016*, page 1. 4

[47] F.C. De Lucia Jr., A.C. Samuels, R.S. Harmon, R.A. Walters, K.L. McNesby, A. LaPointe, R.J. Winkel Jr., and A.W. Miziolek. Laser-induced breakdown spectroscopy (libs): A promising versatile chemical sensor technology for hazardous material detection. *IEEE Sensors Journal*, 5:681–689, 2005. 4

[48] A.C. Samuels, F.C. De Lucia Jr., K.L. McNesby, and A.W. Miziolek. Laser-induced breakdown spectrsocopy of bacterial spores, mold, pollens and protein: initial studies of discrimination potential. *Applied Optics*, 42:6205–6209, 2003. 4

[49] F.C. DeLucia Jr., R.S. Harmon, K.L. McNesby, R.J. Winkel Jr., and A.W. Miziolek. Laser-induced breakdown spectrsocopy analysis of energetic materials. *Applied Optics*, 42:6148–6152, 2003. 4

[50] C.A. Munson, J.L. Gottfried, E.G. Snyder, F.C. De Lucia Jr., B. Gullett, and A.W. Miziolek. Laser-induced breakdown spectrsocopy analysis of energetic materials. *Applied Optics*, 47(31):G48–G57, 2008. 4

[51] M.M. El-Deftar, N. Speers, S. Eggins, Foster S., Robertson J., and Lennard C. Assessment and forensic application of laser-induced breakdown spectroscopy (libs) for the discrimination of australian window glass. *Forensic Science International*, 241:46–54, 2014. 4

[52] A.K. Pathak, N.K. Rai, A. Singh, A.K. Rai, P.K. Rai, and P.K. Rai. Medical applications of laser induced breakdown spectroscopy. *Journal of Physics: Conference Series, XXII International Conference on Spectral Line Shapes (ICSLS), Tullahoma, Tennessee, United States of America June 1-6, 2016*, 548. 4

[53] A. Miziolek, V. Palleschi, and I. Schechte. *Laser Induced Breakdown Spectroscopy (LIBS): fundamentals and applications*. Cambridge University Press: Cambridge, United Kingdom, 2006. 4

[54] D.A Cremers and L.J. Radziemski. *Handbook of Laser-Induced Breakdown Spectroscopy*. John Wiley and Sons, Ltd: Hoboken, New Jersey, United States of America, 2006. 4, 11

[55] D.A. Rusak, B.C Castle, B.W. Smith, and J.D. Winefordner. Fundamentals and applications of laser-induced breakdown spectroscopy. *Critical Reviews in Analytical Chemistry*, 27(4):257–290, 1997. 4

[56] K. Song, Y.I. Lee, and J. Sneddon. Applications of laser-induced breakdown spectrometry (libs). *Applied Spectroscopy Reviews*, 32:183–235, 1997. 4

[57] D.A. Rusak, B.C Castle, B.W. Smith, and J.D. Winefordner. Recent trends and the future of laser-induced breakdown spectroscopy. *Trends Analytical Chemistry*, 17:453–461, 1998. 4

[58] J.D. Winefordner, I.B. Gomushkin, D. Pappas, O.I. Matveev, and B.W. Smith. Novel uses of lasers in atomic spectroscopy. *Journal of Analytical Atomic Spectrometry*, 15:1161–1189, 2000. 4

[59] J.D. Winefordner, I.B. Gomushkin, T. Correll, E. Gibb, B.W. Smith, and N. Omenetto. Comparing several atomic spectrometric methods to the super stars: special emphasis on laser induced breakdown spectrometry, libs, a future super star. *Journal of Analytical Atomic Spectrometry*, 19:1061–1083, 2004. 4

[60] B.H. Bransden and C.J. Joachain. *Physics of atoms and molecules*. Prentice Hall: New York, United States of America, 2003. 5

[61] V.N. Ochkin. *Spectroscopy of Low Temperature Plasma*. Wiley-VCH, 2009. 5

[62] G. Gautam, C.M. Helstern, K.A. Drake, and C.G. Parigger. Imaging of laser-induced plasma expansion dynamics in ambient air. *International Review of Atomic and Molecular Physics*, 7:45–51, 2016. 9, 18, 31

[63] C.G. Parigger, C.M. Helstern, and G. Gautam. Molecular emission spectroscopy of cyanide in laser-induced plasma. *International Review of Atomic and Molecular Physics*, 8:25–35, 2017. 12, 21, 29

[64] H.A. Bethe, K. Fuchs, J.O. Hirschfelder, J.L. Magee, R.E. Peierls, and J. van Neumann. *Blastwave*. Los Alamos Scientific Laboratory, University of California: Los Alamos, New Mexico, United States of America, 1947. 17

[65] G.I. Taylor. The formation of a blast wave by a very intense explosion i. theoretical discussion. *Proceedings of the Royal Society A: Mathematical, Physical and Engineering Sciences*, 201:159–174, 1950. 17

[66] L.I. Sedov. *Similarity and Dimensional Methods in Mechanics*. Academic Press: Cambridge, Massachusetts, United States of America, 1959. 17

[67] L.I. Sedov. Propagation of strong blast waves. *Prikladnaya Matematika i Mekhanika (Appl. Math. Mech. Leningrad)*, 10:241–250, 1946. 17

[68] M.A. Harith, V. Palleschi, A. Salvetti, D.P. Singh, G. Tropiano, and M. Vaselli. Hydrodynamic evolution of laser driven diverging shock waves. *Laser and Particle Beams*, 8(1):247–252, 1990. 18

[69] C.G. Parigger, C.M. Helstern, and G. Gautum. Temporally and spatially resolved emission spectroscopy of cyanide, hydrogen, and carbon in laser-induced plasma. *MDPI*, 7(3):74, 2019. 21, 29, 152

[70] C.G. Parigger, C.M. Helstern, B.S. Jordan, D.M. Surmick, and R. Splinter. Laser-plasma spatio-temporal cyanide spectroscopy and applications. *Molecules*, 25(3):615, 2020. 21, 29, 31

[71] C.M. Helstern, Parigger C.G., B.S. Jordan, D.M. Surmick, and R. Splinter. Hypersonic laser-plasma expansion measurements with cyanide spectroscopy. *International Review of Atomic and Molecular Physics*, 10(1):7–15, 2019. 21, 29, 31

[72] M. Dackman. *Laser-Induced Breakdown Spectroscopy for Analysis of High-Density Methane-Oxygen Mixtures*. Master's Thesis, University of Tennessee Knoxville: Knoxville, Tennessee, United States of America, 2014. 24

[73] H.R. Griem. *Spectral Line Broadening by Plasmas*. Academic Press: New York, New York, United States of America, 1974. 24

[74] D.M. Surmick. *Spectroscopic Imaging of Aluminum Containing Plasma*. PhD Dissertation, University of Tennessee Knoxville: Knoxville, Tennessee, United States of America, 2016. 24, 27, 132

[75] O'Haver T. *peakfit.m, MATLAB Central File Exchange*, 2019 (accessed May 22, 2019). 25, 65, 70, 141

[76] C.G. Parigger and J.O. Hornkohl. *Quantum Mechanics of the Diatomic Molecule with Applications*. IOP Publishing: Bristol, United Kingdom, 2019. 27

[77] C.G. Parigger, A.C. Woods, D.M. Surmick, G. Gautam, M.J. Witte, and Honrkohl J.O. Computation of diaotmic molecular spectra for selected transitions of aluminum

monoxide, cyanide, diatomic carbon, and titanium monoxide. *Spectrochimica Acta Part B: Atomic Spectroscopy*, 107:132–138, 2015. 27

[78] J.A. Nelder and R. Mead. A simplex method for function minimization. *The Computer Journal*, 7(4):308–313, 1965. 27

[79] G. Pretzler. A new method for numerical abel-inversion. *Zeitschrift für Naturforschung A*, 46(7):639–641, 1991. 29, 31

[80] G. Pretzler, H. Jaeger, T. Neger, H. Philipp, and J. Woisetschläger. Comparison of different methods of abel inversion using computer simulated and experimental side-on data. *Zeitschrift für Naturforschung A*, 47(9):955–970, 1992. 29, 31

[81] Y.P. Kandel. *An experimental study of Hydrogen Balmer Lines in pulsed laser plasma*. PhD Dissertation, Wesleyan Univeristy: Middletown, Connecticut, United States of America, 2009. 29

[82] I.B. Gornushkin, S.V. Shabanov, and U. Panne. Abel inversion applied to a transient laser induced plasma: implications from plasma modeling. *Journal of Analytical Atomic Spectrometry*, 26(7):1457–1465, 2011. 29

[83] C. Killer. *Abel Inversion Algorithm, MATLAB Central File Exchange*, 2019 (accessed June 30, 2019). 29, 31

[84] C.G. Parigger, G. Gautam, and D.M. Surmick. Radial electron density measurements in laser-induced plasma from abel inverted hydrogen balmer beta line profiles. *International Review of Atomic and Molecular Physics*, 6:43–57, 2015. 29, 31

[85] G. Gautum, C.G. Parigger, C.M. Helstern, and K.A. Drake. Emission spectroscopy of expanding laser-induced gaseous hydrogen-nitrogen plasma. *Applied Optics*, 56(33):9277–9284, 2017. 29, 31

[86] G. Gautum. *On Laser-induced Plasma Containing Hydrogen*. PhD Dissertation, University of Tennessee Knoxville: Knoxville, Tennessee, United States of America, 2017. 29, 31

[87] C.G. Parigger, D.M. Surmick, and G Gautam. Self-absorption characteristics of measured laser-induced plasma line shapes. *Journal of Physics: Conference Series*, 810, 2017. 29, 31

[88] M. Thiyagarajan and J.E. Scharer. Experimental investigation of 193-nm laser breakdown in air. *IEEE Transactions on Plasma Science*, 36(5):2512–2521, 2008. 31

[89] H. Sobral, M. Villagrán-Muniz, R. Navarro-González, and A.C. Raga. Temporal evolution of the shock wave and hot core air in laser induced plasma. *Applied Physics Letters*, 77(20):3158–3160, 2000. 31

[90] N.B. Zorov, A.M. Popov, S.M. Zaystev, and T.A. Labutin. Qualitative and quantitative analysis of environmental samples by laser-induced breakdown spectrometry. *Russian Chemical Reviews*, 84:1021–1050, 2015. 117

[91] F. Liu, L. Ye, J. Peng, K. Song, T. Shen, and Y. Zhang, C.and He. Fast detection of copper content in rice by laser-induced breakdown spectroscopy with uni-and multivariate analysis. *Sensors*, 18:705, 2018. 117

[92] C.A. Akpovo, J.A. Martinez, D.E. Lewis, J. Branch, A. Schroeder, M.D. Edington, and L. Johnson. Regional discrimination of oysters using laser-induced breakdown spectroscopy. *Analytical Methods*, 5:3596–3968, 2013. 117

[93] E.C. Ferreira, E.A. Menezes, W.O. Matos, D.M.B.P. Milori, A.R.A. Nogueira, and L. Martin-Neto. Determination of ca in breakfast cereals by laser induced breakdown spectroscopy. *Food Control*, 21:1327–1330, 2010. 117

[94] P. Yang, R. Zhou, W. Zhang, R. Yi, S. Tang, L. Guo, Z. Hao, X. Li, Y. Lu, and X. Zeng. High-sensitivity determination of cadmium and lead in rice using laser-induced breakdown spectroscopy. *Food Chemistry*, 272:323–328, 2019. 117

[95] G. Bilge, I.H. Boyaci, K.E. Eseller, U. Tamer, and S. Cakir. Analysis of bakery products by laser-induced breakdown spectroscopy. *Food Chemistry*, 181:186–190, 2015. 117

[96] J. Peng, W. Xie, J. Jiang, Z. Zhao, F. Zhou, and F. Liu. Fast quantification of honey adulteration with laser-induced breakdown spectroscopy and chemometric methods. *Foods*, 9(3), 2020. 117

[97] B.J. McBride and S. Gordon. *Computer Program for Calculating and Fitting Thermodynamic Functions. NASA RP-1271*, 1992 (accessed May 22, 2019). 152

[98] Parigger C.G., D.M. Surmick, C.M. Helstern, G. Gautam, A.A. Bol'shakov, and R.E. Russo. *Molecular Laser-Induced Breakdown Spectroscopy in chapter 7: Laser Induced Breakdown Spectroscopy, 2nd ed., J.P. Singh, S.N. Thakur (Eds.)*, pages 167–209. Elsevier Science, Amsterdan, NL, 2020. 152

Appendices

Appendix A

Matlab NMT Fitting Routine

In this appendix, the NMT fitting routines in the Matlab scripting language are discussed. Cyanide spectra collected from the Intensified Charged Couple Device (ICCD) and processed by the Andor SOLIS software allow for the CN spectra data to be exported as DAT files. The data within these DAT files are extracted by a Matlab script and fit parameters are specified to be used in the NMT Matlab code [74].

```
% The methods of this program are based off of the private
% communications with David Surmick.
clear;

fstring = fileread('03icorr385.dat'); % read the file as one string

fblocks = regexp(fstring,'Zone I=1024 F=POINT','split'); % splits into blocks

fblocks(1) = []; % delete first row (it's empty)

data = cellfun(@(x) textscan(x, "%f %f", "CollectOutput", true), fblocks);

fID = fopen('out.dat', 'w');
```

```
for i = 1:2 %length(data)
    WL_exp = data{i}(:, 1) + .22;
    Dat = data{i}(:, 2);
    FWHM = 0.1;
    T = 3000;
    tol = 1e-8;
    x = 'CNv-LSF.txt';
    FIT = 2;
    [profile,vals] = NMT(WL_exp, Dat, FWHM, T, tol, x, FIT);

 % writes the output to file
    fprintf(fID, '%d\t%s\n', i, mat2str(vals(4)));

% saves figure
    savefig(sprintf('Figure %d.fig', i));

i
end
fclose(fID);
```

Tables of diatomic line strengths are transformed into theoretical diatomic, molecular spectra for a specific spectral resolution and temperature by the NMT program. Experimentally measured spectra are then fitted by the theoretically produced spectrum using the Nelder-Mead Algorithm, discussed in Chapter 3, where temperature and spectral resolution are used as fit parameters. The NMT Matlab code was developed by David Surmick during his doctoral work at the University of Tennessee Space Institute based on the Fortran codes developed by Jim Hornkohl at the University of Tennessee Space Institute.

```
% NMT.m
%
```

```
% Fits measured diatomic molecular spectra to theoretically calculated
% spectra. Fitting uses a Nelder Mead algorithm to fit a liner base line
% offset in addition to the temperature or temperature and fwhm, based off
% of a user input. The methods of this program are based off of the
% publication:
%     "Computation of diatomic molecular spectra for selected transitions of
%     aluminum monoxide, cyanide, diatomic carbon and titanium monoxide"
%     C.G. Parigger et al., Spectrochim. Act. B, 107, 132-138, 2015.
% as well as from private communications with James O. Hornkohl.
%
% inputs: WL_exp - exerimental wavelengths (n x 1 array)
%         Dat    - experimental spextrum (n x 1 array)
%         FWHM   - measured spectral resolution, seed for varried FWHM or
%                  fixed
%         T      - temperature seed for fitting
%         tol    - tolerance of Nelder-Mead fit
%         x      - name of line strength file for calculating theory spectra
%         FIT    - enter 1 for fitting linear offset and temperature
%                  enter 2 for fitting linear offset, temperature, and FWHM
% outputs: profile - matrix containing experimental wavelengths, measured
%                    spectrum, fitted spectrum, fitted baseline offset
%                    (n x 4 matrix)
%          vals    - array containing fitted paramters (3x1 or 4x1 array),
%                    temperature is always last entry
% sub-functions: FitSpec, FitSpec1, SynthSpec
% Example call: [I,v]=NMT(x,y1,0.15,3000,1e-8,'AlO-LSF.txt',2);
%
% David M. Surmick, 04-28-2016

function [profile,vals] = NMT (WL_exp,Dat,FWHM,T,tol,x,FIT)
```

```
tic % start code timer

% global variables
global bFac gFac WLk Tuk TuMin Sk n0 nSpec fwhm delWL temp wl_max;

% constants in mks units
h=6.62606957e-34;
c=2.99792458e8;
kb=1.3806488e-23;
bFac=(100*h*c)/kb; % Boltzmann factor in cgs units
gFac=2*sqrt(log(2));
nSpec=length(Dat);
temp=T;
fwhm=FWHM;

% get fitting range
wl_min=min(WL_exp);
wl_max=max(WL_exp);
delWL=(wl_max-wl_min)/(nSpec);

% read MatLab LSF file
[p]=load(x);
WN=p(:,1);
Tu=p(:,2);
S=p(:,3);

% convert vacuum wavenumber to air wavelength
a0=2.72643e-4;
a1=1.2288;
a2=3.555e4;
```

```
r=1+a0+(a1./(WN.*WN))+(a2./(WN.*WN.*WN.*WN));
WL=1e7./(r.*WN);

% get LSF table wavelengths in experimental range
A=find(WL>wl_min & WL<wl_max);
WLk=WL(A);

% get Term Values and LineStrengths at WLk
Sk=S(A);
Tuk=Tu(A);
TuMin=min(Tuk);

% get exerpimenal wavelength position that most closely matches Line
% Strength Table wavelength
n0=zeros(length(WLk),1);
for i=1:length(WLk)
    [~,n0(i)]=min(abs(WL_exp-WLk(i)));
end

% normalize data
%Dat=Dat/max(Dat);

% Fitting
options=optimset('TolX',tol,'MaxIter',1e8,'MaxFunEvals',1e8); % Nelder Mead Paramters
switch FIT
    case 1 % fit offset, temperature
        theta=ones(3,1);
        theta(3)=T; % temperature seed
        vals=fminsearch(@(x) FitSpec(x,WL_exp,Dat),theta,options);
        bkg=vals(1)+vals(2)*WL_exp; % calculate fitted offset
```

```
        [I,bkg1]=SynthSpec(WL_exp,vals(3),FWHM,Dat,bkg); % calculate fit
    case 2 % fit offset, fwhm, temperature
        theta=ones(4,1);
        theta(3)=FWHM; % fwhm seed
        theta(4)=T; % temperature seed
        vals=fminsearch(@(x) FitSpec1(x,WL_exp,Dat),theta,options);
        bkg=vals(1)+vals(2)*WL_exp; % calculate fitted offset
        [I,bkg1]=SynthSpec(WL_exp,vals(4),vals(3),Dat,bkg); % calculate fit
end
profile=[WL_exp Dat I bkg1];

% Visualize Fit
fname=regexprep(x,'-LSF.txt','-FIT:');
figure
switch FIT
    case 1
        plot(WL_exp,Dat,WL_exp,I,WL_exp,bkg1)
        legend('Experiment','Fit','BaseLine')
        title([num2str(fname),'T=',num2str(vals(3)),'K ,FWHM=',num2str(FWHM),'nm'])
        xlabel('Wavelength (nm)')
        ylabel('Scaled Intensity (a.u.)')
    case 2
        plot(WL_exp,Dat,WL_exp,I,WL_exp,bkg1)
        legend('Experiment','Fit','BaseLine')
        title([num2str(fname),'T=',num2str(vals(4)),'K ,FWHM=',num2str(vals(3)),'nm'])
        xlabel('Wavelength (nm)')
        ylabel('Scaled Intensity (a.u.)')
end

toc % end code timer
```

```
end % main function

% temperature, offset fit function
function [err] = FitSpec (p,WL_exp,Dat)

global fwhm

bkg=p(1)+p(2)*WL_exp;
[F,~]=SynthSpec(WL_exp,p(3),fwhm,Dat,bkg);
c=F\Dat;
z=F*c;
err=norm(z-Dat);

end % fit spec

% temperature, fwhm, offset fit function
function [err] = FitSpec1 (p,WL_exp,Dat)

bkg=p(1)+p(2)*WL_exp;
[F,~]=SynthSpec(WL_exp,p(4),p(3),Dat,bkg);
c=F\Dat;
z=F*c;
err=norm(z-Dat);

end % fit spec 1

% calculate synthetic spectrum for fit
function [I1,bkg1] = SynthSpec (WL_exp,T,FWHM,Dat,bkg)
```

```
global bFac gFac WLk Tuk TuMin Sk n0 nSpec delWL wl_max ;

FWHMk=(FWHM*WLk)/wl_max; % wavelength dependent FWHM

% Calculate Peak Intensities
peak=20-4*log(WLk)+log(Sk)-(bFac/T)*(Tuk-TuMin);
peak_k=exp(peak);

% calculate syntehtic spectrum
I=zeros(nSpec,1); % initialize synthetic spectrum output
for i=1:length(WLk)
    deln=round(2.5*FWHMk(i)/delWL);
    nMin=n0(i)-deln;
    if nMin < 1
        nMin=1;
    end
    nMax=n0(i)+deln;
    if nMax > nSpec
        nMax=nSpec;
    end
    for j=nMin:nMax
        u=abs(gFac*(WLk(i)-WL_exp(j))/FWHMk(i));
        I(j)=I(j)+peak_k(i)*exp(-u*u);
    end
end % synthetic spectrum loop

% normailze data to measured spectrum
I=I/max(I);
I=I+bkg;
sxy=sum(Dat.*I);
```

```
syy=sum(I.*I);
nf= sxy/syy;
I1=I*nf;
bkg1=bkg*nf;

end % SynthSpec
```

Appendix B

Matlab Peak Fitting Routine

The program shows the procedure followed for the peak fitting of cyanide spectra to determine the full width at half-maximum and peak locations. As in appendix A, the data from DAT files are extracted and fit parameters are specified to be used in the peak fitting Matlab script [75]. Of specific interest is the full width at half maximum and peak location of the (2,2) CN violet band head of 386.19 nm.

```
clear;

fstring = fileread('01icorr385.dat'); % read the file as one string

fblocks = regexp(fstring,'Zone I=1024 F=POINT','split'); % splits into blocks
fblocks(1) = []; % delete first row (it's empty)
data = cellfun(@(x) textscan(x, "%f %f", "CollectOutput", true), fblocks);

fID = fopen('out.dat', 'w');

for i = 1:length(data)
    % Stores output of peakfit

      [FitResults,FitError] = peakfitNOplots(data{i}, 386, 10, 5, 2);
```

```
    % writes the output to file
    fprintf(fID, '%d: %s\n', i, mat2str(FitResults));

    % saves figure
    savefig(sprintf('Figure %d.fig', i));



    i
end

fclose(fID);
```

Appendix C

Matlab Abel Inversion

The code for the Abel inversion for the symmetric profiles is shown in this section. Each one of the 1024 wavelengths are used for the creation of lateral profiles, where two points are averaged from the top and bottom side of the central point of the lateral profiles to produce the symmetric profile. Application of the Abel inversion to the symmetrized profiles allows for radial information to be extracted as described in Chapter 3.

```
function [ f_rec , X ] = abel_inversion(h,R,upf,plot_results,lsq_solve)
upfin=10;
nspectra=256;
nwavel=1001;
midpoint=138;
npoints=64;
ninvertedspectra=2*npoints-1;
dr=1024./nspectra*13.6/1000.;
R=npoints*dr;                          % radius
X=(0:dr:R-dr)';          % spatial coordinates
ndim=length(X);
nsymmetric=1; %=1 for symmetric, =0 for asymmetric
nfilestart=1;
nfileend=21;
```

```
nlambda(1)=385;
nlambda(2)=490;
nlambda(3)=438;
nlambda(4)=414;
for i=1:1
nlam=nlambda(i)
for nfile=nfilestart:nfileend%:13
fnamein=sprintf('%02dabelc%03d.dat',nfile,nlam);

if nsymmetric == 1
    fnameout=sprintf('%02dabelc%03d_symmetric.dat',nfile,nlam);
    fnameout3D=sprintf('%02dabelc%03d_symmetric3D.dat',nfile,nlam);
else
    fnameout=sprintf('%02dabelc%03d_asymmetric.dat',nfile,nlam);
    fnameout3D=sprintf('%02dabelc%03d_asymmetric3D.dat',nfile,nlam);
end
fileID=fopen(fnamein,'r');%'08abelc.dat','r');
tline=fgetl(fileID);
formatSpec='%f %f %f';
sizeDor=[3 Inf];
D=fscanf(fileID,formatSpec,sizeDor);
fclose(fileID);
D=D';
L=D(:,[1]);
Warr=L(1:nwavel);%L(1:1001);
H=D(:,[2]);
Val =D(:,[3]);
for j=1:nspectra %256
    for i=1:nwavel %1001
       Arr(i,j)=Val(i+1001*(j-1));
```

```
    end
end
Arr=Arr';

yarr=zeros(length(X),1);
garrR=zeros(length(X),1);
garrL=zeros(length(X),1);
f_rec_l=zeros(length(X),1);
f_rec_r=zeros(length(X),1);

%jwave=86;
for jwave=1:1001
    for k=1:ndim
        yarr0(k,1)=1./2.*(Arr(k-1+midpoint,jwave)+Arr(midpoint-k+1,jwave));
        if (yarr0(k,1) < 0.0001)
            yarr0(k,1)=0.0001;
        end
        garrR(k,1)=Arr(k-1+midpoint,jwave);%/yarr0(k,1);
        garrL(k,1)=Arr(midpoint-k+1,jwave);%/yarr0(k,1);
    end
garrL=garrL.\yarr0;
garrR=garrR.\yarr0;
for c=1:length(X)
 h(c,1)=yarr0(c,1);%Arr(c+66,jwave);
end
%
if ~exist('h', 'var') || isempty(h)
    [X,h,R]=generate_test_data;
    plot_results=1;
else
```

```
    plot_results=0;
    X=linspace(0,R-0.1,length(h))';
end

% default value for number of expansion elements
if ~exist('upf', 'var'); upf=upfin; end;

% avoiding problems if flags are not given in input
if ~exist('plot_results', 'var'); plot_results=0; end;
if ~exist('lsq_solve', 'var'); lsq_solve=0; end;

[fn,hn] = compute_expansion( X,upf,R );

if lsq_solve ~= 1

    B = zeros(1,upf+1); L = zeros(upf+1,upf+1);  %create arrays

    for k=1:upf+1

        for l=1:upf+1
            L(l,k)=2.*sum(hn(:,k).*hn(:,l));
        end

        B(k)=sum(h(:).*hn(:,k));
    end

    A=B/L;

else

    x0=1*ones(upf+1,1);       % guess some initial values for optimisation
```

```
    A=solve_lsq(h,hn,x0);     % solve for amplitudes A
end

% create vector for resulting reconstructed distribution
f_rec=zeros(length(h),1);

% special case for n=0 (where f_0(r) = 1)
f_rec = f_rec + A(1)*1;

% iterate eq. (1) for n=1:upf
for c=1:upf+1
    f_rec = f_rec + A(c).*fn(:,c);
end

for c=1:ndim
    f_rec_r(c,1)=f_rec(c,1)*garrR(c,1);
    f_rec_l(ndim-c+1,1)=f_rec(c,1)*garrL(c,1);
end

for c=1:ndim
     f_rec_all(c,1)=f_rec_l(c,1);
     h_all(c,1)=h(ndim-c+1,1);
     x_all(c,1)=-X(ndim-c+1);
     f_rec_all(ndim+c-1,1)=f_rec_r(c,1);
     h_all(ndim+c-1,1)=h(c,1);
     x_all(ndim+c-1,1)=X(c,1);
     g_all(ndim+c-1,1)=garrR(c,1);
     g_all(c,1)=garrL(ndim-c+1,1);
     inp_all(ndim-c+1,1)=garrR(c,1)*yarr0(c,1);
     inp_all(ndim+c-1,1)=garrL(c,1)*yarr0(c,1);
     f_rec_sym(ndim+c-1,1)=f_rec(c,1);
```

```
     f_rec_sym(ndim-c+1,1)=f_rec(c,1);
end

%jwave loop
fileID=fopen(fnameout,'a');%'08abelc_symmetric.dat','a');
if nsymmetric == 1
    fprintf(fileID,'%f %f ',Warr(jwave),f_rec_sym);
else
    fprintf(fileID,'%f %f ',Warr(jwave),f_rec_all);
end
fprintf(fileID,'\n');
fclose(fileID);

if plot_results==1
    figure; % normalized profiles for better comparison
    set(gca,'linewidth',1.5,'fontsize',16);
    plot(x_all,f_rec_all,'g','Linewidth',1.5);
    hold on; plot(x_all,inp_all,'r','Linewidth',1.5);
    grid on; box on;
    title(sprintf('number of cos-expansions: %i',upf))
    legend('Abel reconstructed profile','measured profile','Location','South')

    figure; % normalized profiles for better comparison
    set(gca,'linewidth',1.5,'fontsize',16);
    plot(x_all,f_rec_sym,'g','Linewidth',1.5);
    hold on; plot(x_all,h_all,'k','Linewidth',1.5);
    grid on; box on;
    title(sprintf('wavelength position: %i',jwave))
    legend('Abel reconstructed profile','symmetrized profile','Location','South')
```

```
%    figure; % normalized profiles for better comparison
%    set(gca,'linewidth',1.5,'fontsize',16)
%    plot(-X,garrL,'m','Linewidth',1.5);
%    hold on; plot(X,garrR,'c','Linewidth',1.5);
%    grid on; box on;
%    title(sprintf('number of cos-expansions: %i',upf))
%    legend('Garray Left','Garray right','Location','South')
end

end
%prepare for 3D plot of Abel-inverted data
fileID=fopen(fnameout,'r');
formats='%f';
%ndim=56;
jspectra=(ndim-1)*2+1;
%nwavel=1001;
sizeResult=[jspectra+1 nwavel];
Result=fscanf(fileID,formats,sizeResult);
fclose(fileID)
Result=Result';
fileID3D=fopen(fnameout3D,'a')
fprintf(fileID3D,'Zone f=point i=%d j=%d\n',nwavel,jspectra);
      for jdummy=2:jspectra+1
        wave=Result(:,[1]);
        waveout=wave(1:nwavel);
        waveout=waveout';
        spectrum=Result(:,[jdummy]);
        spectrumout=spectrum(1:nwavel);
        spectrumout=spectrumout';
        for iout=1:nwavel
            x=waveout(iout);
```

```
            y=(jdummy-(ndim+1))*dr;
            z=spectrumout(iout);
            fprintf(fileID3D,'%f %f %f \n',x,y,z);
            %fprintf(fileID3D,'\n');
        end
      end
fclose(fileID3D);
end
end

%convert tecplot3D to Origin3D

ninvertedspectra=2*npoints-1;
for nfile=nfilestart:nfileend
if nsymmetric == 1
    fnameinorigin=sprintf('%02dabelc%03d_symmetric3D.dat',nfile,nlam);
    fout3Dorigin=sprintf('%02dabelc%03d_symmetric3Dorigin.dat',nfile,nlam);
else
    fnameinorigin=sprintf('%02dabelc%03d_asymmetric3D.dat',nfile,nlam);
    fout3Dorigin=sprintf('%02dabelc%03d_asymmetric3Dorigin.dat',nfile,nlam);
end
%fnamein=sprintf('%02dabelc385_symmetric.dat',nfile);

fileIDorigin=fopen(fnameinorigin,'r');
tline=fgetl(fileIDorigin);
formatSpec='%f %f %f';
sizeDor=[3 Inf];
Dor=fscanf(fileIDorigin,formatSpec,sizeDor);
fclose(fileIDorigin);
Dor=Dor';
```

```
Lor=Dor(:,[1]);
Warror=Lor(1:nwavel);%L(1:1001);
Hor=Dor(:,[2]);
Valor =Dor(:,[3]);
for j=1:ninvertedspectra %256
    for i=1:nwavel %1001
       Arror(i+1,j+1)=Valor(i+1001*(j-1));
    end
end
%Arr=Arr';
Arrorr(1:1)=0;
for i=1:nwavel
    Arror(i+1,1)=Warror(i);
end
for j=1:ninvertedspectra
    Arror(1,j+1)=j*dr-ninvertedspectra/2*dr;
end
%Arr=Arr';
fileID3Dor=fopen(fout3Dorigin,'a');
for i=1:ninvertedspectra+1
    Lineor = Arror(:,[i]);
    Lineor=Lineor';
    fprintf(fileID3Dor,' %f',Lineor(1:nwavel+1));
    fprintf(fileID3Dor,' \n',' ');
end
fclose(fileID3Dor);
end
```

Appendix D

Chemical Equilibrium with Applications (CEA)

Chemical equilibirum compositions and properties of complex mixtures can be calculated using the NASA program CEA (Chemical Equilibrium with Applications) [97]. Using the CEA code, CN mass fractions versus temperature can be determined for air at 1 atm and for a 1:1 mole ratio CO_2:N_2 at 1 atm as seen in Figures D.1 and D.2 [69]. Figures D.1 and D.2 show CN has a maximum temperature near 7 kK for the 1:1 mole ratio CO_2:N_2 at 1 atm and fractions in air are approximately three orders of magnitude lower than in the CN mixture. In addition to CN the CEA code also computes a range of species that are included for completeness [69, 98] as seen in Figure D.3: C, C^+, C^-, CN+, CN-, CNN, CO, CO+, CO_2, CO_2^+, C_2, C_2+, C_2-, CCN, CNC, C_2O, C_3, N, N^+, N^-, NCO, NO, NO^+, NO_2, N_2, N_2^+, N_2^-, NCN, N_2O, N_3, O, O^+, O^-, O_2, and O_2^+ [69].

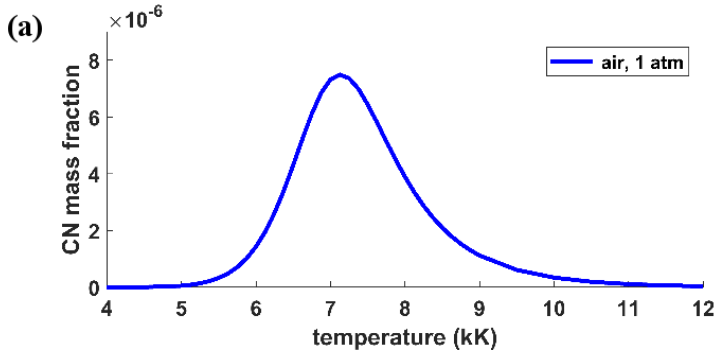

Figure D.1: CN air at 1 atm versus temperature in chemical equilibirum.

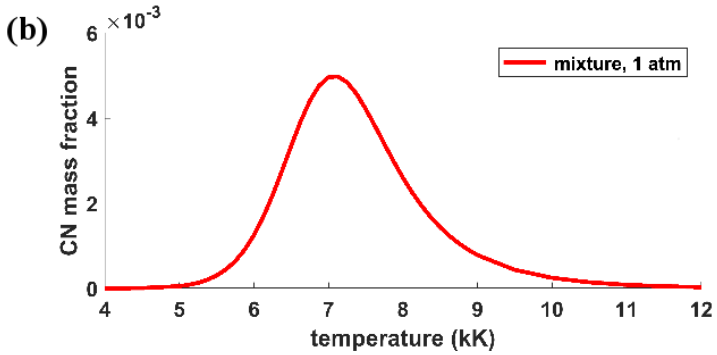

Figure D.2: CN 1:1 mole ratio CO_2:N_2 mixture at 1 atm versus temperature in chemical equilibirum.

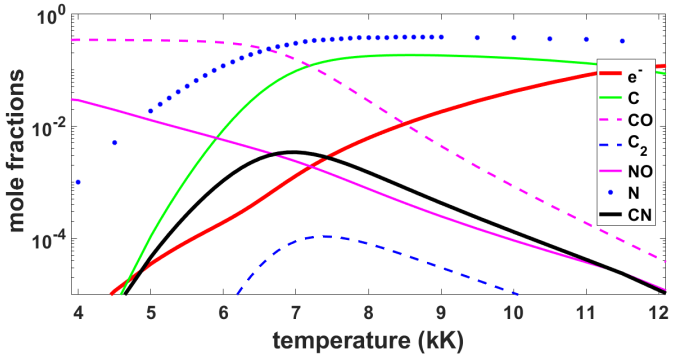

Figure D.3: Computed mole fractions of serveral species versus temperature for CN 1:1 mole ratio CO_2:N_2 mixture at 1 atm in chemical equilibirum.

Appendix E

Publications and Presentations

Publications: Peer Reviewed

1. C. G. Parigger, C. M. Helstern, B.S. Jordan, D. M. Surmick, and R. Splinter. Laser-Plasma Spectroscopy of Hydroxyl with Applications. Molecules 2020, 25(4), 988; https://doi.org/10.3390/molecules25040988

2. C. G. Parigger, C. M. Helstern, B.S. Jordan, D. M. Surmick, and R. Splinter. Laser-Plasma Spatio-Temporal Cyanide Spectroscopy and Applications. Molecules 2020, 25(3), 615; https://doi.org/10.3390/molecules25030615

3. C. M. Helstern and C. G. Parigger, B.S. Jordan, D. M. Surmick, and R. Splinter. Hypersonic Laser-Plasma Expansion Measurements with Cyanide Spectroscopy. Int. Rev. At. Mol. Phys. 2019, 10(1), 7-15; http://www.auburn.edu/academic/cosam/departments/physics/iramp/

4. C. G. Parigger, C. M. Helstern, and G. Gautum. Temporally and Spatially Resolved Emission Spectroscopy of Cyanide, Hydrogen, and Carbon in Laser-Induced Plasma. Atoms 2019, 7(3), 74; https://doi.org/10.3390/atoms7030074

5. C. G. Parigger, C. M. Helstern, and G. Gautum. Laser-Plasma and Self-Absorption Measurements with Applications to Analysis of Atomic and Molecular Stellar Astrophysics Spectra. Atoms 2019, 7(3), 63; https://doi.org/10.3390/atoms7030063

6. C. M. Helstern and C. G. Parigger. Time-Resolved Plasma Spectroscopy of Diatomic Molecular Cyanide. IOP J. Phys.: Conf. Ser. 2019; 1289 012016; https://doi.org/10.1088/1742-6596/1289/1/012016

7. C. G. Parigger, C. M. Helstern, G. Gautum, and K. A. Drake. Atomic and Molecular Spectral Line Shapes in Laboratory and Selected Astrophysical Plasma. IOP J. phys.: Conf. Ser.; 1289(2019) 012001; https://doi.org/10.1088/1742-6596/1289/1/012001

8. C. G. Parigger, K. A. Drake, C. M. Helstern, and G. Gautam. Laboratory Hydrogen-Beta Emission Spectroscopy for Analysis of Astrophysical White Dwarf Spectra. Atoms 2018, 6(3), 36; https://doi.org/10.3390/atoms6030036

9. C. G. Parigger, C. M. Helstern, K. A. Drake, and G. Gautam. Balmer-Series Hydrogen-Beta Line Dip-Shifts for Electron Density Measurements. Int. Rev. At. Mol. Phys. 2017, 8, 53-61; https://www.auburn.edu/cosam/departments/physics/iramp/8_2/parigger_et_al.pdf

10. C. G. Parigger, C. M. Helstern, and G. Gautam. Molecular Emission Spectroscopy of Cyanide in Laser-induced Plasma. Int. Rev. At. Mol. Phy. 2017, 8(1), 25-35; https://www.auburn.edu/cosam/departments/physics/iramp/8_1/Parigger%20et%20al.pdf

11. G. Gautum, C. G. Parigger, C. M. Helstern, and K. A. Drake. Emission Spectroscopy of Expanding Laser-Induced Gaseous Hydrogen-Nitrogen Plasma. Applied Optics. 2017, 56(33), 9277-9284; https://doi.org/10.1364/AO.56.009277

12. G. Gautum, C. M. Helstern, K. A. Drake, and C. G. Parigger. Imaging of Laser-induced Plasma Expansion Dynamics in Ambient Air. Int. Rev. At. Mol. Phy. 2016, 7(1), 45-51; https://www.auburn.edu/cosam/departments/physics/iramp/7_1/gautam_et_al.pdf

Book Chapters

1. C. G. Parigger, D. M. Surmick, C. M. Helstern, G. Gautam, A. A. Bol'shakov and R. E. Russo, "Molecular Laser-Induced Breakdown Spectroscopy," In: Laser Induced Breakdown Spectroscopy, 2nd ed., J.P. Singh, S.N. Thakur (Eds.), Elsevier Science, Amsterdam, NL, 2020, Ch.7, 167-209

Publications: Accepted and in Press

1. C. G. Parigger, C. M. Helstern, B.S. Jordan, D. M. Surmick, and R. Splinter. Cyanide Spectroscopy in Laser-Induced Plasma. Int. Rev. At. Mol. Phys. 2020, (in press)

2. C. G. Parigger, G. Gautum, and C. M. Helstern. Time-Resolved Spectroscopy of Atomic and Molecular Species in Laser-Induced Plasma. Preprints 2018, 2018070324 (in press)

Conference Proceedings

1. C. G. Parigger, C. M. Helstern, and G. Gautum. "Laser Spectroscopy: Selected Medical and Astrophysical Applications," 1st International Conference on Particles, Materials and Energy: Advanced Medical and Industrial Applications, Luxor, Egypt, December 2-8, 2018, Book of Abstracts 1st FICPME, p. 5.

2. C. M. Helstern and C. G. Parigger. "Applications of Laser-Induced Breakdown Spectroscopy for Diatomic Cyanide Measurements," Federation of Analytical Chemistry and Spectroscopy Societies (FACSS): The Great Scientific Exchange (SCIX2018), Technical Program, Atlanta, GA, USA, October 21-26, 2018; https://www.scixconference.org/program/archive-search?paperid=9828

3. C. G. Parigger, G. Gautam, C. M. Helstern, and K. A. Drake, "Electron Density and Temperature Distribution in Expanding Laser-Induced Plasma," 9th Euro-Mediterranean Symposium on Laser-Induced Breakdown Spectroscopy (EMSLIBS 2017), Proceedings Booklet, Pisa, Italy, (June 11 - 16, 2017); http://www.emslibs.org/

Invited Presentations

1. C. G. Parigger, C. M. Helstern, G. Gautam, and A.M. EL Sherbini, "Laser Spectroscopy: Selected Medical and Astrophysical Applications," 1st International Conference on Particles, Materials and Energy: Advanced Medical and Industrial Applications, Invited Plenary Lecture, Topic 1: PL11, December 3, 2018, Luxor, Egypt.

Contributed Presentations

1. C. G. Parigger, G. Gautum, C. M. Helstern, and K. A. Drake. Electron density and Temperature Distribution in Expanding Laser-Induced Plasma. 9th Euro-Mediterranean Symposium on Laser-Induced Breakdown Spectroscopy [EMSLIBS 2017], Poster presentation, Pisa, Italy: June 11-16, 2017

2. C. M. Helstern, and C. G. Parigger. Radial Distribution of Cyanide in Laser-Induced Plasma. 24th International Conference on Spectral Line Shapes (ICSLS), ICSLS 2018, Poster presentation, Dublin, Ireland: June 17-22, 2018

3. C. M. Helstern, and C. G. Parigger, "Application of Laser-Induced Breakdown Spectroscopy for Diatomic Cyanide Measurements," Federation of Analytical Chemistry and Spectroscopy Societies (FACSS): The Great Scientific Exchange (SCIX2018), Oral Presentation, Atlanta, GA, USA, October 23, 2018

Vita

Christopher Matthew Helstern was born on April twenty-third, 1987 in El Monte, CA. He graduated from Glendora High School located in Glendora, CA in 2005. Christopher went to the Univeristy of California located in Irvine, CA and in 2009 graduated with a Bachelor of Science in Physics. In June of 2011, Christopher began work with the State of Tennessee Department of Environment and Conservation Division of Radiological Health as a health physicist. In May of 2012, Christopher was accepted to the University of Tennessee and began graduate school, while continuing to work full-time. In May 2014, Christopher earned his Master's of Science degree under advisor Dr. Lloyd Davis. Christopher changed employment in August 2014 and began work as a health physicist at Vanderbilt University and Vanderbilt University Medical Center. In January 2017, Christopher returned to the Univeristy of Tennessee to pursue a Doctor of Philosophy in Physics under Dr. Christian Parigger, while continuing to work full-time. Later that year, Christopher became a diplomate of the American Board of Health Physics (ABHP) by completing the ABHP certified health physicist certification process. Christopher finished his doctoral dissertation in December 2020.